

# Shear Flow Instabilities in Quasi-Geostrophic Shallow-Water Magnetohydrodynamics



Luke Gostelow

Submitted in accordance with the requirements for the degree of Doctor of Philosophy

University of Leeds

Department of Applied Mathematics

September 2024

The candidate confirms that the work submitted is his own and that appropriate credit has been given where reference has been made to the work of others.

This copy has been supplied on the understanding that it is copyright material and that no quotation from the thesis may be published without proper acknowledgement.

©2024 The University of Leeds and Luke Gostelow

The right of Luke Gostelow to be identified as Author of this work has been asserted by him in accordance with the Copyright, Designs and Patents Act 1988.

# Abstract

Motivated by astrophysical considerations, the rotating shallow-water equations, originally derived in the context of the terrestrial atmosphere, have recently been extended to include a magnetic component. These are quasi-2D equations which can improve our ability to simulate the dynamics of thin, stratified, rotating magnetised layers, such as the tachocline, in a simpler setting. In the rapidly rotating limit a set of quasi-geostrophic shallow-water (QG SW) equations can be obtained; the analogous QG equations in the hydrodynamic case have been used successfully to model large-scale flows in the terrestrial atmosphere and oceans.

The QG SWMHD equations have not previously been used to study shear instability. Approximating the solar differential rotation as a zonal shear flow, we investigate the effects of rotation, stratification, and a magnetic field on the linear and nonlinear development of shear flow instabilities in the QG SWMHD system by deriving general linear stability results, investigating the linear instability of particular velocity profiles, and performing fully nonlinear direct numerical simulations.

We will first derive necessary conditions for the presence of linearly unstable modes and bound the phase speed and growth rate of these instabilities. We then consider the linear instability of the vortex sheet profile which can represent the limiting case of a wide class of shear profiles, and for which analytic solutions can be derived. We then investigate a smooth profile, the hyperbolic tangent profile, which naturally extends the study of the vortex sheet, and show that a second unstable mode appears which may be particularly relevant when the magnetic field is strong. We conclude by performing fully nonlinear simulations of the QG SWMHD equations, which provide new insight into features of the long-term evolution of the QG SWMHD system including flux expulsion and vortex disruption.



# Acknowledgements

First and foremost, I would like to thank my supervisors, David Hughes and Stephen Griffiths for their help and support in producing this thesis. Their thoughtful discussions over the last few years have been invaluable. I would also like to give particular thanks to Stephen, who as my undergraduate supervisor encouraged me to pursue postgraduate studies, and to David, who introduced me to this interesting and dynamic subject.

I would like to thank my friends, family and colleagues for their conversations and support throughout my study. In particular, Rob, Nils, Sam, Alexander, and Joseph, who have critiqued and enlightened me over numerous discussions, and also Phoebe and Bex, whose support outside of academia has been just as important. Finally, I would also like to thank my parents who have been beside me for much more than just this work and have been significant throughout. There are many others who I could mention, though sadly there is not the time here, I hope you know who you are.



# Contents

Abstract . . . . .	iii
Acknowledgements . . . . .	v
Contents . . . . .	vii
List of Figures . . . . .	xii
List of Tables . . . . .	xix
<b>1 Introduction</b>	<b>1</b>
<b>2 The Equations of QG Shallow-Water MHD</b>	<b>9</b>
2.1 Introduction . . . . .	9
2.2 Shallow-Water Equations in MHD . . . . .	10
2.2.1 Non-dimensionalisation . . . . .	11
2.2.2 The Momentum Equation . . . . .	12
2.2.3 The Induction Equation . . . . .	13
2.2.4 Non-dimensional Parameters . . . . .	13
2.2.5 Flux Function . . . . .	14
2.3 Quasigeostrophic Magnetohydrodynamics . . . . .	15
2.3.1 Diffusion Terms . . . . .	16
2.4 Quantities of Interest . . . . .	17
2.4.1 Potential Vorticity . . . . .	17
2.4.2 Conservation of Cross-Helicity . . . . .	18

2.4.3	Conservation of Energy . . . . .	18
2.5	Discussion . . . . .	19
2.5.1	The Solar Tachocline . . . . .	19
2.5.2	Rotating Shallow Water and Shear Flows . . . . .	21
2.5.3	Leading order magnetic field . . . . .	22
2.5.4	Conclusion . . . . .	22
<b>3</b>	<b>General Stability Results</b>	<b>23</b>
3.1	Introduction . . . . .	23
3.2	Linearisation . . . . .	25
3.2.1	Growth Rate Bound . . . . .	25
3.3	Normal Modes . . . . .	28
3.3.1	Transformations of the Linearised Equation . . . . .	28
3.4	Waves . . . . .	29
3.4.1	Waves in a Zonal Flow with Aligned Field . . . . .	29
3.4.2	Waves in an Arbitrary Uniform Field . . . . .	30
3.5	Profile Restrictions . . . . .	31
3.6	Semicircle Theorems . . . . .	32
3.6.1	Phase Speed Bounds . . . . .	33
3.6.2	Rest-Frame Semicircle . . . . .	34
3.6.3	Canonical-Frame . . . . .	34
3.6.4	Canonical-Frame Semicircle . . . . .	35
3.6.5	Semicircles in Two-Layer QG . . . . .	36
3.7	Discussion . . . . .	39
<b>4</b>	<b>Linear Instability of a Vortex Sheet</b>	<b>41</b>
4.1	Introduction . . . . .	41
4.2	Dispersion Relation . . . . .	42
4.2.1	Dispersion Relation: Derivation From A Prescribed Profile . . . . .	42

4.2.2	Dispersion Relation: Derivation From Long Wavelength Analysis . . . .	43
4.3	Spuriousity . . . . .	45
4.4	Stability Criteria . . . . .	47
4.5	Parameter Asymptotics . . . . .	48
4.5.1	Variation of $k$ . . . . .	48
4.5.2	Variation of $\mu$ . . . . .	55
4.5.3	Variation of $\beta$ . . . . .	58
4.5.4	Variation of $F^2$ . . . . .	60
4.6	Eigenfunctions . . . . .	63
4.7	Summary . . . . .	69
<b>5</b>	<b>Linear Instability of a Shear Layer</b>	<b>71</b>
5.1	Introduction . . . . .	71
5.2	Non-Singular Neutral Modes: $\beta$ -Plane QG . . . . .	73
5.2.1	Sturm-Liouville Theory . . . . .	74
5.2.2	Singularities . . . . .	74
5.2.3	Rayleigh Quotient . . . . .	75
5.2.4	An Exact Solution . . . . .	76
5.3	Singular Neutral Modes: $\beta$ -Plane QG . . . . .	80
5.3.1	First Solution . . . . .	81
5.3.2	Second Solution . . . . .	82
5.3.3	Jump at the singularity . . . . .	84
5.3.4	Numerical determination of leading coefficients . . . . .	85
5.4	Neutral Modes: QG SWMHD . . . . .	85
5.5	Numerical Results . . . . .	86
5.5.1	Verification of Results . . . . .	87
5.5.2	Variation with $F^2$ . . . . .	89
5.5.3	Variation with $M$ . . . . .	91
5.6	Existence of Multiple Modes . . . . .	96

5.6.1	The Trapped Mode . . . . .	97
5.6.2	The Radiating Mode . . . . .	98
5.6.3	Radiating vs Trapped . . . . .	98
5.6.4	Overlap Region . . . . .	100
5.7	Mode of Maximum Growth . . . . .	103
5.7.1	Variation with $\beta$ . . . . .	103
5.7.2	Variation with $M$ . . . . .	103
5.7.3	Variation with $F^2$ . . . . .	106
5.8	Properties of Unstable Modes . . . . .	106
5.8.1	Reynolds Stress of the Radiating and Trapped Modes . . . . .	107
5.9	Conclusions . . . . .	112
5.A	Appendix: Shooting Method . . . . .	115
<b>6</b>	<b>Vortex Disruption in Rotating, Magnetised Fluids</b>	<b>121</b>
6.1	Introduction . . . . .	121
6.2	Numerical Model and Verification . . . . .	124
6.2.1	Linear Development . . . . .	124
6.2.2	Nonlinear Kelvin-Helmholtz Evolution . . . . .	126
6.2.3	Magnetohydrodynamic Evolution . . . . .	127
6.3	$f$ -plane QGMHD - Disruption Scaling . . . . .	133
6.4	$f$ -plane QGMHD - Kinematic Evolution . . . . .	135
6.4.1	Potential Vorticity Dynamics . . . . .	135
6.4.2	Magnetic Field Growth . . . . .	136
6.5	$f$ -plane QGMHD - General Observations . . . . .	142
6.5.1	Oscillations of $\Delta$ . . . . .	142
6.6	$f$ -plane QGMHD - Mean Flow Changes . . . . .	143
6.A	Numerical Method . . . . .	145
6.A.1	Equations of Motion . . . . .	145
6.A.2	Basic State . . . . .	145

6.A.3	Boundary Conditions . . . . .	146
6.A.4	Initial Conditions . . . . .	146
6.A.5	Normalisation Transformation . . . . .	147
6.A.6	Temporal Discretisation . . . . .	148
6.A.7	Spatial Discretisation . . . . .	148
6.B	Fast (Quasi-Tridiagonal Matrix) Solver . . . . .	149
6.B.1	Transformation to normal form . . . . .	149
6.B.2	Solving a Split-Quasi-Tridiagonal System . . . . .	150
6.B.3	Solving in Fourier-Chebyshev space . . . . .	152
6.B.4	Example: The Vorticity Equation . . . . .	152
6.C	The Okubo-Weiss Parameter . . . . .	156
6.C.1	Definition . . . . .	156
6.C.2	The O-W Parameter for QG Flows . . . . .	157
6.C.3	Example: Two-dimensional MHD . . . . .	157
6.C.4	The Mak Disruption Parameter . . . . .	157
6.C.5	Example: Calculating $W$ with a Gaussian-averaging of $h$ . . . . .	158
6.D	Ellipticity and Eccentricity . . . . .	159
6.E	Growth Rate Tables . . . . .	162
6.E.1	2DMHD Simulations . . . . .	162
6.E.2	QG $F^2$ -varied Simulations . . . . .	162
6.E.3	QG $M$ -varied Simulations . . . . .	163
<b>7</b>	<b>Conclusions</b> . . . . .	<b>165</b>
7.1	Summary . . . . .	165
7.2	Future Work . . . . .	168



# List of Figures

1.1	The azimuthally averaged rotation rate of the interior of the Sun as determined by satellite observations. The figure is displayed so that the solar equator is along the horizontal axis and the rotation axis is along the vertical. The rate of rotation is specified in units of $\Omega/2\pi$ , in nHz (from Thompson et al., 2003).	2
1.2	Physical interpretation of the Kelvin-Helmholtz instability. Spirals represent the sign and magnitude of vorticity. Based on Huerre and Rossi (1998, p.169).	4
2.1	The Shallow Water Model	11
2.2	Variation in the dynamic (convective) Rossby number as a function of depth, given as a proportion of the Stellar radius. (Vasil et al., 2021)	20
4.1	The initial vortex sheet flow profile	41
4.2	The three solutions of the cubic equation (4.22) are plotted above (green, pink, cyan) for varied $k$ , $M^2 = 0.0$ , $\beta = 1.0$ , $F^2 = 1.0$ . Those roots which solve the dispersion relation (4.6) and satisfy the boundary conditions plotted with a filled line. The asymptotic approximations derived in section §4.5.1 are plotted in black and the spurious asymptotes derived in §4.3 are plotted as vertical red lines. The lower two plots show the real and imaginary parts of $\alpha_+$ , left, and $\alpha_-$ , right, showing the origin of spuriousity.	49
4.3	Plot of the three solutions of the cubic equation (4.22) for varied $k$ , $M^2 = 2.0$ , $\beta = 1.0$ , $F^2 = 1.0$ . Colours as in Figure 4.2.	50
4.4	Plot of the three solutions of the cubic equation (4.22) for varied $k$ , $M^2 = 0.0$ , $\beta = 1.0$ , $F^2 = 0.0$ . Colours as in Figure 4.2.	51
4.5	Plot of the three solutions of the cubic equation (4.22) for varied $k$ , $M^2 = 2.0$ , $\beta = 1.0$ , $F^2 = 0.0$ . Colours as in Figure 4.2.	52
4.6	Plot of the three solutions of the cubic equation (4.22) for varied $M$ , $k = 1.0$ , $\beta = 1.0$ , $F^2 = 1.0$ . Colours as in Figure 4.2.	55
4.7	Plot of the three solutions of the cubic equation (4.22) for varied $M$ , $k = 1.0$ , $\beta = 0.0$ , $F^2 = 1.0$ . Colours as in Figure 4.2.	56
4.8	Plot of the three solutions of the cubic equation (4.22) for varied $\beta$ , $k = 1.0$ , $M^2 = 0.0$ , $F^2 = 1.0$ . Colours as in Figure 4.2.	58
4.9	Plot of the three solutions of the cubic equation (4.22) for varied $\beta$ , $k = 1.0$ , $M^2 = 2.0$ , $F^2 = 1.0$ . Colours as in Figure 4.2.	59
4.10	Plot of the three solutions of the cubic equation (4.22) for varied $F^2$ , $k = 1.0$ , $M^2 = 0.0$ , $\beta = 1.0$ . Colours as in Figure 4.2.	61

4.11	Plot of the three solutions of the cubic equation (4.22) for varied $F^2$ , $k = 1.0$ , $M^2 = 2.0$ , $\beta = 1.0$ . Colours as in Figure 4.2. . . . .	62
4.12	Eigenfunction, $G(x, y)$ , of the vortex sheet instability, $\hat{\beta} = \hat{F}^2 = 0$ . . . . .	63
4.13	Variation of the eigenfunction, $G(x, y)$ , with $\hat{\beta}$ . $M^2 = \hat{F}^2 = 0$ . . . . .	65
4.14	Variation of the eigenfunction, $G(x, y)$ , with $M^2$ . $\hat{F}^2 = 0$ . . . . .	66
4.15	Variation of the eigenfunction, $G(x, y)$ , with $\hat{F}^2$ . $\hat{\beta} = M^2 = 0$ . . . . .	67
4.16	Variation of the eigenfunction, $G(x, y)$ , with $M^2$ . $\hat{\beta} = 0$ . . . . .	68
4.17	Example of the eigenvalues of dispersion relation (4.22) (with $c_i \geq 0$ ) in relation to the semicircle bound (3.62). $M^2 = 0.6$ , $\hat{\beta} = \beta/k^2 \in (0, 50)$ , $F^2 = 0$ . . . . .	69
5.1	The initial ‘‘tanh profile’’ flow . . . . .	71
5.2	Plots of the imaginary part $c_i = \mathbb{I}(c)$ of the eigenvalue, $c$ , and the growth rate, $\sigma = kc_i$ when $M = \beta = F^2 = 0$ , reproducing the solutions given by Michalke (1964). . . . .	87
5.3	Plots of the real $c_r = \mathbb{R}(c)$ and imaginary parts $c_i = \mathbb{I}(c)$ of the eigenvalue, $c$ , and the growth rate, $\sigma = kc_i$ when $M = F^2 = 0$ , mirroring the solutions given by Dickinson and Clare (1973). . . . .	88
5.4	Plots of the imaginary part of the eigenvalue, $\mathbb{I}(c) = c_i$ for varied $F^2$ with $k = 0.1$ (blue) and $k = 0.4$ (green). The upper plot is scaled linearly, whilst the lower plot is scaled logarithmically to highlight the large $F^2$ variation of $c$ . . . . .	90
5.5	Plots of the imaginary part of the eigenvalue, $\mathbb{I}(c) = c_i$ for varied $k$ with $F^2 = 0.1$ (blue), $F^2 = 0.5$ (green), $F^2 = 1.0$ (red), and $F^2 = 2.0$ (cyan). . . . .	91
5.6	Contour plots of the real and imaginary parts of the eigenvalue, $c$ , in $(\beta, k)$ space for $F^2 = 0.1, 0.5, 1.0$ . Overlaid is the neutral mode curve found in §5.2. The jump at around $k = 0.4$ is due to the mode tracking algorithm switching between the trapped and radiating modes. For small $c_i$ , close to the neutral mode, the shooting method struggles to converge to an eigenvalue due to singularities in the dispersion relation. . . . .	92
5.7	Plots of the imaginary part of the eigenvalue, $\mathbb{I}(c) = c_i$ for varied $k$ with $M^2 = 0.0$ (blue), $M^2 = 0.1$ (green), $M^2 = 0.3$ (red), $M^2 = 0.6$ (cyan), and $M^2 = 0.9$ (purple). . . . .	93
5.8	Imaginary part of the eigenvalue, $c_i = \mathbb{I}(c)$ , and the growth rate, $\sigma = kc_i$ , with varied $k$ for a case with moderate magnetic field $M^2 = 0.6$ , $\beta = 0$ and several values of $F^2$ . . . . .	94
5.9	Contour plots of the real and imaginary parts of the eigenvalue across a range of $\beta$ , $k$ , selected values of $M$ , and $F^2 = 0$ . Compare with the case $M = 0$ in Figure 5.3. White regions show where $c_i < 10^{-3}$ , or where the shooting method has failed to converge, particularly when two unstable modes co-exist. . . . .	95
5.10	Plot of the radiating eigenfunction (blue) at $\beta = 0.3$ , $k = 0.1$ ( $c \approx -0.394 + 0.058i$ , $\alpha_+ = -0.010 + 0.453i$ ) and the trapped eigenfunction (green) at $\beta = 0.6$ , $k = 0.8$ ( $c \approx -0.458 + 0.055i$ , $\alpha_+ = -0.479 + 0.016i$ ). The eigenfunctions are integrated in the normal way (§5.A) and then normalised so that $h(y = 0) = 1$ . . . . .	96
5.11	Contours of $\alpha_r$ and $\alpha_i$ (c.f. (5.104)) calculated from the numerically obtained eigenvalues, $c(k; \beta, M, F^2)$ . Here with $M = F^2 = 0$ . Note the different scales on the two plots. . . . .	98

5.12 Contours of  $\alpha_r$  and  $\alpha_i$  (c.f. (5.104)) calculated from the numerically obtained eigenvalues,  $c(k; \beta, M, F^2)$ . Here with  $F^2 = 0$  and  $M^2 = 0.5, 0.8$ . Note the different scales on the four plots. . . . . 99

5.13 Contour plots of  $c_r$  and  $c_i$  across varied  $\beta$  and  $k$  showing lines (parameterised by  $k$ ) over which the dominant mode of instability switches from the radiating to the trapped mode. The two unstable eigenvalues, along these curves, are shown in Figure 5.14 with corresponding colours. ( $M = F^2 = 0$ ) . . . . . 100

5.14 Plots of the eigenvalue,  $c$ , showing all unstable modes for particular fixed values of  $\beta$  and varied  $k$  ( $M = F^2 = 0$ ) given in Figure 5.13. The crosses on Figure 5.14c correspond to the eigenfunctions shown in Figure 5.15. . . . . 101

5.15 Plots of the real and imaginary parts of eigenfunctions for  $\beta = 0.17, k = 0.316$ , ( $M = F^2 = 0$ ) close to the exchange of dominance, normalised so that  $h(0) = 1$ . These correspond to the points on Figure 5.14c. The Wronskian,  $W(y)$ , is defined in equation (5.107). . . . . 102

5.16 Contours of the growth rate,  $\sigma = kc_i$  across varied  $\beta, k$ , when  $M = F^2 = 0$ . Stable (white) regions are defined by  $\sigma < 5 \times 10^{-3}$ . . . . . 104

5.17 The maximum growth rate,  $\sigma_{max}$  (orange), and the wavenumber,  $k_{max}$  (blue), at which this value of  $\sigma$  is attained across varied  $\beta$ , when  $M = F^2 = 0$ . . . . . 104

5.18 Contours of the growth rate,  $\sigma = kc_i$  across varied  $\beta, k$ , when  $F^2 = 0, M^2 = 0.5, 0.8$ . Stable (white) regions are defined by  $\sigma < 10^{-3}$ . . . . . 105

5.19 The maximum growth rate,  $\sigma_{max}$  (orange), and the wavenumber,  $k_{max}$  (blue), at which this value of  $\sigma$  is attained across varied  $\beta$ , when  $F^2 = 0, M^2 = 0.5, 0.8$ . (Note: the numerical imprecision in (b) is due to the smallness of the eigenvalue,  $c$ .) . . . . . 105

5.20 Variation of the growth rate,  $\sigma$ , with  $k$  for several values of  $F^2$  ( $\beta = M = 0$ ). The mode of maximum growth is marked with a black cross in each case. . . . . 106

5.21 Plots showing the maximum growth rate as a function of  $F^2$  when  $\beta = M^2 = 0$ . The asymptote in (b) has gradient  $\lambda = -0.175$ . . . . . 107

5.22 Eigenfunctions of the trapped mode. . . . . 108

5.23 Eigenfunctions of the radiating mode. . . . . 109

5.24 The radiating eigenfunction when  $c_i$  is small ( $k, \beta$ ) = (0.2, 0.36), normalised so that  $h(y) = 1$  when  $U(y) = \tanh y = c_r$ . The green line denotes the numerically determined solution and overlaid are the Frobenius solution (red) and the exponential solution (black). . . . . 110

5.25 Eigenfunctions corresponding to solutions when  $F^2 = 1.0$ . The blue and green curves show radiating modes ( $k, \beta$ ) = (0.1, 0.7), (0.2, 0.7), respectively, and the magenta and yellow curves show trapped modes, ( $k, \beta$ ) = (0.6, 1.2), (0.8, 1.2), respectively. (c.f. Figures 5.6e and 5.6f). . . . . 111

5.26 Eigenfunctions corresponding to solutions when  $M^2 = 0.5$ . The blue curve shows the radiating mode ( $k, \beta$ ) = (0.1, 0.18), and the green and magenta curves show trapped modes, ( $k, \beta$ ) = (0.35, 0.14), (0.55, 0.12), respectively. (c.f. Figures 5.9c and 5.9d). . . . . 111

5.27 Eigenfunctions corresponding to solutions when  $M^2 = 0.8$ . The blue curve shows the radiating mode ( $k, \beta$ ) = (0.1, 0.055), and the green and magenta curves show trapped modes, ( $k, \beta$ ) = (0.22, 0.021), (0.23, 0.005), respectively. (c.f. Figures 5.9e and 5.9f). . . . . 112

5.28	Plot of the normalised eigensolution of (3.27) with $k = 0.5$ , $\beta = 0$ , $M^2 = 0.5$ , and $F^2 = 0.5$ . The separate shots from the left and right are given in blue and orange, and the solution is only shown over $(-3, 3)$ but is calculated fully over the domain $(-10, 10)$ with Robin boundary conditions. . . . .	116
5.29	Contour plots of the logarithm of the objective function, $\log  f[G] $ , for a range of input values of $c_0$ . The topology of $f$ determines the convergence of the shooting method, Figure 5.30. . . . .	118
5.30	Contour plots showing regions where the shooting method converges (yellow) and diverges (blue) for a range of values of $c_0$ . Compare with the corresponding plots of the objective function, $f$ , in Figure 5.29. . . . .	119
6.1	A pictographic explanation of the phenomenon of <i>flux expulsion</i> given by Weiss (1964). . . . .	122
6.2	The steady state following <i>flux expulsion</i> by convective rolls when there is no reaction of the magnetic field back upon the fluid, given by Weiss (1964). . . . .	122
6.3	Comparison at $M = \beta = F^2 = 0$ between the numerical streamfunction, $h$ , at $t = 3$ , with $\text{Re}$ , $\text{Rm} = 1000, 500$ and the linear eigenfunction, $h$ , with critical $k = 0.446$ . . . . .	125
6.4	Plots of the kinetic energy split into its mean flow and perturbed components (left) and split using a Fourier mode decomposition (right) as compared to the expected energy growth (black dashed line) from linear theory ( $2\sigma = 2 \times 0.190$ ). This simulation was run with parameters $M = \beta = F^2 = 0$ , and $\text{Re}$ , $\text{Rm} = 1000, 500$ . . . . .	125
6.5	Grid showing (relative) vorticity and magnetic field lines (contours of $A$ ) during the early nonlinear evolution of the kinematic ( $M = 0$ ) instability ( $\text{Re} = 1000$ , $\text{Rm} = 500$ ). . . . .	126
6.6	Grid showing (relative) vorticity and magnetic field lines (contours of $A$ ) during the nonlinear evolution of the kinematic ( $M = 0$ ) instability ( $\text{Re} = 1000$ , $\text{Rm} = 500$ ). . . . .	127
6.7	Snapshots of the flow at increasing values of the non-dimensionalised initial magnetic field strength, $M$ , (top-to-bottom) at three times steps (left-to-right). ( $\text{Re} = 1000$ , $\text{Rm} = 500$ in simulations). . . . .	128
6.8	Snapshots of the Okubo-Weiss parameter, $W$ , (defined in §6.C), where vorticity-dominated regions (blue) and those regions where the shear is more important (orange) are distinguished. Large patches of vorticity-dominated flow are identified as vortices with the integral of $W$ giving some estimate of its strength. This allows us to quantify, as the magnetic field strength, $M$ , increases, the breakup of the Kelvin-Helmholtz vortex by magnetic effects ( $\text{Re} = 1000$ , $\text{Rm} = 500$ in simulations). . . . .	130
6.9	Plots of $\Delta(t)$ using the Okubo-Weiss parameter in Figure 6.8. $\Delta(t)$ approaches 1 (fully disrupted) as $M$ is increased and although $\Delta$ initially varies greatly with time, it eventually approaches a constant value, which can be compared with scaling estimates (§6.2.3) and results of Mak et al. (2017) ( $F^2 = \beta = 0$ , $\text{Re} = 1000$ , $\text{Rm} = 500$ in simulations). . . . .	131

6.10	A comparison of the theoretical scaling of disruption, $M^2\text{Rm}$ , against the numerically determined disruption, $\bar{\Delta}$ , for a number of simulations with fixed $\text{Rm} = 500$ and $F^2 = 0.0, 0.5$ . . . . .	132
6.11	The potential, magnetic and kinetic energies split into mean and perturbation components (left) and a breakdown of the kinetic energy into its Fourier modal components (right) for a QGMHD simulation with $F^2 = 0.5$ , $\beta = 0.0$ , $M = 0.08$ , $\text{Re} = 1000$ , $\text{Rm} = 500$ . . . . .	133
6.12	Plots of the disruption, $\Delta(t)$ , for simulations with $F^2 = 0.5$ . $\Delta = 1$ indicates that no vortex is present whilst $\Delta = 0$ indicates that a vortex equivalent to the QG ( $M = 0$ ) one is present. The top plot uses the same values of $M^2$ as Figure 6.9 ( $F^2 = 0.0$ ) and shows a significant decrease in disruption. The bottom plot shows a wider range of $M^2$ showing the variation of $\bar{\Delta} : 0 \rightarrow 1$ . ( $\text{Re} = 1000$ , $\text{Rm} = 500$ ) . . . . .	134
6.13	Snapshots of the relative vorticity, $\omega = \nabla^2 h$ , at increasing $F^2$ , showing a tendency towards jet-like, rather than vortex-like, dynamics. When $F^2$ is larger, the linear instability also grows more slowly, matching predictions ( $\text{Re} = 1000$ ). . . . .	137
6.14	Energy of discrete Fourier modes over time for simulations with $F^2 = 1.0$ (left) and $F^2 = 5.0$ (right) showing agreement with the expected growth rate of the $k = 1$ mode from linear instability analysis ( $\text{Re} = 1000$ , $\text{Rm} = 500$ , $M, \beta = 0$ ). . . . .	137
6.15	Lateral extent of the vortices, $\mathcal{L}$ against the growth rate, $\sigma$ . . . . .	138
6.16	The relative vorticity, $\omega = \nabla^2 h$ , magnetic field lines, $A$ , and magnetic Jacobian $\mathcal{J}(A, \nabla^2 A)$ at three times just after saturation of the linear instability ( $t \approx 50$ ) ( $\text{Re} = 1000$ , $\text{Rm} = 500$ , $\beta = F^2 = M = 0$ ). . . . .	139
6.17	Logarithm of the (spatial) maximum of the magnetic Jacobian, $\mathcal{J}(A, \nabla^2 A)$ , over time for two simulations with $F^2 = 0.0, 0.5$ showing the initial phase of exponential growth (straight line) transitioning into super-exponential growth during the flux expulsion stage, followed by algebraic dissipative decay ( $\text{Re} = 1000$ , $\text{Rm} = 500$ , $\beta = M = 0$ ). . . . .	140
6.18	Maxima of the magnetic Jacobian and field strength for several kinematic simulations with varied $F^2$ showing a decrease in the (temporal) maximum of both quantities as $F^2$ is increased ( $\text{Re} = 1000$ , $\text{Rm} = 500$ , $\beta = M = 0$ ). . . . .	141
6.19	The relative vorticity, $\omega = \nabla^2 h$ , and magnetic field lines (contours of $A$ ) during the main disruption stage corresponding to the peak and trough of $\Delta$ ( $90 \lesssim t \lesssim 120$ , cf. Figure 6.12). The parameters for this simulation are $F^2 = 0.5$ , $\beta = 0.0$ , $M = 0.08$ , $\text{Re} = 1000$ , $\text{Rm} = 500$ but the qualitative description (in text) remains unchanged for a surprisingly wide range of $M$ and a reasonably wide range of $F^2$ . . . . .	142
6.20	Relative vorticity, $\bar{\omega}(y)$ , averaged over $x$ , for $M = 0.00, 0.04, 0.06$ at several times ( $F^2 = 0$ , $\beta = 0$ , $\text{Re} = 1000$ , $\text{Rm} = 500$ ). . . . .	143
6.21	Relative vorticity, $\bar{\omega}(y)$ , averaged over $x$ , for $M = 0.00, 0.04, 0.06$ at several times ( $F^2 = 0.5$ , $\beta = 0$ , $\text{Re} = 1000$ , $\text{Rm} = 500$ ). . . . .	143
6.22	Relative vorticity, $\bar{\omega}(y)$ , averaged over $x$ , for $M = 0.00, 0.08, 0.10$ at several times ( $F^2 = 0.5$ , $\beta = 0$ , $\text{Re} = 1000$ , $\text{Rm} = 500$ ). . . . .	144
6.23	Plots of the vorticity, $\omega$ (left), and the vortex parameter, $W$ (right), for three flows with increasing disruption ( $\text{Re} = \text{Rm} = 500$ , $N_x = N_y = 512$ , $M = 0.01, 0.03, 0.05$ , $F^2 = \beta = 0$ , $L_x = 2\pi/0.446$ , $L_y = 8.0$ ; plot for $ y  \leq L_y/2$ ). . . . .	157

6.24	An example of calculating $W$ after averaging $h$ over several time with a Gaussian weighting. The rows show different values of $\sigma$ with time steps weighted by (6.85). . . . .	159
6.25	Constructions used to calculate the ellipticity. . . . .	161

# List of Tables

- 5.1 Values of the wavenumber,  $k$ , and eigenvalue,  $c$ , on the neutral mode at specific value of  $\beta$  used in Figure 5.14. . . . . 102
  
- 6.1 Table summarising the development in simulations of vortex disruption. (\*Not provided. † No explicit diffusion. <sup>1</sup>Compressible MHD. <sup>2</sup>Incompressible MHD. <sup>3</sup>Hydrostatic SWMHD. <sup>4</sup>Non-hydrostatic SWMHD. <sup>5</sup>Axisymmetric flow restriction. <sup>6</sup>Doubly-periodic domain.) . . . . . 123
- 6.2 Table of the wavenumber,  $k$ , and growth rate,  $\sigma$ , expected in simulations with  $M \geq 0$  (central column) compared to the wavenumber from linear theory that maximises growth rate (right column). . . . . 162
- 6.3 Parameters for a selection of simulations. (Re = 1000, Rm = 500,  $M = \beta = 0$ ) . 163
- 6.4 Table of the wavenumber,  $k$ , and growth rate,  $\sigma$ , expected in simulations with  $M \geq 0$  (central column) compared to the wavenumber from linear theory that maximises growth rate (right column). . . . . 164



# Chapter 1

## Introduction

Shear flows and shear instabilities are ubiquitous in the Universe; their interaction, with physical effects such as stratification, rotation, and magnetic field, can be critical to the evolution of many astrophysical systems, e.g., stars, planets, exo-planets and accretion disks. The effect on shear instability of each of these physical features, in isolation, is well-understood. This thesis investigates shear instability under the combined action of all these physical features to better understand dynamics, mixing, and turbulence inside rapidly rotating, thin astrophysical layers, such as the solar tachocline.

Of particular interest in this context is the solar tachocline, a thin transitional region in the solar interior that separates the convectively-driven outer layer of the Sun from the stably stratified radiative interior. Helioseismology, which involves the inversion of acoustic waves propagating in the solar interior, has established properties of these layers (e.g. Spiegel and Zahn, 1992; Schou et al., 1998; Christensen-Dalsgaard, 2002; Gough, 2007; Spiegel, 2007; Christensen-Dalsgaard and Thompson, 2007; Priest, 2014). The inner, radiative region is relatively quiescent with vertical motion impeded by strong stratification; it rotates uniformly, at a rate of about once every month. The convective region, meanwhile, is driven by the vertical upwellings of thermal convection and is significantly more turbulent than the radiative zone. The Reynolds stresses of these motions drive differential rotation in the convective region (Figure 1.1) whilst vertical convective motions mix the density across this layer. The net upshot of this is that the tachocline, which separates these regions, is strongly stratified and contains intense zonal shear flows with either predominantly meridional or radial shear depending on latitude and depth.

The existence of a magnetic field in the Sun has been confirmed by the observations of sunspots, coronal mass ejections, and the eleven-year activity cycle (22-year magnetic cycle) (Hale, 1908; Priest, 2014) and is driven by a solar dynamo (e.g. Jones et al., 2010). This dynamo is likely to be centred around the solar tachocline, where a toroidal magnetic field, which can be stored in the stably-stratified radiative interior, can be wound up by the zonal differential rotation which stretches the poloidal field; the poloidal field can then itself be excited by an  $\alpha$ -effect derived from the turbulent motions of the tachocline (Parker, 1955; Moffatt, 1978; Krause and Rädler, 2016; Tobias and Weiss, 2007; Charbonneau, 2014). The origins of these motions have been widely discussed. Possibilities include magnetic buoyancy

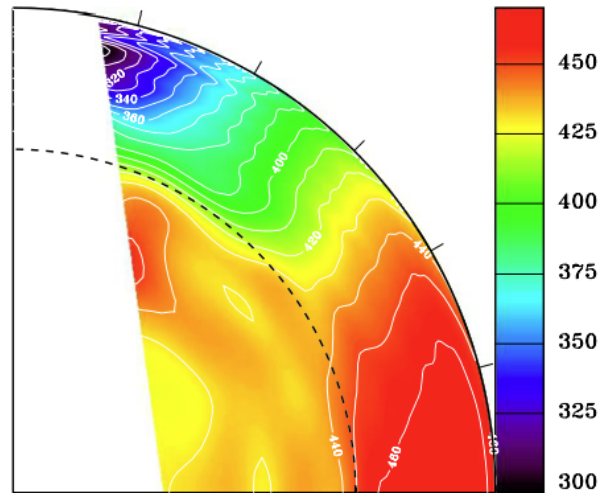


Figure 1.1: The azimuthally averaged rotation rate of the interior of the Sun as determined by satellite observations. The figure is displayed so that the solar equator is along the horizontal axis and the rotation axis is along the vertical. The rate of rotation is specified in units of  $\Omega/2\pi$ , in nHz (from Thompson et al., 2003).

instability (Moffatt, 1978; Schmitt, 1993; Thelen, 2000; Davies and Hughes, 2011; Duguid et al., 2023), magneto-convection (Miesch, 2005, and references therein), and instabilities of the differential rotation (Watson, 1980; Gilman and Fox, 1997; Dikpati and Gilman, 2001a,b; Gilman and Dikpati, 2002; Dikpati et al., 2003, 2004).

An efficient way of modelling the solar tachocline that captures the effect of stratification is using a shallow-water (SW) model, which has been well-studied in the past primarily owing to its relevance to geophysical fluid dynamics in the oceans and atmosphere (Lamb, 1993; Gill, 1982; Pedlosky, 1987; Vallis, 2017). The SW model describes the dynamics of a quasi-two-dimensional layer of constant density bounded by a free surface above and a fixed topography below. It is well-suited to thin, stably stratified regions such as the solar tachocline since key dynamics such as gravity waves are represented by the free surface whilst other features such as sound waves and overturning motions, which would increase the computational difficulty and complexity of the model, are filtered out. Layers without truly fixed lower or free upper boundaries, such as in the solar tachocline, can be modelled by associating the free surface with an internal surface, with an effectively reduced gravity inferred from internal gravity waves. Whilst seemingly simplistic, the SW equations can also be obtained by depth-averaging the full Navier-Stokes equations, indicating a more fundamental relationship with the fully three-dimensional dynamics (Jeffreys, 1926; Obukhov, 1949; Zeitlin, 2007). Stratification can be more accurately included by stacking several layers with decreasing densities.

Magnetic effects can be brought into the shallow water model, leading to the shallow-water MHD (SWMHD) equations of Gilman (2000). The SWMHD system can model the interaction of shear flows, magnetic fields, and stratification and has been used extensively as a model of the solar tachocline, particularly to investigate the instability of differential rotation (Gilman and Dikpati, 2002; Dikpati et al., 2003), but also for general features such as conservation laws (De Sterck, 2001; Dellar, 2002; Gilbert et al., 2025), waves (Schechter et al., 2001;

Zaqarashvili et al., 2007, 2009; Hunter, 2015), and instabilities (Mak et al., 2016, 2017) which may correspond to smaller scale phenomena and mixing.

There are several ways to incorporate rotation into a model, the simplest of which is to simulate the entire domain, or rather with the shallow-water model, a spherical shell (e.g. Dikpati and Gilman, 2001a). The rotation is then a natural feature of the initial fluid flow. However, global models such as these often suffer from an inability to capture small-scale effects due to resolution limits. Instead, one could consider a smaller region of the Sun, modelled as a (uniformly) rotating tangent plane; effects of sphericity can then be included through a latitudinally varying (Coriolis) force. This can be readily extended to the shallow-water equations. Rotation introduces a new parameter, the Rossby number,  $Ro$ , representing the relative importance of inertia and the Coriolis force. On large scales, the Rossby number is small (Pedlosky, 1987, reverses this and defines “large scale” on, for example, the Earth, as scales where  $Ro \ll 1$ ), and the Coriolis force is significantly larger than inertial forces resulting in a leading order “geostrophic” balance with pressure. A similar balance can be reached by systematically neglecting fast motion in rotating shallow water, which often has a negligible effect on bulk fluid motion, in favour of slow motions mostly responsible for vorticity propagation (Majda and Wang, 2006).

Geostrophic balance provides a leading order ( $\mathcal{O}(1)$ ) constraint on the velocity field but does not predict its evolution since time derivatives appear only at  $\mathcal{O}(Ro)$  in the Navier-Stokes equations. Consideration of the  $\mathcal{O}(Ro)$  term leads to a quasi-geostrophic equation that expresses the conservation of potential vorticity and can be used to model the evolution of fluids on large scales (Charney, 1948). Similar to how the three-dimensional Navier-Stokes equations can be simplified to the shallow-water equations, the quasi-geostrophic (QG) equations represent a significant reduction in complexity over the rotating SW equations whilst important features, particularly vorticity dynamics, are largely unaffected. The QG equations have been widely used, particularly in atmospheric contexts where efficient integration of large-scale motion is desired for weather and climate predictions (e.g., Pedlosky, 1987; Zeitlin, 2007).

QG equations can also be derived from the rSW MHD equations (Zeitlin, 2013; Zeitlin et al., 2015), in much the same way, provided that the Lorentz force enters the balance at  $\mathcal{O}(Ro)$  (see also “magnetoquasigeostrophic equations”: Umurhan, 2013). The QG (SW)MHD equations obtained represent the evolution of potential vorticity (with conservation broken by the inclusion of MHD effects) and the evolution of magnetic flux. Several authors have used this model to investigate properties of waves, instabilities, and zonal flows in the solar tachocline (Fedotova et al., 2020; Petrosyan et al., 2020; Zaqarashvili et al., 2021).

## Vorticity

An important concept in all of these reduced systems is vorticity, the curl of the velocity field,  $\boldsymbol{\omega} = \nabla \times \mathbf{u}$ , which represents the local rotation of a fluid element. It is relevant to fluid dynamics in general (e.g. Kundu and Cohen, 2002, §5), but especially to the discussion of shear flows and shear instabilities since shear flows correspond to non-zero vorticity and instability to the redistribution of vorticity in these flows, often into vortices. Vorticity is generally a vector quantity with an axis about which (local) rotation occurs. However in two-dimensional flows, since this rotation axis is always perpendicular to the plane, vorticity

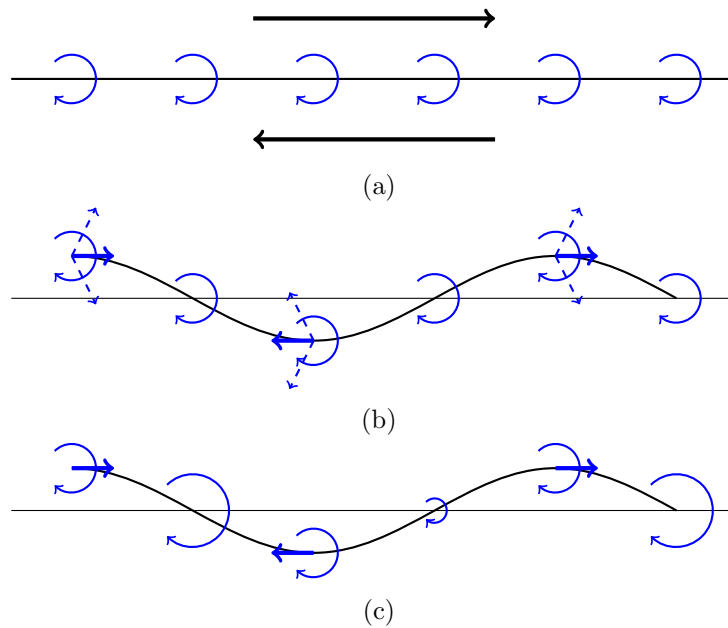


Figure 1.2: Physical interpretation of the Kelvin-Helmholtz instability. Spirals represent the sign and magnitude of vorticity. Based on Huerre and Rossi (1998, p.169).

effectively becomes a scalar quantity, with only one non-zero component. Additionally, it is materially conserved and is therefore a useful tracer and indicative of how the flow will develop (e.g. Batchelor, 1967).

Vorticity will naturally be measured differently depending on whether a global velocity field (absolute vorticity) or the velocity field on a rotating tangent plane (relative vorticity) is used to calculate it; the difference is known as planetary vorticity. In shallow water, the horizontal components of the relative and planetary vorticity are non-zero, but (asymptotically) small (see §2.2.1). The vertical component of the absolute vorticity, a scalar known as the potential vorticity, is materially conserved by the rotating shallow-water and quasigeostrophic equations and is a natural extension of the 2D vorticity.

In the presence of a magnetic field vorticity conservation is broken, by a degree proportional to the magnetic field strength. This means that local vorticity transfers are still important to consider (e.g. §6), particularly where the magnetic field is weak, but it is more difficult to establish general theorems based on vorticity conservation (e.g. §3).

## Linear Stability Theory

Shear flows can be another source of vorticity. The vortex sheet flow, consisting of two distinct constant velocity regions, has all the vorticity of the flow contained at the infinitesimally thin separating interface. Thomson (1871) and Helmholtz (1868) showed that this was an unstable configuration and determined the rate at which the instability grows. Batchelor (1967) (see also Huerre and Rossi, 1998) offers an interpretation of this *vortex sheet* instability in terms

of induced vorticity perturbations (Figure 1.2): The vorticity of a vortex sheet is initially evenly spread over the interface (Figure 1.2a). If this interface is perturbed (Figure 1.2b), velocity perturbations, corresponding to the dashed arrows, are induced by the vorticity of neighbouring crests/troughs; the net effect of this is the velocity perturbation given by the bold arrow. Since vorticity is conserved, these perturbations lead to a depletion of vorticity at the peaks/troughs of the instability and corresponding accumulations at the inflexion points (Figure 1.2c). Redistributing vorticity like this promotes the initial perturbation's growth, leading to instability.

Increasing the perturbation's wavenumber increases the instability's growth rate since adjacent peaks are brought closer together, however, this suggests that infinitesimally short waves grow infinitely quickly. One way this apparent paradox can be resolved is by removing the discontinuity of velocity from the basic state. A simple way to do this is to split the velocity jump into two vorticity jumps, i.e., separate the two regions of constant velocity flow with a transition region of linearly decreasing velocity (constant vorticity). The instability growth rate ( $\sigma$ ) can be found to be

$$\sigma \propto \left( e^{-2k} - (k-1)^2 \right)^{1/2} = \left( k + \mathcal{O}(k^2) \right), \quad (1.1)$$

(Rayleigh, 1880; Chandrasekhar, 1961), where  $k$  is the zonal wavenumber. So, whilst the growth rate is still the same for asymptotically small  $k$  (long wavelengths), there is now a finite value of  $k$  at which the growth rate becomes imaginary, i.e. the profile becomes stable.

The two examples above can be solved analytically and are useful for showing important elements of shear instability. Realistic flows, however, are rarely so simple in structure and often require numerical techniques to determine instability. Integral methods can also be used, with the advantage that they can be applied generally, though they lead to bounds rather than complete solutions. Rayleigh (1913) was the first to establish a general theorem showing, by integration of the linearised vorticity equation, that an inflexion point (an extremum of the vorticity) is necessary for a continuous velocity profile to be unstable. Fjørtoft (1950) extended this result to show that this must be a vorticity maximum.

In the first half of the twentieth century, this problem was expanded upon to include the effects of density stratification (Taylor, 1915; Synge, 1933) which lead to the Miles-Howard theorem that *a necessary condition for instability is that the Richardson number,  $Ri = N^2/u'^2$  is somewhere less than  $\frac{1}{4}$ , where  $N$  is the Brunt-Väisälä frequency* (Miles, 1961). Howard (1961) then discovered an additional bound on the growth rate of unstable modes, known as the semicircle theorem for the shape of the bound in the complex plane. This can be applied to the Solar tachocline using the values of Gough (2007) and it is easy to show that baroclinic shear flows here should be well inside the stable region, hence our focus on barotropic flows.

The shear instability problem was separately expanded upon by Kuo (1949) to include the effects of rotation. The constant part of the Coriolis force does not affect instability whilst the contribution from its latitudinal variation can lead to multiple unstable modes which travel anti-rotationally (Dickinson and Clare, 1973), and can even suppress the instability entirely (Fjørtoft, 1950). The overall effect of this can be exceptionally complex, and we will discuss some of the more interesting results later.

The magnetic field, assumed to be, at least initially, aligned with the flow is often a stabilising influence (Chandrasekhar, 1961; Michael, 1955; Kent, 1966b) since the field acts as a tensile force on streamlines; it can be shown that all flows of this type are stable if the magnetic energy exceeds the kinetic (Kent, 1968). However, it is possible to construct flows which are hydrodynamically stable yet unstable in the presence of a field (Kent, 1966a); it seems that any simple heuristic understanding of the effects of magnetism is usually insufficient. Considerable effort has been spent in attempting to generalise even simple hydrodynamic results, with a notable success being the discovery of an extended semicircle theorem which gives bounds on the growth rate and phase speeds of unstable modes (Hughes and Tobias, 2001).

## Nonlinear Simulations

Linear instability is characterised by the exponential growth of small perturbations. Such rapid growth cannot persist eternally since the pool of available energy and vorticity is finite and thus linear growth gives way to the nonlinear evolution of shear instability.

The nonlinear phase of instability begins as the nonlinear terms in the equation of motion develop to leading order. Comparing the relative sizes of linear and nonlinear terms, with knowledge of the fastest growing mode(s), can be used to predict the structure of the flow at the outset (Arnol'd, 1965). Since shear instability is generally two-dimensional (Squire, 1933), and vorticity tends to accumulate in such flows, the onset of the nonlinear phase of shear instability is often associated with the formation of a vortex.

Vortices are a fundamental feature of many fluid systems. They are observed in various scales within Earth's atmosphere, ranging from small-scale eddies to large-scale phenomena like cyclones and hurricanes. These vortices play crucial roles in atmospheric dynamics, influencing weather patterns, heat distribution, and air circulation. In the ocean, vortices can be seen in the form of eddies, whirlpools, and large-scale currents. These vortices affect ocean circulation, the mixing of water masses, and nutrient distribution, impacting marine ecosystems and climate patterns (e.g. Green, 1995). In astrophysics, vortices exist too across a wide selection of scales from the polar vortices and the Great Red Spot on Jupiter, where competing convective and Coriolis forces give rise to spectacular visuals, to Sunspots, where vortical flows have wound the magnetic field into thin flux ropes that break through the heliosphere, to accretion and protostellar discs.

The lifetime of vortices is determined by their stability, which itself depends on the physics of the system they inhabit. If more than one vortex is present in the system, vortices tend to combine, known as the vortex-pairing instability. This sort of instability often occurs in shear instability simulations as vortices form at scales determined by the width, rather than the length, of shear layers. The result of this is the formation of a single vortex possessing the majority of the (relative) vorticity of the system.

In planar, hydrodynamic, and barotropic flows, isolated vortices are unstable only to diffusion. Batchelor (1956) has shown that diffusion will initially homogenise vorticity (Rhines and Young, 1983, and other passive scalars) within closed streamlines over relatively short timescales, even in geo- and astrophysical flows where viscosity may be exceptionally small. Over much longer timescales, the homogenised vortex will expand and dilute until vorticity

is fully diffused over the domain.

In three-dimensional systems, energy cascades towards small scales, meaning that vortices, which are fundamentally two-dimensional phenomena, must be destroyed. This can occur through the elliptical instability (e.g. Kerswell, 2002).

In SW systems elliptical instability is impossible due to the model assumptions (or equivalently, due to the effect of stable stratification along the axis of rotation). Vortices in SW can instead be depleted by the emission of gravity or similarly, by Rossby waves in the presence of rotation. This instability, known as Lighthill radiation (Lighthill, 1957), can lead to the dissipation of vortices over much more rapid timescales than viscous diffusion.

In magnetohydrodynamic flows, vortices can be subject to rapid instability that occurs due to the homogenisation of magnetic flux, which can behave (initially) as a passive scalar when the background magnetic field is weak (this often being a condition for the initial formation of a vortex) (Weiss, 1966; Parker, 1966). As magnetic flux is evened out within the closed streamlines of the vortex, a significant flux gradient, corresponding to a large magnetic field, can develop at the vortex edges (Weiss, 1964). The radial force from this field, sometimes combined with vortex inhomogeneities, can lead to the destruction (or disruption) of the vortex. Since the energy cascade, even in two-dimensional flows, is to small scales, the result of vortex breakup is often turbulent.

Exploring the nonlinear evolution of shear instability usually requires numerical simulations. This has been the path of numerous authors, who have explored nonlinear shear instability in a variety of systems. Often though, the aim is to associate the nonlinear evolution with the phenomena described above. Of particular interest is vortex disruption, since it is associated with the  $\alpha$ -effect and the formation of magnetic flux ropes around the solar tachocline (e.g. Mak et al., 2017). Another interest in vortex disruption is as an explanation for the reduction in the inward spreading of the tachocline into the solar interior. Spiegel and Zahn (1992) show that such an inward spreading would be inevitable if diffusion in the tachocline were isotropic (which arises, for example, from molecular diffusion), however, if diffusion arises from turbulent sources, it may be anisotropic and horizontally preferential. In this case, the rate of inward spreading of the tachocline is greatly reduced, matching observations. One possibility for the source of such turbulence is shear instability and vortex disruption.

## Aims of Thesis

We begin in Chapter 2 with a derivation of the equations of (rotating) shallow-water MHD following Gilman (2000), from the inviscid, constant density Navier-Stokes and induction equations in a rotating, stably stratified, and laterally unbounded system. We then proceed to derive the QG SWMHD equations of Zeitlin (2013), which aims to simplify the rotating aspect of the flow, following standard geophysical lines (Zeitlin, 2007; Pedlosky, 1987). These equations are designed to model large-scale instabilities in the solar tachocline, but could also be applied to other systems such as accretion disk models (Balbus and Hawley, 1998), planetary atmospheres (Busse, 1994; Jones et al., 2003) and the solar differential rotation (Thompson et al., 2003; Miesch et al., 2006). Chapters 3, 4, and 5 will then discuss aspects of the linear shear instability problem in this system. Chapter 3 will derive the governing equation, given an arbitrary initial shear flow and magnetic field, and use this equation to derive

general instability results including a semicircle theorem and growth rate bound, discussing both, as well as why they may (or may not) differ from similar results in other models. We will also derive a QG SWMHD version of Rayleigh's inflexion point, and Fjörtoft's criteria. As Kent (1966a) and Hughes and Tobias (2001) also note though, these are of limited practical use due to the inclusion of the eigenvalue as part of the criteria.

Following the discussion of general shear flows, we will discuss in chapters 4 and 5 two archetypal shear flows, which are both hydrodynamically unstable, to investigate particular properties of the shear instability mechanism and, particularly in chapter 5, develop a prediction of the structure of the instability before nonlinearity sets in, which will be discussed in chapter 6. The magnetic field, for the flows of both chapters, is assumed to be constant so that the underlying mechanism is fundamentally shear, rather than magnetically, driven. Chapter 4 will discuss the piece-wise constant, vortex sheet instability, which is useful to begin with since it is one of the few profiles that can be solved analytically. We will use it to demonstrate the stabilising influence of the magnetic field and some of the effects of rotation and stratification. The vortex sheet can also be derived, rather than prescribed, from long-wavelength asymptotics of smooth shear profiles. This means that the results of Chapter 4 can also be used to verify, and contrast, those of Chapter 5, which examines the tanh profile that has been used by Michalke (1964), among others, to look at the effect of broadening the shear layer, on shear instability. The tanh profile is often used for this purpose since particular limits exist with analytic solutions, although in general a numerical eigenvalue solver is required. We begin Chapter 5 by investigating the properties of some of these analytic solutions and also examine the difficulty of finding such solutions when magnetic effects are included. The second half of Chapter 5 will then build from these analytic results and use a shooting method to investigate the effect of rotation, stratification, and magnetic field on instability.

Finally, in Chapter 6, we will investigate the nonlinear phase of shear instability. In particular, we will use an initially weak magnetic field and allow the development of a vortex to investigate the processes of flux expulsion and vortex disruption. We examine the effects of stratification and rotation on the development of the vortex and use several different techniques to investigate how the underlying mechanism is altered by this physics, which are both important to the development of flows in the solar tachocline.

## Chapter 2

# The Equations of QG Shallow-Water MHD

### 2.1 Introduction

In this chapter we derive the equations of motion for a (shallow) rapidly rotating layer of magnetised fluid under gravity. This is based on the shallow water magnetohydrodynamic (SWMHD) model of Gilman (2000) and the quasigeostrophic (QG) SWMHD model of Zeitlin (2013). These governing equations will provide a foundation for the rest of the work in this thesis.

The hydrodynamic shallow-water model has been used extensively in geophysical problems since it can accurately describe the large-scale dynamics of the stably-stratified atmosphere and oceans (e.g. Gill, 1982). The essence of the model is to exploit the small aspect ratio of vertical-to-horizontal length scales to derive quasi-two-dimensional equations, independent of the vertical coordinate  $z$ , which still possess many of the dynamics of the three-dimensional system, such as gravity waves. The  $z$ -dependence of the flow can then be inferred after the fact, if necessary. These equations can also be derived by vertically averaging the Navier-Stokes equations (Jeffreys, 1926; Zeitlin, 2007).

Flows on these scales also tend to be in geostrophic balance (Holton, 1979) since fast motion is rapidly propagated away from disturbances by inertia-gravity waves (Obukhov, 1949; Blumen, 1972). As such, an asymptotic expansion in the Rossby number ( $Ro$ , the ratio of rotational to inertial time scales) can be performed. The leading-order equations then produce geostrophic balance whilst the first-order equations determine the evolution of the flow (Charney, 1948). This procedure reduces the number of dependent variables from three ( $u, v, h$ ) to one ( $h$ ) yet still accurately represents synoptic-scale dynamics.

The discovery of the solar tachocline (Spiegel and Zahn, 1992) then prompted the derivation of shallow-water MHD equations which could be relevant, in particular, to the stably-stratified lower layer of the tachocline (Gilman, 2000). A major assumption of these equations, however, is that the magnetic field must be tangential to the upper and lower boundaries, ruling out dynamo action, for example (Gilbert et al., 2025). Although it is possible to derive

SWMHD equations without this assumption, they then have a more complex form, and vortex disruption evolves similarly in both cases (Dritschel and Tobias, 2023). We also do not expect this assumption to significantly affect the results of Chapter §3. The SWMHD equations have since been used extensively to describe the dynamics of the tachocline (Dikpati and Gilman, 2001a,b; Schecter et al., 2001; Gilman and Dikpati, 2002; Dikpati et al., 2003; Heng and Spitkovsky, 2009; Hunter, 2015; Mak et al., 2016; Márquez-Artavia et al., 2017; Dikpati et al., 2018; Fedotova et al., 2020; Horstmann et al., 2023).

Zeitlin (2013) then proceeded to show that the SWMHD equations can be derived by vertical averaging, much like the SW equations, and also that quasigeostrophic (QG) SWMHD equations can be derived in much the same way as the hydrodynamic case. Several authors have then investigated properties of the QG SWMHD equations, such as Zeitlin et al. (2015) who have studied the process by which general states adjust towards a quasi-geostrophic equilibrium, and Raphaldini et al. (2023) who studied the Hamiltonian properties of the system. Generally, the equations are used as a simplified model for the solar tachocline (Teruya et al., 2022; Lahaye and Zeitlin, 2022; Raphaldini et al., 2024), they have also been shown to be useful in studying the uppermost stratified layer of Earth’s outer core (Raphaldini and Raupp, 2020).

The chapter begins by re-deriving the SWMHD equations (§2.2) and then the QG SWMHD equations (§2.3) in the usual way. In §2.4 we will discuss some general properties of these equations such as conserved quantities. We conclude in §2.5.

## 2.2 Shallow-Water Equations in MHD

The Navier-Stokes equations for an incompressible magnetised fluid with velocity,  $\mathbf{U}$ , magnetic field,  $\mathbf{B}$ , and total (gas plus magnetic) pressure,  $P$ , are given by

$$\frac{\partial \mathbf{U}}{\partial t} + \mathbf{U} \cdot \nabla \mathbf{U} + f(y) \hat{\mathbf{z}} \times \mathbf{U} = -\nabla \frac{P}{\rho} - g \hat{\mathbf{z}} + \frac{1}{\mu_0 \rho} \mathbf{B} \cdot \nabla \mathbf{B} + \nu \nabla^2 \mathbf{U}, \quad (2.1)$$

$$\frac{\partial \mathbf{B}}{\partial t} + \mathbf{U} \cdot \nabla \mathbf{B} = \mathbf{B} \cdot \nabla \mathbf{U} + \eta \nabla^2 \mathbf{B}, \quad (2.2)$$

where  $\rho$  represents the density,  $\mu_0$  represents the permittivity of free space, and  $\nu, \eta$ , are the (constant) kinematic viscosity and magnetic diffusivity respectively. We will drop the diffusive terms here and reintroduce them in the final equations for reasons that will be clarified later. The Coriolis force,  $f(y) \hat{\mathbf{z}} \times \mathbf{U}$ , is also introduced in the tangent-plane approximation with standard geometry, i.e,  $y$  is the relative latitude and  $\hat{\mathbf{z}}$  is the effective direction of gravity (with magnitude  $g$ ), perpendicular to surfaces of constant geopotential.

Solenoidal conditions then supplement these two equations

$$\nabla \cdot \mathbf{U} = 0, \quad (2.3)$$

$$\nabla \cdot \mathbf{B} = 0, \quad (2.4)$$

which are constraints on the flow,  $\mathbf{U}$ ,  $\mathbf{B}$ , that must be satisfied by the initial conditions and are then preserved by the momentum and induction equations, (2.1), (2.2), and at boundaries.

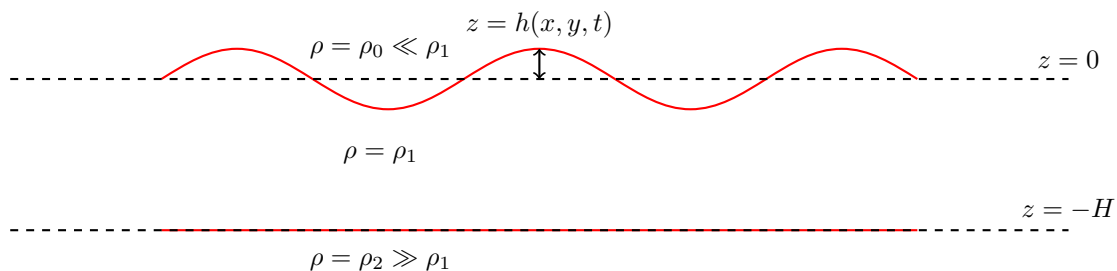


Figure 2.1: The Shallow Water Model

These equations can then be applied to a fluid layer in e.g. the solar tachocline, with density  $\rho_1$ , and stratification modelled by supposing the presence of a less dense ( $\rho_0 \ll \rho_1$ ) fluid above and a more dense and dynamically inactive fluid,  $\rho_2 \gg \rho_1$ , below. The motion of this layer may penetrate the lighter fluid above but not the heavier fluid below, hence the upper boundary of the fluid is given by a free interface,  $z = h(x, y, t)$ , with mean height,  $z = 0$ , and the lower boundary by the fixed level,  $z = -H$ . Both interfaces are assumed to be perfectly conducting. Such a model could be extended with the use of multiple layers (e.g. Hunter, 2015). The geometry described is shown in Figure 2.1.

### 2.2.1 Non-dimensionalisation

Let us assume the existence of characteristic scales for the horizontal and vertical velocity,  $U$  and  $W$  respectively, as well as the horizontal and vertical magnetic field,  $B$  and  $B_z$ . Furthermore, suppose that motions occur on a horizontal scale,  $L$ , much larger than the layer depth,  $H$  i.e. the aspect ratio  $\varepsilon = H/L \ll 1$ . Consideration of the solenoidal conditions, (2.3) and (2.4), then imply that  $W \sim \varepsilon U$ , and  $B_z \sim \varepsilon B$ .

It is then useful to split the equations into horizontal and vertical components such that  $\mathbf{U} = U(\mathbf{u} + \varepsilon w \hat{\mathbf{z}})$  and  $\mathbf{B} = B(\mathbf{b} + \varepsilon b_z \hat{\mathbf{z}})$  and non-dimensionalise the variables

$$x = L\hat{x}, \quad y = L\hat{y}, \quad z = H\hat{z}, \quad t = T\hat{t} = \frac{L}{U}\hat{t}, \quad h = \delta\hat{h}, \quad (2.5)$$

where the height-scale of surface perturbations,  $\delta$ , is unknown and will be determined in the following steps. We also use the  $\beta$ -plane approximation,

$$f(y) \approx f(0) + y \frac{df}{dy}(0) = f_0 + \beta_0 L \hat{y}, \quad (2.6)$$

since  $L$  is significantly smaller than  $R_\odot$ , the solar radius, and higher-order terms in the expansion of  $f$  are  $\mathcal{O}(L^2/R_\odot^2)$ .

### 2.2.2 The Momentum Equation

First, let us consider the vertical component of the momentum equation, which with the scalings above becomes

$$\varepsilon \frac{U^2}{L} \frac{\partial w}{\partial \hat{t}} + \varepsilon \frac{U^2}{L} \left( \mathbf{u} \cdot \nabla w + w \frac{\partial w}{\partial \hat{z}} \right) = -\frac{1}{\rho H} \frac{\partial P}{\partial \hat{z}} - g + \varepsilon \frac{B^2}{\mu_0 \rho L} \left( \mathbf{b} \cdot \nabla b_z + b_z \frac{\partial b_z}{\partial \hat{z}} \right), \quad (2.7)$$

where

$$\nabla = \frac{\partial}{\partial \hat{x}} \hat{\mathbf{x}} + \frac{\partial}{\partial \hat{y}} \hat{\mathbf{y}} \quad (2.8)$$

is the horizontal component of the full gradient operator.

The pressure,  $P$ , has not been non-dimensionalised and will enter the leading order balance in (2.7). Assuming  $\varepsilon \ll 1$  then the leading order balance is magnetohydrostatic,

$$-\frac{1}{\rho H} \frac{\partial P}{\partial \hat{z}} - g = \mathcal{O}(\varepsilon) \approx 0. \quad (2.9)$$

This can be integrated from an arbitrary depth  $-H < H\hat{z} < \delta\hat{h}$  in the fluid to some reference height at which the pressure is assumed to be approximately constant, say  $P_0$ . In oceanic contexts, this is generally taken as  $h(x, y, t)$ , i.e. that  $h$  is a free surface and so

$$P = P_0 - \rho_1 g \left( H\hat{z} - \delta\hat{h} \right). \quad (2.10)$$

However, in continuously stratified fluids, such as the solar tachocline, one cannot neglect the density of the fluid above, so we can integrate instead to a reference height,  $z = z_0$ , in the layer above (assumed to be at constant pressure), to get

$$\begin{aligned} P &= P_0 - \rho_1 g \left( H\hat{z} - \delta\hat{h} \right) - \rho_0 g \left( \delta\hat{h} - z_0 \right), \\ &= P_0 - \rho_1 \left( gH\hat{z} - g'\delta\hat{h} \right) + \rho_0 g z_0, \end{aligned} \quad (2.11)$$

where  $g' = g(\rho_1 - \rho_0)/\rho_1$  is known as the reduced gravity and can be estimated from the observed speed of internal gravity waves ( $c_g \approx \sqrt{g'H}$ ). Equation (2.11) can be used to determine the horizontal pressure gradient,

$$\nabla P = \rho_1 g' \delta \nabla \hat{h}, \quad (2.12)$$

which can be substituted into the horizontal momentum equation to give

$$\frac{U^2}{L} \frac{\partial \mathbf{u}}{\partial \hat{t}} + \frac{U^2}{L} \left( \mathbf{u} \cdot \nabla \mathbf{u} + w \frac{\partial \mathbf{u}}{\partial \hat{z}} \right) + f_0 U f(y) \hat{\mathbf{z}} \times \mathbf{u} = -\frac{g'\delta}{L} \nabla \hat{h} + \frac{B^2}{\mu_0 \rho L} \left( \mathbf{b} \cdot \nabla \mathbf{b} + b_z \frac{\partial \mathbf{b}}{\partial \hat{z}} \right). \quad (2.13)$$

Since  $\nabla h$  is independent of  $z$ , there exists a consistent solution  $\mathbf{u}$ ,  $\mathbf{b}$  of (2.13) that is also independent of  $z$ . Eliminating the derivatives of  $z$  gives

$$\frac{U^2}{L} \frac{\partial \mathbf{u}}{\partial \hat{t}} + \frac{U^2}{L} \mathbf{u} \cdot \nabla \mathbf{u} + U(f_0 + \beta_0 L \hat{y}) \hat{\mathbf{z}} \times \mathbf{u} = -\frac{g'\delta}{L} \nabla h + \frac{B^2}{\mu_0 \rho_1 L} \mathbf{b} \cdot \nabla \mathbf{b}. \quad (2.14)$$

Since  $\mathbf{u}$  is independent of  $\hat{z}$ , we can integrate the mass conservation equation (2.3),

$$0 = \int_{-1}^{\frac{\delta\hat{h}}{H}} \left( \frac{\partial w}{\partial \hat{z}} + \nabla \cdot \mathbf{u} \right) d\hat{z}, \quad (2.15)$$

provided that we know  $w$  at the boundaries. The lower boundary is fixed, hence  $w(H\hat{z} = -H) = 0$ , whilst  $w$  on the upper boundary is determined by the material derivative of  $\hat{h}$ ,

$$w(H\hat{z} = \delta\hat{h}) = \frac{\delta}{H} \frac{\partial \hat{h}}{\partial \hat{t}} + \frac{\delta}{H} \mathbf{u} \cdot \nabla \hat{h}.$$

Hence,

$$\frac{\delta}{H} \frac{\partial \hat{h}}{\partial \hat{t}} + \nabla \cdot \left( \frac{\delta \hat{h}}{H} + 1 \right) \mathbf{u} = 0. \quad (2.16)$$

### 2.2.3 The Induction Equation

The horizontal component of the induction equation is

$$\frac{UB}{L} \frac{\partial \mathbf{b}}{\partial \hat{t}} + \frac{UB}{L} \mathbf{u} \cdot \nabla \mathbf{b} = \frac{UB}{L} \mathbf{b} \cdot \nabla \mathbf{u}, \quad (2.17)$$

with derivatives in  $\hat{z}$  dropped since  $\mathbf{u}$ ,  $\mathbf{b}$  are independent of  $\hat{z}$ . We can also integrate the solenoidal condition (2.4),

$$\frac{\partial b_z}{\partial \hat{z}} + \nabla \cdot \mathbf{b} = 0. \quad (2.18)$$

Since  $\mathbf{b}$  is independent of  $\hat{z}$  and assuming that the upper and lower boundaries are magnetic field lines, we have  $b_z(H\hat{z} = -H) = 0$  and

$$b_z(H\hat{z} = \delta\hat{h}) = \frac{\delta}{H} \mathbf{b} \cdot \nabla \hat{h},$$

and hence,

$$\nabla \cdot \left( \frac{\delta \hat{h}}{H} + 1 \right) \mathbf{b} = 0. \quad (2.19)$$

### 2.2.4 Non-dimensional Parameters

We introduce the total layer depth  $\mathcal{H} = \frac{\delta\hat{h}}{H} + 1$ , and the non-dimensional parameters

$$\text{Ro} = \frac{U}{Lf_0}, \quad \beta = \frac{\beta_0 L^2}{U}, \quad F^2 = \frac{f_0^2 L^2}{g'H}, \quad \text{M}^2 = \frac{B^2}{\mu_0 \rho_1 U^2} \quad (2.20)$$

which are the Rossby number, non-dimensionalised  $\beta$ -parameter, Charney number, inverse Alfvén-Mach number respectively. Note that, instead of the Charney, the Burger number  $\text{Bu} = F^{-2}$  is often used, and instead of the Alfvén-Mach number, the Cowling number  $\text{C} = \text{M}^2$  is sometimes used. No assumption is yet made about the relative sizes of these parameters.

With (2.20), and dropping the remaining hats, the equations of motion (2.14), (2.16), (2.17),

and (2.19) become

$$\text{Ro} \left( \frac{\partial \mathbf{u}}{\partial t} + \mathbf{u} \cdot \nabla \mathbf{u} \right) + (1 + \text{Ro}\beta y) (\hat{\mathbf{z}} \times \mathbf{u}) = -\frac{\delta}{H\text{Ro}F^2} \nabla h + \text{Ro}M^2 \mathbf{b} \cdot \nabla \mathbf{b}, \quad (2.21)$$

$$\frac{\partial \mathbf{b}}{\partial t} + \mathbf{u} \cdot \nabla \mathbf{b} = \mathbf{b} \cdot \nabla \mathbf{u}, \quad (2.22)$$

$$\frac{\partial h}{\partial t} + \nabla \cdot \mathcal{H} \mathbf{u} = 0, \quad (2.23)$$

$$\nabla \cdot \mathcal{H} \mathbf{b} = 0. \quad (2.24)$$

### 2.2.5 Flux Function

Let us take condition (2.24) and introduce a magnetic (shallow-water) flux function

$$(1 + \text{Ro}F^2 h) \mathbf{b} = \mathcal{H} \mathbf{b} = -\nabla \times A \hat{\mathbf{z}}. \quad (2.25)$$

Substituting this into (2.21) is relatively straightforward given that

$$\mathbf{b} \cdot \nabla \mathbf{b} = \frac{1}{\mathcal{H}} \hat{\mathbf{z}} \times \mathcal{J} \left( A, \frac{\nabla A}{\mathcal{H}} \right), \quad (2.26)$$

with  $\mathcal{J}(\cdot, \cdot)$  denoting the Jacobian determinant. Then, instead of substituting  $A$  directly into (2.22), it is simpler to consider

$$\begin{aligned} \frac{\partial}{\partial t} (\mathcal{H} \mathbf{b}) &= \frac{\partial \mathcal{H}}{\partial t} \mathbf{b} + \mathcal{H} \frac{\partial \mathbf{b}}{\partial t} \\ &= -\nabla \cdot (\mathcal{H} \mathbf{u}) \mathbf{b} + \mathcal{H} [\nabla \times (\mathbf{u} \times \mathbf{b}) + (\nabla \cdot \mathbf{u}) \mathbf{b} - (\nabla \cdot \mathbf{b}) \mathbf{u}], \end{aligned} \quad (2.27)$$

substituting in (2.22), (2.23). We can then substitute the divergence of  $\mathbf{b}$  using (2.24) and cancel, after expanding the divergence of  $\mathcal{H} \mathbf{u}$ , to obtain

$$\begin{aligned} \frac{\partial}{\partial t} (\mathcal{H} \mathbf{b}) &= \mathbf{u} (\mathbf{b} \cdot \nabla) \mathcal{H} - \mathbf{b} (\mathbf{u} \cdot \nabla) \mathcal{H} + \mathcal{H} \nabla \times (\mathbf{u} \times \mathbf{b}), \\ &= \nabla \mathcal{H} \times (\mathbf{u} \times \mathbf{b}) + \mathcal{H} \nabla \times (\mathbf{u} \times \mathbf{b}), \\ &= \nabla \times (\mathcal{H} (\mathbf{u} \times \mathbf{b})). \end{aligned} \quad (2.28)$$

Into this, we can now easily substitute the magnetic stream function which, after uncurling, gives that

$$\frac{\partial A}{\partial t} + C(t) = \hat{\mathbf{z}} \cdot [\mathbf{u} \times (\nabla \times A \hat{\mathbf{z}})] = -\mathbf{u} \cdot \nabla A, \quad (2.29)$$

where  $C$  is an arbitrary function of time. Since only spatial derivatives of  $A$  are considered everywhere except on the left side of (2.29),  $C(t)$  can be set to zero. The system of equations

is then

$$\hat{\mathbf{z}} \times \mathbf{u} + \frac{\delta}{H\text{Ro}F^2} \nabla h = \text{Ro} \left( \frac{M^2}{\mathcal{H}} \hat{\mathbf{z}} \times \mathcal{J} \left( A, \frac{\nabla A}{\mathcal{H}} \right) - \frac{\partial \mathbf{u}}{\partial t} - \mathbf{u} \cdot \nabla \mathbf{u} - \beta y (\hat{\mathbf{z}} \times \mathbf{u}) \right), \quad (2.30)$$

$$0 = \frac{\partial A}{\partial t} + \mathbf{u} \cdot \nabla A, \quad (2.31)$$

$$0 = \frac{\partial \mathcal{H}}{\partial t} + \nabla \cdot (\mathcal{H} \mathbf{u}). \quad (2.32)$$

## 2.3 Quasigeostrophic Magnetohydrodynamics

Taking the limit  $\text{Ro} \ll 1$  (with  $\beta, F^2 = \mathcal{O}(1)$ ), which assumes that rotation is rapid so that the size of advective terms is at least an order of magnitude less than Coriolis or pressure terms, results in the dominance of the rotation term in equation (2.30). Leading order balance is therefore between the Coriolis and pressure terms, defining a necessary scale for surface perturbations,  $h, \delta = H\text{Ro}F^2$ .

This balance is well-supported by observations (e.g. Vasil et al., 2021). The remaining terms are first-order in  $\text{Ro}$ , motivating an asymptotic expansion in  $\text{Ro}$ ,

$$\mathbf{u} = \mathbf{u}_0 + \text{Ro} \mathbf{u}_1 + \mathcal{O}(\text{Ro}^2), \quad (2.33)$$

$$A = A_0 + \text{Ro} A_1 + \mathcal{O}(\text{Ro}^2), \quad (2.34)$$

$$h = h_0 + \text{Ro} h_1 + \mathcal{O}(\text{Ro}^2). \quad (2.35)$$

The lowest order of (2.30) is therefore

$$\hat{\mathbf{z}} \times \mathbf{u}_0 = -\nabla h_0, \quad (2.36)$$

which, with  $\mathbf{u}_0 = (u_0, v_0, 0)$ , is

$$u_0 = -\frac{\partial h_0}{\partial y}, \quad v_0 = \frac{\partial h_0}{\partial x} \quad (2.37)$$

Meanwhile, the first order of equation (2.32) is the incompressibility equation,  $\nabla \cdot \mathbf{u}_0 = 0$ , which is already satisfied by (2.37). Substituting (2.37) into the leading order of (2.31) yields

$$0 = \frac{\partial A_0}{\partial t} + \mathcal{J}(h_0, A_0). \quad (2.38)$$

We then require the  $\mathcal{O}(\text{Ro})$  terms of (2.30) to determine the evolution (time-derivative) of  $\mathbf{u}_0$ ,

$$\frac{\partial \mathbf{u}_0}{\partial t} + \mathbf{u}_0 \cdot \nabla \mathbf{u}_0 + \hat{\mathbf{z}} \times \mathbf{u}_1 + \nabla h_1 + \beta y (\hat{\mathbf{z}} \times \mathbf{u}_0) - M^2 \hat{\mathbf{z}} \times \mathcal{J}(A_0, \nabla A_0) = 0. \quad (2.39)$$

This two-dimensional equation has three terms ( $u_1, v_1, h_1$ ) which we now seek to eliminate

to form a closed set of equations. Including the  $\mathcal{O}(\text{Ro})$  terms of (2.32),

$$F^2 \left[ \frac{\partial h_0}{\partial t} + \nabla \cdot (h_0 \mathbf{u}_0) \right] + \nabla \cdot \mathbf{u}_1 = 0, \quad (2.40)$$

provides a condition on  $u_1$  and  $v_1$ , which is sufficient to close the system. We eliminate  $h_1$  from (2.39) by taking a component of the three-dimensional curl ( $\hat{\mathbf{z}} \cdot \nabla_3 \times$ ). For completeness, we show this component-wise below

$$\begin{aligned} \frac{\partial}{\partial t} (\hat{\mathbf{z}} \cdot \nabla \times \mathbf{u}_0) &= \frac{\partial}{\partial t} \nabla^2 h_0, \\ \hat{\mathbf{z}} \cdot \nabla \times (\mathbf{u}_0 \cdot \nabla \mathbf{u}_0) &= \frac{\partial}{\partial x} (\mathbf{u}_0 \cdot \nabla v_0) - \frac{\partial}{\partial y} (\mathbf{u}_0 \cdot \nabla u_0), \\ &= -\frac{\partial h_0}{\partial y} \frac{\partial^3 h_0}{\partial x^3} + \frac{\partial h_0}{\partial x} \frac{\partial^3 h_0}{\partial x^2 \partial y} - \frac{\partial h_0}{\partial y} \frac{\partial^3 h_0}{\partial x \partial y^2} + \frac{\partial h_0}{\partial x} \frac{\partial^3 h_0}{\partial y^3}, \\ &= \mathcal{J}(h_0, \nabla^2 h_0) \\ \hat{\mathbf{z}} \cdot \nabla \times (\hat{\mathbf{z}} \times \mathbf{u}_1) &= \nabla \cdot \mathbf{u}_1, \\ \hat{\mathbf{z}} \cdot \nabla \times \beta y (\hat{\mathbf{z}} \times \mathbf{u}_0) &= \beta y \hat{\mathbf{z}} \cdot \nabla \times (\hat{\mathbf{z}} \times \mathbf{u}_0) + \hat{\mathbf{z}} \cdot (\nabla(\beta y) \times (\hat{\mathbf{z}} \times \mathbf{u}_0)), \\ &= \beta \frac{\partial h_0}{\partial x} + \nabla \cdot \mathbf{u}_0 = \beta \frac{\partial h_0}{\partial x} \\ \hat{\mathbf{z}} \cdot \nabla \times (M^2 \hat{\mathbf{z}} \times \mathcal{J}(A_0, \nabla A_0)) &= M^2 \nabla \cdot \mathcal{J}(A_0, \nabla A_0). \end{aligned}$$

By applying (2.37) to (2.40) we also have

$$0 = F^2 \frac{\partial h_0}{\partial t} + \nabla \cdot \mathbf{u}_1, \quad (2.41)$$

and with this, we can eliminate  $\mathbf{u}_1$ . Since the remaining variables are all  $\mathcal{O}(\text{Ro}^0)$ , we can stop using the subscript notation, and write down

$$\frac{\partial}{\partial t} \nabla^2 h + \mathcal{J}(h, \nabla^2 h) - M^2 \mathcal{J}(A, \nabla^2 A) - F^2 \frac{\partial h}{\partial t} + \beta \frac{\partial h}{\partial x} = 0, \quad (2.42)$$

$$\frac{\partial A}{\partial t} + \mathcal{J}(h, A) = 0. \quad (2.43)$$

These are the equations of quasi-geostrophic SWMHD, first given by Zeitlin (2013). The first step in deriving these equations considered the leading order,  $\mathcal{O}(\text{Ro}^0)$ , terms. This leads to a geostrophic balance between  $h$  and  $\mathbf{u}_0$  that is diagnostic, in the sense that it leads to a constraint on  $\mathbf{u}_0$  at all times, but does not predict how  $\mathbf{u}_0$  evolves over time. To derive prognostic equations, we had to consider terms of order  $\mathcal{O}(\text{Ro})$  leading to a closed system of equations that describes the evolution of  $\mathbf{u}_0$  (Charney, 1948; Zeitlin, 2007).

### 2.3.1 Diffusion Terms

Flows in the solar tachocline are expected to be almost inviscid, with kinetic and magnetic Reynolds of approximate order  $10^{15}$  and  $10^{13}$  respectively (Gough, 2007). One could then consistently leave the evolutionary equations in the form (2.42), (2.43). If one does wish to model the effect of diffusion, for numerical or physical purposes, (e.g. §6) then these can be

included as

$$\frac{\partial}{\partial t} \nabla^2 h + \mathcal{J}(h, \nabla^2 h) - M^2 \mathcal{J}(A, \nabla^2 A) - F^2 \frac{\partial h}{\partial t} + \beta \frac{\partial h}{\partial x} = \frac{1}{\text{Re}} \nabla^4 h, \quad (2.44)$$

$$\frac{\partial A}{\partial t} + \mathcal{J}(h, A) = \frac{1}{\text{Rm}} \nabla^2 A, \quad (2.45)$$

where  $\text{Re} = UL/\nu$  and  $\text{Rm} = UL/\eta$  are the Reynolds and magnetic Reynolds numbers respectively. We have omitted a derivation of diffusion terms since this would require an involved derivation of the diffusion term in the SWMHD equations, which has received some interest in recent years (Marche, 2007; Gilbert et al., 2014, 2025). The two commonly used shallow-water viscous diffusion terms,  $\nabla^2 \mathbf{u}$ , and  $\mathcal{H}^{-1} \nabla \cdot \mathcal{H} \nabla \mathbf{u}$  (similarly  $\nabla^2 \mathbf{b}$ , and  $\mathcal{H}^{-1} \nabla \cdot \mathcal{H} \nabla \mathbf{b}$  for ohmic diffusion) both reduce to the form given in (2.44) and (2.45) in the quasigeostrophic limit,  $\text{Ro} \ll 1$ .

The important properties of the diffusion terms in (2.44) and (2.45) are that the solenoidal conditions are preserved and energy strictly decays (§2.4.3).

## 2.4 Quantities of Interest

### 2.4.1 Potential Vorticity

The relative vorticity of the fluid,  $\boldsymbol{\omega}$ , is given by the curl of the velocity field  $\nabla \times \mathbf{u}$ . Since  $u$  and  $v$  are independent of  $z$  and  $w$  is asymptotically small, thus the horizontal components of the relative vorticity are negligible and we can define  $\boldsymbol{\omega} \approx \omega \hat{\mathbf{z}}$ . In terms of the streamfunction,  $h$ ,  $\omega$  is defined as

$$\omega(x, y, t) = \nabla^2 h(x, y, t). \quad (2.46)$$

We can also define the potential vorticity as

$$q_s = \frac{1}{\text{Ro}} \frac{\omega + 1 + \beta y}{\mathcal{H}} = \frac{1}{\text{Ro}} + \omega - F^2 h + \beta y + \mathcal{O}(\text{Ro}). \quad (2.47)$$

Since the constant value of  $q_s$  is arbitrary, we will generally only consider the varying potential vorticity,

$$q = \omega - F^2 h + \beta y, \quad (2.48)$$

which, when substituted into equation (2.42), gives

$$\frac{\partial q}{\partial t} + \mathcal{J}(h, q) - M^2 \mathcal{J}(A, J) = 0, \quad (2.49)$$

where  $J = \hat{\mathbf{z}} \cdot \nabla \times \mathbf{B} = \nabla^2 A$ . When  $M = 0$ , (2.49) is an advection equation for potential vorticity. This implies that fluid parcels conserve potential vorticity, which has an important effect on the formation of zonal flows and other phenomena in geophysical fluid dynamics (e.g. Pedlosky, 1987; Vallis, 2017). When  $M > 0$ , the conservation of potential vorticity is broken. Exactly how conservation is broken can be important for the evolution of the flow, particularly when  $M$  is small (Tobias et al., 2007; Dritschel et al., 2018; Chen and Diamond, 2020).

### 2.4.2 Conservation of Cross-Helicity

There exists, in three-dimensional and non-rotating conducting flow, a different conserved quantity, the magnetic helicity,  $H_e = \mathbf{A} \cdot \mathbf{B}$ . It is easy to see from our definitions that  $H_e = \mathcal{O}(\varepsilon)$  and therefore does not play a role in flow dynamics.

A related quantity is the (quasi-)cross-helicity which we define here as

$$H_q = Aq. \quad (2.50)$$

It is straightforward to show that this is conserved by equations (2.49) and (2.43), in a domain  $\mathcal{D}$  where  $A$ ,  $J$ , and  $q$  are fixed at the boundaries:

$$\begin{aligned} \frac{d}{dt} H_q &= \frac{d}{dt} \int_{\mathcal{D}} Aq \, dA = \int_{\mathcal{D}} \left( q \frac{\partial A}{\partial t} + A \frac{\partial q}{\partial t} \right) dA \\ &= \int_{\mathcal{D}} (M^2 A \mathcal{J}(A, J) - A \mathcal{J}(h, q) - q \mathcal{J}(h, A)) \, dA \\ &= \int_{\mathcal{D}} (M^2 \mathcal{J}(A^2/2, J) - \mathcal{J}(h, H_q)) \, dA = 0, \end{aligned} \quad (2.51)$$

The transport of quasi-cross-helicity around the solar tachocline may have important consequences for the solar dynamo (e.g. Heinonen et al., 2023, for  $\beta$ -plane MHD).

### 2.4.3 Conservation of Energy

The total kinetic energy on a domain  $\mathcal{D}$  is given by

$$\text{KE} = \frac{1}{2} \int_{\mathcal{D}} \mathbf{u}^2 \, dA \approx \frac{1}{2} \int_{\mathcal{D}} |\nabla h|^2 \, dA, \quad (2.52)$$

where  $\hat{\mathbf{z}} \times \mathbf{u} = -\nabla h$ . For  $\mathcal{D}$  a periodic channel with  $h$  constant on each wall this means that

$$\text{KE} = -\frac{1}{2} \int_{\mathcal{D}} h\omega \, dA \implies \frac{d}{dt} \text{KE} \, dA = - \int_{\mathcal{D}} h \frac{\partial \omega}{\partial t} \, dA. \quad (2.53)$$

The total magnetic energy meanwhile is given by

$$\text{ME} = \frac{M^2}{2} \int_{\mathcal{D}} \mathbf{B}^2 \, dA \approx \frac{M^2}{2} \int_{\mathcal{D}} |\nabla A|^2 \, dA, \quad (2.54)$$

where  $\mathbf{B} = -\nabla \times A \hat{\mathbf{z}} + \mathcal{O}(\text{Ro})$ . We can write this as, with  $A$  constant on our walls,

$$\text{ME} = -\frac{M^2}{2} \int_{\mathcal{D}} AJ \, dA \implies \frac{d}{dt} \text{ME} = -M^2 \int_{\mathcal{D}} J \frac{\partial A}{\partial t} \, dA. \quad (2.55)$$

Finally, we can derive an expression for the total potential energy of the flow. This must also be considered to close the system since within shallow water surface variations are an expression of the flow dynamics. Since the density,  $\rho_0$ , is constant within the layer, the

potential energy of a fluid column is given by

$$\text{PE}_{\text{col}} = \int_{-H}^h \rho_0 g' z \, dz = \frac{\rho_0 g'}{2} (h^2 - H^2). \quad (2.56)$$

In non-dimensional terms this is

$$\text{PE}_{\text{col}} = \frac{F^2}{2} h^2 - \bar{H}^2, \quad (2.57)$$

with  $\bar{H}$  an arbitrary constant (varies depending on the definition of the depth  $z = 0$ ). We hence obtain that

$$\frac{d}{dt} \text{PE} = \frac{\partial}{\partial t} \left( \frac{F^2}{2} \int_{\mathcal{D}} h^2 \, dA \right) = F^2 \int_{\mathcal{D}} h \frac{\partial h}{\partial t} \, dA. \quad (2.58)$$

Combining equations (2.53), (2.55), and (2.58), the evolution of the total energy of the system is

$$\frac{dE}{dt} = \frac{d}{dt} (\text{KE} + \text{PE} + \text{ME}) = \int_{\mathcal{D}} \left( F^2 h \frac{\partial h}{\partial t} - h \frac{\partial \omega}{\partial t} - M^2 J \frac{\partial A}{\partial t} \right) \, dA. \quad (2.59)$$

We can then substitute  $h \cdot (2.44)$  and  $J \cdot (2.45)$  which gives

$$\begin{aligned} \frac{dE}{dt} = & \\ & \int_{\mathcal{D}} \left( \beta h \frac{\partial h}{\partial x} + \mathcal{J}(h, \omega) h - M^2 \mathcal{J}(A, J) h + M^2 \mathcal{J}(h, A) J - \frac{1}{\text{Re}} h \nabla^2 \omega - \frac{M^2}{\text{Rm}} J^2 \right) \, dA. \end{aligned} \quad (2.60)$$

The first term vanishes from periodicity whilst the next three can be rewritten to give that

$$\frac{dE}{dt} = \int_{\mathcal{D}} \left( \mathcal{J}(h^2/2, \omega) + M^2 \mathcal{J}(hJ, A) - \frac{1}{\text{Re}} \omega^2 - \frac{M^2}{\text{Rm}} J^2 \right) \, dA. \quad (2.61)$$

If  $h$ ,  $\omega$ ,  $J$ , and  $A$  are constant or periodic at the boundaries then the Jacobian terms vanish and we are left with

$$\frac{dE}{dt} = - \int_{\mathcal{D}} \left( \frac{1}{\text{Re}} \omega^2 + \frac{M^2}{\text{Rm}} J^2 \right) \, dA, \quad (2.62)$$

and hence the total energy is strictly decreasing.

## 2.5 Discussion

### 2.5.1 The Solar Tachocline

Throughout this chapter, we have tried to derive the QG SWMHD equations independently from any particular system, although the obvious motivation is the solar tachocline. It is worth checking that the parameters we have assumed apply there.

$\text{Ro} \sim \frac{U}{L f_0}$ , characterises the relative importance of Coriolis and Inertial forces in a flow. The QG approximation involves the comparison of terms in an asymptotic expansion in the Rossby number. Hence, for this model to be valid, we must consider a system for which  $\text{Ro} < 1$ , and

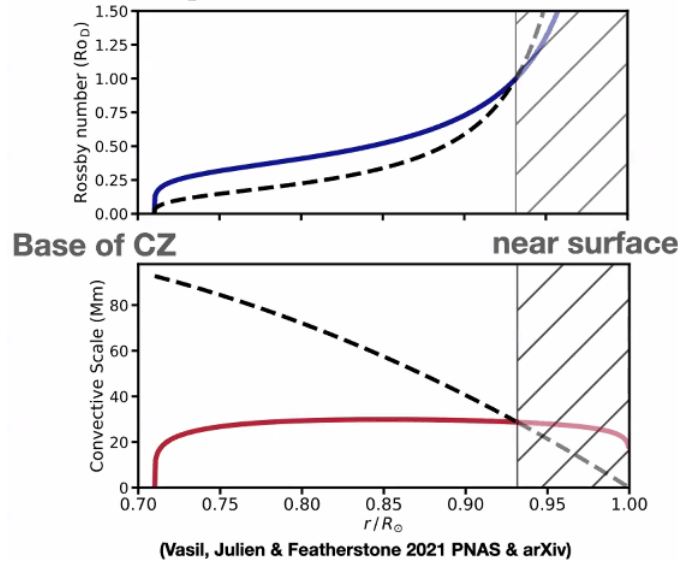


Figure 2.2: Variation in the dynamic (convective) Rossby number as a function of depth, given as a proportion of the Stellar radius. (Vasil et al., 2021)

ideally,  $Ro \ll 1$ .

In stellar physics, there is a broad estimated range of the Rossby number, strongly dependent on the scale and location of the dynamics within that particular star. Across G-type stars, estimates generally fall in the range of 0.1 – 1.2. Though this is close to the boundary of our region of QG validity, it is well-argued by Vasil et al. (2021) that the Solar convective zone is largely quasi-geostrophic, at least below 0.93 Solar radii. In our context estimates give that

$$Ro \approx 0.25, \quad (2.63)$$

and the QG approximation is good, at least within the lower convective zone and the solar tachocline ( $R = 0.7R_{\odot}$ ) (Figure 2.2).

The  $f$ -plane parameter,  $f_0$ , can be defined by the rotation frequency,  $\Omega$ , as  $f_0 = 2\Omega \sin \theta$ , with  $\theta$  the latitude. Similarly, the  $\beta_0$  can be defined by

$$\beta_0 = \frac{2L\Omega \cos \theta}{R} \quad (2.64)$$

where  $R$  is the radius of rotation,  $R \approx 0.7R_{\odot}$ . The non-dimensional  $\beta$ -parameter,  $\beta$ , can therefore be written as

$$\beta = \frac{\beta_0 L}{f_0 Ro} = \frac{1}{Ro} \frac{L \cot \theta}{0.7R_{\odot}}. \quad (2.65)$$

For motions around mid-latitude and large, but subglobal length scales, the  $\beta$  parameter may be  $\mathcal{O}(1)$ , but can vary significantly.

The Charney (inverse Burger) number was defined as

$$F = \frac{f_0 L}{\sqrt{g' H}}. \quad (2.66)$$

Here  $g'$  is the effective gravity, reduced by radial stratification. The denominator,  $c_g = \sqrt{g' H}$  can be estimated from the speed of the fastest gravity waves in the tachocline. Gough (2007) estimate this to be

$$c_g = \frac{NH}{\pi} \approx 5000 \text{ ms}^{-1}, \quad (2.67)$$

where  $N$  is the Brunt-Vaisala frequency. For slow, geostrophic, flows when  $\text{Ro}$  is only moderately small,

$$F = \frac{U}{c_g} \frac{1}{\text{Ro}}$$

is therefore likely to be small,  $\lesssim \mathcal{O}(10^{-1})$ .

The Alfvén-Mach number,

$$\text{M}^2 = \frac{1}{\mu_0 \rho} \frac{\mathcal{B}^2}{U^2} \quad (2.68)$$

is difficult to estimate since the strength and scale of the magnetic field in the solar tachocline is unknown. The estimate given by Mak (2013) is,

$$0.03 \lesssim M \lesssim 3.0, \quad (2.69)$$

although this is difficult to exactly pin down and one of the motivations for investigating possible instabilities in the tachocline.

### 2.5.2 Rotating Shallow Water and Shear Flows

We originally intended to use the rotating SWMHD equations for this work; however, we soon realised that many normal shear flows,  $U(y)$ , do not satisfy the governing equations.

Consider, for example, a zonal shear flow,  $\mathbf{u} = U(y)\hat{\mathbf{x}}$ , allowed to vary in the latitudinal direction, and neglect any magnetic effects,  $\mathbf{B} = \mathbf{0}$ . Equations (2.31), and the zonal component of (2.30) are trivially satisfied, whilst (2.32) and the lateral component of (2.30) simplify to

$$(1 + \text{Ro}\beta y) U(y) + \frac{\delta}{H\text{Ro}F^2} \frac{\partial h}{\partial y} = 0, \quad (2.70)$$

$$\frac{\partial h}{\partial x} U(y) = 0. \quad (2.71)$$

Thus

$$h = \int_y -\frac{H\text{Ro}F^2}{\delta} (1 + \text{Ro}\beta y) U(y) dy. \quad (2.72)$$

This presents a problem in rSW (MHD) since shear profiles that could be compared to existing theory often have  $U \rightarrow \pm U_0$  ( $U_0$  constant) as  $y \rightarrow \pm\infty$ . Although this issue still present in the quasi-geostrophic approximation,  $\text{Ro} = U/Lf \ll 1$ , and  $F^2 = f^2 L^2 / g' H = \mathcal{O}(1)$ , so the right side of (2.72) is asymptotically small.

If one were to extend the work in this thesis to the rSWMHD equations, they would either need to assume a bounded domain, or  $U \rightarrow 0$  or  $h \rightarrow \infty$  as  $y \rightarrow \infty$ . The latter case corresponding to jet-like flows.

### 2.5.3 Leading order magnetic field

One could also include the Lorentz force in the leading-order balance. This is possible to do (e.g. Umurhan, 2013), however previous work on magnetohydrodynamic shear instabilities has shown that if the energy of the large-scale magnetic field is larger than the energy of the shear flow (nondimensionally,  $B^2/U^2\mu_0\rho > 1$ ) then shear instability is prevented (Michael, 1955). Secondly, the large-scale field in the solar tachocline may not be strong, as a result of the turbulent motion of the convective layer above it. For these reasons, we have assumed that the Lorentz force enters at the same order as the inertial terms.

### 2.5.4 Conclusion

In this chapter, motivated by considerations of the solar tachocline, we have derived the equations of SWMHD (2.30)-(2.32) and, in the limit  $\text{Ro} \ll 1$ , the QG SWMHD equations with and without diffusion (2.42), (2.43) and (2.44), (2.45) respectively. We have then shown that the inviscid QG SWMHD equations conserve cross-helicity and total energy and that, in the viscous QG SWMHD equations, the total energy is strictly decreasing.

## Chapter 3

# General Stability Results

### 3.1 Introduction

In this chapter, we derive necessary conditions for, and bounds on, the growth of small perturbations to general ideal shear flows in QG Shallow-Water MHD. The basic flow is assumed to be zonal ( $\mathbf{u} = U\hat{\mathbf{x}}$ ), corresponding to the differential rotation and zonal jets within the solar tachocline (e.g. Christensen-Dalsgaard and Thompson, 2007), and likely applicable to many other systems since it is common for large scale zonal flows to develop when rotation is a leading-order effect (e.g. Tobias et al., 2007). The strength of this flow is allowed to vary latitudinally (in  $y$ ) whilst its vertical variation can be obtained retroactively from the shallow-water equations (§2.2). The magnetic field is assumed to align with the flow since, physically, this corresponds to the expected presence of a large-scale toroidal magnetic field in the solar tachocline. Furthermore, mathematically, this is the only configuration initially in equilibrium.

In 2D hydrodynamics, particularly the vortex sheet case, a cross-stream variation of the flow speed,  $U(y)$ , leads to shear instability in a range of systems since small oscillations in the flow then experience a pressure imbalance due to the relative speeds of the flow (e.g. Hillier, 2020). In smooth velocity profiles, this instability is often characterised instead as an interaction of anti-phase counter-propagating Rossby (potential vorticity) waves inducing vorticity perturbations that lead to mutual amplification (Bretherton, 1966; Heifetz and Methven, 2005; Heifetz and Mak, 2014; Heifetz et al., 2015).

This physical description can offer insight into the instability criteria that emerge from the mathematics. For example, Rayleigh’s criterion, that the profile must contain an inflexion point where  $U''$  (the gradient of vorticity) changes sign (Rayleigh, 1913), can be interpreted as a requirement for regions with oppositely signed vorticity gradients, allowing for counter-propagating Rossby waves. Fjørtoft’s criterion builds upon Rayleigh’s criterion and requires that for instability  $U''(U - U_s)$  must also be somewhere negative for any constant  $U_s$  (Fjørtoft, 1950). In particular, for monotonically increasing profiles with a single inflexion point, we can choose  $U_s = U(y = y_0)$  where  $U''(y_0) = 0$  so that  $U''(U - U_s)$  becomes single-signed. Therefore, Fjørtoft’s criterion tells us that the flow direction must complement the vorticity gradients so that generated Rossby waves in these two regions can have equal phase speeds

(Bretherton, 1966; Heifetz and Methven, 2005).

These two criteria can be generalised to flows on a  $\beta$ -plane (Kuo, 1949), stratified flows (Satomura, 1981) and quasigeostrophic flows (Pedlosky, 1987; Shivamoggi and Rollins, 2001), with the important result that a sufficiently large  $\beta$  (background vorticity gradient) can lead to stabilisation since  $\beta$  directly affects the vorticity gradient.

Magnetohydrodynamic shear instabilities have also been extensively studied, and it was shown early on (Michael, 1955; Northrop, 1956; Chandrasekhar, 1961) that only magnetic fields that are parallel to the flow affect stability. Furthermore, if this magnetic field is sufficiently large the flow can be stabilised (Kent, 1966b). That is not to say that the magnetic field is universally stabilising. Kent (1966b) showed that Rayleigh’s criterion is no longer applicable and that no *a priori* requirement on the shear and magnetic profiles is possible.

In addition to the “shear mode”, characterised by the interaction of waves arising from the vorticity of the shear, other sources of vorticity can exist within the system, providing sources for waves that can become unstable. In particular, a far-field potential vorticity gradient can support Rossby waves that can become unstable by “over-reflection” (McIntyre and Weissman, 1978; Lindzen and Tung, 1978; Lindzen, 1988). We will not need to consider this mode explicitly until §5 however, it is worth noting that any general theorems we derive in this chapter will, and must, account for both types of instability.

One powerful class of general theorems is the (Howard, 1961) semicircle theorem that bounds the phase speed and growth rate of instability to a semicircle on the complex plane. Several authors have derived generalisations to Howard’s original result (Eckart, 1963; Hasimoto, 1969; Hall, 1980; Gnevyshev and Shrira, 1990; Gupta, 1992; Thuburn and Haynes, 1996; de Szoeké, 1999; Cally, 2000; Mak et al., 2016), however, of particular relevance to our case are those derived by Pedlosky (1987) and Hughes and Tobias (2001) for quasigeostrophic and magnetohydrodynamic flows respectively, which we build upon in §3.6.

This chapter starts by deriving, from (2.42) and (2.43), the linearised evolution equation for an asymptotically small perturbation to the basic flow (§3.2) and showing (§3.3.1) a few possible representations of these equations and explaining where and why these may be relevant. Section §3.4 then examines two cases where the perturbation equations can be solved analytically and have constant amplitude solutions i.e. waves in stable profiles. These solutions are relevant to results later in the chapter. The remainder of the chapter is dedicated to instability, with the penultimate section (§3.5) containing several important general instability results and a brief discussion of some results that cannot be generalised to QG SWMHD, whilst in the final section (§3.6) we derive semicircle theorems for this system and discuss their mathematical and physical meaning.

### 3.2 Linearisation

As described above, let us consider a small perturbation to the flow,  $\mathbf{u} = U(y)\hat{\mathbf{x}} + \tilde{\mathbf{u}}$ , and field,  $\mathbf{b} = B(y)\hat{\mathbf{x}} + \tilde{\mathbf{b}}$ . Hence,

$$h = - \int_y U(y) dy + \tilde{h}, \quad A = - \int_y B(y) dy + \tilde{a}, \quad (3.1)$$

from (2.37) and (2.25). When these perturbations are significantly smaller than the basic flow, we can neglect quadratic orders of  $\tilde{h}$  and  $\tilde{a}$  in (2.42) and (2.43) and consider only the simplified equations,

$$\left( \frac{\partial}{\partial t} + U \frac{\partial}{\partial x} \right) \nabla^2 \tilde{h} - U'' \frac{\partial \tilde{h}}{\partial x} + M^2 B'' \frac{\partial \tilde{a}}{\partial x} - M^2 B \frac{\partial}{\partial x} (\nabla^2 \tilde{a}) - F^2 \frac{\partial \tilde{h}}{\partial t} + \beta \frac{\partial \tilde{h}}{\partial x} = 0 \quad (3.2)$$

$$\frac{\partial \tilde{a}}{\partial t} - B \frac{\partial \tilde{h}}{\partial x} + U \frac{\partial \tilde{a}}{\partial x} = 0 \quad (3.3)$$

which are linear in  $\tilde{a}$  and  $\tilde{h}$ . From here, we use a prime to denote derivatives of the basic state in  $y$  since  $U(y)$  and  $B(y)$  are functions of a single variable only.

#### 3.2.1 Growth Rate Bound

Equations (3.2) and (3.3) describe the evolution of small perturbations  $h$ ,  $a$  (tildes have been dropped) about a mean flow  $\mathbf{U}$  and field  $\mathbf{B}$ . The perturbations can grow as energy is transferred out of the mean flow and magnetic field and the growth rate of instabilities is determined by the rate at which energy can be drawn out.

First, we will derive an evolution equation for the perturbation energy,

$$\tilde{E} = \widetilde{KE} + \widetilde{PE} + \widetilde{ME} = \frac{(\nabla h)^2}{2} + \frac{F^2 h^2}{2} + \frac{M^2 (\nabla a)^2}{2}, \quad (3.4)$$

by multiplying (3.2) by  $-h$ , (3.3) by  $-M^2 \nabla^2 a$ , and using the identities

$$\nabla \cdot \left( h \nabla \frac{\partial h}{\partial t} \right) = \frac{\partial}{\partial t} \frac{(\nabla h)^2}{2} + h \frac{\partial}{\partial t} \nabla^2 h, \quad (3.5)$$

$$\nabla \cdot \left( \frac{\partial a}{\partial t} \nabla a \right) = \frac{\partial}{\partial t} \frac{(\nabla a)^2}{2} + \frac{\partial a}{\partial t} \nabla^2 a. \quad (3.6)$$

Adding together these two equations then gives an expression for the evolution of perturbation energy:

$$\begin{aligned} \frac{\partial}{\partial t} \left( \frac{(\nabla h)^2}{2} + \frac{F^2 h^2}{2} + \frac{M^2 (\nabla a)^2}{2} \right) &= \nabla \cdot \left( h \nabla \frac{\partial h}{\partial t} + M^2 \frac{\partial a}{\partial t} \nabla a + \left( \frac{\beta h^2}{2} - M^2 B h \nabla^2 a \right) \hat{\mathbf{x}} \right) \\ &\quad + U \left( h \frac{\partial}{\partial x} \nabla^2 h - M^2 a \frac{\partial}{\partial x} \nabla^2 a \right) - U'' h \frac{\partial h}{\partial x} + M^2 B'' h \frac{\partial a}{\partial x}. \end{aligned} \quad (3.7)$$

The left side of equation (3.7) represents the evolution of the perturbation energy at a single

point. Integrating this over some domain leads to an expression for the energy transferred from the mean flow to perturbations. The integral of the divergence term on the right side then reduces to boundary conditions (Gauss' theorem). This term vanishes under a wide range of boundary conditions. Here, let us assume that  $y \in (y_1, y_2)$  and  $\frac{\partial h}{\partial t}$  and  $\frac{\partial a}{\partial t}$  are either zero at finite values of  $y_1, y_2$  (consistent with, e.g., wall-bounded flow) or tend towards zero with  $y_1, y_2 = \pm\infty$  (unbounded flow).

Since the perturbation equations, (3.2), (3.3), are linear and autonomous in  $x$ , the evolution of each zonal mode is independent. Hence, let us consider the growth of the energy of the mode with wavenumber  $k > 0$  and domain  $x \in [0, 2\pi/k)$  corresponding to a single wavelength so that  $h$  and  $a$  are periodic.

The divergence term then vanishes and

$$\begin{aligned} \frac{d}{dt} \int_0^{2\pi/k} \int_{y_1}^{y_2} \tilde{E} \, dy \, dx = \\ \int_0^{2\pi/k} \int_{y_1}^{y_2} \left( U \left( h \frac{\partial}{\partial x} \nabla^2 h - M^2 a \frac{\partial}{\partial x} \nabla^2 a \right) - U'' h \frac{\partial h}{\partial x} + M^2 B'' h \frac{\partial a}{\partial x} \right) \, dy \, dx, \end{aligned} \quad (3.8)$$

with  $\tilde{E}$  defined in (3.4). Equation (3.8) represents the evolution of the perturbation energy over a wavelength of an arbitrary mode and we can write

$$h(x, y, t) = \hat{h}(y, t)e^{ikx} + \hat{h}^*(y, t)e^{-ikx}, \quad a(x, y, t) = \hat{a}(y, t)e^{ikx} + \hat{a}^*(y, t)e^{-ikx}. \quad (3.9)$$

Since  $\int_x e^{ikx} \, dx = 0$ , only the cross terms of  $\hat{h}$  and  $\hat{h}^*$  in (3.8) prevail. For example, the integrand of the LHS becomes

$$\tilde{E} \rightarrow E_k = \left( |kh|^2 + |h'|^2 + F^2 |h|^2 + M^2 |ka|^2 + M^2 |a'|^2 \right), \quad (3.10)$$

where  $|h|^2 = \hat{h}\hat{h}^*$  (there should be little ambiguity, so we drop hats for convenience). The  $x$ -derivatives also simplify ( $\partial/\partial x \rightarrow ik$ ), and we are left with a one-dimensional integral equation,

$$\begin{aligned} \frac{d}{dt} \int_{y_1}^{y_2} E_k \, dy = ik \int_{y_1}^{y_2} [Uh^*(h'' - k^2 h) - M^2 Ua^*(a'' - k^2 a) - U''h^*h + M^2 B''h^*a] \, dy \\ - ik \int_{y_1}^{y_2} [Uh(h'' - k^2 h)^* - M^2 a(a'' - k^2 a)^* - U''hh^* + M^2 B''ha^*] \, dy, \end{aligned} \quad (3.11)$$

which simplifies to

$$\begin{aligned} \frac{d}{dt} \int_{y_1}^{y_2} E_k \, dy = \\ ik \int_{y_1}^{y_2} [U(h^*h'' - h(h^*)'') - M^2 U(a^*a'' - a(a^*)'') + M^2 B''(h^*a - ha^*)] \, dy. \end{aligned} \quad (3.12)$$

Now integrating one of these terms by parts, for example, we have

$$ik \int_{y_1}^{y_2} U (h^* h'' - h (h'')^*) dy = [ikU (h^* h' - h (h')^*)]_y - ik \int_{y_1}^{y_2} U ((h')^* h' - h' (h')^*) dy - \int_{y_1}^{y_2} U' (ikh^* h' - ikh (h')^*) dy, \quad (3.13)$$

$$= -2 \int_{y_1}^{y_2} U' \mathbb{R} (ikh^* h') dy, \quad (3.14)$$

and so

$$\frac{d}{dt} \int_{y_1}^{y_2} E_k dy = 2 \int_{y_1}^{y_2} (U' (-\mathbb{R} (ikh^* h') + M^2 (\mathbb{R} (ika^* a')) + B' (\mathbb{R} (ika^* h') - \mathbb{R} (ikh^* a')))) dy. \quad (3.15)$$

with  $\mathbb{R}()$  denoting the real part of a complex term. Using the identity,  $\pm 2\mathbb{R}(pq^*) \leq |p|^2 + |q|^2$ , we can therefore derive the inequality

$$\frac{d}{dt} E_k \leq \int_{y_1}^{y_2} (|U'| + |B'|) (|kh|^2 + |h'|^2 + |ka|^2 + |a'|^2) dy. \quad (3.16)$$

Assuming that  $E_k$  grows exponentially with a rate  $2\sigma$  (cf. §3.3) and bringing the shear term out of the integrand, we obtain

$$2\sigma E_k \leq (|U'|_{max} + |B'|_{max}) \int_{y_1}^{y_2} (|kh|^2 + |h'|^2 + |ka|^2 + |a'|^2) dy, \quad (3.17)$$

where subscripts denote the maximum of  $U'$  and  $B'$  over the domain. The integral on the right side of (3.17) represents the total kinetic and magnetic energy. Therefore, adding the (positive) potential energy (3.4), we can eliminate  $E_k$  from both sides and derive the bound,

$$\sigma < \frac{1}{2} (|U'|_{max} + |B'|_{max}). \quad (3.18)$$

Equation (3.18) implies a criterion for instability that somewhere either  $U'$  or  $B'$  must be non-zero, and also bounds the energy growth rate by the size of the (kinetic and magnetic) shear. Unfortunately, this bound does not include the parameters  $\beta$  or  $F^2$  which generally reduce the growth of instabilities. The damping effect of  $F^2$  gives a strictly less than sign in (3.18), assuming that  $h$  is non-zero, but that is all.

Høiland (1953) and Howard (1961) were the first to show a version of this result, for 2D hydrodynamic flows. Similar results have since been derived for QG flows by Pedlosky (1987) and SWMHD by Mak et al. (2016). Using similar methods, growth rate bounds for the Taylor-Couette and inertial instabilities were derived by Yavneh et al. (2001) and Griffiths (2008) respectively.

### 3.3 Normal Modes

In the previous section, we used the fact that equations (3.2) and (3.3) are linear and independent of  $x$  and  $t$ , to assume exponential forms of the perturbation variables; with this, it is possible to derive an ODE from the PDEs (3.2) and (3.3). To do so, let us now explicitly write  $\tilde{h}$  in the standard wave ansatz,

$$\tilde{h} = \mathbb{R} \left( h(y) e^{ik(x-ct)} \right), \quad (3.19)$$

where the cross-stream ( $y$ ) structure is yet to be determined, and equivalently for  $\tilde{a}$ . We also introduce the phase speed,  $c$ , which is allowed to be a complex number whose imaginary part determines the growth rate,  $\sigma = kc_i = k\mathbb{I}(c)$ . Unstable growing solutions correspond to  $kc_i > 0$ , neutrally stable or wavelike modes to  $kc_i = 0$ , and stable, decaying modes to  $kc_i < 0$ . On substituting (3.19), the linearised PDEs simplify to the ordinary differential equations,

$$(U - c)(h'' - k^2h) + (\beta - U'' + cF^2)h - M^2B(a'' - k^2a) + M^2B''a = 0, \quad (3.20)$$

$$(U - c)a - Bh = 0. \quad (3.21)$$

Eliminating  $a$  in favour of  $h$  gives the single equation,

$$(U - c)(h'' - k^2h) + (\beta - U'' + cF^2)h + M^2 \left( \frac{k^2B^2h}{U - c} - B \left( \frac{Bh}{U - c} \right)'' + \frac{BB''h}{U - c} \right) = 0, \quad (3.22)$$

which, with a little manipulation, can be written in the concise form

$$(T^2h')' - \left( k^2T^2 + \frac{(T^2U')' - \beta - cF^2}{U - c} \right) h = 0, \quad (3.23)$$

where

$$T^2(y) = 1 - \frac{M^2B^2(y)}{(U(y) - c)^2}. \quad (3.24)$$

In the same way that equation (2.42) reduces to the two-dimensional potential vorticity equation when  $F^2 = 0$ , so does (3.23) reduce to the normal mode equation of shear instability, of Rayleigh (1913), when  $F^2 = \beta = M = 0$ , of Chandrasekhar (1961) when  $F^2 = \beta = 0$ , and of Kuo (1949) when  $F^2 = M = 0$ . This equation with  $F^2 \neq 0$ , but  $M = 0$ , has been studied by Shivamoggi and Rollins (2001) and is also closely related to the continuously stratified quasigeostrophic case of Pedlosky (1987, §7.4).

#### 3.3.1 Transformations of the Linearised Equation

The linearised equation for  $h$ , (3.23), is not always the most convenient form. We include here a couple of useful transformations that can help express different quantities of the system and lead to various stability criteria (§3.5 and §3.6).

Let us consider first a transformation,  $\Psi = Th$ , which removes the  $\Psi'$  term from (3.23) since

$(T^2 h')' = T\Psi'' - T''\Psi$ . This gives us that

$$\Psi'' - \frac{2U'T' + T''(U - c) + U''T}{T(U - c)}\Psi + \frac{(U - c)(\beta + cF^2)}{(U - c)^2 - M^2 B^2}\Psi = k^2\Psi. \quad (3.25)$$

Additionally, defining the linearised cross-stream displacement,  $G$ , through

$$v = ikh =: ik(U - c)G \sim \frac{D}{Dt}G, \quad (3.26)$$

following, e.g., Hughes and Tobias (2001), we can then transform to an equation for  $G$ ,

$$(S^2 G')' - [k^2 S^2 - (U - c)(\beta + cF^2)]G = 0, \quad (3.27)$$

where

$$S^2 = (U - c)^2 - M^2 B^2. \quad (3.28)$$

As Howard (1961) and Mak et al. (2016) remark, the definition of  $G$  can be extended to a family of variables,  $G = v(U - c)^{-n}$ , with equation (3.27) corresponding to the  $n = 1$  case.

## 3.4 Waves

Shear instabilities can often be interpreted as the destabilising interaction of waves, therefore, investigating the properties of waves in simple situations can be useful in understanding the (de)stabilisation of complex fluid profiles which can be compared with the compounding of simpler ones.

Earlier (§3.2.1), we showed that a necessary condition for instability is a non-constant magnetic field or a velocity shear. Therefore a configuration with a constant aligned (non-dimensionalised) velocity  $U(y) = 1$  and magnetic field  $B(y) = 1$  is guaranteed to be a stable setup to investigate wave dynamics (§3.4.1). When there is no background flow, we can also investigate the case where a constant magnetic field has an arbitrary (horizontal) direction since there is no background flow with which to align to prevent initial nonequilibrium (§3.4.2). This requires that we return (briefly) to the nonlinear PDEs (2.42) and (2.43) since a different scaling will be necessary.

### 3.4.1 Waves in a Zonal Flow with Aligned Field

Let us substitute  $U = 1$ ,  $B = 1$ , into the linearised equation (3.23), which now has constant coefficients. We can therefore perform a Fourier decomposition in the  $y$ -direction to obtain

$$-l^2 T^2 h - k^2 T^2 h + \frac{k\beta + \omega F^2}{k - \omega} h = 0, \quad (3.29)$$

where  $T^2 = 1 - \frac{k^2 M^2}{(k-\omega)^2}$ ,  $l$  is the latitudinal wavenumber such that  $\mathbf{k} = (k, l, 0)$ , and we have replaced  $c$  with  $\omega = kc$ . Multiplying (3.29) by  $(k - \omega)^2/h$ , gives

$$(k^2 + l^2) \left( (k - \omega)^2 - k^2 M^2 \right) - (k - \omega) (\beta k + \omega F^2) = 0 \quad (3.30)$$

leading to the quadratic dispersion relation

$$(k^2 + l^2 + F^2) \omega^2 + (\beta k - F^2 k - 2(k^2 + l^2)) \omega + k^2 (k^2 + l^2) (1 - M^2) - \beta k^2 = 0, \quad (3.31)$$

and hence

$$\omega = k - \frac{\omega_\beta}{2} \pm \sqrt{\left(\frac{\omega_\beta}{2}\right)^2 + \omega_\alpha^2}, \quad (3.32)$$

where

$$\omega_\alpha = kM \sqrt{\frac{k^2 + l^2}{k^2 + l^2 + F^2}}, \quad \omega_\beta = \frac{k(\beta + F^2)}{k^2 + l^2 + F^2} \quad (3.33)$$

are the Alfvén and Rossby frequencies respectively, generalised to one-layer QG. As a reminder,  $\beta = \beta_0 L^2/U$  and  $F^2 = f_0^2 L^2/g'H$  (and  $M = B/U\sqrt{\mu_0\rho}$ ), so the term  $(\beta + F^2)$  contains a factor of the (constant) flow speed  $U$  attached to the  $F^2$  and (3.32) is not simply a Galilean shift of the  $U = 0$  case. This agrees with the  $M = 0$  limit (Vallis, 2017) and occurs because when  $F^2 \neq 0$  the constant flow modifies the vorticity gradient, which sustains  $\beta$ -plane Rossby waves.

The dispersion relation for two-dimensional flows can be derived by setting  $F^2 = 0$ , i.e. magnetic Rossby waves in  $\beta$ -plane MHD (Hide, 1969; Acheson and Hide, 1973). Without rotation ( $\beta = 0$ ), then leads to the Alfvén wave dispersion relation. If  $F^2 \neq 0$ , the Alfvén dispersion relation is modified by a damping factor.

The dispersion relation (3.32) matches that of Gilman (1969), albeit derived from a different system. Gilman's is derived from a baroclinic system which then reduces to an identical one when  $\rho = \text{const}$  and  $U = 0$ . Gilman also notes the factor of  $F^2$  that modifies the Alfvén wave speed and points out that Alfvén waves (like Rossby waves) propagate vorticity through the Lorentz force and their propagation is opposed by the vertical motion (of the free surface) of the fluid.

### 3.4.2 Waves in an Arbitrary Uniform Field

Without a background flow, we can propose an arbitrary magnetic field,  $\mathbf{B}$ , and examine the waves produced by its amalgamation with rotation and stratification. This, though, requires us to return to the nonlinear equations (2.42), (2.43) since a different scaling is necessary. As there is no flow in this setup, we set the velocity scaling instead to be  $U = v_A = B/\sqrt{\mu_0\rho}$ , the Alfvén speed (i.e.  $M = 1$ ), and hence:

$$\frac{\partial}{\partial t} \nabla^2 h + \mathcal{J}(h, \nabla^2 h) - \mathcal{J}(A, \nabla^2 A) - F^2 \frac{\partial h}{\partial t} + \beta \frac{\partial h}{\partial x} = 0, \quad (3.34)$$

$$\frac{\partial A}{\partial t} + \mathcal{J}(h, A) = 0. \quad (3.35)$$

Defining the magnetic field as  $\mathbf{B} = (B_x, B_y)$ , we linearise in perturbed variables  $\tilde{h}$ ,  $\tilde{a}$ , where  $h = \tilde{h}$  and  $A = B_y x - B_x y + \tilde{a}$  to get

$$\frac{\partial}{\partial t} \nabla^2 \tilde{h} - F^2 \frac{\partial \tilde{h}}{\partial t} + \beta \frac{\partial \tilde{h}}{\partial x} - \left( B_x \frac{\partial}{\partial x} + B_y \frac{\partial}{\partial y} \right) \nabla^2 \tilde{a} = 0, \quad (3.36)$$

$$\frac{\partial \tilde{a}}{\partial t} - \left( B_x \frac{\partial}{\partial x} + B_y \frac{\partial}{\partial y} \right) \tilde{h} = 0. \quad (3.37)$$

Solving for Fourier modes,  $\tilde{h} = \hat{h} e^{(i\mathbf{k}\cdot\mathbf{x} - \omega t)}$ , where  $\mathbf{k} = (k, l)$ , as before, we obtain

$$\left( i\omega |\mathbf{k}|^2 + i\omega F^2 + ik\beta \right) \hat{h} + i |\mathbf{k}|^2 \mathbf{k} \cdot \mathbf{B} \hat{a} = 0, \quad (3.38)$$

$$-i\omega \hat{a} - i\mathbf{k} \cdot \mathbf{B} \hat{h} = 0. \quad (3.39)$$

The dispersion relation is derived by substituting (3.39) into (3.38), giving

$$\left( |\mathbf{k}|^2 + F^2 \right) \omega^2 + \beta k\omega - M^2 |\mathbf{k}|^2 (\mathbf{k} \cdot \mathbf{B})^2 = 0, \quad (3.40)$$

and hence

$$\omega = -\frac{\omega_\beta}{2} \pm \sqrt{\left( \frac{\omega_\beta}{2} \right)^2 + \omega_\alpha^2}, \quad (3.41)$$

where

$$\omega_\alpha = \frac{|\mathbf{k}| (\mathbf{k} \cdot \mathbf{B})}{\sqrt{|\mathbf{k}|^2 + F^2}}, \quad \omega_\beta = \frac{k\beta}{|\mathbf{k}|^2 + F^2}. \quad (3.42)$$

Note that, equivalent to (3.32), the Alfvén term in (3.41) contains a factor of  $F^2$ , implying that pure Alfvén waves are slowed by stratification. This differs from the expressions given by Zeitlin (2013) and Raphaldini and Raupp (2020) for this dispersion relation.

### 3.5 Profile Restrictions

Stability results that apply to a large class of flow profiles are the holy grail of linear stability analysis. For non-rotating and hydrodynamic problems, a wide class of results has been derived, e.g., Rayleigh and Fjørtoft's criteria (Rayleigh, 1913; Fjørtoft, 1950) and Howard's semicircle theorem (Howard, 1961). The addition of magnetic field and rotation complicates matters in many cases but some results are possible, and we will show those where we have been able to reproduce these (albeit often with limitations) for QG SWMHD instabilities.

Taking equation (3.25),

$$-\Psi'' + \frac{2U'T' + T''(U - c) + U''T}{T(U - c)} \Psi - \frac{(U - c)(\beta + cF^2)}{(U - c)^2 - M^2 B^2} \Psi = -k^2 \Psi. \quad (3.43)$$

and multiplying by  $\Psi^*$ , integrating across the domain, and rearranging we obtain

$$\int_{\mathcal{D}} Q(y) |\Psi|^2 dy = - \int_{\mathcal{D}} \left( |\Psi'|^2 + k^2 |\Psi|^2 \right) dy, \quad (3.44)$$

where

$$Q(y) = \frac{2U'T' + T''(U - c) + U''T}{T(U - c)} - \frac{(U - c)(\beta + cF^2)}{(U - c)^2 - M^2B^2}. \quad (3.45)$$

For (3.44) to be satisfied, since the RHS is real, the imaginary part of  $Q$  must either be identically zero or change sign in the domain. For smooth field and velocity profiles this means that instability requires at least one point where  $\Im(Q) = 0$ .

When  $F^2 = 0$  and  $M = 0$  ( $\implies T = 1$ ), one can easily verify that  $Q(y)$  simplifies to  $(U'' - \beta)/(U - c)$ , and  $\Im(Q) = c_i(U'' - \beta)/|U - c|^2$ , giving the Rayleigh-Kuo criterion for the  $\beta$ -plane (Kuo, 1949). When  $\beta = 0$ ,  $F^2 = 0$  and  $M \neq 0$ , we instead have

$$Q(y) = \frac{2U'T' + T''(U - c) + U''T}{T(U - c)} = \frac{2S^2(S^2)'' - (S^2)'^2}{4S^4} \quad (3.46)$$

(Kent, 1968). In this case, the condition  $\Im(Q) = 0$  is of limited practical use in restricting flow profiles since it requires *a priori* knowledge of the eigenvalue  $c$ . Of course, if we know  $c$ , we already know whether or not that particular flow is stable. This same limitation is true in our more general case  $\beta, F^2 \neq 0$ .

Perhaps this result could be combined with the semicircle theorem in the next section to eliminate  $c$ , but whether this would provide a useful constraint is unclear.

We can also consider the real part. Since the RHS is either zero or negative, stability is guaranteed if  $\Re(Q) \geq 0$  throughout the domain. This would generalise Fjørtoft's criterion and is also of little practical use when  $M \neq 0$ .

### 3.6 Semicircle Theorems

A method which has yielded results in both MHD flows (Hughes and Tobias, 2001) and QG flows (Pedlosky, 1987) extends the semicircle theorem of Howard (1961), which bounds the complex phase speed ( $c = c_r + ic_i$ ) of instabilities to a semicircle on the complex plane.

Considering equation (3.27), multiplying by the complex conjugate of  $G$ , and integrating across the domain  $\mathcal{D}$  gives

$$\int_{\mathcal{D}} \left( (S^2 G')' G^* - (k^2 S^2 - (U - c)(\beta + cF^2)) |G|^2 \right) dy = 0. \quad (3.47)$$

Assuming that  $G$  vanishes at the domain boundaries, integrating the first term by parts yields

$$\int_{\mathcal{D}} \left( S^2 |G'|^2 + (k^2 S^2 - (U - c)(\beta + cF^2)) |G|^2 \right) dy = 0. \quad (3.48)$$

Then, splitting (3.48) into real and imaginary parts gives

$$\int_{\mathcal{D}} \left( (U - c_r)^2 - c_i^2 - M^2 B^2 \right) \Lambda dy = \int_{\mathcal{D}} \left( (U - c_r)(\beta + c_r F^2) + c_i^2 F^2 \right) \Sigma dy \quad (3.49)$$

as the real part and,

$$c_i \int_{\mathcal{D}} (U - c_r) (\Lambda + F^2 \Sigma) \, dy = \frac{c_i}{2} \int_{\mathcal{D}} (\beta + F^2 U) \Sigma \, dy \quad (3.50)$$

as the imaginary part, where we have denoted

$$\Lambda = |G'|^2 + k^2 |G|^2 > 0, \quad \Sigma = |G|^2 > 0. \quad (3.51)$$

In the absence of rotation ( $\beta = F^2 = 0$ ) the above equations can be used to derive eigenvalue bounds following Hughes and Tobias (2001), and with  $M^2 = 0$ , following Pedlosky (1963, 1964). We will show that we can use the ideas of both to obtain a similar set of bounds on the eigenvalue,  $c = c_r + ic_i$ , in the general case.

### 3.6.1 Phase Speed Bounds

Considering only equation (3.50), with  $c_i \neq 0$  we can immediately obtain a generalisation of the phase speed bound for unstable modes (Synge, 1933) by considering the maxima and minima of the LHS and RHS respectively. Bounding in one way yields

$$(U_{\min} - c_r) \int_{\mathcal{D}} (\Lambda + F^2 \Sigma) \, dy \leq (\beta + F^2 U_{\max}) \int_{\mathcal{D}} \Sigma \, dy, \quad (3.52)$$

since  $F^2 \geq 0$  and  $\Lambda, \Sigma > 0$  for non-trivial solutions, and, since  $\Lambda > k^2 \Sigma$ ,

$$c_r \geq U_{\min} - \frac{\max(0, \beta + F^2 U_{\max})}{2(k^2 + F^2)} > U_{\min} - \frac{\max(0, \beta + F^2 U_{\max})}{2F^2}. \quad (3.53)$$

Bounding in another then gives

$$(U_{\max} - c_r) \int_{\mathcal{D}} (\Lambda + F^2 \Sigma) \, dy \geq (\beta + F^2 U_{\min}) \int_{\mathcal{D}} \Sigma \, dy, \quad (3.54)$$

and hence

$$c_r \leq U_{\max} + \frac{\min(0, \beta + F^2 U_{\min})}{2(k^2 + F^2)} < U_{\max} + \frac{\min(0, \beta + F^2 U_{\min})}{2F^2}. \quad (3.55)$$

Since the coefficient  $(\beta + F^2 U)$  is the basic state vorticity, we see that the phase speed must be within the range of the flow, except possibly where there is a speed shift by Rossby waves. For example, in the case  $F^2 = 0$ ,  $\beta > 0$ , we return immediately to the result of Pedlosky (1987),

$$U_{\min} - \frac{\beta}{2k^2} \leq c_r \leq U_{\max}. \quad (3.56)$$

### 3.6.2 Rest-Frame Semicircle

Let us now include the real part of the integral, (3.49), and use (3.50) to eliminate terms of  $U\Lambda$  on the LHS of (3.49) (with  $c_i \neq 0$ ). Thus we get that

$$\int_{\mathcal{D}} (U^2 - (c_r^2 + c_i^2) - M^2 B^2) \Lambda \, dy = \int_{\mathcal{D}} (\beta U + F^2 (c_r^2 + c_i^2)) \Sigma \, dy. \quad (3.57)$$

Let us consider this equation in the  $f$ -plane case, which allows access to a broader set of results since the equations become symmetric with  $y \rightarrow -y$ . With  $\beta = 0$ , this simplifies (3.57) to

$$(c_r^2 + c_i^2) \int_{\mathcal{D}} (\Lambda + F^2 \Sigma) = \int_{\mathcal{D}} (U^2 - M^2 B^2) \Lambda, \quad (3.58)$$

from which an important result is possible. Neglecting the  $F^2$  term on the LHS and bounding the RHS with the maximum of  $(U^2 - M^2 B^2)$ , we have that

$$c_r^2 + c_i^2 < (U^2 - M^2 B^2)_{\max}. \quad (3.59)$$

This provides us with an upper bound on the magnitude of the eigenvalue,  $c$ , a corollary of which is that if the magnetic energy everywhere exceeds the kinetic ( $M^2 B^2 > U^2$ ), then the above equation is a contradiction. Thus  $c_i \equiv 0$  and instability cannot occur.

A lower bound on  $|c|^2$  can be obtained by considering the opposite limit. In this case, we obtain

$$c_r^2 + c_i^2 > \frac{k^2}{k^2 + F^2} (U^2 - M^2 B^2)_{\min}. \quad (3.60)$$

The upper bound on  $|c|^2$ , when  $\beta \neq 0$ , is

$$c_r^2 + c_i^2 < \begin{cases} (U^2 - M^2 B^2)_{\max}, & F^2 (U^2 - B^2)_{\max} > |\beta U|_{\max}, \\ \frac{k^2 (U^2 - M^2 B^2)_{\max} + |\beta U|_{\max}}{k^2 + F^2}, & F^2 (U^2 - B^2)_{\max} < |\beta U|_{\max}. \end{cases} \quad (3.61)$$

The radius of the semicircle (3.61) is maximised when  $k \rightarrow 0$ . In this case, the bound can be expressed in the simpler form:

$$c_r^2 + c_i^2 < \max \left\{ (U^2 - M^2 B^2)_{\max}, \frac{|\beta U|_{\max}}{F^2} \right\}. \quad (3.62)$$

Unlike in 2D MHD (Kent, 1966a; Hughes and Tobias, 2001), note that  $M^2 B^2 > U^2$  everywhere is insufficient to guarantee stability.

### 3.6.3 Canonical-Frame

The LHS of equation (3.62) contains the phase speed,  $c_r$ , and we might expect that adding a constant value to  $U$  would add an equal value to  $c_r$  without affecting the value of  $c_i$ . The RHS of (3.62) is also dependent on  $U$  and so a tighter bound on  $c_i$  could be derived by minimising

$c_r$ . If we define the two quantities

$$\bar{U} = \frac{U_{\min} + U_{\max}}{2}, \quad \Delta U = \frac{U_{\max} - U_{\min}}{2}, \quad (3.63)$$

perhaps we could find a tighter bound by instead considering  $(c_r - \bar{U})$ .

Note that it is always possible to shift to a frame where  $\bar{U} = 0$ . Consider equation (3.27) and let  $U(y) = \bar{U} + U_0(y)$ ,  $\beta = \tilde{\beta} - F^2\bar{U}$ ,

$$(S^2 G')' - \left[ k^2 S^2 - (U_0 + \bar{U} - c) \left( \tilde{\beta} - F^2\bar{U} + cF^2 \right) \right] G = 0, \quad (3.64)$$

where  $S^2 = (U_0 + \bar{U} - c)^2 - M^2 B^2$ . It is clear to see that we can then form the group,  $c - \bar{U} = \tilde{c}$ , and hence return to our original eigenvalue problem, now with  $\tilde{c}$ ,  $\tilde{\beta}$ ,  $U_0$ . The analysis can then proceed as before and we can obtain an equation equivalent to (3.57),

$$\int_{\mathcal{D}} (U_0^2 - (\tilde{c}_r^2 + c_i^2) - M^2 B^2) \Lambda \, dy = \int_{\mathcal{D}} \left( \tilde{\beta} U_0 + F^2 (\tilde{c}_r^2 + c_i^2) \right) \Sigma \, dy. \quad (3.65)$$

### 3.6.4 Canonical-Frame Semicircle

Following Howard (1961) we now use the identity:

$$(U_0 + \Delta U)(U_0 - \Delta U) \leq 0, \quad (3.66)$$

with equality only when  $U_0$  is everywhere zero ( $\implies \Delta U = 0$ ). Hence we can obtain the bound on  $U_0^2$  terms,

$$\int_{\mathcal{D}} U_0^2 \Lambda \, dy < \int_{\mathcal{D}} \Delta U^2 \Lambda \, dy, \quad (3.67)$$

which can be substituted into equation (3.65) to get

$$\int_{\mathcal{D}} (\Delta U^2 - (\tilde{c}_r^2 + c_i^2) - M^2 B^2) \Lambda \, dy \geq \int_{\mathcal{D}} \left( -|\tilde{\beta}| \Delta U + F^2 (\tilde{c}_r^2 + c_i^2) \right) \Sigma \, dy. \quad (3.68)$$

If we discard the positive  $F^2$  term on the RHS then, since  $\Lambda > k^2 \Sigma$ , we realise the standard two-dimensional  $\beta$ -plane bound, including now a magnetic component,

$$\tilde{c}_r^2 + c_i^2 < \Delta U^2 + \frac{|\tilde{\beta}|}{k^2} \Delta U - M^2 B_{\min}^2, \quad (3.69)$$

which unfortunately involves the wavelength  $k$  in such a way that the semicircle radius tends to infinity as  $k \rightarrow 0$ . Instead, rearranging (3.68) so that the two integrals are  $(\Lambda + F^2 \Sigma)$  and  $(F^2 \Sigma)$ , we can divide through by the former to get

$$\tilde{c}_r^2 + c_i^2 + M^2 B_{\min}^2 - \Delta U^2 < \left( M^2 B_{\min}^2 - \Delta U^2 + \Delta U \left| \frac{\tilde{\beta}}{F^2} \right| \right) \frac{\int_{\mathcal{D}} F^2 \Sigma \, dy}{\int_{\mathcal{D}} (\Lambda + F^2 \Sigma) \, dy}. \quad (3.70)$$

We now need to consider the two cases for the sign of the RHS coefficient. First, if  $F^2(\Delta U^2 - M^2 B_{\min}^2) > \Delta U |\tilde{\beta}|$  then the RHS coefficient is negative and we ask what the minimum value of the fraction

$$\frac{\int_{\mathcal{D}} F^2 \Sigma \, dy}{\int_{\mathcal{D}} (\Lambda + F^2 \Sigma) \, dy} = \frac{\int_{\mathcal{D}} F^2 |G|^2 \, dy}{\int_{\mathcal{D}} (|G'|^2 + k^2 |G|^2 + F^2 |G|^2) \, dy} \quad (3.71)$$

on the RHS of (3.70) is. Since  $G'$  is unbounded (with respect to  $G$ ) this fraction is bounded below only by zero. Hence, we get that

$$\tilde{c}_r^2 + c_i^2 < \Delta U^2 - M^2 B_{\min}^2, \quad (3.72)$$

(equivalent to the Hughes and Tobias (2001) semicircle). If instead we have that  $\Delta U |\tilde{\beta}| > F^2(\Delta U^2 - M^2 B_{\min}^2)$ , then we ask what the maximum value of the integral is. In this case, we note that  $G = \text{const}$  is a solution which minimises  $\Lambda$  and so we get that

$$\tilde{c}_r^2 + c_i^2 + M^2 B_{\min}^2 - \Delta U^2 < \left( M^2 B_{\min}^2 - \Delta U^2 + \Delta U \left| \frac{\tilde{\beta}}{F^2} \right| \right) \frac{F^2}{k^2 + F^2}, \quad (3.73)$$

$$\implies \tilde{c}_r^2 + c_i^2 < \frac{k^2 (\Delta U^2 - M^2 B_{\min}^2) + |\tilde{\beta}| \Delta U}{k^2 + F^2}, \quad (3.74)$$

$$< \frac{|\tilde{\beta}| \Delta U}{F^2}. \quad (3.75)$$

The tightest semicircle is, returning to our rest-frame variables,

$$(c_r - \bar{U})^2 + c_i^2 < \begin{cases} \Delta U^2 - M^2 B_{\min}^2, & F^2 (\Delta U^2 - M^2 B_{\min}^2) > \Delta U |\beta + F^2 \bar{U}|, \\ \frac{k^2 (\Delta U^2 - M^2 B_{\min}^2) + |\tilde{\beta}| \Delta U}{k^2 + F^2}, & F^2 (\Delta U^2 - M^2 B_{\min}^2) < \Delta U |\beta + F^2 \bar{U}|. \end{cases} \quad (3.76)$$

This is widest in the limit  $k \rightarrow 0$ , and then gives

$$(c_r - \bar{U})^2 + c_i^2 < \max \left\{ \Delta U^2 - M^2 B_{\min}^2, \Delta U \left| \frac{\beta}{F^2} + \bar{U} \right| \right\}. \quad (3.77)$$

Semicircle (3.76) makes semicircle (3.69) redundant, as expected when the effects of stratification are also included, whilst, unlike the semicircle of Pedlosky (1963), our semicircle in (3.77) has a finite radius and so provides a general growth rate limit for a given flow profile,  $U(y)$ ,  $B(y)$ .

We have considered two reference frames here and it is also possible to consider any arbitrary reference frame which can improve the semicircle bound for particular flows. Hughes and Tobias (2001) note, however, that this criterion is often difficult to use practically. For many flows, either (3.62) or (3.77) are optimal semicircles.

### 3.6.5 Semicircles in Two-Layer QG

It is not obvious why we can derive a finite radius semicircle in one-layer QG, but in two-layer QG a finite radius semicircle is possible only when boundaries in the  $y$ -direction are present (Pedlosky, 1963, 1964). To investigate this, we will first re-derive the two-layer semicircle.

The linearised equations of two-layer QG (equation (4.2.2) of Pedlosky (1963), without underlying topology) are

$$\frac{d}{dy} (U_1 - c)^2 \frac{dG_1}{dy} - k^2 (U_1 - c)^2 G_1 = F_1 (U_1 - c) (U_2 - c) (G_1 - G_2) - \beta (U_1 - c) G_1, \quad (3.78)$$

$$\frac{d}{dy} (U_2 - c)^2 \frac{dG_2}{dy} - k^2 (U_2 - c)^2 G_2 = F_2 (U_1 - c) (U_2 - c) (G_2 - G_1) - \beta (U_2 - c) G_2, \quad (3.79)$$

where  $G_i = \psi_i / (U_i - c)$  and  $\psi_i$  are the streamfunctions,  $U_i$  are the flow profiles, and  $F_i = f^2 L^2 / g'_i H_i$  are the equivalent to our  $F^2$  parameter in each layer. This is an eigenvalue problem with eigenvalue,  $c$ , the phase speed, and  $G_1, G_2$ , the eigenfunctions of each layer. Note that equation (3.78) reduces to the one-layer governing equation, ((3.27) without field), when  $U_2 = G_2 = 0$ .

Dividing each equation by  $F_i$  and integrating over the domain, we obtain

$$\int_{\mathcal{D}} (U_1 - c)^2 \Lambda_1 = \beta \int_{\mathcal{D}} (U_1 - c) \Sigma_1 - \int_{\mathcal{D}} (U_1 - c) (U_2 - c) (|G_1|^2 - G_2 G_1^*), \quad (3.80)$$

$$\int_{\mathcal{D}} (U_2 - c)^2 \Lambda_2 = \beta \int_{\mathcal{D}} (U_2 - c) \Sigma_1 - \int_{\mathcal{D}} (U_1 - c) (U_2 - c) (|G_2|^2 - G_1 G_2^*), \quad (3.81)$$

where  $\Lambda_i = (|G'_i|^2 + k^2 |G_i|^2) / F_i$ , and  $\Sigma_i = |G_i|^2 / F_i$  are positive functions. Adding these two equations we also obtain a third quantity,  $|G_1|^2 - G_2 G_1^* - G_1 G_2^* + |G_2|^2 = |G_1 - G_2|^2 = X > 0$ , and so

$$\begin{aligned} \int_{\mathcal{D}} (U_1 - c)^2 \Lambda_1 + \int_{\mathcal{D}} (U_2 - c)^2 \Lambda_2 = \\ \beta \int_{\mathcal{D}} (U_1 - c) \Sigma_1 + \beta \int_{\mathcal{D}} (U_2 - c) \Sigma_2 - \int_{\mathcal{D}} (U_1 - c) (U_2 - c) X. \end{aligned} \quad (3.82)$$

This we split into real and imaginary parts to get

$$\begin{aligned} \int_{\mathcal{D}} \left( (U_1 - c_r)^2 - c_i^2 \right) \Lambda_1 + \int_{\mathcal{D}} \left( (U_2 - c_r)^2 - c_i^2 \right) \Lambda_2 = \\ \beta \int_{\mathcal{D}} (U_1 - c_r) \Sigma_1 + \beta \int_{\mathcal{D}} (U_2 - c_r) \Sigma_2 + \int_{\mathcal{D}} (c_i^2 - (U_1 - c_r) (U_2 - c_r)) X, \end{aligned} \quad (3.83)$$

from the real part, and

$$\begin{aligned} -2c_i \int_{\mathcal{D}} (U_1 - c_r) \Lambda_1 - 2c_i \int_{\mathcal{D}} (U_2 - c_r) \Lambda_2 = \\ -c_i \beta \int_{\mathcal{D}} (\Sigma_1 + \Sigma_2) + c_i \int_{\mathcal{D}} (U_1 + U_2 - 2c_r) X. \end{aligned} \quad (3.84)$$

from the imaginary. If we have instability,  $c_i > 0$ , then we divide (3.84) through by  $c_i$ ,

multiply by  $c_r$ , and substitute into (3.83) to get

$$\int_{\mathcal{D}} (U_1^2 - c_r^2 - c_i^2) \Lambda_1 + \int_{\mathcal{D}} (U_2^2 - c_r^2 - c_i^2) \Lambda_2 = \beta \int_{\mathcal{D}} (U_1 \Sigma_1 + U_2 \Sigma_2) + \int_{\mathcal{D}} (c_r^2 + c_i^2 - U_1 U_2) X, \quad (3.85)$$

(cf. (3.57), (3.65)). We now reintroduce the parameters

$$\bar{U} = \frac{U_{\min} + U_{\max}}{2}, \quad \Delta U = \frac{U_{\max} - U_{\min}}{2}, \quad (3.86)$$

and with these can write down the inequality

$$(\bar{U} - \Delta U - U_i) (\bar{U} + \Delta U - U_i) \leq 0, \quad i = 1, 2, \quad (3.87)$$

$$\implies U_i^2 \leq \Delta U^2 - \bar{U}^2 + 2\bar{U}U_i. \quad (3.88)$$

Additionally, from (3.84), we have that

$$2\bar{U} \int_{\mathcal{D}} U_1 \Lambda_1 + 2\bar{U} \int_{\mathcal{D}} U_2 \Lambda_2 = 2c_r \bar{U} \int_{\mathcal{D}} (\Lambda_1 + \Lambda_2) + \beta \bar{U} \int_{\mathcal{D}} (\Sigma_1 + \Sigma_2) - \bar{U} \int_{\mathcal{D}} (U_1 + U_2 - 2c_r). \quad (3.89)$$

Combining equations (3.85) and (3.89), and the inequality (3.88), we therefore get that

$$\int_{\mathcal{D}} \left( \Delta U^2 - (c_r - \bar{U})^2 - c_i^2 \right) (\Lambda_1 + \Lambda_2) \geq \int_{\mathcal{D}} \left( (U_1 - \bar{U}) \Sigma_1 + (U_2 - \bar{U}) \Sigma_2 \right) + \int_{\mathcal{D}} \left( (c_r - \bar{U})^2 + c_i^2 - (U_1 - \bar{U})(U_2 - \bar{U}) \right) X, \quad (3.90)$$

which can be rearranged to

$$\int_{\mathcal{D}} \left( (c_r - \bar{U})^2 + c_i^2 - \Delta U^2 \right) (\Lambda_1 + \Lambda_2 + X) \leq \beta \int_{\mathcal{D}} \left( (\bar{U} - U_1) \Sigma_1 + (\bar{U} - U_2) \Sigma_2 \right) + \int_{\mathcal{D}} \left( (\bar{U} - U_1) (\bar{U} - U_2) - \Delta U^2 \right) X. \quad (3.91)$$

$\Delta U^2 > (\bar{U} - U_1) (\bar{U} - U_2)$ , so we can drop the RHS  $\int X$  term and since  $\beta (\bar{U} - U_i) < |\beta| \Delta U > 0$ , we are left only with the task of bounding the fraction

$$\frac{\int_{\mathcal{D}} (\Sigma_1 + \Sigma_2)}{\int_{\mathcal{D}} (\Lambda_1 + \Lambda_2 + X)} \quad (3.92)$$

from above. In one-layer QGSW, this is possible since  $X$  is replaced by  $\Sigma$ , however here the fraction is bounded only from the  $k^2 \Sigma_i$  terms in  $\Lambda_i$ . Hence we obtain the semicircle

$$(c_r - \bar{U})^2 + c_i^2 < \Delta U^2 + \frac{|\beta|}{k^2} \Delta U \quad (3.93)$$

which has an infinite radius in the limit  $k \rightarrow 0$ .

### 3.7 Discussion

What can explain the critical difference between semicircle theorems in one- and two-layer QG (equations (3.77) and (3.93))? One possible explanation is linked to the mechanism behind shear instability, counter-propagating Rossby waves. In this explanation, instability arises from the interaction of waves (resulting from the shear, or otherwise) which hold each other in phase and provide amplification for the other wave proportional to their amplitude (Bretherton, 1966). This then leads to exponential growth. For the two waves to hold each other in phase, they need to be travelling with the same speed, and therefore, in the absence of any other physics, these waves would be generated by the shear and so be moving with a speed within the range of the flow. However, with the addition of a  $\beta$ -effect, these waves could travel arbitrarily fast up to the speed of Rossby waves. However, the speed of  $\beta$ -plane Rossby waves is different in one- and two-layer QG. When a free surface is present (in one-layer QGSW) the maximum speed of Rossby waves is finite (cf. (3.41) with  $M = 0$ ), as opposed to in two-layer QG, in which two modes exist with

$$\omega_1 = \frac{-\beta k}{k^2 + l^2}, \quad \omega_2 = \frac{-\beta k}{k^2 + l^2 + F_1 + F_2}, \quad (3.94)$$

(Pedlosky, 1987, using the notation of (3.78), (3.79)), and hence there is no upper limit on the speed of Rossby waves. In the two-layer case the “free surface” now lies between the layers, and the outer boundaries are fixed. The two modes correspond to barotropic and baroclinic modes, respectively (Pedlosky, 1987). The lack of an upper bound on Rossby wave speeds could explain the different semicircle radii between the two cases. Hall (1980) made a similar suggestion in a different context.



# Chapter 4

## Linear Instability of a Vortex Sheet

### 4.1 Introduction

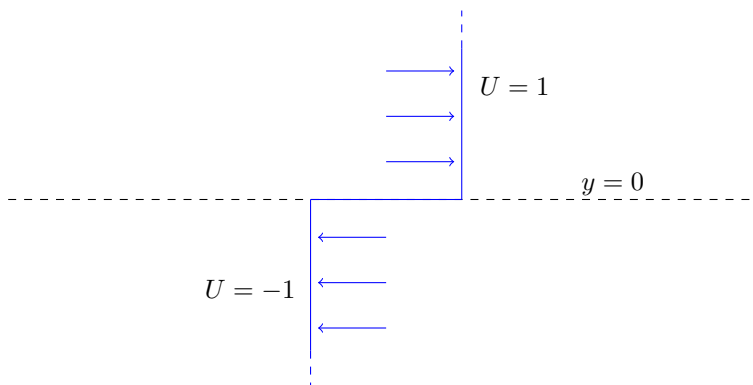


Figure 4.1: The initial vortex sheet flow profile

The integral theorems of the previous chapter show that the shape of the initial flow is crucial to the development of the (linear) instability. In this chapter we will discuss the flow profile

$$U(y) = \begin{cases} +1, & y > 0 \\ -1, & y < 0 \end{cases} \quad (4.1)$$

which is the archetypal shear flow, also known as the *Vortex Sheet* since all of the (relative) vorticity of the flow is concentrated to an infinitesimally thin interface initially at  $y = 0$ . One benefit of starting with this profile is that it has been discussed, for various fluid approximations, since the mid-19th century, going back to the work of Thomson (1871) and Helmholtz (1868). Its solutions can often provide insight into the solutions of a large set of more general fluid profiles (Drazin and Howard, 1962; Mak et al., 2016). Its simplicity means we can often tackle this problem analytically where more general profiles require numerical techniques (cf. §5).

Important generalisations were made by Kuo (1949) to the  $\beta$ -plane approximation, Miles

(1958) with continuous stratification and Michael (1955), Northrop (1956) for magnetised plasmas. Here, and in the rest of our linear stability analysis, we will assume that the basic field has a constant strength,

$$B^2(y) = 1, \quad (4.2)$$

everywhere in our domain and is aligned with the fluid flow (as in §3). The magnetic field strength is set by the non-dimensional parameter  $M$ . The constant field approximation models physical situations where the flow varies, and gives rise to instabilities, on a scale much smaller than the magnetic field, and means that the underlying instability mechanism is shear-driven. Generalisations with a variable magnetic field can modify the vortex sheet (Michael, 1955), and even give rise to additional instabilities in other cases (e.g. Kent, 1968; Chen and Morrison, 1991; Wang et al., 2022).

This chapter proceeds by first deriving a dispersion relation based on the profiles (4.1) and (4.2) (§4.2.1). We will then show that the same dispersion relation can be derived asymptotically from a long wavelength analysis (§4.2.2). This isomorphism is one of the key reasons we are interested in the vortex sheet problem. The next section (§4.3) will then discuss the existence of solutions to the dispersion relation, which may or may not satisfy boundary conditions and existence criteria. Naturally following this, we then determine conditions for the existence of *complex* solutions of the dispersion relation, i.e., the conditions under which the vortex sheet profile is unstable to small perturbations (§4.4). We end this chapter by examining the individual effect of each parameter and investigating how variations affect the properties of the solutions including any broad regimes that can be defined (§4.5).

## 4.2 Dispersion Relation

### 4.2.1 Dispersion Relation: Derivation From A Prescribed Profile

Substituting (4.1) into the linearised perturbation equation (3.27), we obtain the two constant coefficient ODEs

$$G''(y) - \left( k^2 - \frac{(\pm 1 - c)(\beta + cF^2)}{(\pm 1 - c)^2 - M^2} \right) G(y) = 0, \quad \pm y > 0. \quad (4.3)$$

These give simple exponential solutions of which we choose the part, in each half-plane, that decays away from the interface, i.e.

$$G = \begin{cases} Ae^{-\alpha_+ y}, & y > 0, \\ Be^{\alpha_- y}, & y < 0, \end{cases} \quad (4.4)$$

where  $\alpha_{\pm}$  are defined to be the roots of

$$\alpha_{\pm}^2 = k^2 + \frac{(c \mp 1)(\beta + cF^2)}{(c \mp 1)^2 - M^2} \quad (4.5)$$

with  $\Re(\alpha_{\pm}) > 0$ .

There are now two interfacial conditions that come directly from the physical interpretation

of the problem. One of these is that any cross-stream ( $\hat{y}$ ) disturbance in one half-plane must match the disturbance in the other, i.e.  $[G]_{0-}^{0+} = 0$  (where  $0^+/0^-$  denotes the limit as  $y$  approaches zero from the positive/negative direction) and hence  $A = B$ <sup>1</sup>. The second interfacial requirement, which gives rise to our dispersion relation, is that pressure must be continuous. It can be shown that this is equivalent to continuity of the integral of equation (3.27) over the interface i.e.  $[S^2 G']_{0-}^{0+} = 0$ . Substituting our general solution (4.5) into these conditions we obtain the eigenvalue equation

$$- \left( (c-1)^2 - M^2 \right) \alpha_+ = \left( (c+1)^2 - M^2 \right) \alpha_-. \quad (4.6)$$

Although (4.6) appears simple, much of the complexity is hidden in  $\alpha_{\pm}$  (4.5), including a square root. In the next section, we derive (4.6) via alternate means.

#### 4.2.2 Dispersion Relation: Derivation From Long Wavelength Analysis

Although it is traditional to consider the vortex sheet profile as an independent flow, the same dispersion relation can be derived in the long-wavelength limit for any shear flow which tends to different constant values, e.g.  $U(y) \rightarrow \pm 1$  as  $y \rightarrow \pm\infty$ . Heuristically, as the wavelength considered becomes larger, the relative width of the shear layer decreases and in the absolute limit becomes the vortex sheet. This interpretation can be made mathematically rigorous. The derivation below is based on Griffiths (2021, private communication).

Let us start with the equation for  $G(y)$ , (3.27),

$$(S^2 G')' - (k^2 S^2 - (U - c)(\beta + cF^2)) G = 0, \quad (4.7)$$

(recalling  $S^2 = (U - c)^2 - M^2 B^2$ ) and note that without loss of generality, we can set  $k > 0$ . We now introduce a small parameter  $0 < \varepsilon \ll 1$  and assume that  $k = \mathcal{O}(\varepsilon)$ ,  $\beta, F^2 = \mathcal{O}(\varepsilon^2)$  (i.e. each of the parameters enters at the same order). We then define

$$k = \varepsilon \tilde{k}, \quad \beta = \varepsilon^2 \tilde{\beta}, \quad F^2 = \varepsilon^2 \tilde{F}^2 \quad (4.8)$$

so that we have

$$(S^2 G')' = \varepsilon^2 R^2 G, \quad R^2 = \tilde{k}^2 S^2 - (U - c)(\tilde{\beta} + c\tilde{F}^2). \quad (4.9)$$

We proceed assuming that (after non-dimensionalisation)  $U(y) \rightarrow \pm 1$  as  $y \rightarrow \pm\infty$  (shear flow rather than jet ( $U(y) \rightarrow 1$ )), and also that  $B \rightarrow 1$  as  $y \rightarrow \pm\infty$  (i.e. the far-field is even, but of arbitrary strength  $M$  relative to the flow). Finally, we restrict ourselves to unstable modes  $c_i > 0$ , which allows us to avoid some of the complexities associated with critical modes.

A far-field solution can now be constructed using the scaled variable  $Y = \varepsilon y$ . With this (4.9) becomes

$$\frac{d}{dY} \left( S^2 \frac{dG}{dY} \right) = R^2 G, \quad (4.10)$$

---

<sup>1</sup>A nonphysical consequence of this is that  $[h]_{0-}^{0+}$  is generally non-zero as  $h = (U - c)G$  (equation (3.26)), i.e. there is a jump in the surface height across the interface. This is a consequence of the nonphysical (discrete flow) setup and is rectified when  $U$  is continuous.

and provided that  $U'$  and  $B'$  tend exponentially to zero as  $|y| \rightarrow \infty$ , then  $S(y)$  and  $R(y)$  in (4.10) differ from their limiting values  $S_{\pm}$  and  $R_{\pm}$  by only an exponentially small amount as  $\varepsilon \rightarrow 0$ . We can therefore perform a regular perturbation expansion in  $\varepsilon$  with these limiting values inserted in (4.10). The leading-order outer solution is thus

$$G(Y) = A_{\pm} e^{\mp \alpha_{\pm} Y}, \text{ where } \alpha_{\pm} = \frac{R_{\pm}}{S_{\pm}}, \quad (4.11)$$

with the square roots taken when calculating  $R_{\pm}$  and  $S_{\pm}$  so that  $\Re(\alpha_{\pm}) > 0$  (which is always possible for  $c_i > 0$ ). On this outer length scale, all variations in the flow and field appear to be compressed into a small region around  $Y = 0$ , i.e. the flow looks like a vortex sheet, and the field appears to give a current sheet.

In due course, this outer solution will need to be matched to an inner solution. This is perhaps best done using an intermediate variable  $\mu = \varepsilon^{1/2} y = Y/\varepsilon^{1/2}$ , and considering  $\mu = \mathcal{O}(1)$  whilst  $\varepsilon \rightarrow 0$ . Then our leading-order outer solution gives

$$G = A_{\pm} \left( 1 \mp \varepsilon^{1/2} \alpha_{\pm} \mu + \dots \right) + \mathcal{O}(\varepsilon) \text{ as } \varepsilon \rightarrow 0. \quad (4.12)$$

The inner solution is constructed directly from (4.9). Writing  $G = G_0 + \varepsilon G_1 + \dots$ , at leading order we find

$$\frac{d}{dy} \left( S^2 \frac{dG_0}{dy} \right) = 0 \implies \frac{dG_0}{dy} = \frac{\phi_0}{S^2} \implies G_0 = 1 + \phi_0 I(y), \text{ where } I(y) = \int_0^y \frac{d\nu}{S^2(\nu)}, \quad (4.13)$$

for some constant  $\phi_0$ , and normalised so that  $G(0) = 1$ . But  $I(y) \sim y/S_{\pm}^2$  as  $y \rightarrow \pm\infty$ . So our leading-order inner solution becomes large as  $y \rightarrow \pm\infty$ , and it cannot match to (4.12). So  $\phi_0 = 0$ , and  $G_0(y) = 1$ . The  $\mathcal{O}(\varepsilon)$  terms give  $G_1(y) = \phi_1 I(y)$  (since  $G_1(0) = 0$  by our normalisation condition), so the two-term inner solution is

$$G(y) = 1 + \varepsilon \phi_1 I(y) + \mathcal{O}(\varepsilon^2), \text{ as } \varepsilon \rightarrow 0. \quad (4.14)$$

Since  $I(y) \sim y/S_{\pm}^2$  as  $y \rightarrow \infty$ , in terms of the matching variable  $\mu$  (and again with  $\mu = \mathcal{O}(1)$  as  $\varepsilon \rightarrow 0$ ) the inner becomes

$$G = 1 + \varepsilon^{1/2} \frac{\phi_1 \mu}{S_{\pm}^2} + \dots \quad (4.15)$$

To match to (4.11), we thus need  $A_{\pm} = 1$ , and then

$$-\alpha_+ = \frac{\phi_1}{S_+^2} \text{ and } +\alpha_- = \frac{\phi_1}{S_-^2} \implies S_+^2 \alpha_+ + S_-^2 \alpha_- = 0. \quad (4.16)$$

Given the definition of  $\alpha_{\pm}$  in (4.10), this becomes

$$R_+ S_+ + R_- S_- = 0. \quad (4.17)$$

This is the dispersion relation for  $c$ , given the definition of  $S(y)$  and  $R(y)$  in (4.9).

When  $\tilde{\beta} = 1/\tilde{B} = 0$ ,  $R_{\pm} = \tilde{k}S_{\pm}$  and (4.17) gives  $S_+^2 + S_-^2 = 0$  so that

$$(1 - c)^2 - M^2 + (-1 - c)^2 - M^2 = 0 \implies c = \pm i\sqrt{1 - M^2}. \quad (4.18)$$

So, the entire analysis (which assumed  $c_i \neq 0$ ) is self-consistent provided

$$M < 1. \quad (4.19)$$

From the outset here we have assumed a normalised shear flow ( $U(y) \rightarrow \pm 1$ , as  $y \rightarrow \pm\infty$ ) and hence the real part of  $c$  is zero. Had we left this arbitrary, we would have found that  $c_r = (U_+ + U_-)/2$  (and a scaled  $c_i$ ), however, we would have also had to consider the case  $U_- = U_+$ , the jet.

When  $M < 1$  the leading order dispersion relation (4.17) is sufficient since it always possesses a complex root, showing that instability is guaranteed for sufficiently small  $k$ . When  $\beta > 0$  and  $M, F^2 = 0$ , Howard and Drazin (1964) (following their  $\beta = 0$  case (Drazin and Howard, 1962)) included an additional term in their expansion and showed that a second mode can exist which may also be unstable for small  $k$ , but  $\beta$  not necessarily asymptotically small. This relates to the two modes discussed in §5. A similar expansion may be possible here, but we have not attempted it.

### 4.3 Spuriousity

The dispersion relations, (4.6) and (4.17),

$$\left((c - 1)^2 - M^2\right) \alpha_+ + \left((c + 1)^2 - M^2\right) \alpha_- = 0, \quad (4.20)$$

where  $\alpha_{\pm}$  is defined in (4.5), is combined with the boundary conditions,

$$\Re(\alpha_{\pm}) > 0, \quad (4.21)$$

which specifies that the eigenfunction decays in the limit  $|y| \rightarrow \infty$ . Equation (4.20) can be squared and written as a cubic for  $c$ ,

$$(4k^2 + 3F^2) c^3 + 3\beta c^2 + (4k^2 + F^2) (1 - M^2) c + \beta (1 - M^2) = 0. \quad (4.22)$$

This has three solutions which are either a real root and complex conjugate pair or three real roots. These roots do not necessarily give  $\alpha_{\pm}$  values such that (4.21) can be satisfied. We use the term *spurious*, to denote roots which are solutions of (4.22) but not eigenvalues. Spurious roots can also arise from squaring (4.20) to (4.22).<sup>2</sup>

The boundary conditions, (4.21), can always be satisfied when  $\alpha_{\pm}^2$  are complex. The only case where it cannot be is when  $\alpha_{\pm}^2$  is real and negative. In this case  $\alpha_{\pm}$  will be purely imaginary, corresponding to an oscillating, rather than a decaying eigenfunction as  $y \rightarrow \pm\infty$ .

---

<sup>2</sup>Consider, e.g.,  $x - 1 = 0$  which has one solution but may arise from  $x^{1/2} + 1 = 0$ , which has no solutions, or  $x^{1/2} - 1 = 0$ , which has one.

The imaginary part of  $\alpha_{\pm}^2$  is,

$$\Im(\alpha_{\pm}^2) = c_i \left[ -\beta \left( |c \mp 1|^2 + M^2 \right) + F^2 \left( \mp |c \mp 1|^2 - M^2 (2c_r \mp 1) \right) \right]. \quad (4.23)$$

If  $c$  is real ( $c_i = 0$ ), it may not satisfy the boundary conditions and be spurious. Sporadic solutions where  $\Im(\alpha_{\pm}^2) = 0$  and  $c_i \neq 0$  may also exist.

The main source of spurious solutions comes during the squaring of (4.20) and it is difficult to be sure, for any given solution of (4.22), that (4.20) is also satisfied without simply substituting in and calculating. We can make some headway by considering when a root becomes spurious in this way. This occurs when the signs of the left and right sides of (4.20) change, i.e. when both sides of (4.20) are equal to zero.

Setting both sides of equation (4.20) to zero gives us four cases:

- i  $\alpha_+ = \alpha_- = 0$ . This may also correspond to breaking the boundary conditions (4.21).
- ii The case  $(c+1)^2 - M^2 = (c-1)^2 - M^2 = 0$ , which has only the solution  $M = 1, c = 0$ .
- iii And finally, either  $\pm: \alpha_{\pm} = (c \pm 1)^2 - M^2 = 0$ .

We will see in §4.5.1 that  $k = 0$  gives rise to simple analytic solutions. The first of these,  $c = -\beta/F^2$  has  $\alpha_{\pm} = 0$  and corresponds to case (i) of the above and shall be discussed later. Let us continue investigating the case (i) with  $k > 0$  and define some temporary variables,  $\phi = F^2/k^2$  and  $\psi = \beta/k^2$ . This reduces the order of the system by one. Taking  $\alpha_{\pm} = 0$  gives us

$$(c \pm 1)^2 - M^2 + (c \pm 1)(\psi + c\phi) = 0, \quad (4.24)$$

which are a pair of equations that must be solved simultaneously in both the positive and negative cases. Hence, considering (4.24) as a quadratic equation for  $(c \pm 1)$ , clearly  $(c+1)$  and  $(c-1)$  must take different roots. This allows us to skip past a bit of algebra and write down two simpler equations for  $c$  that must be satisfied:

$$(c+1)(c-1) = -M^2 \implies c^2 = 1 - M^2, \quad (4.25)$$

$$(c+1) + (c-1) = -\psi - c\phi \implies c = -\frac{\psi}{2 + \phi}. \quad (4.26)$$

Cancelling for  $c$  between (4.25) and (4.26) gives the relation

$$1 - M^2 = \frac{\psi^2}{(2 + \phi)^2} \implies 1 - M^2 = \frac{\beta^2}{(2k^2 + F^2)^2}. \quad (4.27)$$

Turning to case (iii), we have the equation  $(c \pm 1)^2 - M^2 = 0$  giving rise to four real solutions for  $c$  for any given  $M$ . We'll distinguish these using  $\delta, \varepsilon = \pm 1$  (with  $\varepsilon$  corresponding to the subscript of  $\alpha$ ) i.e.  $c = \delta M - \varepsilon$ . Substituting this into  $\alpha_{\varepsilon} := \alpha_{\pm} = 0$ , and assuming  $M^2 \neq 1$ , we obtain

$$4k^2(1 - \delta\varepsilon M) + (\delta M - 2\varepsilon)(\beta + F^2(\delta M - \varepsilon)) = 0. \quad (4.28)$$

The important result here is that the spuriousity of the real root changes at several points defined by equations (4.27), (4.28), and possibly also at  $M = 1$ , the case (ii). Meanwhile,

the complex conjugate roots of equation (4.22) never change spuriousity and therefore always represent true roots of the dispersion relation (4.20) since they are contiguous with well-known theoretical unstable modes. The physical meaning of the real roots, spurious or not, is unclear. We will use the results of this section to mark changes in the spuriousity of this root when discussing particular solutions of the dispersion relation in §4.5.

## 4.4 Stability Criteria

The cubic equation, (4.22), has three roots which, since its coefficients are real, are either all real or a complex conjugate pair of roots and a single real root. Denoting these as  $c_1, c_2, c_3$  we can write down a discriminant,

$$\Delta_3 = (c_1 - c_2)^2 (c_2 - c_3)^2 (c_3 - c_1)^2, \quad (4.29)$$

which is independent of the ordering of the roots. If all three roots are real,  $\Delta$  is positive. Conversely,  $\Delta$  is negative if (and only if) a pair of these roots are complex conjugates. By expanding

$$(c - c_1)(c - c_2)(c - c_3) = c^3 + ac^2 + bc + d, \quad (4.30)$$

we can also write  $\Delta_3$  in terms of its polynomial coefficients, as

$$\Delta_3 = 18abd - 4a^3d + a^2b^2 - 4b^3 - 27d^2 \quad (4.31)$$

and hence we can determine the nature of the roots of cubic equation, (4.22), without directly solving it.

Comparing with (4.22),

$$a = \frac{3\beta}{4k^2 + 3F^2}, \quad b = \frac{(4k^2 + F^2)(1 - M^2)}{4k^2 + 3F^2}, \quad d = \frac{\beta(1 - M^2)}{4k^2 + 3F^2}. \quad (4.32)$$

And hence,

$$\Delta_3 = \mu \frac{4\beta^6 (3\phi^4 + 40\phi^3 + 192\phi^2 + 384\phi + 256) \mu^2 + (-18\phi^2 + 72\phi + 144) \mu + 27}{k^{12} (4 + 3\phi)^4} \quad (4.33)$$

where

$$\mu = \frac{k^4 (M^2 - 1)}{\beta^2}, \quad \text{and} \quad \phi = \frac{F^2}{k^2} \geq 0. \quad (4.34)$$

The numerator of (4.33) is a quadratic in  $\mu$  with discriminant

$$\Delta_2 = -6912(\phi + 1)^3 \quad (4.35)$$

and hence is strictly negative for  $\phi > -1$ . Since  $\phi$  is positive, this means that the sign of  $\Delta_3$  is entirely determined by the sign of  $\mu$ , i.e., (4.22) has a pair of complex conjugate solutions if and only if

$$M^2 < 1. \quad (4.36)$$

Perhaps this is a surprising result since the semicircle bound (3.62) suggests that instability

could be possible when  $M^2 > 1$  and  $\beta \neq 0$ . However, it is consistent with the 2DMHD case of Michael (1953) and previous understanding of the effect of  $\beta$  on shear instability, which suggests that it is generally a stabilising influence. Since the vorticity at the interface is unbounded, increasing  $\beta$  cannot lead to stability, unlike in smooth profiles, where the inflexion point criterion can mean that shear flows stabilise at sufficiently large  $\beta$ .

## 4.5 Parameter Asymptotics

Recall the dispersion relation is:

$$(4k^2 + 3F^2) c^3 + 3\beta c^2 - (4k^2 + F^2) \mu c - \beta \mu = 0. \quad (4.37)$$

Although it is possible to write down the full cubic solution to the dispersion relation above it is rarely enlightening to do so. Instead, in this section, we will discuss (linear) asymptotic approximations of  $c$  in terms of the four parameters,  $k^2$ ,  $\mu = M^2 - 1$ ,  $\beta$ , and  $F^2$ . Calculating these is simpler and can provide some insight into the variation of  $c$ .

### 4.5.1 Variation of $k$

Let us start with the important limit  $k \rightarrow 0$ . In the absolute limit, (4.37) reduces to

$$3F^2 c^3 + 3\beta c^2 - F^2 \mu c - \beta \mu = 0 \quad (4.38)$$

which can be factorised as

$$(F^2 c + \beta) (3c^2 - \mu) = (F^2 c + \beta) (3c^2 + 1 - M^2) = 0. \quad (4.39)$$

This gives us the real solution  $c = -\beta/F^2$  (corresponding to  $\alpha_{\pm} = 0$ , cf. §4.3) and the pair of solutions  $c = \pm \sqrt{(M^2 - 1)/3}$  which are complex when  $M^2 < 1$  and real otherwise.

Consider now a formal expansion of  $c$ ,

$$c = \sum_i c_i k^{2i+\lambda}. \quad (4.40)$$

The dominant balance in equation (4.37) depends on the available terms, which are proportional to

$$k^{3\lambda+2}, \quad F^2 k^{3\lambda}, \quad \beta k^{2\lambda}, \quad \mu k^{\lambda+2}, \quad F^2 \mu k^{\lambda}, \quad \beta \mu k^0 \quad (4.41)$$

this leads to a total of eight different possible balances (depending on whether each of the three remaining parameters vanishes). These are summarised in the table below, with roots provided where it is trivial to do so. The first column states which parameters are zero and the second, the possible values of  $\lambda$  (and the order).

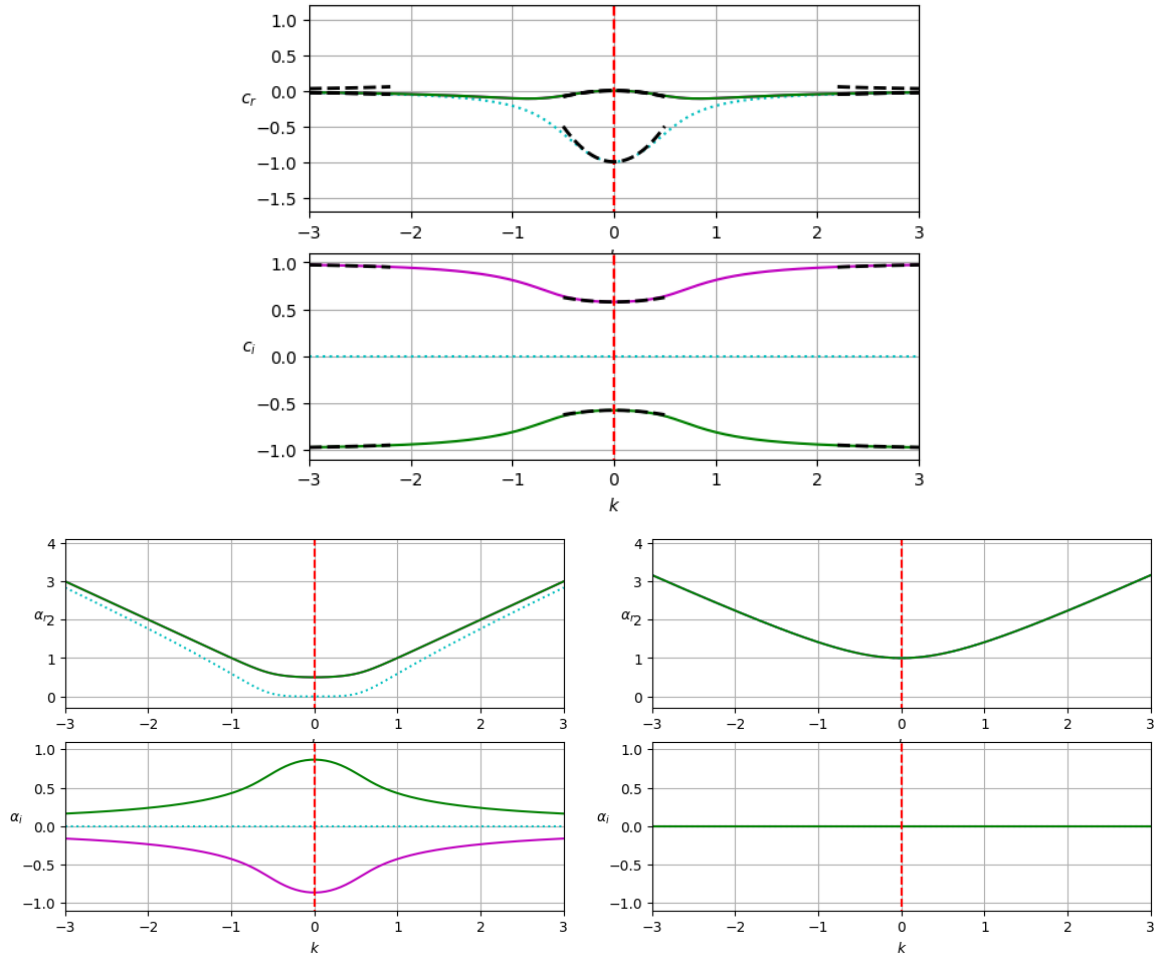


Figure 4.2: The three solutions of the cubic equation (4.22) are plotted above (green, pink, cyan) for varied  $k$ ,  $M^2 = 0.0$ ,  $\beta = 1.0$ ,  $F^2 = 1.0$ . Those roots which solve the dispersion relation (4.6) and satisfy the boundary conditions plotted with a filled line. The asymptotic approximations derived in section §4.5.1 are plotted in black and the spuriosity asymptotes derived in §4.3 are plotted as vertical red lines. The lower two plots show the real and imaginary parts of  $\alpha_+$ , left, and  $\alpha_-$ , right, showing the origin of spuriosity.

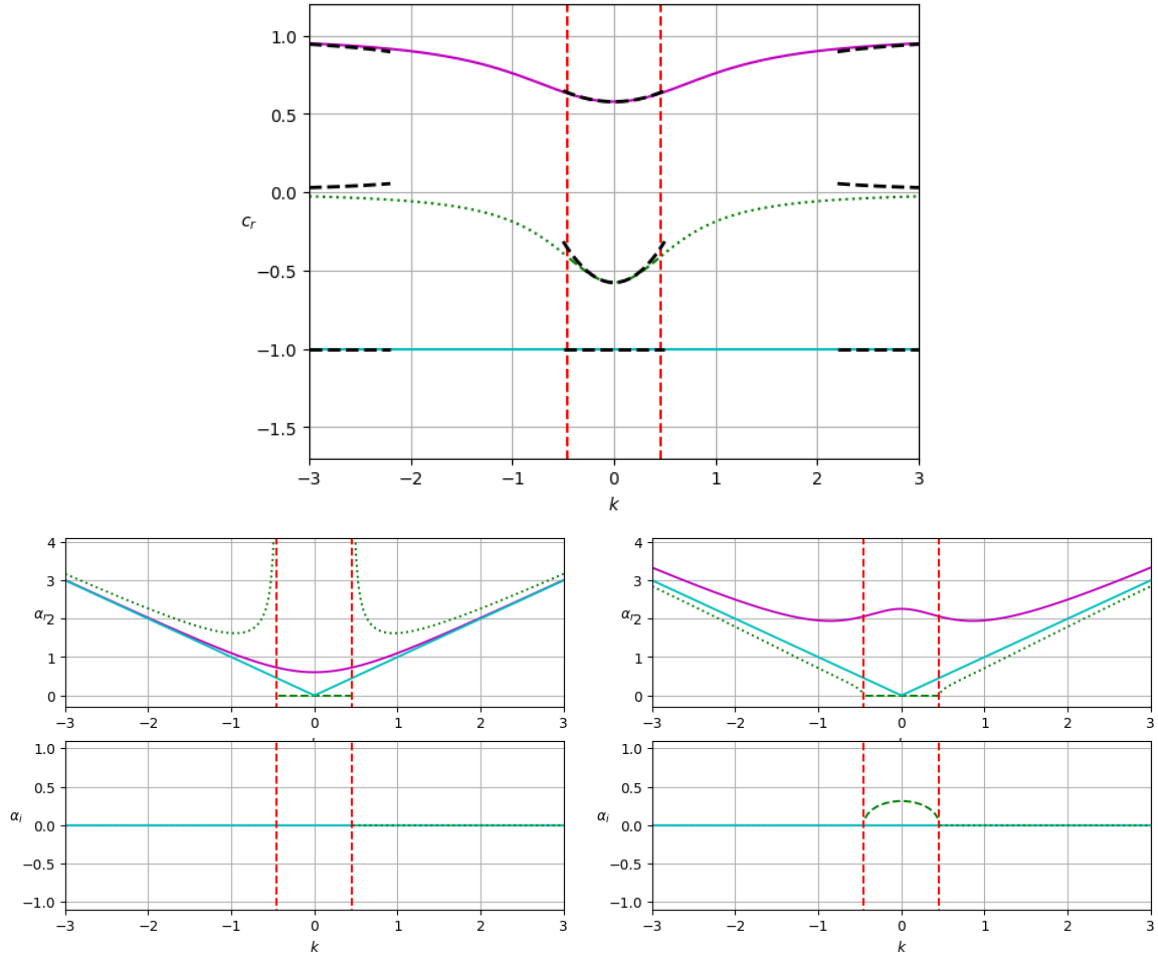


Figure 4.3: Plot of the three solutions of the cubic equation (4.22) for varied  $k$ ,  $M^2 = 2.0$ ,  $\beta = 1.0$ ,  $F^2 = 1.0$ . Colours as in Figure 4.2.

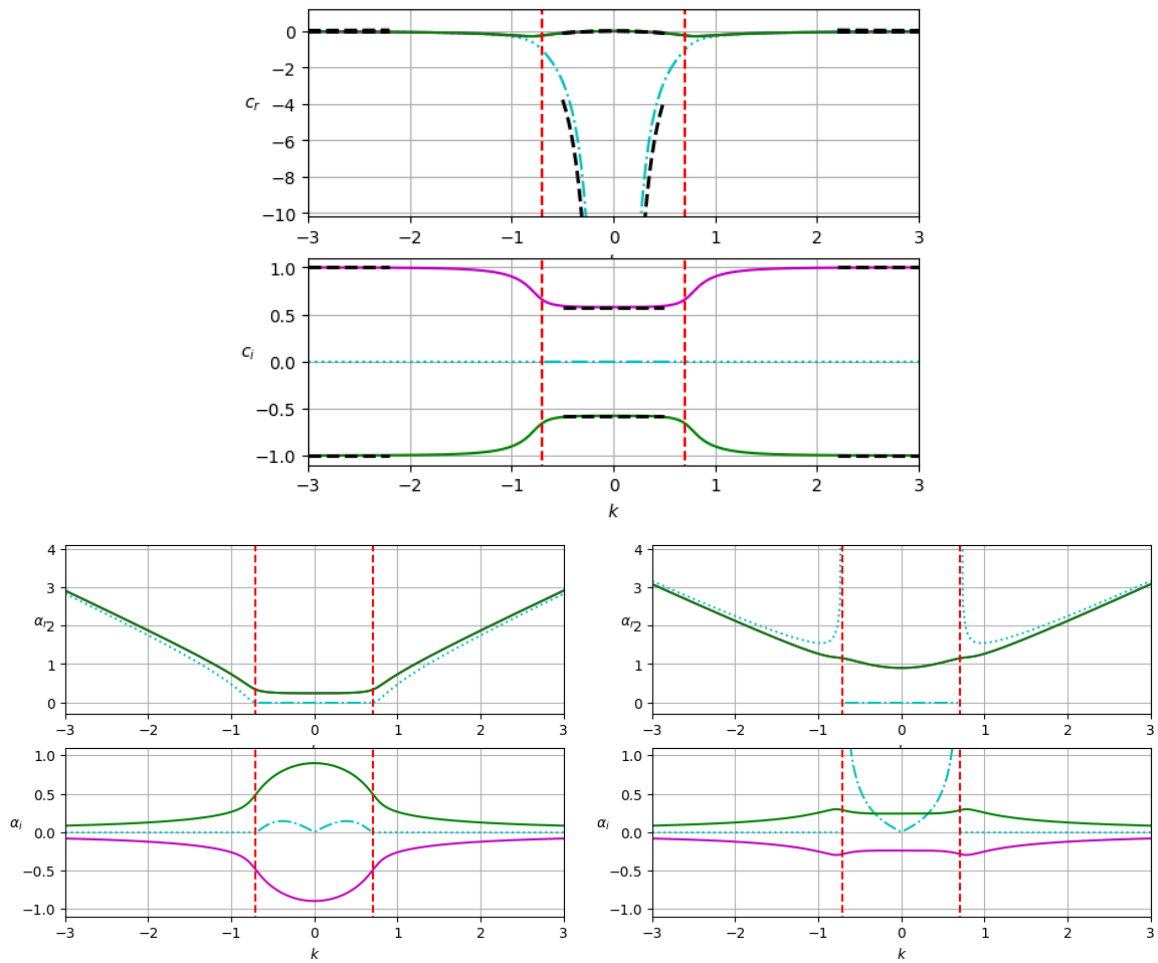


Figure 4.4: Plot of the three solutions of the cubic equation (4.22) for varied  $k$ ,  $M^2 = 0.0$ ,  $\beta = 1.0$ ,  $F^2 = 0.0$ . Colours as in Figure 4.2.

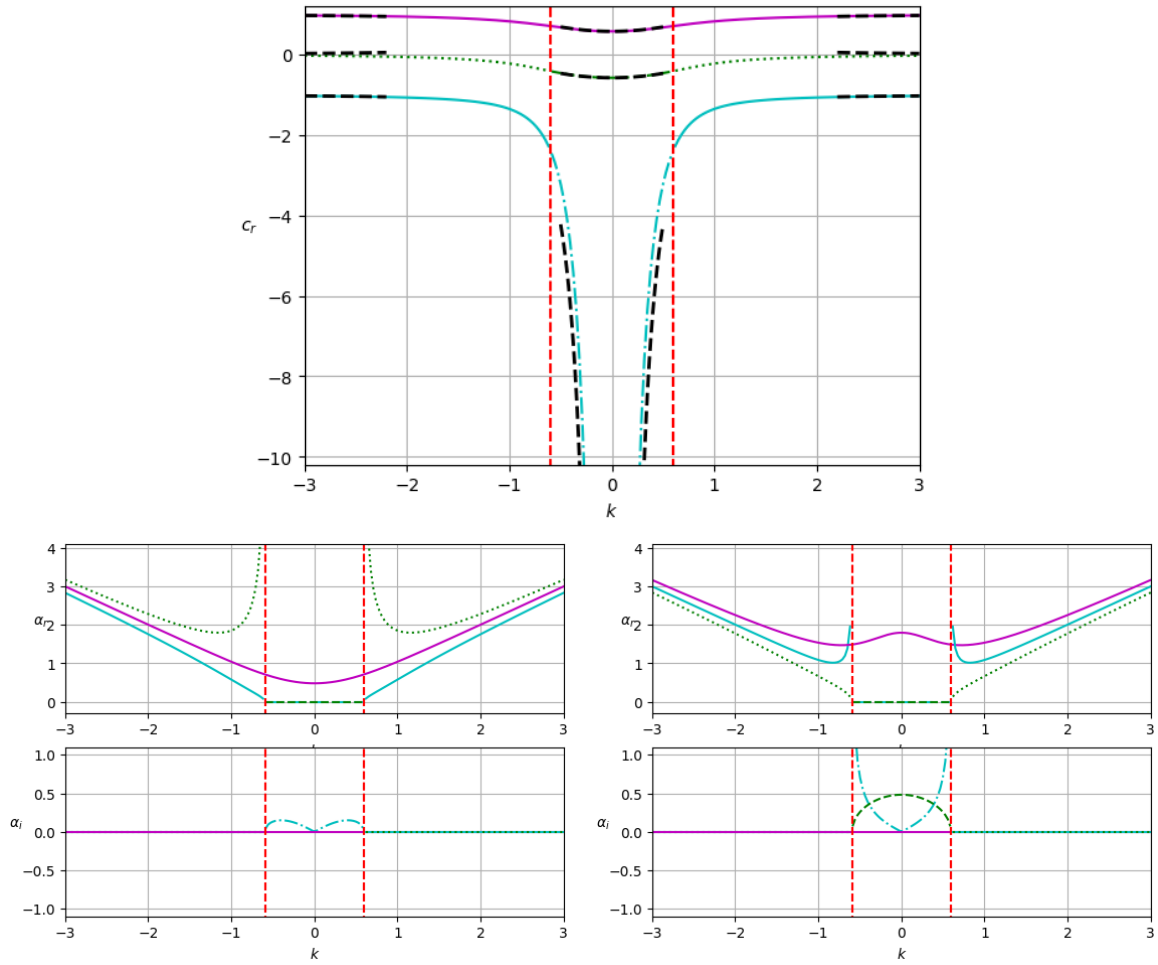


Figure 4.5: Plot of the three solutions of the cubic equation (4.22) for varied  $k$ ,  $M^2 = 2.0$ ,  $\beta = 1.0$ ,  $F^2 = 0.0$ . Colours as in Figure 4.2.

i)	$F^2 = \beta = \mu = 0$	-	$c = 0$ (3)
ii)	$F^2 = \mu = 0$	$\lambda = -2$ (1)	$c = 0$ (2), $c = -3\beta/4k^2$
iii)	$F^2 = \beta = 0$	$\lambda = 0$ (2)	$c = 0$ (1), $c = \pm\sqrt{\mu}$
iv)	$\mu = \beta = 0$	-	$c = 0$ (3)
v)	$\beta = 0$	$\lambda = 0$ (2)	$c = 0$ (1), $c = \pm\sqrt{\frac{4k^2+F^2}{4k^2+3F^2}\mu}$
vi)	$\mu = 0$	$\lambda = 0$ (1)	$c = 0$ (2), $c = \frac{-3\beta}{4k^2+3F^2}$
vii)	$F^2 = 0$	$\lambda = -2$ (1), $\lambda = 0$ (2)	See asymptotics
viii)	All non-zero	$\lambda = 0$ (3)	See asymptotics

First, we will consider (viii), with  $\lambda = 0$ . Then, the relevant powers of  $c$  are

$$c^2 = c_0^2 + 2c_0c_1k^2 + (c_1^2 + 2c_0c_2)k^4 + \dots, \quad (4.42a)$$

$$c^3 = c_0^3 + 3c_0^2c_1k^2 + (3c_0^2c_2 + 3c_0c_1^2)k^4 + \dots, \quad (4.42b)$$

from which we can write down the dispersion relation at the lowest two orders of  $k^2$ :

$$\mathcal{O}(k^0): \quad 3F^2c_0^3 + 3\beta c_0^2 - F^2\mu c_0 - \beta\mu = 0, \quad (4.43a)$$

$$\mathcal{O}(k^2): \quad 4c_0^3 + 9F^2c_0^2c_1 + 6\beta c_0c_1 - 4\mu c_0 - F^2\mu c_1 = 0, \quad (4.43b)$$

$$\mathcal{O}(k^4): \quad 12c_0^2c_1 + 9F^2c_0(c_0c_2 + c_1^2) + 3\beta(c_1^2 + 2c_0c_2) - 4\mu c_1 - F^2\mu c_2 = 0. \quad (4.43c)$$

Higher orders for  $c_i$  are easily obtained by a similar process, although the algebra increases at each step. We have solved for  $c_0$  above and the next two orders of  $c_i$  are

$$c_1 = -\frac{4c_0(c_0^2 - \mu)}{9F^2c_0^2 + 6\beta c_0 - F^2\mu}, \quad (4.44a)$$

$$c_2 = -\frac{c_1(12c_0^2 + 9F^2c_0c_1 + 3\beta c_1 - 4\mu)}{9F^2c_0^2 + 6\beta c_0 - F^2\mu}. \quad (4.44b)$$

The first two terms of the asymptotic expansions are easy to write down. These are

$$c = -\frac{\beta}{F^2} + \frac{4\beta}{F^4} \frac{\beta^2 - F^4\mu}{3\beta^2 - F^4\mu} k^2 + \mathcal{O}(k^4), \quad (4.45a)$$

$$c = \pm\sqrt{\frac{\mu}{3}} + \frac{4\mu}{3(3\beta \pm F^2\sqrt{3\mu})} k^2 + \mathcal{O}(k^4). \quad (4.45b)$$

We will leave it to the reader to carry out the simple process of iterating to higher orders should it be necessary. These asymptotes are plotted for

Let us now consider the case where  $F^2 = 0$ . The three possible values for  $c_0$  are then

$$c_0 = \pm\sqrt{\frac{\mu}{3}}, \quad \lambda = 0, \quad (4.46)$$

and

$$c_0 = -\frac{3\beta}{4}, \quad \lambda = -2. \quad (4.47)$$

The first two roots have essentially the same asymptotics as before, leading to a version of

(4.45b) with  $F^2 = 0$ . The remaining root has  $\lambda = -2$ , with the next terms appearing at  $\mathcal{O}(k^0)$ :

$$\mathcal{O}(k^{-4}) : \quad 4c_0^3 + 3\beta c_0^2 = 0, \quad (4.48a)$$

$$\mathcal{O}(k^0) : \quad 12c_0^2 c_1 + 6\beta c_0 c_1 - 4\mu c_0 - \beta\mu = 0. \quad (4.48b)$$

From these, we can write down the first two terms of the asymptotic expansion of this root, which are

$$c = -\frac{3\beta}{4}k^{-2} - \frac{8\mu}{9\beta}k^2 + \mathcal{O}(k^6). \quad (4.49)$$

This is an approximation of a spurious root, as can be seen in Figures 4.4 and 4.5.

We can now consider a similar analysis at large  $k$ . Defining  $\varepsilon = k^{-2}$  and leading order  $c \sim \varepsilon^\lambda$  each term is proportional to

$$\varepsilon^{3\lambda}, \quad F^2\varepsilon^{3\lambda+1}, \quad \beta\varepsilon^{2\lambda+1}, \quad \mu\varepsilon^\lambda, \quad F^2\mu\varepsilon^{\lambda+1}, \quad \beta\mu\varepsilon^1 \quad (4.50)$$

and so the possible dominant balances are

i)	$F^2 = \beta = \mu = 0$	-	$c = 0$ (3)
ii)	$F^2 = \mu = 0$	$\lambda = 1$ (1)	$c = 0$ (2), $c = -3\beta/4k^2$
iii)	$F^2 = \beta = 0$	$\lambda = 0$ (2)	$c = 0$ (1), $c = \pm\sqrt{\mu}$
iv)	$\mu = \beta = 0$	-	$c = 0$ (3)
v)	$\beta = 0$	$\lambda = 0$ (2)	$c = 0$ (1), $c = \pm\sqrt{\frac{4k^2+F^2}{4k^2+3F^2}\mu}$
vi)	$\mu = 0$	$\lambda = 1$ (1)	$c = 0$ (2), $c = \frac{-3\beta}{4k^2+3F^2}$
vii)	$F^2 = 0$	$\lambda = 1$ (1), $\lambda = 0$ (2)	See asymptotics
viii)	All non-zero	$\lambda = 1$ (1), $\lambda = 0$ (2)	See asymptotics

Note that these are mostly equivalent to the same roots as the small  $k$  case. The exceptions are the cases (vii) and (viii) which are now the same. We no longer need two separate analyses for these cases. First, taking  $\lambda = 0$ , we have

$$\mathcal{O}(\varepsilon^0) : \quad 4c_0^3 - 4\mu c_0 = 0, \quad (4.51a)$$

$$\mathcal{O}(\varepsilon^1) : \quad 12c_0^2 c_1 + 3F^2 c_0^3 + 3\beta c_0^2 - 4\mu c_1 - F^2 \mu c_0 - \beta\mu = 0. \quad (4.51b)$$

The lowest order gives  $c_0 = \pm\sqrt{\mu}$ , and the next gives  $c_1 = -(\beta + F^2 c_0)/4$ . With now  $\lambda = 1$ ,

$$\mathcal{O}(\varepsilon^1) : \quad -4\mu c_0 - \beta\mu = 0, \quad (4.52a)$$

$$\mathcal{O}(\varepsilon^2) : \quad -4\mu c_1 - F^2 \mu c_0 = 0, \quad (4.52b)$$

and hence the large  $k$  asymptotics of the three roots are

$$c = \pm\sqrt{\mu} - \frac{\beta \pm F^2 \sqrt{\mu}}{4}k^{-2} + \mathcal{O}(k^{-4}), \quad (4.53a)$$

$$c = -\frac{\beta}{4}k^{-2} + \frac{F^2 \beta}{16}k^{-4} + \mathcal{O}(k^{-6}). \quad (4.53b)$$

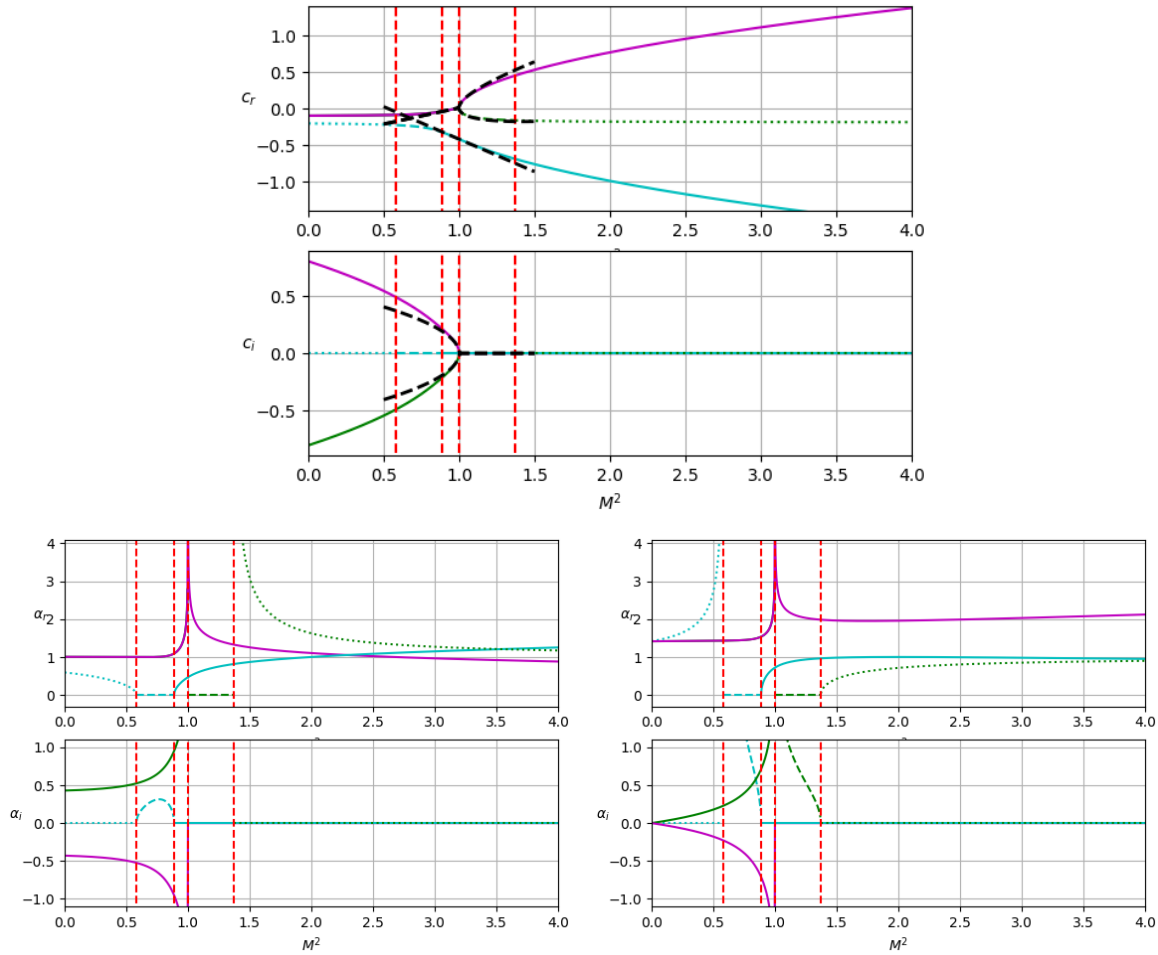


Figure 4.6: Plot of the three solutions of the cubic equation (4.22) for varied  $M$ ,  $k = 1.0$ ,  $\beta = 1.0$ ,  $F^2 = 1.0$ . Colours as in Figure 4.2.

These approximations are plotted in black in Figures 4.2, 4.3, 4.4, and 4.5.

#### 4.5.2 Variation of $\mu$

We now examine the effect of varying  $\mu = M^2 - 1$ . Firstly, we have seen (§4.4) that the parameter domain is divided into two distinct regions,  $\mu < 0$ , and  $\mu > 0$  with the former corresponding to the regime of complex conjugate eigenvalues, and the latter corresponding to (4.37) having three real roots.

Assuming  $c \sim \mu^\lambda$ , and provided that the solutions of (4.37) are nontrivial, we are left with only one regime of interest and can balance terms at least order with either  $\lambda = 0$  or  $\lambda = \frac{1}{2}$ . The former gives rise to one root, and the latter two. Taking first  $\lambda = 0$ , and substituting

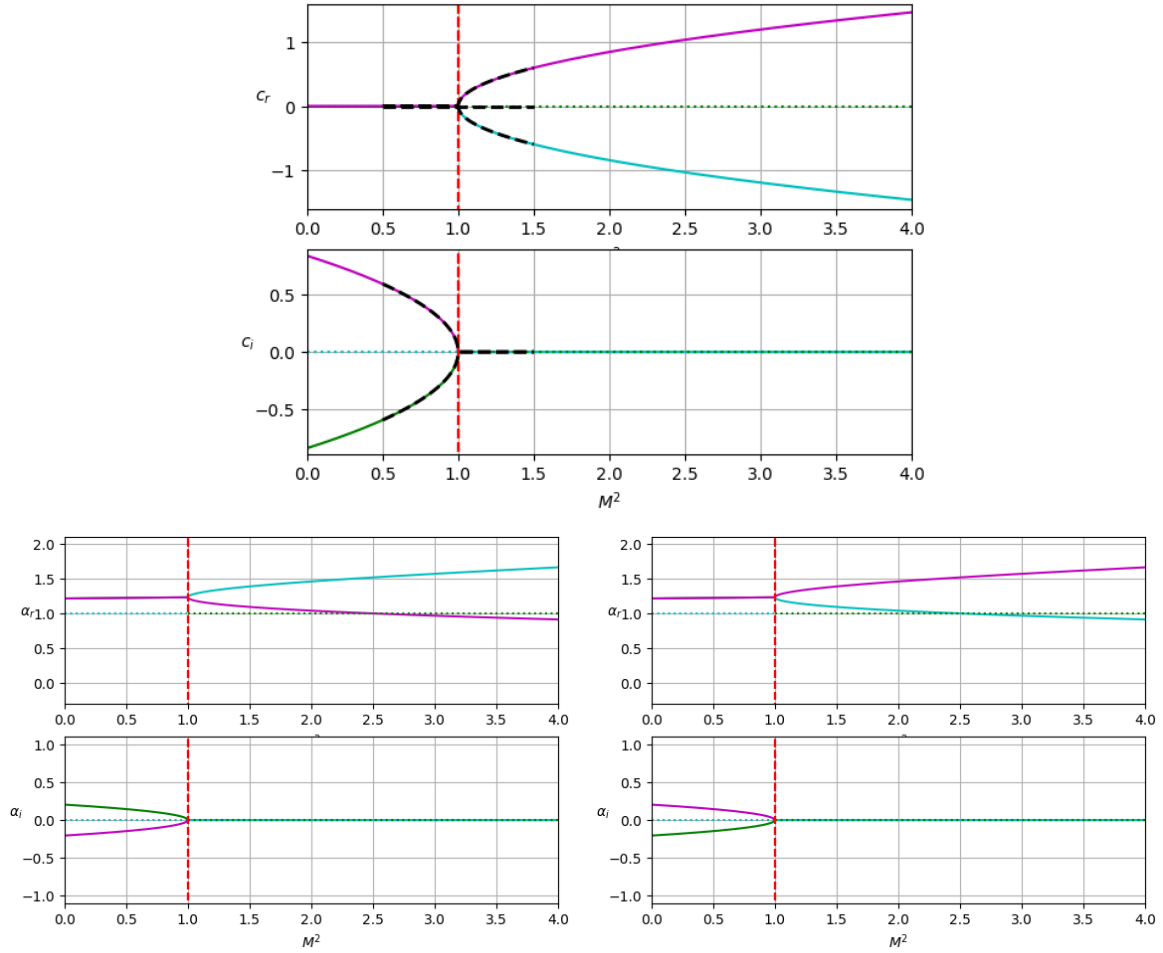


Figure 4.7: Plot of the three solutions of the cubic equation (4.22) for varied  $M$ ,  $k = 1.0$ ,  $\beta = 0.0$ ,  $F^2 = 1.0$ . Colours as in Figure 4.2.

into (4.37), we get that,

$$\mathcal{O}(\mu^0) : \quad -(4k^2 + F^2) c_0 - \beta = 0 \quad (4.54a)$$

$$\mathcal{O}(\mu^1) : \quad (4k^2 + 3F^2) 3c_0^2 c_1 + 6\beta c_0 c_1 - (4k^2 + F^2) c_0 - \beta = 0 \quad (4.54b)$$

This leads to the series

$$c = -\frac{3\beta}{4k^2 + 3F^2} - \frac{8k^2}{9\beta}\mu + \mathcal{O}(\mu^2). \quad (4.55)$$

In the second case,  $\lambda = 1/2$ , we have

$$\mathcal{O}(\mu^1) : \quad 3\beta c_0^2 - \beta = 0, \quad (4.56a)$$

$$\mathcal{O}(\mu^{\frac{3}{2}}) : \quad (4k^2 + 3F^2) c_0^3 + 6\beta c_0 c_1 - (4k^2 + F^2) c_0 = 0. \quad (4.56b)$$

From this, we can write down the approximation

$$c = \pm \sqrt{\frac{\mu}{3}} + \frac{4k^2}{9\beta}\mu + \mathcal{O}(\mu^{\frac{3}{2}}), \quad (4.57)$$

which verifies that  $\mu < 0$  leads to instability. We plot these approximations as black lines over the roots of the cubic in Figure 4.6.

Since  $\beta$  appears as a denominator in the two approximations above, (4.55), (4.57), its worth writing down the explicit solutions that can be derived when  $\beta = 0$ . In this case we find one zero root ( $c = 0$ ), and two roots of opposite signs,

$$c = \pm \sqrt{\frac{4k^2 + F^2}{4k^2 + 3F^2}\mu}. \quad (4.58)$$

We can see these in Figure 4.7.

We can also see though, from Figures 4.6 and 4.7 that the admissibility of our roots can change at  $\mu = 0$ . We can check that this is reflected in our approximations by calculating  $\alpha_{\pm}$  and substituting it into (4.6). Using first  $c \approx \pm \sqrt{\frac{\mu}{3}}$  we can write  $\alpha_{\pm}$  as

$$\begin{aligned} \alpha_{\pm}^2 &= k^2 + \frac{(c - \varepsilon)(\beta + cF^2)}{c^2 - 2\varepsilon c - \mu} \\ &= k^2 + \frac{\frac{\mu}{3} \pm (\beta - \varepsilon F^2) \sqrt{\frac{\mu}{3}} - \varepsilon\beta}{\mp \sqrt{\frac{\mu}{3}} \left( \varepsilon \pm \sqrt{\frac{\mu}{3}} \right)} \\ &\approx k^2 + \frac{\pm \beta \sqrt{\frac{3}{\mu}} \left( \varepsilon \pm \sqrt{\frac{\mu}{3}} \right) - 2\beta + \varepsilon}{\varepsilon \pm \sqrt{\frac{\mu}{3}}} \\ &\approx k^2 \pm \beta \sqrt{\frac{3}{\mu}} \end{aligned} \quad (4.59)$$

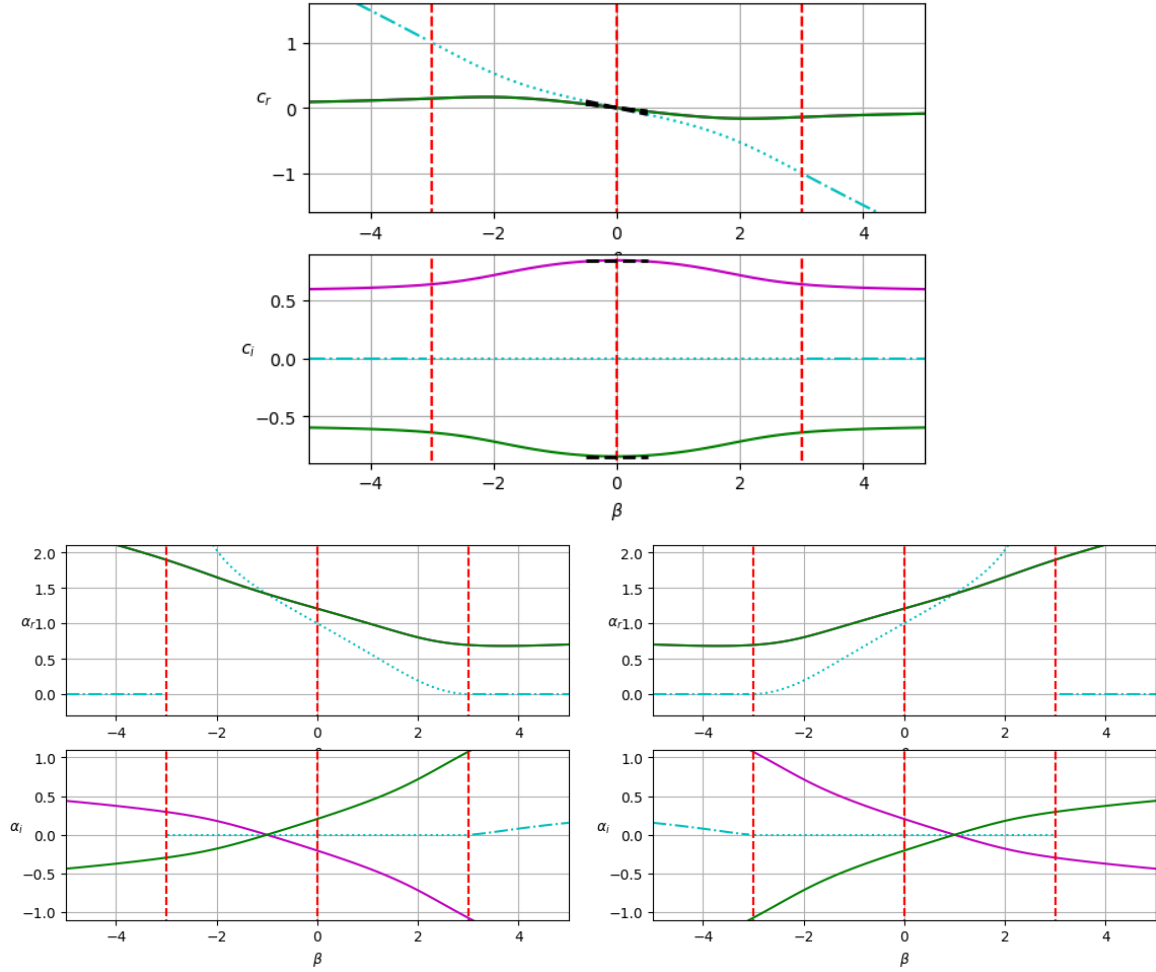


Figure 4.8: Plot of the three solutions of the cubic equation (4.22) for varied  $\beta$ ,  $k = 1.0$ ,  $M^2 = 0.0$ ,  $F^2 = 1.0$ . Colours as in Figure 4.2.

and hence the negative root is inadmissible for sufficiently small  $\mu > 0$  when  $\hat{\beta} > 0$ . We should also examine the case  $\beta = 0$ , which leads to,

$$\alpha_{\pm}^2 = k^2 + F^2 \frac{\varepsilon \mp \sqrt{\frac{\mu}{3}}}{\varepsilon \pm \sqrt{\frac{\mu}{3}}} \approx k^2 + F^2 \quad (4.60)$$

and in this case, we find both roots to be admissible.

### 4.5.3 Variation of $\beta$

The limit  $\beta \rightarrow 0$  is interesting since, provided  $\mu < 0$  ( $M^2 < 1$ ), all roots are stationary. Considering the asymptotics about this limit, we find two “magnetic” roots, with lowest

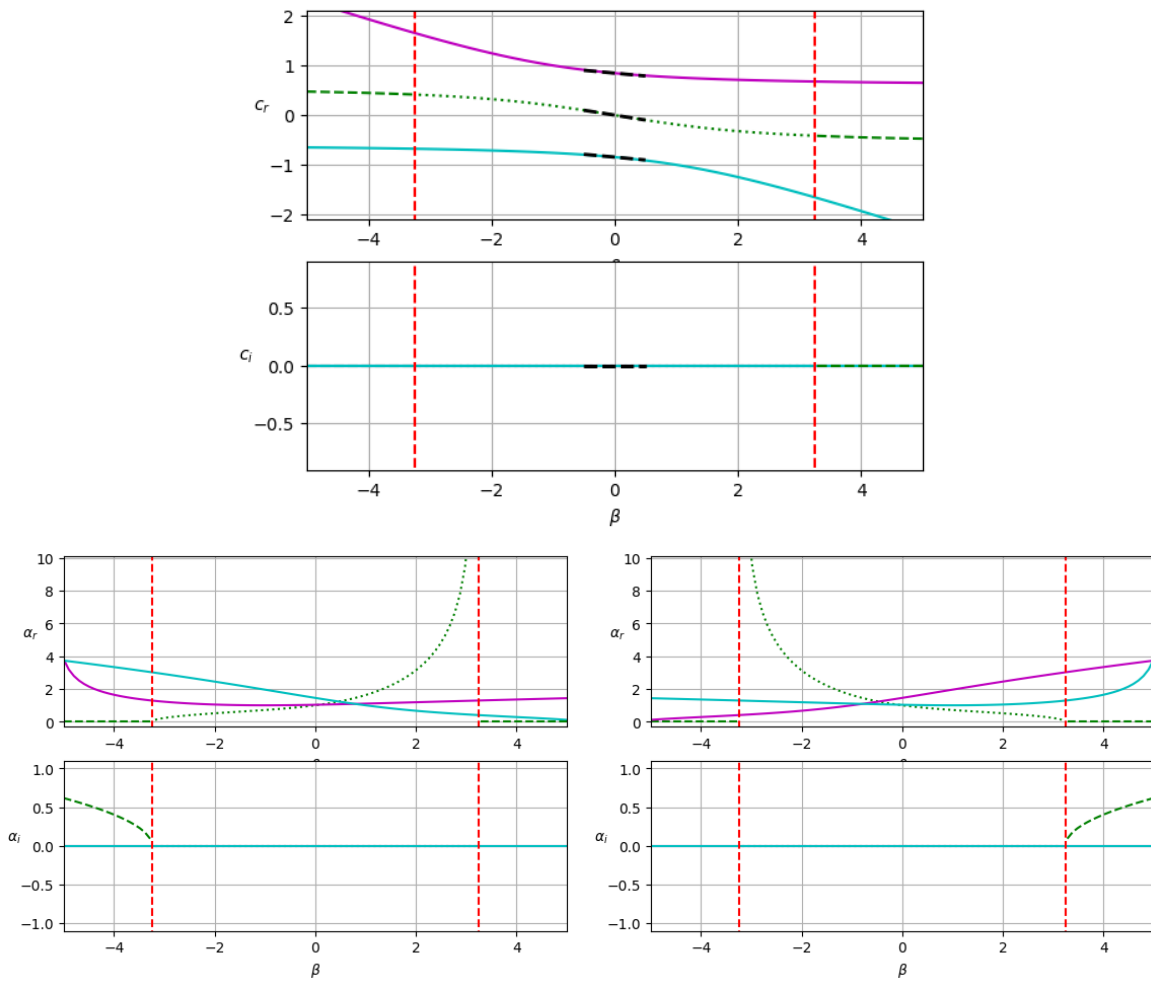


Figure 4.9: Plot of the three solutions of the cubic equation (4.22) for varied  $\beta$ ,  $k = 1.0$ ,  $M^2 = 2.0$ ,  $F^2 = 1.0$ . Colours as in Figure 4.2.

order  $\beta^0$  proportional to  $\mu^{1/2}$  and a real, travelling mode with lowest order  $\beta^1$ . Substituting  $c \approx c_0 + \beta c_1$  into (4.37), we obtain

$$\mathcal{O}(\beta^0) : \quad (4k^2 + 3F^2) c_0^3 - (4k^2 + F^2) \mu c_0 = 0, \quad (4.61a)$$

$$\mathcal{O}(\beta^1) : \quad (4k^2 + 3F^2) 3c_0^2 c_1 + 3c_0^2 - (4k^2 + F^2) \mu c_1 - \mu = 0, \quad (4.61b)$$

from which we get the two root approximations

$$c = \pm \sqrt{\frac{4k^2 + F^2}{4k^2 + 3F^2} \mu} - \frac{4k^2 \beta}{(4k^2 + F^2)(4k^2 + 3F^2)} + \mathcal{O}(\beta^2). \quad (4.62)$$

The third root is derived by substitution of  $c \approx c_0 \beta + c_1 \beta^3$ , which gives

$$\mathcal{O}(\beta^1) : \quad - (4k^2 + F^2) \mu c_0 - \mu = 0, \quad (4.63a)$$

$$\mathcal{O}(\beta^3) : \quad (4k^2 + 3F^2) c_0^3 + 3c_0^2 - (4k^2 + F^2) \mu c_1 = 0, \quad (4.63b)$$

and hence

$$c = -\frac{\beta}{4k^2 + F^2} + \frac{8k^2 \beta^3}{\mu (4k^2 + F^2)^4} + \mathcal{O}(\beta^5). \quad (4.64)$$

These asymptotic approximations are plotted as black lines in Figures 4.8 and 4.9. Additionally, we can plot on these graphs the lines where the spuriousity of (real) roots can change. The locations of these lines are

$$\beta = \begin{cases} \pm (2k^2 + F^2) \sqrt{-\mu}, \\ \varepsilon (\pm \varepsilon M - 1) \left( \frac{4k^2}{\pm \varepsilon M - 2} - F^2 \right), \end{cases} \quad (4.65)$$

which are derived from the equations in §4.3, and  $\varepsilon = \pm 1$  is as defined there.

#### 4.5.4 Variation of $F^2$

Finally we will consider how the roots,  $c$ , of the dispersion relation, (4.37), change as we vary  $F^2$ , the Charney number ( $\equiv \text{Bu}^{-1}$ ). Setting  $F^2 = 0$  unfortunately leaves us with a cubic equation and so there is little point calculating an asymptotic approximation in this limit, although we have done so, as  $k^2 \rightarrow 0$ , in §4.5.1. Instead, we will consider the limit  $F^2 \rightarrow \infty$  which corresponds to the limit in which any vertical ( $\hat{\mathbf{z}}$ ) motion of the fluid is completely repressed by the stratification and/or the rotation of the system. A consequence of this is that the instability is suppressed since, due to the geostrophic approximation, vertical motion corresponds to vorticity.

To investigate this limit, we define the temporary parameter  $\varepsilon = F^{-2}$ . Provided  $\mu \neq 0$  (the case  $\mu = 0$  has been seen in §4.5.2), we have two roots with  $c \sim F^0$  at leading order, and one root with  $c \sim F^{-2}$ . Consider first the former case. Our dispersion relation (4.37) is then, at leading orders

$$\mathcal{O}(\varepsilon^0) : \quad 3c_0^3 - \mu c_0 = 0, \quad (4.66a)$$

$$\mathcal{O}(\varepsilon^1) : \quad 4k^2 c_0^3 + 9c_0^2 c_1 + 3\beta c_0^2 - 4k^2 \mu c_0 - \mu c_1 - \beta \mu = 0. \quad (4.66b)$$

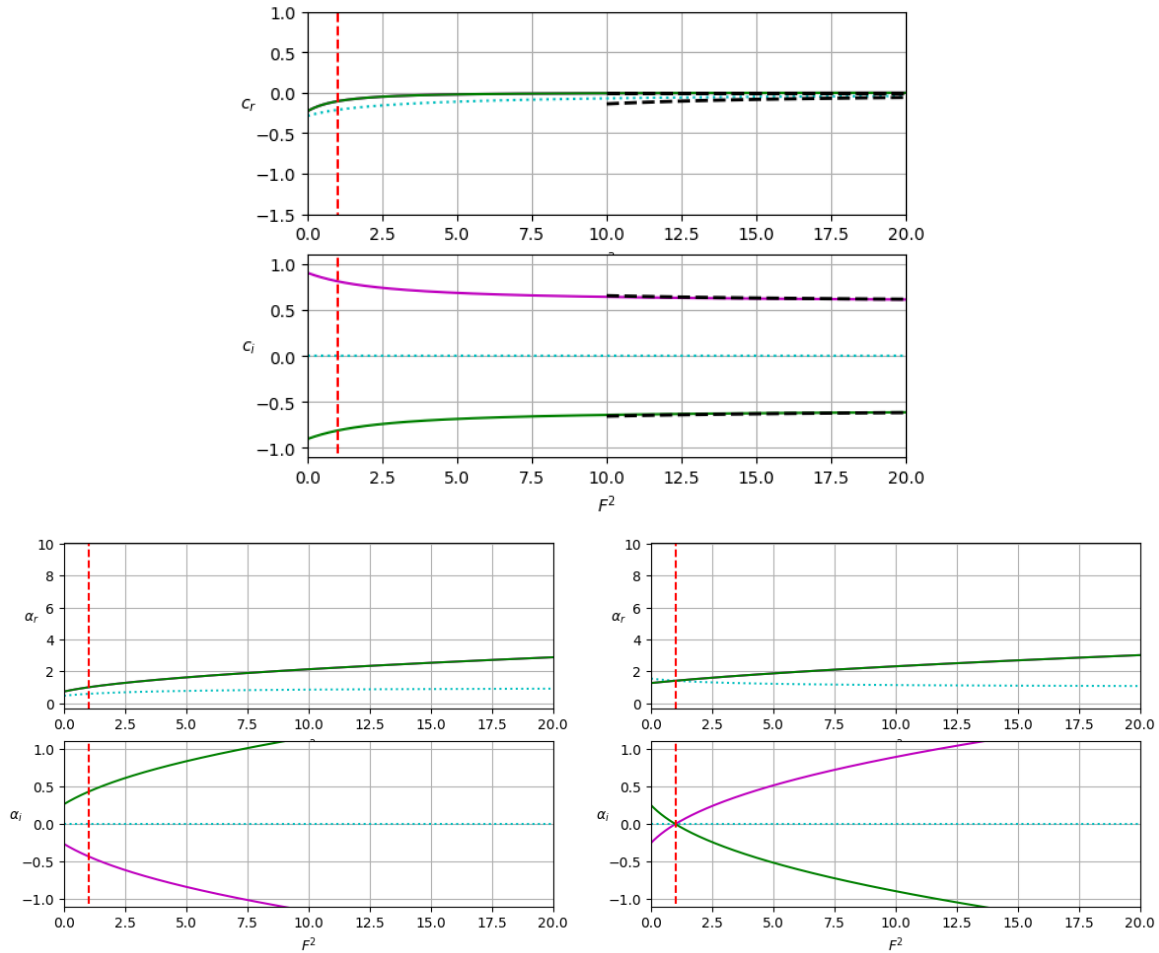


Figure 4.10: Plot of the three solutions of the cubic equation (4.22) for varied  $F^2$ ,  $k = 1.0$ ,  $M^2 = 0.0$ ,  $\beta = 1.0$ . Colours as in Figure 4.2.

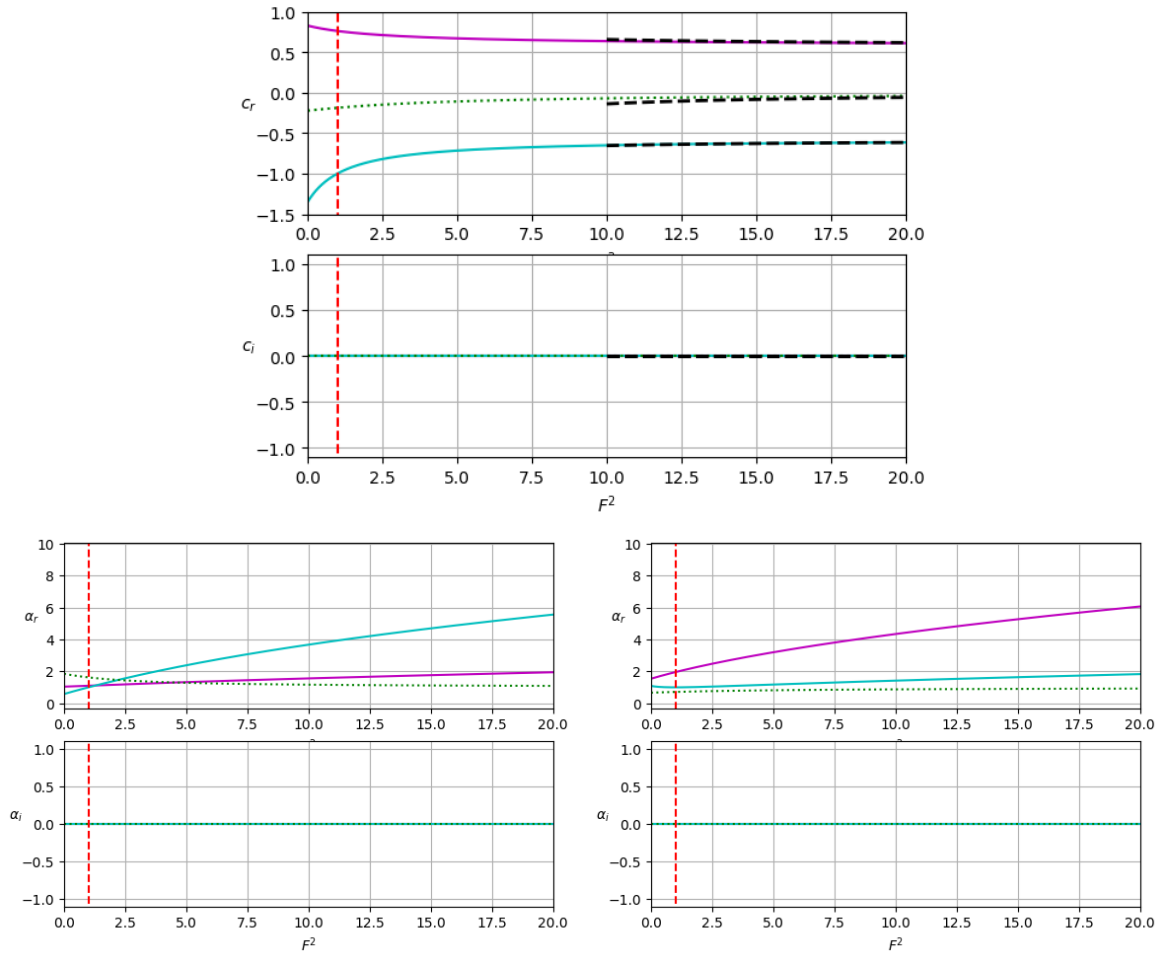


Figure 4.11: Plot of the three solutions of the cubic equation (4.22) for varied  $F^2$ ,  $k = 1.0$ ,  $M^2 = 2.0$ ,  $\beta = 1.0$ . Colours as in Figure 4.2.

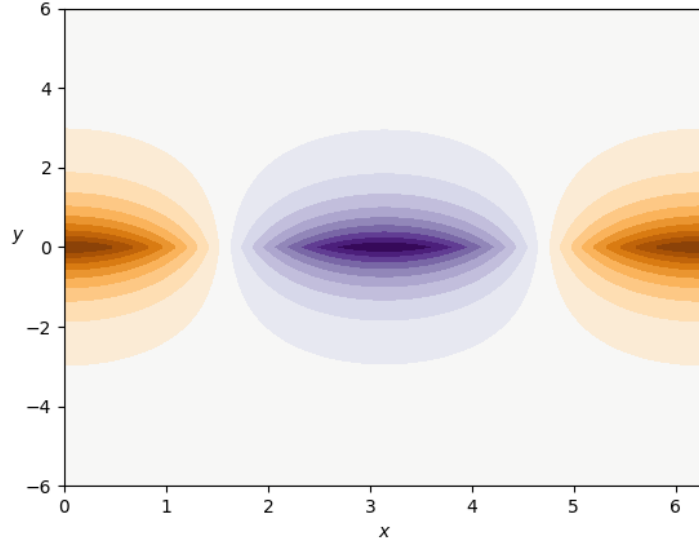


Figure 4.12: Eigenfunction,  $G(x, y)$ , of the vortex sheet instability,  $\hat{\beta} = \hat{F}^2 = 0$ .

Hence, replacing  $\varepsilon$  for  $F^{-2}$ , we have

$$c = \pm \left( 1 + \frac{4k^2}{3F^2} \right) \sqrt{\frac{\mu}{3}} + \mathcal{O}(F^4). \quad (4.67)$$

Similarly, taking the case where  $\varepsilon^1$  is the leading order, we have

$$\mathcal{O}(\varepsilon^1) : \quad -\mu c_0 - \beta\mu = 0, \quad (4.68a)$$

$$\mathcal{O}(\varepsilon^2) : \quad -4k^2\mu c_0 - \mu c_1 = 0. \quad (4.68b)$$

Replacing  $\varepsilon$  with  $F^{-2}$ , this simply gives

$$c = -\frac{\beta}{F^2} \left( 1 + \frac{4k^2}{F^2} \right) + \mathcal{O}(F^6). \quad (4.69)$$

These approximations are plotted against the exact roots in Figures 4.10 and 4.11.

## 4.6 Eigenfunctions

Given that the eigenvalue equation (4.22) is cubic, there is at most a single complex conjugate pair of eigenvalues, of which one represents an unstable root ( $\mathbb{I}(c) > 0$ ). As the instability develops, the perturbation structure will resemble the eigenfunction corresponding to the most unstable eigenvalue (largest growth rate), however for the vortex sheet problem, the growth rate  $\sigma = kc_i$  increases linearly with  $k$ , without bound. This is primarily due to the infinitesimal thickness of the interface and the lack of any reference scale.

To investigate the structure of the most unstable mode, let us therefore remove the  $k$  dependence with the transformation

$$F^2 \rightarrow \hat{F}^2 = \frac{F^2}{k^2}, \quad \beta \rightarrow \hat{\beta} = \frac{\beta}{k^2}, \quad y \rightarrow \hat{y} = ky, \quad x \rightarrow \hat{x} = kx, \quad (4.70)$$

or equivalently, set  $k = 1$ .

The eigenfunction is an exponential function of  $\hat{\alpha}_\pm$ ,

$$G(x, y) = Ae^{i\hat{x}} \begin{cases} e^{-\hat{\alpha}_+ \hat{y}}, & y > 0, \\ e^{\hat{\alpha}_- \hat{y}}, & y < 0, \end{cases} \quad (4.71)$$

where

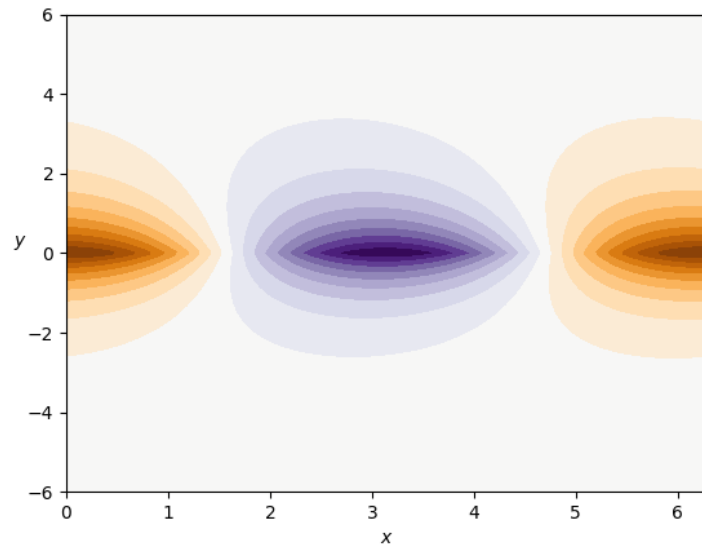
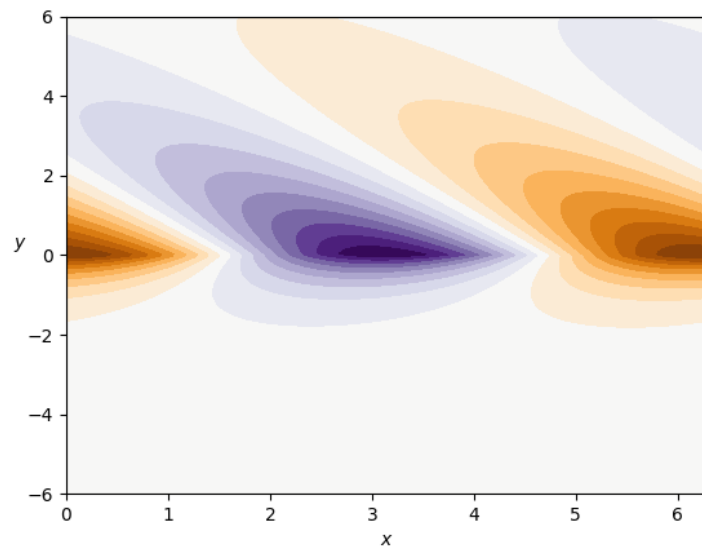
$$\hat{\alpha}_\pm^2 = 1 + \frac{(c \mp 1) (\hat{\beta} + c\hat{F}^2)}{(c \mp 1)^2 - M^2} \quad (4.72)$$

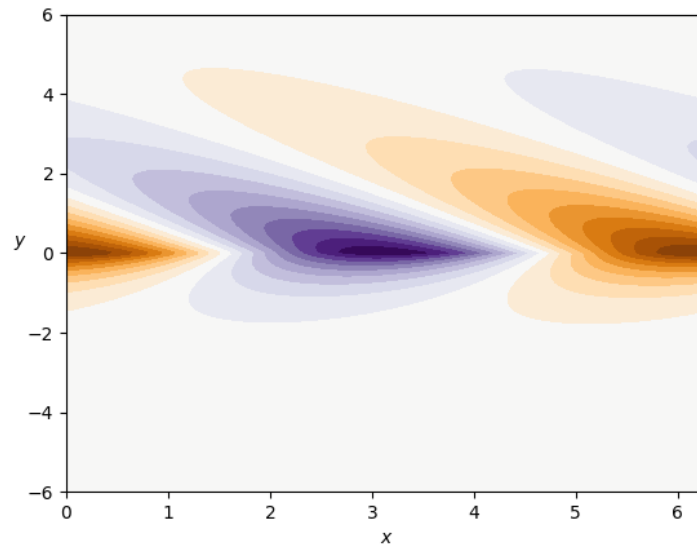
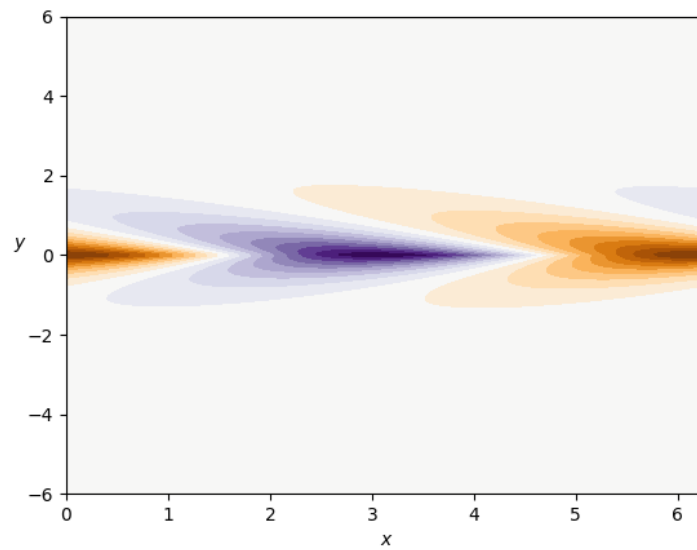
with  $\Re(\hat{\alpha}_\pm) > 0$ . Note that we have enforced continuity on  $G$ , rather than  $h$  (the free surface height or streamfunction), since  $G$  represents the lateral disturbance of the perturbation which defines the location of the interface.

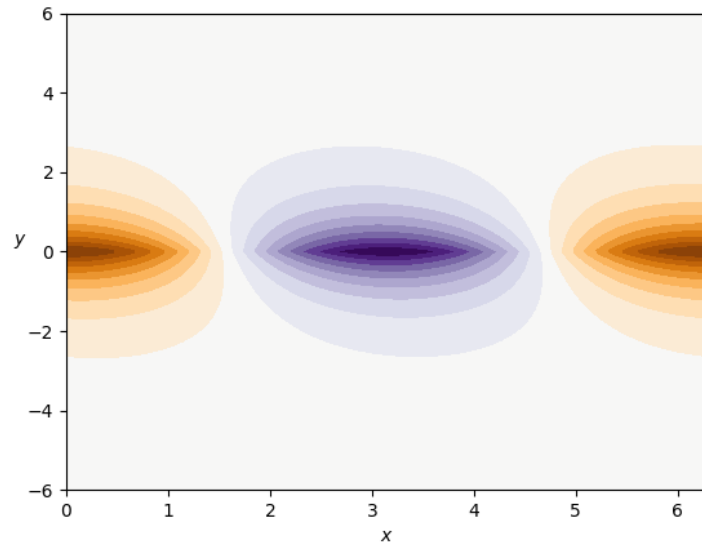
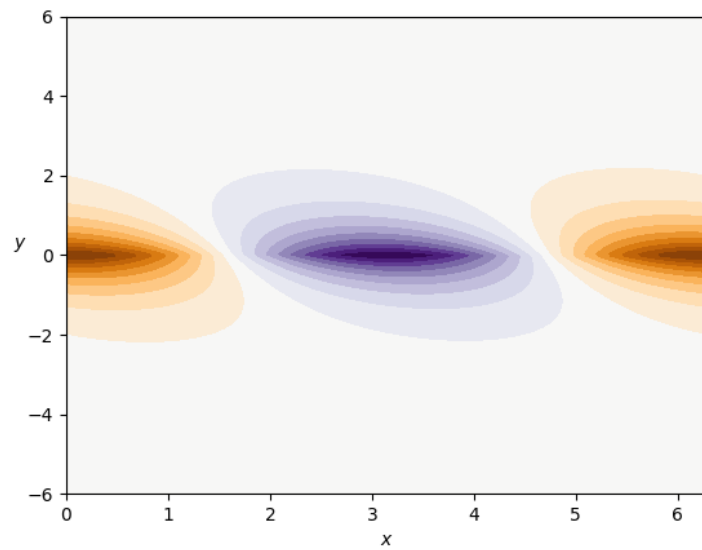
When  $\hat{\beta} = M^2 = \hat{F}^2 = 0$ ,  $\hat{\alpha}_\pm = 1$  and the eigenfunction is symmetric and decays exponentially in the lateral direction (Figure 4.12). Interestingly, given that  $\hat{\alpha}_\pm$  is independent of  $M^2$  when  $\hat{\beta} = \hat{F}^2 = 0$  (4.72), the eigenfunction does not change with  $M^2$ , though the imaginary part of the eigenvalue,  $c_i$ , decreases to zero as  $M^2$  increases to  $M^2 = 1$ . This suggests that the instability mechanism is unaffected by the presence of the magnetic field (alone) but the solitary effect is a growth rate reduction by magnetic tension.

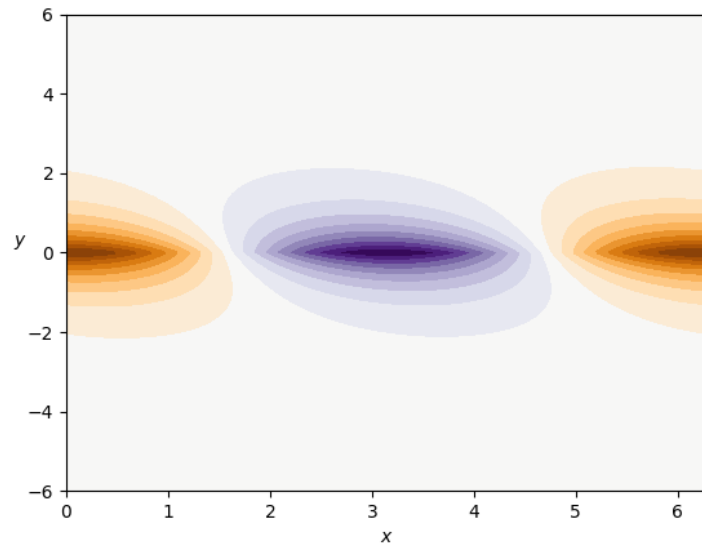
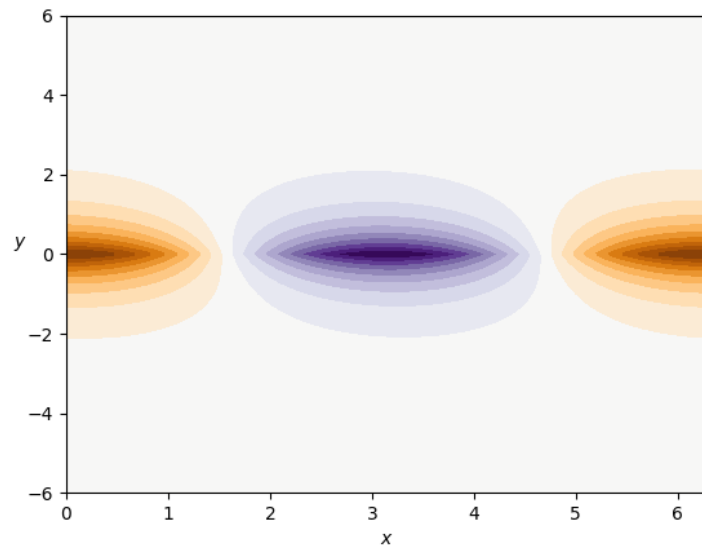
Non-zero  $\hat{\beta}$  introduces a linear vorticity gradient across the domain leading to a wavelike component of the eigenfunction (cf. §3.4.1), effectively extending the eigenfunction out on the positive  $y$  side of the domain (Figure 4.13), restraining it on the other side, and tilting the eigenfunction to the left (corresponding to the direction of propagation of Rossby waves). Figure 4.14 shows the effect of reintroducing the magnetic field on the eigenfunction. See also the values of  $c$ ,  $\alpha_\pm$  in Figure 4.6 for which the parameters have slightly different values, but the same overall trend: as  $M^2 \rightarrow 1$  ( $\beta \neq 0$ ),  $c \rightarrow 0$  (cf. asymptotics equation (4.57)) and hence  $\alpha_\pm \rightarrow \infty$ , i.e., the eigenfunction compresses to a small region about the vortex sheet.

We can also investigate the effect of non-zero  $\hat{F}^2$  (Figure 4.15). The eigenfunction becomes slanted and the lateral extent decreases as  $\hat{F}^2$  increases. This is essentially the same effect as on the negative- $y$  side of the eigenfunction as  $\hat{\beta}$  was increased, since rather than a smooth linear vorticity profile, the vorticity adjustment due to non-zero  $\hat{F}^2$  is linear, but symmetric about  $y = 0$ . The same tilting of the eigenfunction was found by Mak (2013) when the Froude number,  $Fr$ , was increased since  $F^2 = Fr/Ro$ . If we introduce a magnetic field, the eigenvalue tends to zero as  $M^2 \rightarrow 1$ . Unlike in the previous case, this does not lead to a singularity in  $\alpha_\pm$  (provided  $\beta = 0$ ) since the numerator also contains a factor of  $c$ . Figure 4.16 shows that increasing the magnetic field strength mainly removes the tilt from the eigenfunction though there is a small reduction to the lateral extent of the eigenfunction compared to the  $F^2 = M^2 = 0$  case (Figure 4.12).

(a)  $\hat{\beta} = 0.5$ (b)  $\hat{\beta} = 2.0$ Figure 4.13: Variation of the eigenfunction,  $G(x, y)$ , with  $\hat{\beta}$ .  $M^2 = \hat{F}^2 = 0$ .

(a)  $\hat{\beta} = 2.0, M^2 = 0.5$ (b)  $\hat{\beta} = 2.0, M^2 = 0.95$ Figure 4.14: Variation of the eigenfunction,  $G(x, y)$ , with  $M^2$ .  $\hat{F}^2 = 0$ .

(a)  $\hat{F}^2 = 0.5$ (b)  $\hat{F}^2 = 2.0$ Figure 4.15: Variation of the eigenfunction,  $G(x, y)$ , with  $\hat{F}^2$ .  $\hat{\beta} = M^2 = 0$ .

(a)  $\hat{F}^2 = 2.0, M^2 = 0.5$ (b)  $\hat{F}^2 = 2.0, M^2 = 0.95$ Figure 4.16: Variation of the eigenfunction,  $G(x, y)$ , with  $M^2$ .  $\hat{\beta} = 0$ .

## 4.7 Summary

The vortex sheet problem is an idealised profile but this means that the eigenvalue problem simplifies to a cubic equation which can, in principle, be solved completely. §4.2.2 also shows that the vortex sheet often represents the long-wavelength limit of solutions for a wide class of profiles. Hence, the vortex sheet problem is generally the first resource for determining how shear instability might develop in a given model.

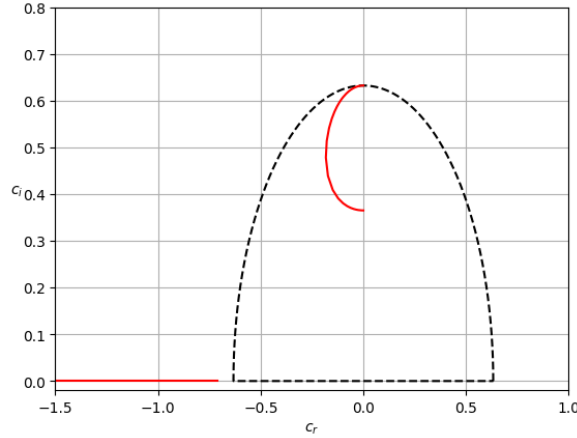


Figure 4.17: Example of the eigenvalues of dispersion relation (4.22) (with  $c_i \geq 0$ ) in relation to the semicircle bound (3.62).  $M^2 = 0.6$ ,  $\hat{\beta} = \beta/k^2 \in (0, 50)$ ,  $F^2 = 0$ .

The vortex sheet profile can be used to establish whether there are any significant differences between QG SWMHD and the models on which it is based (QG, MHD, SWMHD). A priori, it seems possible that there could be key differences. For example, it is possible to show, in MHD and SWMHD, that  $M^2 \geq 1$  is a sufficient condition for stability ( $B^2 > U^2$  everywhere, before normalisation) (MHD: Kent, 1966a, SWMHD: Mak et al., 2016). In §3 we found it impossible to replicate this general stability criterion (at least for  $\beta > 0$ ), although its ghost does remain in the semicircle bound (3.62). Therefore, perhaps surprisingly, we found in §4.4 that  $M^2 < 1$  is a necessary *and sufficient* condition for vortex sheet instability. This gives two possibilities, either  $M = 1$  is a stability boundary, and we have been unable to prove this, or another profile is (more) unstable than the vortex sheet when  $M^2 > 1$ . The latter option here may seem unlikely except that there already is a root which lies outside the smaller semicircle: the real root of (4.22) (Figure 4.17), and there is a possibility that this could become unstable in a slightly different profile.

The general effect of increasing  $M^2$  is given in §4.5.2, and is simple, provided that  $\beta = F^2 = 0$ , with the growth rate uniformly decreasing to zero and the phase speed equal to zero throughout. In this case, the magnetic field only enters through magnetic tension, which suppresses the growth of the instability, but has little additional effect. When  $\beta$  or  $F^2 > 0$  the impact of the magnetic field is complicated since magnetic tension plays the same role in suppressing instability, but also affects waves which can propagate on the vorticity gradient. Figure 4.6 and the asymptotics (4.57) show that the phase speed of the unstable mode tends to zero,  $c \rightarrow 0$ , as  $M^2 \rightarrow 1$  whilst the eigenfunction tends to a  $\delta$ -function if  $\beta > 0$ . This  $\delta$ -function limit is interesting since it occurs when  $\beta$  is arbitrarily small, however, the eigenfunction is

independent of  $M^2$  when  $\beta = 0$ . The strange effect of slightly non-zero  $\beta$  may be a premonition of the extra root found in §5.

Besides the  $\beta \rightarrow 0$  limit, the effect of  $\beta$  on the vortex sheet instability is reasonably straightforward (§4.5.3); it is weakly stabilising but, since vorticity is infinite at the interface, the profile cannot be stabilised by increasing  $\beta$ . The phase speed of the instability also becomes increasingly negative and the lateral structure of the eigenfunction becomes more wavelike, consistent with the reflection of waves, propagating on the vorticity gradient, by the vortex sheet.

Non-zero  $F^2$  also introduces a vorticity gradient, like that from the  $\beta$  effect, due to the effect of the zonal flow on the free surface. The difference from the  $\beta$ -vorticity is that it is symmetric over the interface. Though  $F^2$  does affect the instability, it is muted, perhaps since the vortex sheet acts as a barrier to wave propagation. Since the vorticity induced by  $F^2$  is symmetric, there is no preferred direction for the phase speed and so (in the absence of  $\beta$ ), it remains stationary. The eigenfunction, Figure 4.15, seems to indicate that waves are propagating towards the interface, and absorbed there. However, the growth rate of instability is generally reduced by increasing  $F^2$ , presenting an apparent contradiction.

Rather than considering the dynamics of waves due to  $F^2$ , it is easier to consider instead the energy budget. In the absence of  $F^2$  and  $M^2$  the only available energy is kinetic, and the dominant transfer in the instability is from the kinetic energy of the basic flow to that of the perturbation. The parameter  $F^2$  is proportional to the potential energy of the system, so increasing  $F^2$  means that transfer kinetic energy to the perturbation will be tapped off as potential energy, perhaps explaining two features, why increasing  $F^2$  reduces the growth rate of the instability (§4.5.4), and why increasing  $F^2$  reduces the lateral extent of the eigenfunction.

In this chapter, we have considered the effect of stratification,  $F^2$ , the magnetic field strength,  $M^2$ , and rotation,  $\beta$ , on the vortex sheet instability. This has highlighted some of the mechanisms of shear instability in an idealised setting. The results of this chapter should be compared with those in §5, which considers a smooth shear profile. Smoothing the shear profile is physically important, and can change some properties of the instability, however, we anticipate, based on the asymptotic analysis in §4.5, that the vortex sheet solutions derived in this chapter will appear in the long wavelength limit of that analysis.

## Chapter 5

# Linear Instability of a Shear Layer

### 5.1 Introduction

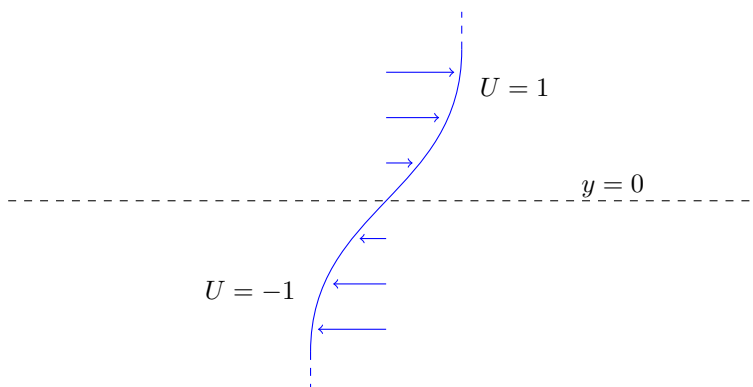


Figure 5.1: The initial “tanh profile” flow

In the previous chapter, we investigated the shear instability of the Vortex Sheet. We saw that this problem could be derived from a piecewise constant profile or equivalently as the long wavelength limit for a large class of smooth flow profiles. The limiting process, however, requires that  $\beta$ ,  $k^2$ , and  $F^2$  are asymptotically small. We need different methods for smooth profiles in the remainder of the parameter space.

A simple smooth profile that has received significant attention is the hyperbolic tanh-profile (Figure 5.1). It has three useful properties: it tends exponentially to a constant in the limit  $|y| \rightarrow \infty$ , exhibits a smooth transition between these constant values and there exist some analytic limits from which numerical approximations can be based. For example, in the hydrodynamic problem ( $F^2 = \beta = M = 0$ ), numerical solutions are provided by Michalke (1964) and build upon the special analytic modes found by Lin (1945, 1955) ( $k \rightarrow 1$ ), Garcia (1956) ( $k = 0, 1$  and  $c_i = 0$ ), and Drazin and Howard (1962) ( $k \rightarrow 0$ ).

The solutions of the tanh-profile eigenvalue problem tend towards the vortex sheet solutions as  $k \rightarrow 0$ , as expected from asymptotics, but (unsurprisingly) deviate significantly as  $k$  increases. In particular, a short-wave cut-off is found at  $k = 1$  and all modes are stable at wavenumbers

above this. Moreover, Lin (1955) shows that the unstable mode tends continuously towards a neutral mode at  $k = 1$ . This feature of smooth shear instability arises from phase conditions on counter-propagating Rossby waves (e.g. Bretherton, 1966). The key result of this cut-off is that, if the growth rate is  $\sigma = kc_i$ , then there is at least one unstable branch with  $\sigma(k = 0) = 0$ ,  $\sigma(k = 1) = 0$ , and  $\sigma > 0$  for some  $0 < k < 1$ . In particular, this means a maximum growth rate (possibly more than one) at a particular value of  $k \in (0, 1)$  exists. Michalke (1964) investigate this maximum and find it to be  $\sigma = 0.190$  at  $k = 0.446$ . This maximal growth rate is important since it identifies a preferred length scale at which instabilities form. We will revisit this in detail later.

A natural next step is introducing a constant magnetic field to the problem, aligned with the flow (Chandrasekhar, 1961). There appears to be no specific discussion of the tanh-profile for 2D MHD flows, so perhaps the best reference is a recent one, Mak et al. (2016) Figure 4, which shows the important elements of introducing a constant magnetic field (in SWMHD). Introducing a uniform field has a few major effects. Firstly, the short-wave cut-off is reduced, so that instability at some small wavelengths is entirely prevented. Logically, this also increases the preferred instability wavelength (decreasing the preferred wavenumber). Finally, at all wavenumbers, the growth rate is reduced meaning that the maximal growth rate of instability is also reduced; the profile is fully stabilised when  $M > 1$ .

The 2D  $\beta$ -plane and QG cases have been much more thoroughly investigated due to their relevance to the terrestrial atmosphere. Several interesting new features arise in these cases. Interestingly, in this problem, a new unstable solution appears at long zonal wavelengths with a significantly oscillatory meridional structure (Dickinson and Clare, 1973; denoted as the *radiating* mode by Talley, 1983). This is in comparison with the non-rotating mode which maintains a strongly exponential decay even when  $\beta > 0$ ; this is denoted the *trapped* mode (Talley, 1983) since its structure is largely confined to the shear layer. The radiating solution was found to be connected to a seemingly otherwise sporadic mode at  $k = 0$  with  $c_i = 0$  (Garcia, 1956). The physical relevance of the radiating mode is limited since its growth rate is generally less than that of the original mode, however, there is some thought that its existence could lead to increased meridional transport of angular momentum. It may have increased relevance in magnetised plasmas since its growth rate is less reduced than the original mode by magnetic effects (§5.6).

Increasing  $\beta$  stabilises both modes, with an absolute cut-off given by the inflexion point criterion. The exact stability boundary of the trapped mode can be shown to be a family of neutral modes (Lipps, 1965). Absolute stabilisation (stability for all wavenumbers,  $k$ ) is guaranteed by the inflexion point criterion, when  $\beta - U''$  is nowhere zero, i.e. when

$$\beta > \beta_{crit} = \max(U''). \quad (5.1)$$

For the case  $U = \tanh y$ ,  $\beta_{crit}$  is simple to evaluate, giving

$$\beta_{crit} = \frac{4}{3\sqrt{3}}. \quad (5.2)$$

The critical wavelength at this value of  $\beta$  can also be calculated using Lipps (1965)'s neutral

solution as

$$k_{crit} = \sqrt{\frac{2}{3}}, \quad (5.3)$$

which increases monotonically (from Michalke (1964)'s 0.446) as  $\beta = 0 \rightarrow \beta_{crit}$  since long wavelengths are most affected by increasing  $\beta$  (Lipps, 1970).

The physically relevant modes of this problem are the unstable eigenmodes, with  $c_i > 0$ , since in a system with initial random noise, these modes grow and eventually dominate the system. Before we discuss these modes, which must, in general, be calculated numerically, we will first discuss the case  $c_i = 0$ , known as neutrally stable or neutral modes (sections §5.2 & §5.4). These modes are interesting for two reasons. Let us consider the two-dimensional, hydrodynamic,  $\beta$ -plane flow example. There exists an upper bound,  $\beta_{crit}$ , on  $\beta$  for which the flow can be unstable. Since eigenvalues,  $c$ , must depend smoothly on the parameters  $\beta$ ,  $k$ , then, if we find an unstable mode with eigenvalue  $c_1$ , at a parameter value  $(\beta_1, k_1)$ , then increasing  $\beta$  from there must eventually lead to point  $(\beta_2, k_1)$  at which there is a mode with eigenvalue  $c_2$  which is real. If we can find a curve  $\beta(k)$  which can be shown to have unstable eigenvalues on only one side, this curve then defines a boundary on unstable modes which supersedes the general condition  $\beta - U'' = 0$ .

The second reason the case  $c_i = 0$  is interesting is that the governing equation (3.23) could possess a singularity where  $U = c$  (or, if  $M > 0$ , singularities where  $(U - c)^2 = M^2$ ). Dealing with this singularity then provides an additional constraint on solutions, and identifying and using this constraint offers an avenue for finding solutions. We will initially consider the  $\beta$ -plane case, first discussed by Lipps (1965) and use this to develop a formal structure for examining the problem, which can then be used to derive an extension of that result to quasigeostrophic flows immediately. We then use this formalism to investigate the magneto-hydrodynamic problem. One result that this formalism helps to show is that the Lipps (1965) neutral mode is the only non-singular neutral mode with phase speed in the range of  $U$ .

Unfortunately, this analysis of neutral modes cannot be extended to MHD flows. We will discuss in section §5.4 some reasons for this. From there, section §5.5 begins a numerical analysis of the problem; detailing the method and presenting some broad results. As covering the full parameter space is challenging, we will highlight some features in the following sections. The final section will then focus on features of the eigenfunctions, that may be of general interest, but are also relevant to the simulations of chapter §6.

## 5.2 Non-Singular Neutral Modes: $\beta$ -Plane QG

An extensive review of neutral modes in barotropic,  $\beta$ -plane flows is given by Drazin et al. (1982) although the detail of many of the proofs of their statements is scattered across several papers from the preceding few decades (e.g. Tollmien, 1935; Kuo, 1949; Foote and Lin, 1950; Lin, 1955; Lipps, 1965, to name a few). Some key results can be extended fairly straightforwardly to QGSW flows ( $F^2 > 0$ ,  $M = 0$ ), as shown below. The next section will address the problem with  $M > 0$ .

With  $M = 0$  ( $\beta, F^2 > 0$ ) and  $U = \tanh y$  the linearised equation, (3.23), becomes

$$h'' - k^2 h + \frac{\beta + cF^2 - U''}{U - c} h = 0, \quad (5.4)$$

where

$$U(y) = \tanh y \quad (5.5a)$$

$$U''(y) = 2 \tanh y (\tanh^2(y) - 1). \quad (5.5b)$$

The differential equation, (5.4), is then supplemented by the boundary conditions

$$h \rightarrow 0 \quad \text{as} \quad |y| \rightarrow \infty. \quad (5.6)$$

### 5.2.1 Sturm-Liouville Theory

The eigenvalue problem above cannot be written in Sturm-Liouville form with eigenvalue,  $c$ , due to the form of the coefficients. However, if consider instead an eigenvalue  $\lambda = -k^2(c)$ , with  $c$  now an independent variable, equation (5.4) is immediately in Sturm-Liouville form,

$$h'' + \frac{\beta + cF^2 - U''}{U - c} h = -\lambda h, \quad (5.7)$$

or equivalently,

$$h'' + \frac{\beta + UF^2 - U''}{U - c} h = -\nu h, \quad (5.8)$$

where  $\nu = -k^2 + F^2$ .

The major results of Sturm-Liouville theory are only applicable when  $c \in \mathbb{R}$  and  $h$  is non-singular. For  $c \in \text{Ran}(U)$ , regularity of  $h$  cannot be guaranteed due to the presence of a possible singularity when  $U = c$  (discussed in §5.2.2).

### 5.2.2 Singularities

Assuming  $c \in \mathbb{R}$ , and  $-1 < c < 1$  ( $c \in \text{Ran}(U)$ ), equation (5.4) is singular unless

$$\beta + cF^2 - U''(y_s) = 0 \quad (5.9)$$

for  $y_s$  satisfying  $U(y_s) = c = c_s$ . From the definition of  $U''$ ,

$$\beta + c_s F^2 = 2c_s (c_s^2 - 1), \quad (5.10)$$

which has three solutions

$$\begin{aligned} c_s^j &= 2\sqrt{\frac{2 + F^2}{6}} \cos \frac{1}{3} (\theta + 2j\pi), \quad j = 1, 2, 3, \\ \theta &= \arccos \frac{\beta}{\sqrt{2}} \left( \frac{3}{2 + F^2} \right)^{3/2}, \quad 0 \leq \theta \leq \frac{\pi}{2}. \end{aligned} \quad (5.11)$$

Substituting the expression for  $\beta$ , (5.10), into equation (5.4) allows for the cancellation of  $U - c$  and we therefore obtain

$$\begin{aligned} h'' - k^2 h + 2h \frac{c_s (c_s^2 - 1) + \tanh y \operatorname{sech}^2 y}{\tanh y - c_s} &= 0, \\ h'' - k^2 h + 2h \frac{c_s (c_s^2 - 1) - \tanh y (\tanh^2 y - 1)}{\tanh y - c_s} &= 0, \\ h'' - k^2 h + 2h (1 - c_s^2 - c_s \tanh y - \tanh^2 y) &= 0. \end{aligned} \quad (5.12)$$

Since the singularity only needs to be removed when  $c_s$  is real, this substitution is only relevant when  $\theta$  is real, i.e. when  $\beta < \sqrt{2} ((2 + F^2) / 3)^{3/2}$  ( $\beta < 4/3\sqrt{3}$  when  $F^2 = 0$ ). Additionally, the third root,  $c_s^3 > 1$ , is greater than  $U_{\max}$  and cannot satisfy  $U = c_s$ .

### 5.2.3 Rayleigh Quotient

Equation (5.12) can then be written as a Sturm-Liouville problem

$$h'' + K(y) h = -\lambda h, \quad (5.13)$$

where

$$\lambda = -k^2, \quad (5.14a)$$

$$K(y) = 2 (1 - c_s^2 - c_s \tanh y - \tanh^2 y). \quad (5.14b)$$

The problem therefore has an infinite series of eigenvalues

$$\lambda_1 < \lambda_2 < \dots < \lambda_n < \dots < \infty \quad (5.15)$$

and Rayleigh's Quotient is

$$\lambda_n = \frac{\int_{-\infty}^{\infty} \left( \frac{dh_n}{dy} \right)^2 - K(y) h_n^2 \, dy}{\int_{-\infty}^{\infty} h_n^2 \, dy}. \quad (5.16)$$

- If  $K(y) \geq 0$  for some value of  $c_s$ , then this would imply that all eigenvalues are greater than zero and hence that no real values of  $k$  exist for that particular  $c_s$ , thereby restricting  $c_s$ .
- For  $-1 < c_s < 0$  however, there will always be at least one zero of  $K(y)$  (except in trivial cases).

Substituting  $K(y)$  to Rayleigh's Quotient,

$$\lambda_n = 2 (c_s^2 - 1) + \frac{\int_{-\infty}^{\infty} \left( \frac{dh_n}{dy} \right)^2 + 2 (\tanh^2(y) + c_s \tanh y) h_n^2 \, dy}{\int_{-\infty}^{\infty} h_n^2 \, dy}. \quad (5.17)$$

The lowest eigenvalue,  $\lambda_1$ , is defined to be the minimum of this integral over all functions,  $h_n$ , and therefore an upper bound,  $\lambda_1 < \tilde{\lambda}$ , can be found by computing this integral for  $\tilde{\lambda}$  and

some test function, say  $\tilde{h} = \text{sech } y$ ,  $\tilde{h}' = -\tanh y \text{ sech } y$ . This gives that

$$\tilde{\lambda} = 2(c_s^2 - 1) + \frac{\int_{-\infty}^{\infty} (3 \tanh^2(y) \text{sech}^2(y) + 2c_s \tanh(y) \text{sech}^2(y)) dy}{\int_{-\infty}^{\infty} \text{sech}^2(y) dy}, \quad (5.18)$$

and hence

$$\begin{aligned} \tilde{\lambda} &= 2(c_s^2 - 1) + \frac{[\tanh^3(y)]_{-\infty}^{\infty} + c_s [\tanh^2(y)]_{-\infty}^{\infty}}{[\tanh(y)]_{-\infty}^{\infty}} \\ &= 2(c_s^2 - 1) + 1 = 2c_s^2 - 1. \end{aligned} \quad (5.19)$$

In terms of the wavenumber, we can derive from this that

$$c_s^2 > \frac{1 - k^2}{2}. \quad (5.20)$$

#### 5.2.4 An Exact Solution

Starting from equation (5.12), let us use the transformation  $z = \tanh y$  to turn the hyperbolic coefficients into polynomials. We obtain

$$(z^2 - 1)^2 h'' + 2z(z^2 - 1) h' + (2 - 2c_s^2 - k^2 - 2c_s z - 2z^2) h. \quad (5.21)$$

Dividing through by  $(z^2 - 1)^2$ , this can then be written in the form

$$h'' + \left( \frac{1}{z+1} + \frac{1}{z-1} \right) h' + \frac{1}{z^2-1} \left( \frac{-(c_s - c_s^2 - \frac{k^2}{2})}{z+1} + \frac{(-c_s - c_s^2 - \frac{k^2}{2})}{z-1} - 2 \right) h = 0, \quad (5.22)$$

which is the form of a Papperitz equation with regular singularities at  $z = \pm 1, \infty$ . Before we proceed, let us first investigate the singularity at  $z = \infty$ . To do so, we transform  $z \rightarrow 1/t$ , so

$$\frac{d}{dz} = -t^2 \frac{d}{dt}, \quad \frac{d^2}{dz^2} = t^4 \frac{d^2}{dt^2} + 2t^3 \frac{d}{dt},$$

and therefore

$$t^4 h'' + \left( \frac{-t^3}{1+t} + \frac{-t^3}{1-t} + 2t^3 \right) h' + \frac{t^2}{1-t^2} \left( \frac{-t(c_s - c_s^2 - \frac{k^2}{2})}{1+t} + \frac{t(-c_s - c_s^2 - \frac{k^2}{2})}{1-t} - 2 \right) h = 0. \quad (5.23)$$

In the limit  $t \rightarrow 0$  ( $z \rightarrow \infty$ ) this reduces to

$$t^2 h'' - 2h = 0, \quad (5.24)$$

demonstrating that  $t = 0$  ( $z = \infty$ ) is a regular singular point of equation (5.22) with exponents  $-1, 2$ .

The Papperitz equation is the general form of a second-order differential equation with exactly

three regular singularities and can be written as

$$h'' + \left( \frac{1-\alpha-\alpha'}{z-a} + \frac{1-\beta-\beta'}{z-b} + \frac{1-\gamma-\gamma'}{z-c} \right) h' + \frac{1}{(z-a)(z-b)(z-c)} \left( \frac{\alpha\alpha'(a-b)(a-c)}{z-a} + \frac{\beta\beta'(b-c)(b-a)}{z-b} + \frac{\gamma\gamma'(c-a)(c-b)}{z-c} \right) h = 0, \quad (5.25)$$

where the three singularities are at  $z = a, b, c$ , and have exponents  $\alpha, \alpha'; \beta, \beta'; \gamma, \gamma'$  respectively. Of particular use is that this equation (and its solution) can be expressed using the Riemann P-symbol,

$$h = P \left\{ \begin{matrix} a & b & c & \\ \alpha & \beta & \gamma & z \\ \alpha' & \beta' & \gamma' & \end{matrix} \right\}. \quad (5.26)$$

Our equation (5.22) is of a particular form where  $\gamma + \gamma' = 1$ ,  $c \rightarrow \infty$ , and  $a = -1$ ,  $b = +1$ , say. The exponents therefore satisfy the equations

$$\alpha + \alpha' = 0, \quad (5.27a)$$

$$\beta + \beta' = 0, \quad (5.27b)$$

$$2\alpha\alpha' = c_s - c_s^2 - \frac{k^2}{2}, \quad (5.27c)$$

$$2\beta\beta' = -c - c_s^2 - \frac{k^2}{2}, \quad (5.27d)$$

$$\gamma + \gamma' = 1, \quad (5.27e)$$

$$\gamma\gamma' = -2. \quad (5.27f)$$

The latter two equations (5.27e & 5.27f) can be quickly shown to produce the two exponents that we derived earlier,  $\gamma = -1$ ,  $\gamma' = 2$ , say. The remaining pairs of equations give that  $\alpha = -\alpha'$ ,  $\beta = -\beta'$ , and so

$$\alpha = \pm \frac{1}{2} \sqrt{k^2 + 2c_s^2 - 2c_s}, \quad (5.28a)$$

$$\beta = \pm \frac{1}{2} \sqrt{k^2 + 2c_s^2 + 2c_s}, \quad (5.28b)$$

where the pairs of exponents can be freely interchanged. Our Riemann P-symbol therefore looks like

$$h = P \left\{ \begin{matrix} -1 & +1 & \infty & \\ \alpha & \beta & -1 & z \\ -\alpha & -\beta & 2 & \end{matrix} \right\}. \quad (5.29)$$

One advantage of using the Riemann symbol is that it represents the equation and any or all of its Frobenius solutions. Some transformations are therefore evident (e.g. Morse and Feshbach, 1953). For example, applying a Möbius transform to the independent variable will move singularities of the equation, but preserve their exponent. In particular, the transformation

$$\eta = (z + 1)/2 \quad (5.30)$$

brings the singularities into their “normal” positions,  $0, +1, \infty$ . With this, the Riemann

symbol becomes

$$h = P \left\{ \begin{array}{ccc} 0 & +1 & \infty \\ \alpha & \beta & -1 + \alpha + \beta \\ -\alpha & -\beta & 2 + \alpha + \beta \end{array} \eta \right\}. \quad (5.31)$$

Considering that the Riemann symbol also represents the Frobenius solutions (with exponents given) we can also factorise out arbitrary powers of  $\eta$ ,  $(\eta - 1)$  which changes the exponents of the 0 and +1 singularities along with the exponent at  $\infty$ .

$$h = \eta^\alpha (\eta - 1)^\beta P \left\{ \begin{array}{ccc} 0 & +1 & \infty \\ 0 & 0 & -1 + \alpha + \beta \\ -2\alpha & -2\beta & 2 + \alpha + \beta \end{array} \eta \right\}. \quad (5.32)$$

This is helpful, since the hypergeometric equation,

$$\eta(1 - \eta)\psi'' + (c - (a + b + 1)\eta)\psi' - ab\psi = 0 \quad (5.33)$$

has known solutions and the Riemann symbol,

$$\psi = P \left\{ \begin{array}{ccc} 0 & +1 & \infty \\ 0 & 0 & a \\ 1 - c & c - a - b & b \end{array} \eta \right\}. \quad (5.34)$$

The hypergeometric solution has two linearly independent series solutions about  $\eta = 0$  with leading order terms  $\eta^0$  and  $\eta^{1-c}$ ,

$$\psi_1(\eta) = F(a, b; c; \eta), \quad (5.35a)$$

$$\psi_2(\eta) = \eta^{1-c} F(1 + a - c, 1 + b - c; 2 - c; \eta) \quad (5.35b)$$

where  $F$  is the hypergeometric series, and these solutions correspond to series solutions of  $h$  with leading order terms  $\eta^\alpha$  and  $\eta^{-\alpha}$ . We left the sign of  $\alpha$  arbitrary, but now, let us set  $\alpha > 0$  so that the boundary condition,  $h(\eta) \rightarrow 0$  as  $\eta \rightarrow 0$  ( $z \rightarrow -1$ ), is satisfied by the solution equivalent to  $\psi_1$ . Therefore

$$h(\eta) = \eta^\alpha (\eta - 1)^\beta F(-1 + \alpha + \beta, 2 + \alpha + \beta; 1 + 2\alpha; \eta), \quad (5.36)$$

with  $\alpha > 0$ , is the solution that now needs to be matched at the other boundary ( $h(\eta) \rightarrow 0$  as  $\eta \rightarrow 1$ ).  $F$  represents an infinite series,

$$F(a, b; c; \eta) = \sum_{k=0}^{\infty} \frac{(a)_n (b)_n}{(c)_n} \frac{\eta^k}{k!}, \quad (5.37)$$

which converges, as  $\eta \rightarrow 1$ , to

$$F(a, b; c; 1) = \frac{\Gamma(c - a - b) \Gamma(c)}{\Gamma(c - a) \Gamma(c - b)} \quad (5.38)$$

provided that  $c > a + b$ , equivalent to  $\beta < 0$ , and  $\Gamma$  is the standard Gamma-function (with singularities at non-positive integers). The numerator of (5.38) cannot be zero, and so given

that  $h$  already has the prefactor  $(\eta - 1)^\beta$ ,  $\beta < 0$ , the boundary condition as  $\eta \rightarrow 1$  can only possibly be satisfied when

$$c - a = 2 + \alpha - \beta, \quad c - b = -1 + \alpha - \beta \quad (5.39)$$

are non-positive integers. Since  $\alpha > 0$ ,  $\beta < 0$ , we have only  $\alpha - \beta = 1$  (and  $\alpha - \beta = 0$  if we are slightly generous with our inequalities). This does not guarantee that the boundary condition,  $h(\eta) \rightarrow 0$  as  $\eta \rightarrow 1$ , is satisfied since there is the prefactor  $(\eta - 1)^\beta$  that we must concern ourselves with. Since the prefactor is the problem, let us instead consider  $\beta > 0$  so that  $h(\eta) \rightarrow 0$  is guaranteed as long as the hypergeometric series does not diverge. However, the infinite series cannot be convergent since  $c - a - b = -2\beta < 0$  and so  $F$  can now only be non-divergent if it truncates to a finite series. Examining expression (5.37), this requires  $a$  or  $b$  to be non-positive integers i.e.

$$a = 2 + \alpha + \beta \in \mathbb{Z}/\mathbb{N}, \quad b = -1 + \alpha + \beta \in \mathbb{Z}/\mathbb{N}. \quad (5.40)$$

and since  $\alpha, \beta > 0$

$$\alpha = \beta = 0, \quad \text{or} \quad \alpha + \beta = 1, \quad (\alpha, \beta > 0) \quad (5.41)$$

equivalent to condition (5.39) with the sign of  $\beta$  switched. Therefore (5.41) specifies all possibilities of matching the boundary condition. Let us investigate the two cases, starting with  $\alpha = \beta = 0$ . If  $\alpha = \beta = 0$  then

$$\begin{aligned} h(\eta) &= CF(-1, 2; 1; \eta) \\ &= C(1 - 2\eta) = -Cz, \end{aligned} \quad (5.42)$$

where  $C$  is an arbitrary constant and  $\eta$  is defined in (5.30). To match the boundary conditions we therefore require  $C = 0$  (although, since  $h = -Cz$ , so  $C \neq 0$  may be of interest as a near solution). Combining (5.28a) and (5.28b), we can see that this solution occurs when  $k = c_s = 0$ .

The more interesting case is  $\alpha + \beta = 1$ . Substituting  $\beta = 1 - \alpha$  into expression (5.36), we have

$$\begin{aligned} h(\eta) &= C\eta^\alpha (\eta - 1)^{1-\alpha} F(0, 2; 1 + 2\alpha; \eta) \\ &= C\eta^\alpha (\eta - 1)^{1-\alpha} \\ &= \tilde{C}(z + 1)^\alpha (z - 1)^{1-\alpha}, \end{aligned} \quad (5.43)$$

where  $C, \tilde{C}$  are arbitrary constants and  $F$  is a constant since  $a = 0$ . Now using (5.28a), (5.28b), we can calculate the value of  $\alpha$  in terms of the original parameters of the problem. Taking the square of (5.28a) from the square of (5.28b) we can derive that

$$\beta^2 - \alpha^2 = c_s. \quad (5.44)$$

Combining this with  $\alpha + \beta = 1$  implies that  $\beta - \alpha = c_s$  and therefore

$$\beta = \frac{1 + c_s}{2}, \quad \alpha = \frac{1 - c_s}{2}. \quad (5.45)$$

Considering  $\alpha^2$  from above and in (5.28a), we can derive

$$c_s^2 = 1 - k^2 \quad (5.46)$$

and so

$$\begin{aligned} h &= \tilde{C} (1 - z)^{\frac{1}{2} \mp \frac{\sqrt{1-k^2}}{2}} (1 + z)^{\frac{1}{2} \pm \frac{\sqrt{1-k^2}}{2}} = \tilde{C} \operatorname{sech} y \left( \frac{1 + \tanh y}{1 - \tanh y} \right)^{\frac{\pm \sqrt{1-k^2}}{2}} \\ &= \tilde{C} \operatorname{sech} y e^{\pm y \sqrt{1-k^2}}. \end{aligned} \quad (5.47)$$

Reiterating (5.10),

$$\beta + c_s F^2 = 2c_s (c_s^2 - 1), \quad (5.48)$$

this means that for any  $k$  we have the relationship

$$\beta = (2k^2 + F^2) (1 - k^2)^{1/2}, \quad (5.49)$$

which identifies a unique curve in  $(\beta, k, F^2)$  space for which neutrally stable waves exist, with their form given by equation (5.47). This is the unique set of neutrally stable modes, and with  $F^2 = 0$ , this is the neutral mode given by Lipps (1965). These curves often represent a boundary or limit of unstable modes see, e.g., Figures 5.3, 5.6. Note that in each of the cases plotted, this neutral mode curve forms some, but not the entirety, of the stability boundary (particularly the stability boundary for modes with shorter zonal wavelengths,  $k \lesssim 1$ ). A singular neutral mode (which is the limit of a non-singular unstable mode) must therefore make up the remainder of the stability boundary.

### 5.3 Singular Neutral Modes: $\beta$ -Plane QG

In section §5.2, we determined analytically the non-singular neutral mode solutions of (3.23) when  $M = 0$ . Although it was initially conjectured that these were the unique neutral modes of this problem (Lipps, 1965, 1970), it was then shown numerically (Howard and Drazin, 1964; Dickinson and Clare, 1973) that a second solution exists at small wavenumber,  $k$ . This solution must vanish for sufficiently large  $\beta$  (via the inflexion point criterion), hence there must exist another neutral mode bounding this unstable mode. Since we have ruled out, by the arguments of the previous section, the possibility of this mode being non-singular, we will here instead investigate singular solutions of (3.23) in an attempt to find this mode. We will focus here on the case  $F^2 = 0$ , for simplicity, although like the neutral mode in §5.2 we anticipate this could be extended straightforwardly to the case  $F^2 > 0$ . It would likely be harder to include magnetic effects.

Starting with equation (3.23) and making the substitution  $z = U(y) = \tanh y$ , we obtain

$$(1 - z^2)^2 h''(z) - 2z(1 - z^2) h'(z) + \left( k^2 - \frac{\beta + 2z(1 - z^2)}{(z - c)} \right) h(z) = 0. \quad (5.50)$$

Equation (5.50) possesses a singularity at  $z = c$  which may not lie in the domain of  $h(z)$  but can nonetheless affect  $h$  inside the domain. In §5.2 we removed this singularity by setting

$\beta - U'' = \mathcal{O}(U - c)$  (for  $c \in \mathbb{R}$ ), and therefore found the trapped neutral boundary.

Later in this section we will look particularly at the case with  $\mathbb{I}(c)$  zero or asymptotically small, in which case this singularity moves inside the domain provided that the real part of  $c$  lies inside the range of the flow ( $-1 < \mathbb{R}(c) < 1$ ). In §5.8 we will probe the approximate solution, for small  $\mathbb{I}(c)$ , and show that both  $h$  and  $h'$  are non-zero and finite. Hence  $h'' \rightarrow \infty$  as  $z \rightarrow c$ .

We consider an asymptotic expansion of  $h$  about  $z$ , and begin by transforming with  $\eta = c - z$ . This gives that

$$A(\eta)h'' + B(\eta)h' + C(\eta)h = 0, \quad (5.51)$$

where

$$A(\eta) = \eta^4 - 4c\eta^3 - 2(1 - 3c^2)\eta^2 + 4c(1 - c^2)\eta + (1 - c^2)^2, \quad (5.52a)$$

$$B(\eta) = 2\eta^3 - 6c\eta^2 - 2(1 - 3c^2)\eta + 2c(1 - c^2), \quad (5.52b)$$

$$C(\eta) = -2\eta^2 + 6c\eta - k^2 + 2(1 - 3c^2) - (\beta + 2c(1 - c^2))\eta^{-1}. \quad (5.52c)$$

Following the method of Frobenius, we posit a solution

$$y = \eta^\sigma \sum_{n=0}^{\infty} a_n \eta^n \quad (5.53)$$

and at the lowest order obtain

$$(1 - c^2)^2 \sigma(\sigma - 1) a_0 = 0. \quad (5.54)$$

Hence we have that  $\sigma = 0, 1$  and the two independent solutions take the form

$$h_1 = \eta \sum_{n=0}^{\infty} a_n \eta^n, \quad (5.55a)$$

$$h_2 = \gamma h_1 \ln \eta + \sum_{n=0}^{\infty} b_n \eta^n, \quad (5.55b)$$

with  $a_n, b_n$ , and  $\gamma$  constants to be determined. The presence of a logarithmic singularity appears as a discontinuity in the derivatives of the eigenfunctions in §5.8.1.

### 5.3.1 First Solution

Considering the first solution, we get

$$a_1 = \frac{\beta}{2(1 - c^2)^2} a_0 \quad (5.56)$$

from the  $\mathcal{O}(\eta^0)$  terms. The remaining coefficients and recurrence relation are from  $\mathcal{O}(\eta^1)$ :

$$a_2 = \frac{\beta - 10c(1 - c^2)}{6(1 - c^2)^2} a_1. \quad (5.57)$$

From  $\mathcal{O}(\eta^2)$ :

$$a_3 = \frac{(\beta - 28c(1 - c^2))a_2 + (k^2 + 6(1 - 3c^2))a_1}{12(1 - c^2)^2}. \quad (5.58)$$

From  $\mathcal{O}(\eta^n)$ ,  $n > 3$ :

$$a_{n+1} = \frac{1}{(n+2)(n+1)(1-c^2)^2} \left[ -2n(2n+3)c(1-c^2)a_n + 2(n^2-1)(1-3c^2)a_{n-1} + 2c(2n+1)(n-2)a_{n-2} - n(n-3)a_{n-3} \right]. \quad (5.59)$$

### 5.3.2 Second Solution

Considering now the second solution,  $h_2$ , its derivatives are

$$h_2 = \gamma \ln \eta \sum_{n=0}^{\infty} a_n \eta^{n+1} + \sum_{n=0}^{\infty} b_n \eta^n, \quad (5.60a)$$

$$h_2' = \gamma \sum_{n=0}^{\infty} a_n (1 + (n+1) \ln \eta) \eta^n + \sum_{n=0}^{\infty} b_{n+1} (n+1) \eta^n, \quad (5.60b)$$

$$h_2'' = \gamma a_0 \eta^{-1} + \gamma \sum_{n=0}^{\infty} a_{n+1} (n+2) (2 + (n+1) \ln \eta) \eta^n + \sum_{n=0}^{\infty} b_{n+2} (n+2) (n+1) \eta^n. \quad (5.60c)$$

The log terms will cancel out as the  $a_n$  are already specified and so the only terms we need to consider will be

$$h_2 : \sum_{n=0}^{\infty} b_n \eta^n, \quad (5.61a)$$

$$h_2' : \gamma \sum_{n=0}^{\infty} a_n \eta^n + \sum_{n=0}^{\infty} b_{n+1} (n+1) \eta^n, \quad (5.61b)$$

$$h_2'' : \gamma a_0 \eta^{-1} + 2\gamma \sum_{n=0}^{\infty} a_{n+1} (n+2) \eta^n + \sum_{n=0}^{\infty} b_{n+2} (n+2) (n+1) \eta^n. \quad (5.61c)$$

At  $\mathcal{O}(\eta^{-1})$  we find

$$\gamma a_0 = -\frac{\beta + 2c(1 - c^2)}{(1 - c^2)^2} b_0. \quad (5.62)$$

Hence we will define

$$\tilde{a}_n = \gamma a_n, \quad (5.63)$$

and these  $\tilde{a}_n$  satisfy  $\tilde{a}_{n+1} = f_a(\tilde{a}_n, \dots, \tilde{a}_0)$  where  $f_a$  is the recurrence relation for  $a_n$  given above and  $\tilde{a}_0 = \gamma a_0$  satisfies (5.62).

Continuing the calculation of coefficients, the derivatives of  $h$  can be written as

$$h_2 : \sum_{n=0}^{\infty} b_n \eta^n, \quad (5.64a)$$

$$h'_2 : \sum_{n=0}^{\infty} (\tilde{a}_n + (n+1) b_{n+1}) \eta^n, \quad (5.64b)$$

$$h''_2 : \tilde{a}_0 \eta^{-1} + \sum_{n=0}^{\infty} (n+2) (2\tilde{a}_{n+1} + (n+1) b_{n+2}) \eta^n. \quad (5.64c)$$

The next coefficient comes from the  $\mathcal{O}(\eta^0)$  terms which give

$$2(1-c^2)^2 b_2 + \beta b_1 = (2(1-3c^2) - k^2) b_0 - 4\tilde{a}_1 (1-c^2)^2 - 2c(1-c^2) \tilde{a}_0. \quad (5.65)$$

Here both  $b_2$  and  $b_1$  are unconstrained and so, without further restrictions (except those that bring in  $b_n$ ,  $n > 2$ ), we are left with a degree of freedom. This makes sense as this is a ghost of  $h_1$ , which appears within  $h_2$ . Given that  $h_1$  is a solution of (5.51), we can freely take arbitrary quantities of  $h_1$  from  $h_2$ . It makes the most sense to use this to set

$$b_1 = 0, \quad (5.66)$$

and so we have

$$b_2 = -\frac{3\tilde{a}_1}{2} + \frac{1}{2(1-c^2)^2} [(k^2 - 2(1-3c^2)) b_0 - 6c(1-c^2) \tilde{a}_0]. \quad (5.67)$$

No significant simplification can be had by substituting either  $\tilde{a}_0$  or  $\tilde{a}_1$  and so we'll leave the expression in this recursive form. The  $\mathcal{O}(\eta^1)$  terms give that

$$b_3 = -\frac{5\tilde{a}_2}{6} + \frac{1}{6(1-c^2)^2} [\beta - 10c(1-c^2) b_2 - 6cb_0 - 14c(1-c^2) \tilde{a}_1 + 2(1-3c^2) \tilde{a}_0]. \quad (5.68)$$

From the  $\mathcal{O}(\eta^2)$  terms we get

$$b_4 = -\frac{7\tilde{a}_3}{12} + \frac{1}{12(1-c^2)^2} [-28c(1-c^2) b_3 + (k^2 + 6(1-3c^2)) b_2 + 2b_0 - 22c(1-c^2) \tilde{a}_2 + 8(1-3c^2) \tilde{a}_1 + 10c\tilde{a}_0]. \quad (5.69)$$

From the  $\mathcal{O}(\eta^3)$  terms we get

$$b_5 = -\frac{9\tilde{a}_4}{20} + \frac{1}{20(1-c^2)^2} [(\beta - 54c(1-c^2)) b_4 + (k^2 + 16(1-3c^2)) b_3 + 14cb_2 - 30c(1-c^2) \tilde{a}_3 + 12(1-3c^2) \tilde{a}_2 + 18c\tilde{a}_1 - 3\tilde{a}_0]. \quad (5.70)$$

After this order all terms now appear normally and we can therefore write a general recursion

equation using higher order terms at  $\mathcal{O}(\eta^{n-2})$ . This gives

$$b_n = \frac{1-2n}{n(n-1)}\tilde{a}_{n-1} + \frac{1}{n(n-1)(1-c^2)^2} [(\beta - 2(2n-1)(n-2)c(1-c^2))b_{n-1} + (k^2 + 2(n-3)(n-1)(1-3c^2))b_{n-2} + 2(2n-3)(n-4)cb_{n-3} - (n-5)(n-2)b_{n-4} - 2(4n-5)c(1-c^2)\tilde{a}_{n-2} + 4(n-2)(1-3c^2)\tilde{a}_{n-3} + 2c(4n-11)\tilde{a}_{n-4} - (2n-7)\tilde{a}_{n-5}]. \quad (5.71)$$

### 5.3.3 Jump at the singularity

We have derived that the asymptotic expansions of  $h$  and  $h'$  about the singularity are

$$h(\eta) = b_0 + \sum_{n=1}^{\infty} (\tilde{a}_{n-1} \ln \eta + b_n + a_{n-1}) \eta^n, \quad (5.72a)$$

$$h'(\eta) = \sum_{n=0}^{\infty} ((n+1)(\tilde{a}_n \ln \eta + b_{n+1} + a_n) + \tilde{a}_n) \eta^n. \quad (5.72b)$$

As  $\eta \rightarrow 0$ ,  $h'(\eta) \rightarrow \infty$ ; however, consider the quantity

$$C = \left[ \frac{h'}{h} \right]_{\eta=0} \quad (5.73)$$

where  $[f]$  denotes a jump in a function  $f$  as defined by

$$[f]_{\eta=0} = \lim_{\eta \rightarrow 0^+} (f(\eta) - f(-\eta)), \quad (5.74)$$

remains bounded. Hence, from (5.72),

$$C = \frac{\lim_{\eta \rightarrow 0^+} (\tilde{a}_0 (\ln \eta - \ln -\eta) + \mathcal{O}(\eta \ln \eta))}{h(0)} = \frac{\tilde{a}_0 D i \pi}{b_0}, \quad (5.75)$$

where  $D \in \{-1, 1\}$  depends on the branch of the logarithm chosen. This can be determined by considering the limiting solution of the viscous problem, and in this case the relevant branch is  $D = -1$  (Wasow, 1948; Foote and Lin, 1950). Hence, also with (5.62), we have

$$C = \frac{\beta + 2c(1-c^2)}{(1-c^2)^2} i \pi. \quad (5.76)$$

The jump in the equivalent quantity in terms of  $y$ , rather than  $\eta$ , is

$$\left[ \frac{h'}{h} \right]_{y=c} = \left| \frac{d\eta}{dy} \right|_{y=c} \left[ \frac{h'}{h} \right]_{\eta=0} = \frac{\beta + 2c(1-c^2)}{(1-c^2)} i \pi. \quad (5.77)$$

The finite discontinuity derived here is equivalent to the discontinuity of the Wronskian discussed in §5.8.1. This is a specific case of the problem discussed by Foote and Lin (1950).

### 5.3.4 Numerical determination of leading coefficients

Consider now numerical solutions  $h(y)$ , with  $c = c_r + ic_i$  and  $c_i$  small. We seek to estimate the coefficients  $a_0$  and  $b_0$  for the nearby neutral mode. Finding  $b_0$  is simple since

$$h(\eta = 0) = b_0, \implies h(y = y_r) = b_0 + \mathcal{O}(\tilde{c}), \quad (5.78)$$

where  $y_r = \text{artanh}(c_r)$ . To find  $a_0$ , consider the derivative of  $h(\eta)$ .

$$h'(\eta) = \sum_{n=0}^{\infty} a_n (n+1) \eta^n + \sum_{n=0}^{\infty} \tilde{a}_n (1 + (n+1) \ln \eta) \eta^n + \sum_{n=0}^{\infty} b_{n+1} (n+1) \eta^n, \quad (5.79)$$

(note that  $\tilde{a}_n$  is proportional to  $b_0$ ). We cannot simply take  $\eta = 0$  here since  $\ln \eta \rightarrow \infty$  as  $\eta \rightarrow 0$ . Consider instead the solution at  $y = y_r$ , then,  $|\eta| = |\tilde{c}| \ll 1$  and

$$h'(\eta = \tilde{c}) = a_0 + (1 + \ln \tilde{c}) \tilde{a}_0 + b_1 + \mathcal{O}(\tilde{c}), \quad (5.80)$$

but  $b_1 = 0$ . It is also useful to note that  $h'(\eta) = -\text{sech}^{-2}(y)h'(y)$ . Hence,

$$\begin{aligned} a_0 &\approx -(1 + \ln |\tilde{c}|) \tilde{a}_0 - \frac{\mathbb{R}(h'(y = y_r))}{\text{sech}^2(y_r)}, \\ &\approx -b_0 (1 + \ln |\tilde{c}|) \frac{\beta + 2c_r (1 - c_r^2)}{(1 - c_r^2)^2} - \frac{\mathbb{R}(h'(y = y_r))}{1 - c_r^2}. \end{aligned} \quad (5.81)$$

Hence both  $a_0$  and  $b_0$  (and, in principle, higher orders) can be estimated by evaluating the numerical solution at  $y = y_r$ .

## 5.4 Neutral Modes: QG SWMHD

In §5.2 and §5.3 the analysis proceeds straightforwardly since  $M = 0$  and there is a unique singularity at  $U = c$ . When  $M \neq 0$ , it can be seen by comparison with equation (3.27),

$$(S^2 G')' - [k^2 S^2 - (\tanh y - c)(\beta + cF^2)] G = 0, \quad (5.82)$$

that  $U = c$  is a removable singularity in (3.23) and the pair of points defined by

$$S^2 = (\tanh y - c)^2 - M^2 = 0, \quad (5.83)$$

become singular. Under the transformation

$$y \rightarrow z = \tanh y \quad (5.84)$$

equation (5.82) becomes

$$\begin{aligned} (z - z_+) (z - z_-) \left[ (1 - z^2)^2 G'' - 2z (1 - z^2) G' \right] + 2 (1 - z^2)^2 (z - c) G' \\ - (k^2 (z - z_+) (z - z_-) - (z - c)(\beta + cF^2)) G = 0, \end{aligned} \quad (5.85)$$

where

$$z_{\pm} = c \pm M, \quad (5.86)$$

i.e.

$$S^2 = (z - z_+)(z - z_-). \quad (5.87)$$

We can determine the nature of the two singularities using the method of Frobenius. Substituting

$$G = (z - z_{\pm})^r, \quad (5.88)$$

the lowest order,  $\mathcal{O}\left((z - z_{\pm})^{r-1}\right)$ , coefficient is

$$\begin{aligned} \pm(z_+ - z_-)r(r-1)(1 - z_{\pm}^2)^2 + 2r(1 - z_{\pm}^2)^2(z_{\pm} - c) &= 0, \\ \implies \pm r^2(1 - z_{\pm}^2)(z_+ - z_-) &= 0. \end{aligned} \quad (5.89)$$

Therefore, at both points the eigenfunction is logarithmically singular and, since there are two singular points, these cannot be removed by careful choice of the numerator as in §5.2. In principle, expansions can be derived at both of these points, as in §5.3; however, these will not converge everywhere and will depend on the eigenvalue,  $c$ , which is generally unknown.

## 5.5 Numerical Results

We now search for numerical solutions of the eigenvalue problem (3.27), with  $U(y) = \tanh y$  and  $B(y) = 1$ . This is done by first transforming into a two-dimensional first-order ODE,

$$G' = H, \quad (5.90a)$$

$$H' = (k^2 - C(y))G + D(y)H, \quad (5.90b)$$

where the coefficients  $C$ ,  $D$  are coefficients dependent on  $\beta$ ,  $F^2$ ,  $M^2$ ,

$$C(y) = \frac{(\tanh y - c)(\beta + cF^2)}{(\tanh y - c)^2 - M^2}, \quad (5.91a)$$

$$D(y) = \frac{2 \operatorname{sech}^2(y)(\tanh y - c)}{(\tanh y - c)^2 - M^2}. \quad (5.91b)$$

We then solve using a shooting method (§5.A). The method involves solving a boundary value problem with a pair of initial guesses for the eigenvalue,  $c$ , then using an objective function to improve the estimate. Here, we opt to integrate from both sides of the domain and use the matching condition,

$$G(0^-)H(0^+) - G(0^+)H(0^-) = 0. \quad (5.92)$$

as our objective function. This method depends on several factors including the integration method, the integration domain, and the initial eigenvalue estimates. Particularly, the latter is important since the problem can generally have more than one eigenvalue for any given fixed value of the other parameters. Hence, the choice of the initial values is important, and we employ a mode-tracking algorithm through parameter space to improve the probability of convergence.

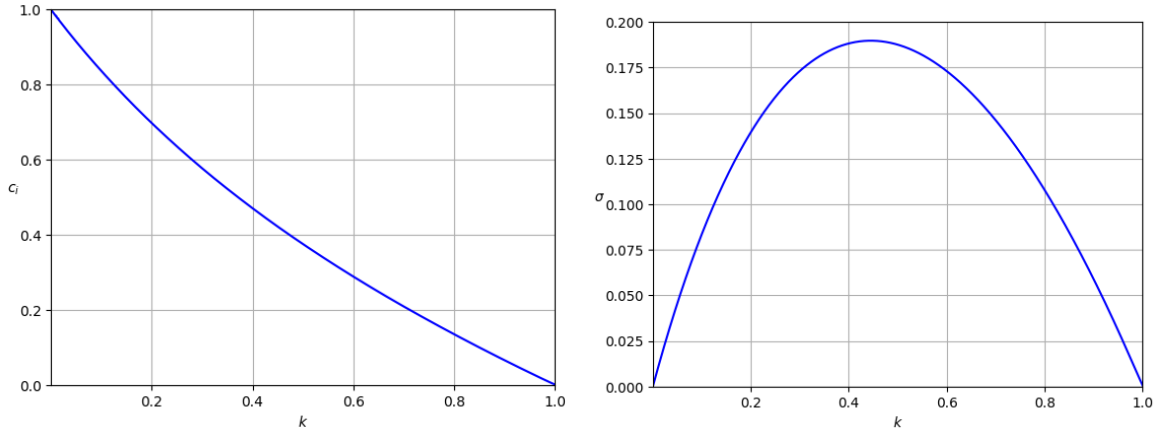


Figure 5.2: Plots of the imaginary part  $c_i = \mathbb{I}(c)$  of the eigenvalue,  $c$ , and the growth rate,  $\sigma = kc_i$  when  $M = \beta = F^2 = 0$ , reproducing the solutions given by Michalke (1964).

### 5.5.1 Verification of Results

The numerical method described above is similar to that of Dickinson and Clare (1973) although we integrate a different differential equation based on  $G$  rather than  $h$  (as in Mak et al., 2016). This helps to deal with the singularities in the differential equation when  $M > 0$  (c.f. §5.4) which become significant as  $k \rightarrow 0$ . It is important to verify this method against the existing results of Michalke (1964) ( $\beta = M = F^2 = 0$ ) and Dickinson and Clare (1973) ( $M = F^2 = 0$ ,  $\beta \neq 0$ ).

First, the case of Michalke (1964) is straightforward since the governing equations possess  $y \rightarrow -y$  and complex conjugate symmetries. This implies that for any eigensolution with eigenvalue  $c$ , there exist additional solutions with eigenvalues  $c^*$ ,  $-c$ , and  $-c^*$ .

If  $c$  is the eigenvalue of an unstable solution ( $\mathbb{I}(c) > 0$ ), then another unstable solution is  $-c^*$ . Combining this with the powerful result of Balmforth and Morrison (1999) (a generalisation of Howard, 1964) that, if there are  $N$  inflexion points (where  $U'' = 0$ ), there can exist at most  $(N + 1)/2$  unstable modes, then since

$$U'' = -\tanh y \operatorname{sech}^2(y) = 0 \implies y = 0, \quad (5.93)$$

the unstable solution must be unique, and therefore

$$c = -c^* \implies \mathbb{R}(c) = 0. \quad (5.94)$$

Thus, we only need to solve for  $c_i := \mathbb{I}(c)$ . Comparison of our method results with Michalke (1964) shows good agreement (Figure 5.2). The imaginary part of the eigenvalue,  $c_i$ , decreases smoothly from  $c_i = 1$ , when  $k = 0$  (Lin, 1945, 's solution) to  $c_i = 0$ , when  $k = 1$  (Drazin and Howard, 1962, 's neutral mode). We can also plot the growth rate,  $\sigma = kc_i$ , and find, in agreement with Michalke (1964), that the growth rate is maximised when  $k = 0.446$ .

Allowing  $\beta > 0$ , or equivalently, including rotation in the problem leads to the problem introduced by Kuo (1949) and tackled numerically by Dickinson and Clare (1973). In Figure

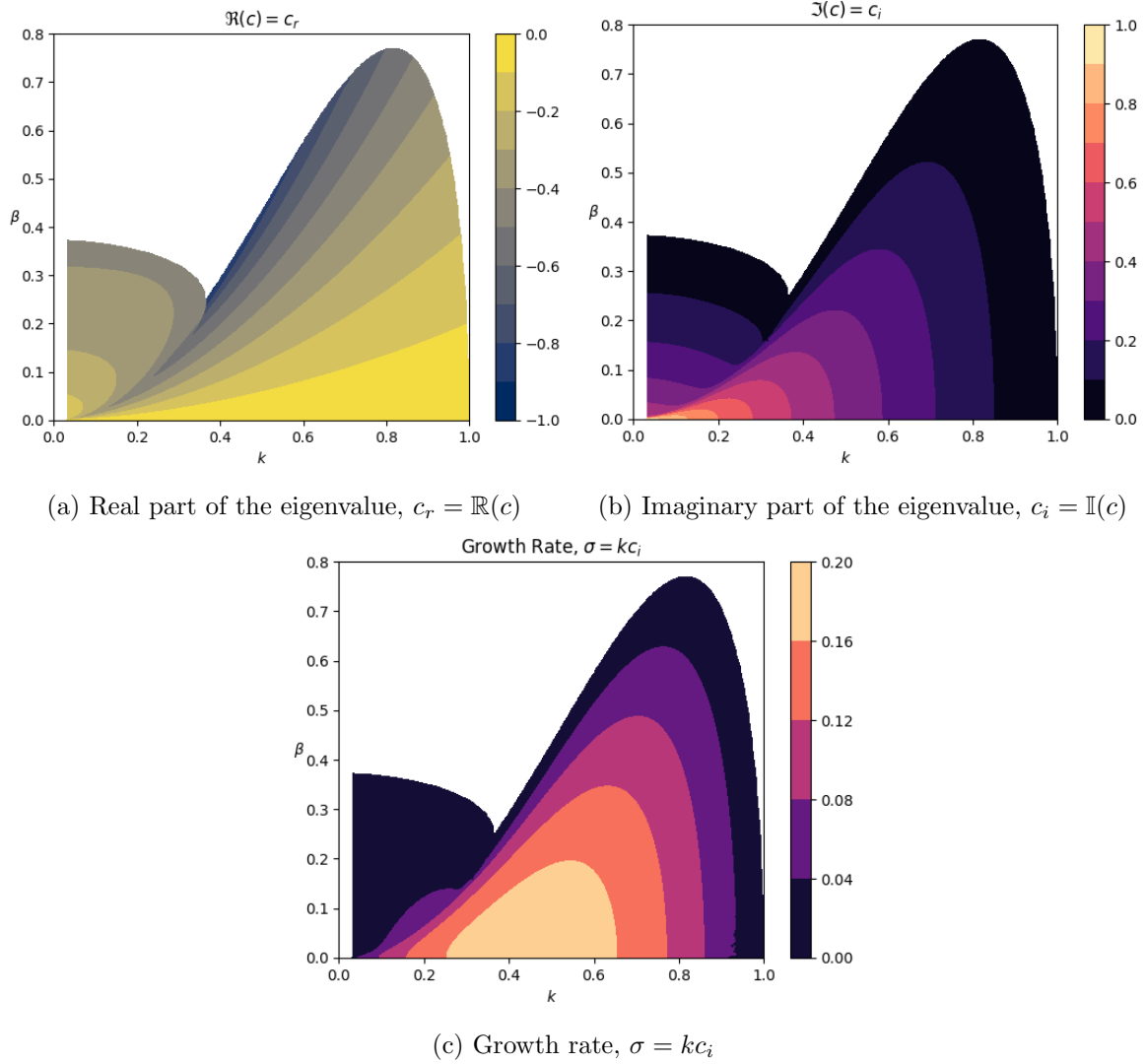


Figure 5.3: Plots of the real  $c_r = \Re(c)$  and imaginary parts  $c_i = \Im(c)$  of the eigenvalue,  $c$ , and the growth rate,  $\sigma = kc_i$  when  $M = F^2 = 0$ , mirroring the solutions given by Dickinson and Clare (1973).

5.3 we have recreated the results of Dickinson and Clare (1973). The  $\beta = 0$  case, discussed above, lies on the  $x$ -axis of the above plot. As we showed previously along this axis the real part of the eigenvalue,  $\Re(c) = c_r$ , must be identically zero. For positive  $\beta$  the phase speed ( $c_r$ ) is negative and decreases as  $\beta$  increases. Across most of the parameter space, the contours of  $c_r$  align with curves of fixed  $\beta/k^2$  (Figure 5.3a). These properties align with the interpretation of the unstable modes as unstable (counter-propagating) Rossby (1939) waves whose neutral phase speed is  $c_r = \beta/k^2$ .

The exception to this description is the region in the bottom-left of the parameter space which can be most clearly distinguished on the  $c_r$  plot (see also §5.6). This is the radiating mode predicted by Howard and Drazin (1964) and denoted the *radiating* mode hereafter. As can be seen in Figure 5.3c, the growth rate of this mode is generally small relative to the *trapped* mode so its physical relevance has been questioned however Dickinson and Clare (1973) have suggested that it might become dominant when the initial noise is inhomogeneous. This is not a case that we will consider here, however, we will return to discuss this mode in §5.5.3 when a new case arises in which this mode may become dominant. We will focus on the radiating mode and the boundary region between the two modes in §5.6.

Instability (when  $M = F^2 = 0$ ) requires  $\beta - U'' = 0$  somewhere (Kuo, 1949). Since  $U''$  has a maximum (and minimum) a necessary (inflexion point) condition for instability is that

$$\beta < \frac{4}{3\sqrt{3}} \approx 0.7698. \quad (5.95)$$

Additionally, Howard and Drazin (1964) showed that the neutral mode which we derived in §5.2 is contiguous to an unstable mode with smaller  $\beta$  which Dickinson and Clare (1973) showed to be the trapped mode. It can be seen (Figure 5.3b) that this also represents a stability criterion. The neutral mode reaches the line  $\beta = 4/3\sqrt{3}$  when

$$k = \sqrt{2/3} \approx 0.8165. \quad (5.96)$$

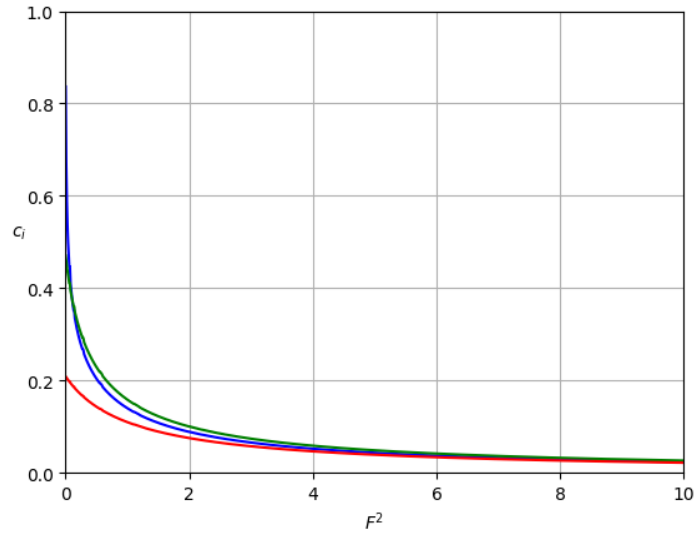
The boundary of the radiating mode cannot be calculated analytically and may lie at the line  $\beta = 4/3\sqrt{3}$ . This is suggested by the results of Talley (1983) who investigates this radiating mode using a profile with regions of constant vorticity, suggested by Dickinson and Clare (1973). Approaching this limit numerically is challenging due to properties of the eigenfunction (discussed in §5.8) and even if it is the case that the radiating mode is present for larger  $\beta$  than is presented in Figure 5.3, the growth rate will be exponentially small.

### 5.5.2 Variation with $F^2$

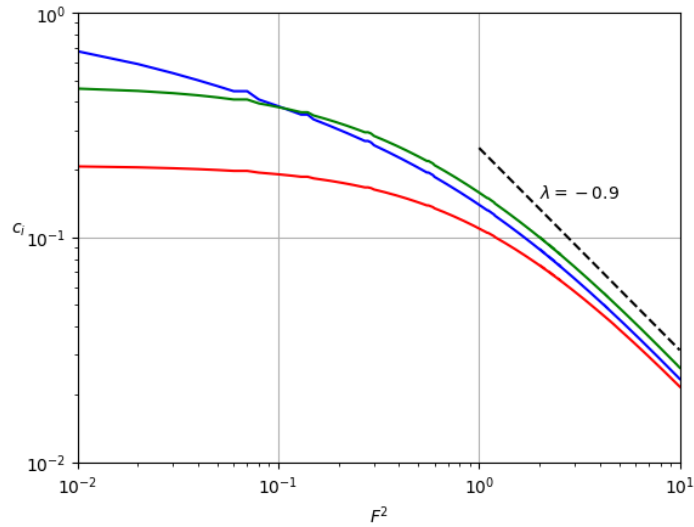
When  $F^2 > 0$  and  $\beta = M = 0$  the equations of motion represent a quasi-geostrophic shallow-water f-plane system, in this case, the necessary (inflexion point) condition for instability, that

$$F^2 U - U'' = \tanh y (F^2 + 2 \operatorname{sech}^2(y)) = 0, \quad (5.97)$$

for some  $y \in \mathbb{R}$ , is always satisfied hence there is no a priori reason to expect that increasing  $F^2$  should lead to stability (across all values of  $k$ ). Figure 5.4 shows that  $c_i$  approaches zero algebraically with dependence  $c_i \sim (F^2)^\lambda$ ,  $\lambda \approx -0.90$ , as  $F^2 \rightarrow \infty$ . The reason for this



(a) Linear axis scales.



(b) Logarithmic axis scales.

Figure 5.4: Plots of the imaginary part of the eigenvalue,  $\mathbb{I}(c) = c_i$  for varied  $F^2$  with  $k = 0.1$  (blue) and  $k = 0.4$  (green). The upper plot is scaled linearly, whilst the lower plot is scaled logarithmically to highlight the large  $F^2$  variation of  $c$ .

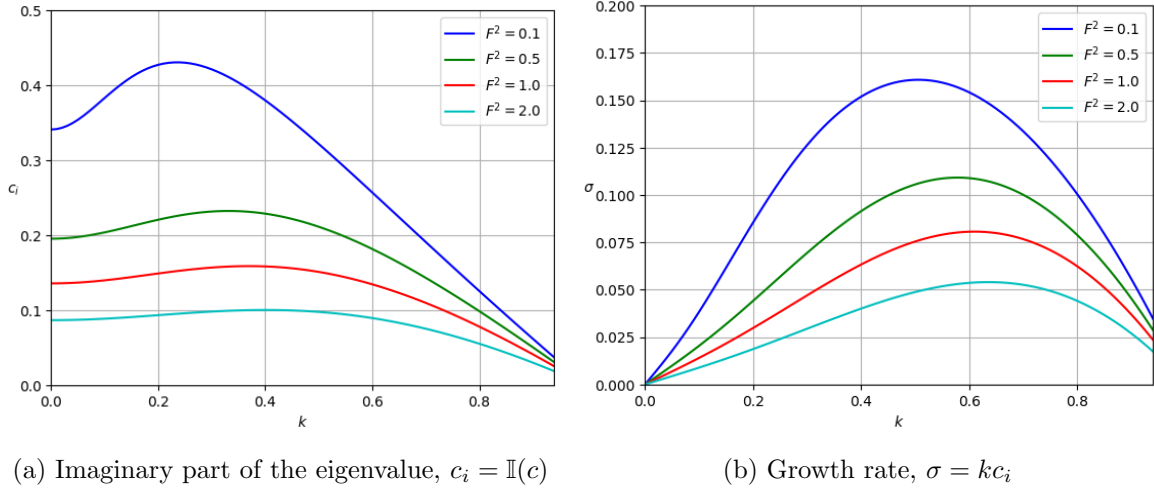


Figure 5.5: Plots of the imaginary part of the eigenvalue,  $\mathbb{I}(c) = c_i$  for varied  $k$  with  $F^2 = 0.1$  (blue),  $F^2 = 0.5$  (green),  $F^2 = 1.0$  (red), and  $F^2 = 2.0$  (cyan).

particular asymptotic dependence is unclear.

In the  $F^2 \rightarrow 0$  limit (Figure 5.2)  $c_i$  decreases monotonically with  $k$ . In Figure 5.4 this is no longer true for large  $F^2$ . Figure 5.5a, which shows the variation of  $c_i$  with  $k$  for a range of values of  $F^2$ , reveals that modes with small  $k$  are disproportionately stabilised relative to modes with larger  $k$ . The impact on the growth rate (Figure 5.5b) is that the wavenumber of maximal instability increases as  $F^2$  does. We revisit this in §5.7.

With  $\beta > 0$ , we are now considering a  $\beta$ -plane quasi-geostrophic shallow-water regime, and the two instability modes are reintroduced. The over-reflected mode does not appear when  $\beta = 0$  since the underlying vorticity gradient is symmetric about  $y = 0$ .

The neutral mode, discussed in §5.2, lies on the curve

$$\beta = (2k^2 + F^2) (1 - k^2)^{1/2}. \quad (5.98)$$

This curve is plotted as a yellow dashed line in Figure 5.6. The unstable mode contour lies at  $c_i = 10^{-3}$  so there is a small gap between the neutral mode and the unstable modes but they are otherwise similar. On the left side of the domain ( $k \lesssim 0.4$ ) the radiating rather than the trapped mode is shown since this generally has a larger growth rate. Over all  $k$ , however, the trapped mode remains the dominant (fastest growing) mode.

### 5.5.3 Variation with M

We saw in §3.6 that, provided  $\beta = 0$ ,  $M^2 B^2(y) > U^2(y)$  everywhere is sufficient to guarantee stability. If  $B$  is constant and  $U = \tanh y$  then this criterion becomes

$$M^2 > 1. \quad (5.99)$$

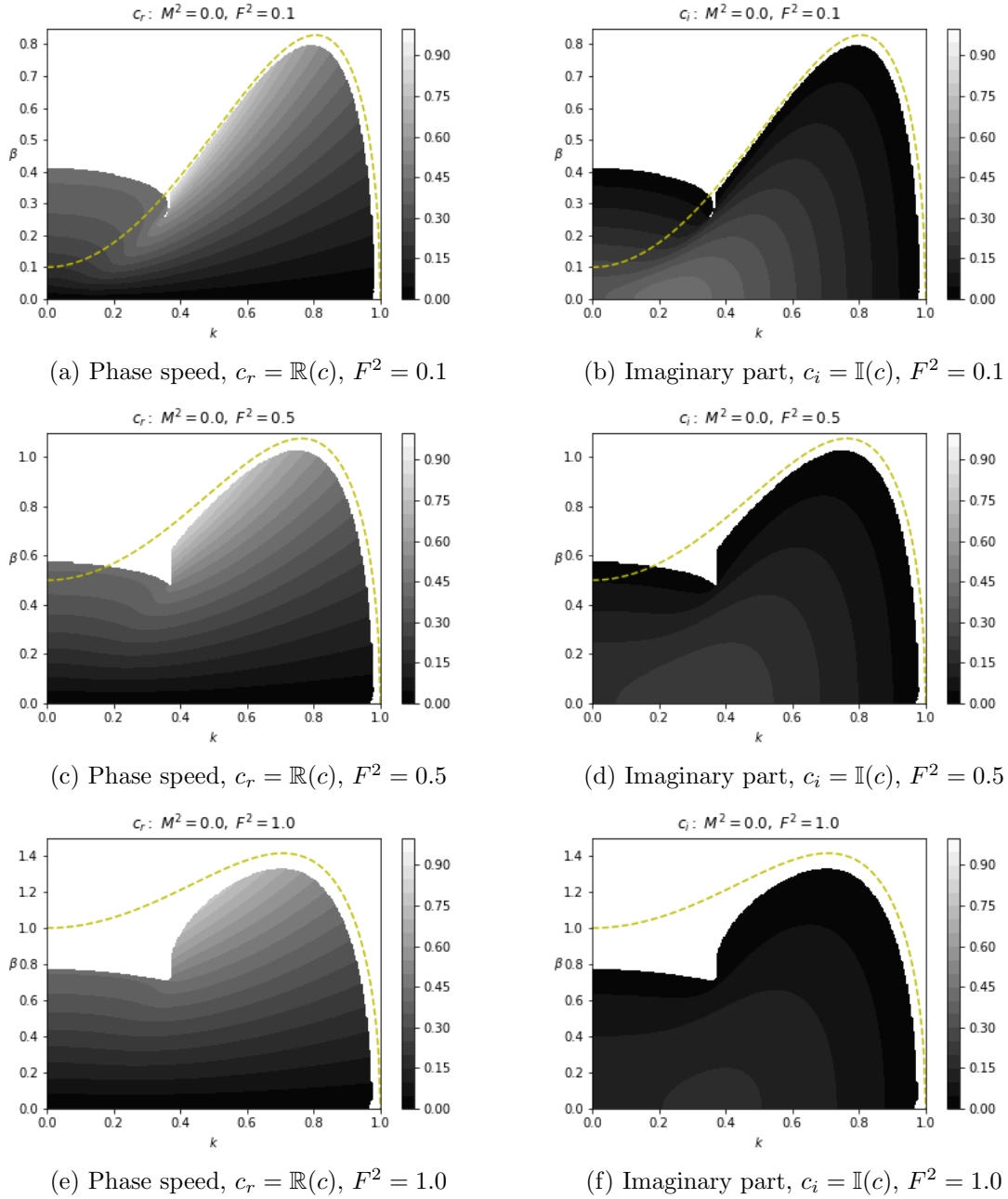


Figure 5.6: Contour plots of the real and imaginary parts of the eigenvalue,  $c$ , in  $(\beta, k)$  space for  $F^2 = 0.1, 0.5, 1.0$ . Overlaid is the neutral mode curve found in §5.2. The jump at around  $k = 0.4$  is due to the mode tracking algorithm switching between the trapped and radiating modes. For small  $c_i$ , close to the neutral mode, the shooting method struggles to converge to an eigenvalue due to singularities in the dispersion relation.

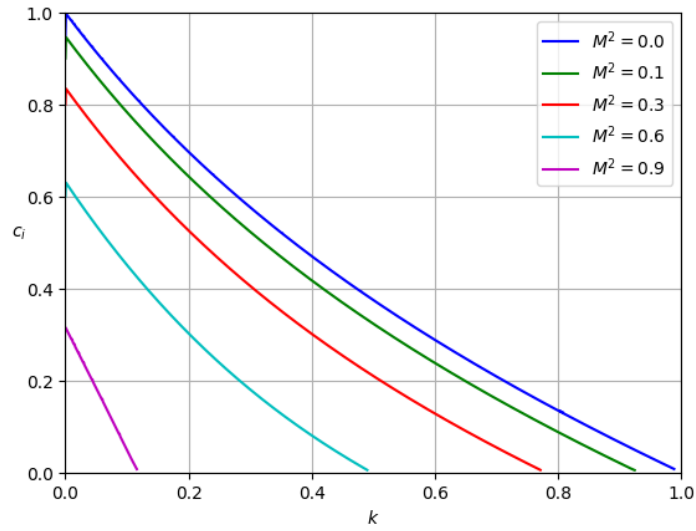
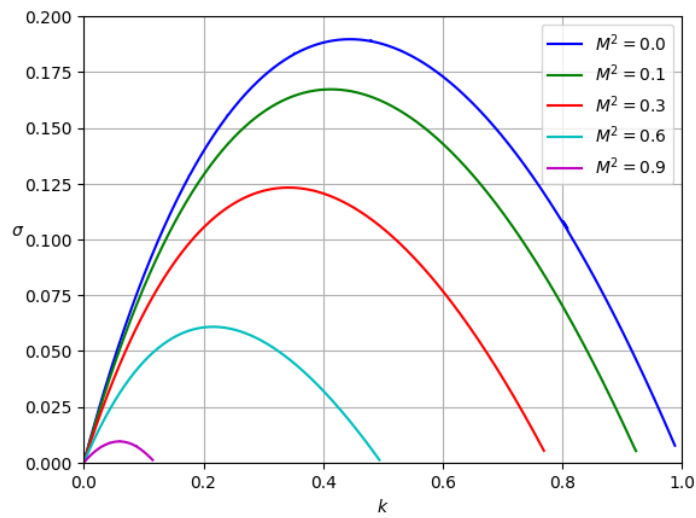
(a) Imaginary part of the eigenvalue,  $c_i = \mathbb{I}(c)$ (b) Growth rate,  $\sigma = kc_i$ 

Figure 5.7: Plots of the imaginary part of the eigenvalue,  $\mathbb{I}(c) = c_i$  for varied  $k$  with  $M^2 = 0.0$  (blue),  $M^2 = 0.1$  (green),  $M^2 = 0.3$  (red),  $M^2 = 0.6$  (cyan), and  $M^2 = 0.9$  (purple).

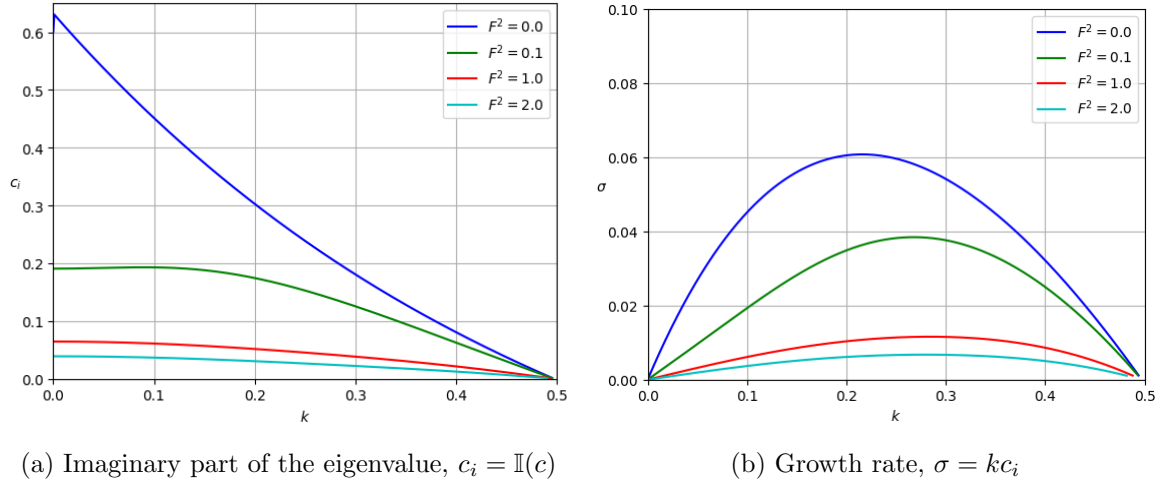


Figure 5.8: Imaginary part of the eigenvalue,  $c_i = \mathbb{I}(c)$ , and the growth rate,  $\sigma = kc_i$ , with varied  $k$  for a case with moderate magnetic field  $M^2 = 0.6$ ,  $\beta = 0$  and several values of  $F^2$ .

For  $M^2 < 1$ , the growth rate is reduced relative to the hydrodynamic,  $M = 0$ , case due to the effects of magnetic tension (Figure 5.7). Here, the magnetic field is always stabilising, because it is constant, however cases have been found, e.g. Ray and Ershkovich (1983), where the presence of a small magnetic field can destabilise an otherwise stable profile. This generally requires a non-constant field profile which can, via the current,  $\mathbf{j} = \nabla \times \mathbf{b}$ , provide a source of vorticity. This can also be seen in the growth rate bound, (3.18), which is the tightest when  $B'$  is zero everywhere.

Figure 5.7 also shows that shorter wavelength (larger wavenumber,  $k$ ) modes are affected more by the presence of a magnetic field with some previously unstable modes ( $k \lesssim 1$ ) sometimes becoming stable. This arises naturally from the interpretation of magnetic tension. The shorter wavelength modes are more curved and so feel the effect of magnetic tension more strongly. An important and natural consequence of this is that the critical wavenumber (that maximises the growth rate,  $\sigma$ ) is reduced as  $M$  increases.

When  $F^2 > 0$  and  $M > 0$ , the trend from each case largely applies independently (Figure 5.8). Increasing  $F^2$  dampens long wavelength modes whilst increasing  $M^2$  predominantly affects smaller wavelength modes. Increasing  $F^2$ , even with non-zero  $M^2$ , does not stabilise any previously unstable modes.

With  $\beta > 0$  and  $M > 0$  (for simplicity,  $F^2 = 0$ ) the situation is complicated by the presence of both the trapped and radiating modes. Figure 5.9 shows a rough pass over the  $(\beta, k)$  parameter space for three values of  $M^2 = 0.1, 0.5, 0.8$ . As we saw when  $\beta = 0$ , whilst the growth rate of modes of any wavenumber is reduced by the magnetic field, shorter wavelength modes are affected more. When  $\beta > 0$  this means that the radiating (over-reflected) mode can become more unstable than the trapped mode at a fixed value of  $\beta$  (across  $k$ ) (e.g. Figure 5.9d). For larger  $M \lesssim 1$ , there are values of  $\beta$  for which only the radiating mode is unstable (Figure 5.9f). We will investigate the radiating mode in more detail in §5.6.

Another interesting feature of Figure 5.9 is that the boundary of the trapped mode becomes

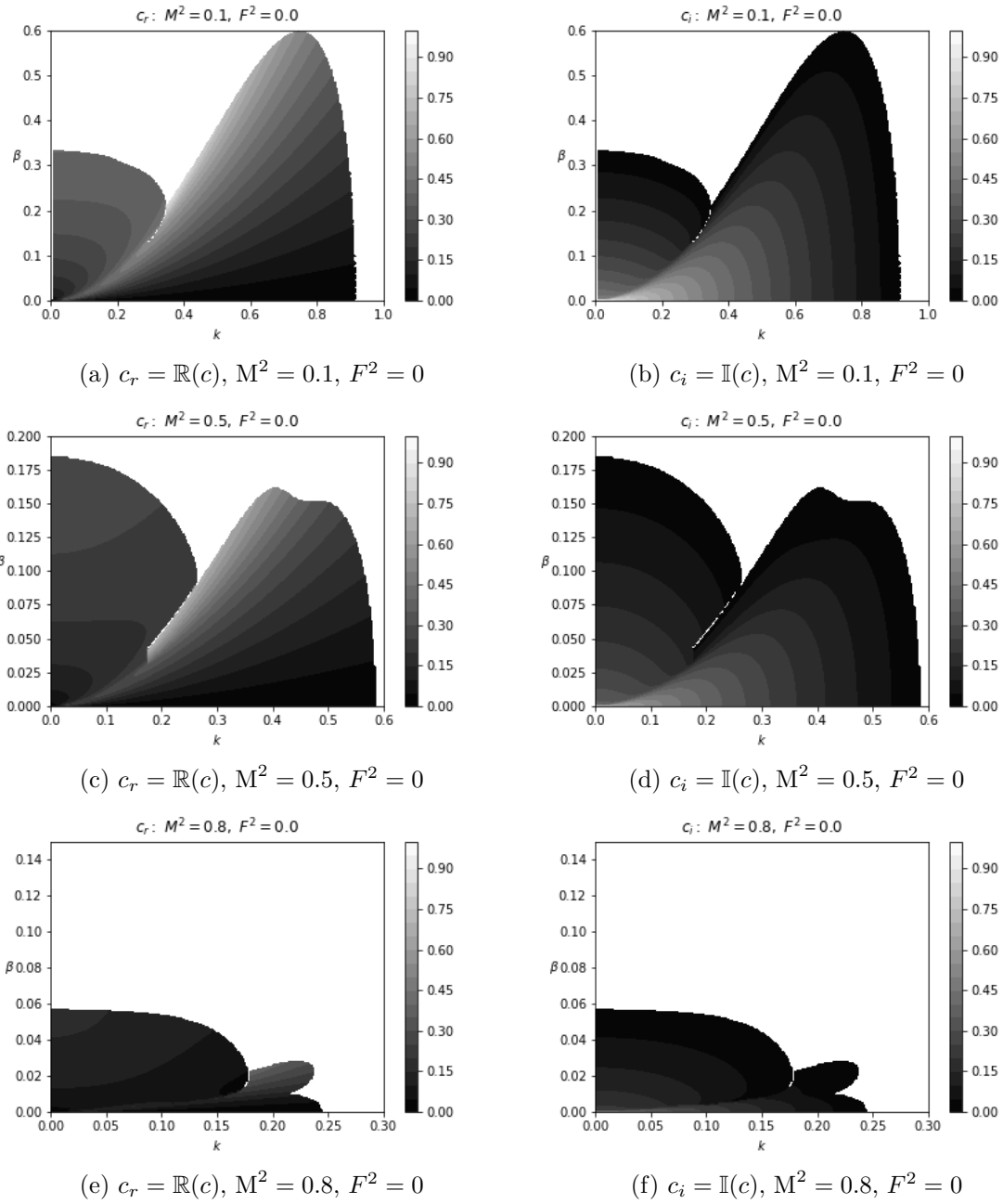


Figure 5.9: Contour plots of the real and imaginary parts of the eigenvalue across a range of  $\beta$ ,  $k$ , selected values of  $M$ , and  $F^2 = 0$ . Compare with the case  $M = 0$  in Figure 5.3. White regions show where  $c_i < 10^{-3}$ , or where the shooting method has failed to converge, particularly when two unstable modes co-exist.

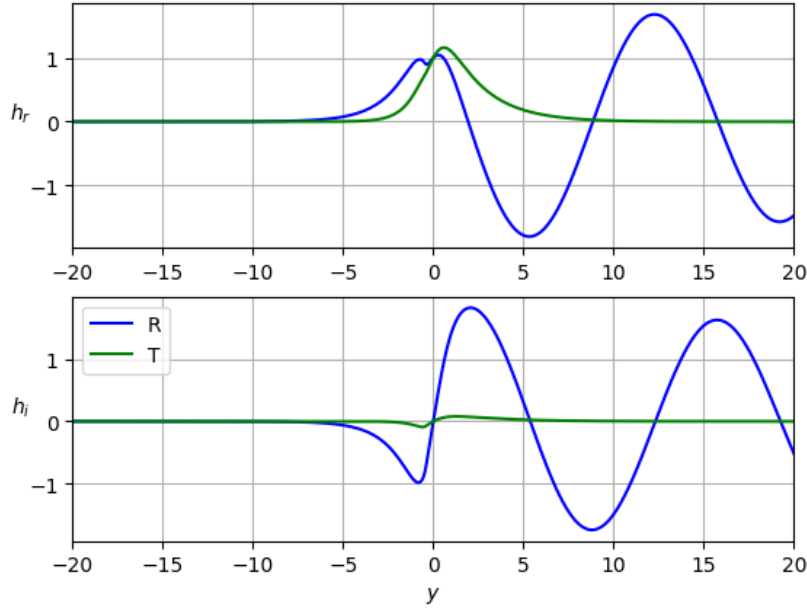


Figure 5.10: Plot of the radiating eigenfunction (blue) at  $\beta = 0.3$ ,  $k = 0.1$  ( $c \approx -0.394 + 0.058i$ ,  $\alpha_+ = -0.010 + 0.453i$ ) and the trapped eigenfunction (green) at  $\beta = 0.6$ ,  $k = 0.8$  ( $c \approx -0.458 + 0.055i$ ,  $\alpha_+ = -0.479 + 0.016i$ ). The eigenfunctions are integrated in the normal way (§5.A) and then normalised so that  $h(y = 0) = 1$ .

non-smooth, with an indent forming when  $M^2 = 0.5$  (Figure 5.9d), which turns into a cusp when  $M^2 = 0.8$  (Figure 5.9f). It is unclear what causes this, but we conjecture that it may be related to the two solutions of (5.10) (strictly (5.10) has three solutions, however only two are relevant to the neutral mode problem) which merge when  $M = 0$  but may have distinct characteristics when  $M > 0$ .

## 5.6 Existence of Multiple Modes

In section §5.5, we introduced the *trapped* and *radiating* modes. Dickinson and Clare (1973) were the first to distinguish these two modes, using a tanh profile and the  $\beta$ -plane equations (e.g. Figure 5.3). Howard and Drazin (1964) though had previously hypothesised the existence of both modes based on a long wavelength asymptotic expansion ( $k \rightarrow 0$ ), which suggested the existence of a mode that was not contiguous with the neutral mode of Lipps (1962, 1965). Talley (1983) then investigated an interesting profile,

$$U(y) = \begin{cases} \frac{\beta}{2}(y^2 - 1) + y, & |y| < 1, \\ \frac{y}{|y|}, & |y| > 1, \end{cases} \quad (5.100)$$

which approximates the tanh profile but has analytic solutions since  $\beta - U''$  is zero everywhere, except at interfaces, where matching conditions must be employed. This problem has at most one unstable solution for a given choice of  $(\beta, k)$ , however, the domain is divided into two regions in which the solutions have distinct characteristics. Talley (1983) linked these regions

with the two solutions of the  $U(y) = \tanh y$  profile and introduced the terms radiating and trapped to distinguish the two modes based on the form of their eigenfunctions (e.g. Figure 5.10).

In this section, we will review the distinctions between the two modes and then see how including shallow-water and magnetic effects ( $F^2$  and  $M^2$ ) changes the established picture.

### 5.6.1 The Trapped Mode

The trapped mode is named for its eigenfunction; it is localised to the shear layer, decaying quickly as  $|y| \rightarrow \infty$  (Figure 5.10). It is the unique unstable mode when  $\beta = 0$ , and is unstable (with  $U = \tanh y$ ) for a range of wavenumbers ( $k \in (0, 1)$  when  $M = 0$ ) bounded at either end by neutral modes that can be written down when  $M = 0$  (c.f. §5.2). As  $\beta$  is increased this mode stabilises and the range of wavenumbers over which it exists decreases (Figure 5.3). It can be intuitively described by counter-propagating Rossby waves (e.g. Bretherton, 1966; Heifetz et al., 1999; Heifetz and Mak, 2014; Heifetz et al., 2015).

A minimal requirement for instability is that regions exist with opposing vorticity gradients and flow directions (Fjørtoft's criterion). In these conditions, vorticity (Rossby) waves can interact to lock each other in phase and induce instability. The strength of this interaction decays with the wavenumber,  $k$ , and the distance between the levels at which these waves are generated (Heifetz et al., 1999). This means that there is a short-wave cut-off (stabilisation at large  $k$ ) for smooth profiles, but not when the interaction distance is infinitesimally small, as in the vortex sheet problem (§4).

The shear flow (relative) vorticity gradient is

$$U'' = -2 \tanh(y) \operatorname{sech}^2(y). \quad (5.101)$$

In the  $\beta$ -plane approximation, the total vorticity gradient ( $\beta - U''$ ) is increased by a uniform amount (proportional to  $\beta$ ) so the region of negative vorticity decreases. The areas with opposite flow speeds and vorticity gradients become separated by an intermediate region thus reducing the strength of interaction between the counter-propagating Rossby waves (CRWs), which can only constructively interact under those conditions. This predominantly affects modes with smaller wavenumbers, but also monotonically stabilises the trapped mode, reducing the range of unstable wavenumbers.

Magnetic field profiles with  $B' \neq 0$  can provide a source of vorticity and allow instability in shear profiles which would otherwise be stable (Heifetz et al., 2015; Wang et al., 2022). When the magnetic field is uniform ( $B' = 0$ ,  $M > 0$ ), as it is here, the magnetic field provides tension and monotonically weakens instability. Magnetic tension is stronger for modes with larger wavenumbers (shorter wavelengths), so the trapped mode is more strongly affected by (a zonal) magnetic field. Additionally, when  $\beta > 0$  and instability is shifted towards larger wavenumbers, the impact of the magnetic field is even greater and this mode stabilises at smaller values of  $M$  (equivalently, it stabilises at smaller values of  $\beta$  as  $M$  is increased).

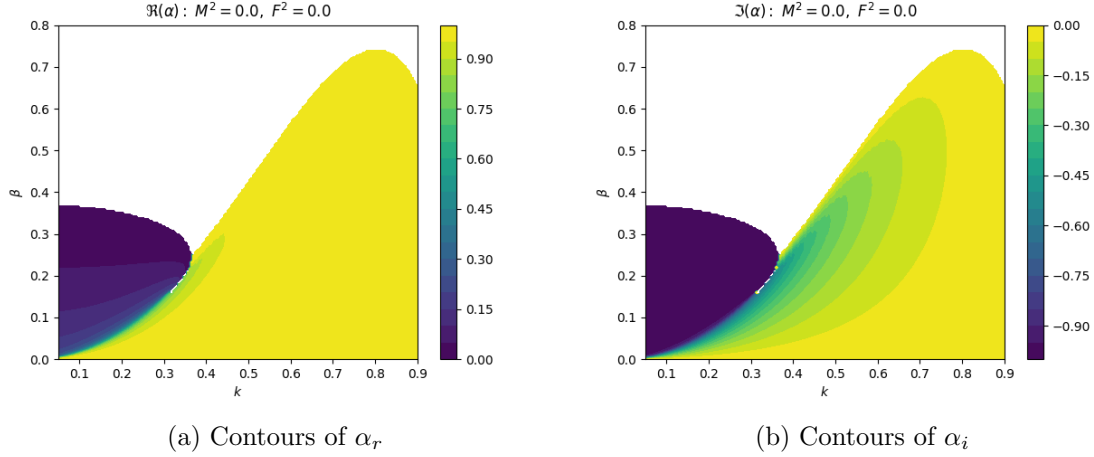


Figure 5.11: Contours of  $\alpha_r$  and  $\alpha_i$  (c.f. (5.104)) calculated from the numerically obtained eigenvalues,  $c(k; \beta, M, F^2)$ . Here with  $M = F^2 = 0$ . Note the different scales on the two plots.

### 5.6.2 The Radiating Mode

The radiating mode has an oscillatory eigenfunction and slowly decays as  $y \rightarrow \infty$ , particularly on the shear layer's northern side ( $y > 0$ ). It appears that a Rossby wave travelling on the vorticity gradient on the north side of the shear layer interacts with the shear and is not simply reflected, but over-reflected, resulting in exponential instability. Lindzen (1988) showed that this mechanism could be formalised. Lindzen and Barker (1985) considered the same system as an initial value problem with an incident wave and demonstrated the evolution of over-reflection on a shear layer.

Heifetz et al. (2015) have shown that over-reflection can be generally described by a CRW mechanism, which may settle the long-standing debate over the fundamental mechanism for instability. Despite this, we suggest that over-reflection may be a more natural lens for examining radiating-type instability since it can elucidate some important features.

### 5.6.3 Radiating vs Trapped

In section §5.8.1 we compare eigenfunctions of the two kinds and show that the radiating mode decays slowly as  $y \rightarrow +\infty$ , whilst the trapped mode is constrained to the shear layer, decaying rapidly as  $|y| \rightarrow \infty$ . The difference between the decay rates is even clearer when one considers (3.23) in the limit  $y \rightarrow \pm\infty$ ,  $U \rightarrow \pm 1$ . Substituting for  $U = \pm 1$ , the governing equation becomes a second-order constant coefficient ODE and can be solved by simple exponential functions. In particular,

$$G = \begin{cases} e^{-\alpha y}, & y > 0, \\ e^{+\alpha y}, & y < 0, \end{cases} \quad (5.102)$$

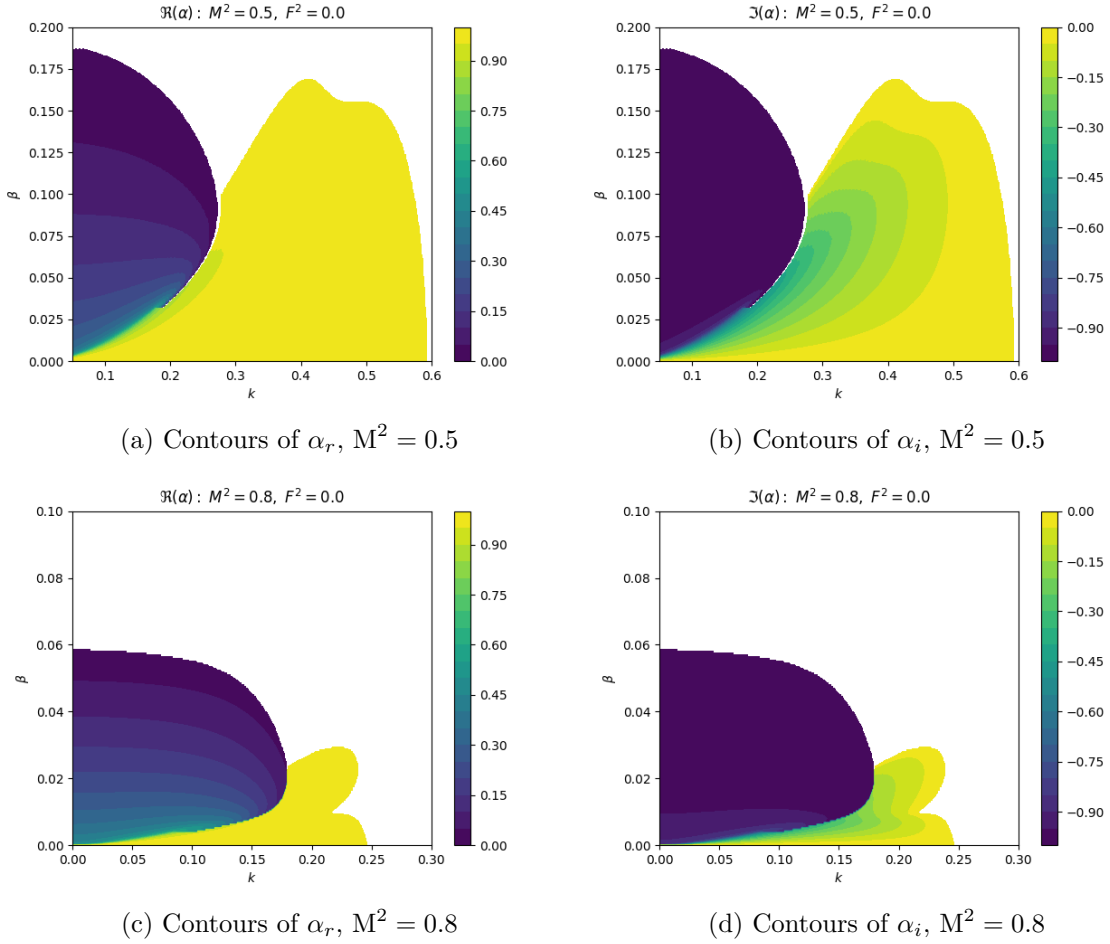
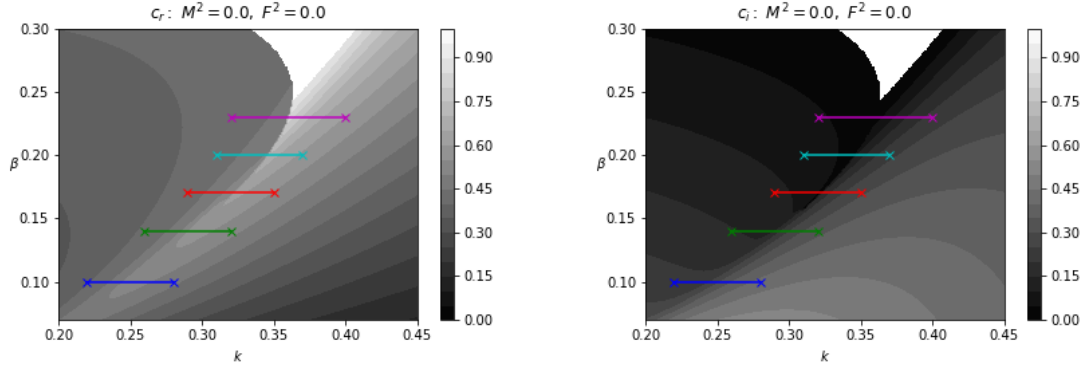


Figure 5.12: Contours of  $\alpha_r$  and  $\alpha_i$  (c.f. (5.104)) calculated from the numerically obtained eigenvalues,  $c(k; \beta, M, F^2)$ . Here with  $F^2 = 0$  and  $M^2 = 0.5, 0.8$ . Note the different scales on the four plots.



(a) Size of the real part of the eigenvalue,  $|c_r|$ . (b) Imaginary part of the eigenvalue,  $c_i$ .

Figure 5.13: Contour plots of  $c_r$  and  $c_i$  across varied  $\beta$  and  $k$  showing lines (parameterised by  $k$ ) over which the dominant mode of instability switches from the radiating to the trapped mode. The two unstable eigenvalues, along these curves, are shown in Figure 5.14 with corresponding colours. ( $M = F^2 = 0$ )

where  $\alpha_{\pm}$  is defined by the root of

$$\alpha_{\pm}^2 = k^2 + \frac{(c \mp 1)(\beta + cF^2)}{(c \mp 1)^2 - M^2} \quad (5.103)$$

with a positive real part. This choice is always possible provided  $\alpha_{\pm}^2$  is not negative real, which is itself guaranteed when  $c_i > 0$ . We first defined  $\alpha_{\pm}$  in §4.2, where the governing equation takes the same form since the flow is uniform ( $U = \pm 1$ ) on either side of an interface.

As we have discussed, the radiating mode oscillates on the north side of the shear layer ( $y > 0$ ), therefore  $\alpha_+$  seems to be the more important term. Defining the normalised real and imaginary parts of  $\alpha_+$  as

$$\alpha_r = \frac{\Re(\alpha_+)}{|\alpha_+|}, \quad \alpha_i = \frac{\Im(\alpha_+)}{|\alpha_+|}, \quad (5.104)$$

we can calculate  $\alpha_r$ ,  $\alpha_i$  straightforwardly using the eigenvalues,  $c(k; \beta, M, F^2)$ , calculated in Figures 5.3 and 5.9.

The exponential coefficients,  $\alpha_r$  and  $\alpha_i$ , are plotted in Figure 5.11 for the case  $M = 0$ . This shows the dominance of the imaginary (oscillatory) component of  $\alpha_+$  for the radiating mode, whilst the trapped mode rapidly decays, with  $\alpha$  almost entirely real. Unsurprisingly, this trend continues with  $M > 0$  (Figure 5.12).

#### 5.6.4 Overlap Region

So far, we have treated the radiating and trapped modes as distinct modes. Figures 5.11 and 5.12 show that the traits of the two modes begin to merge as their values of  $\beta$  and  $k$  come together. To investigate further we fix values of  $\beta$  and vary  $k$  starting from a point where only the radiating mode is unstable and increasing  $k$ , through the exchange of stability, to a point where only the trapped mode is unstable.

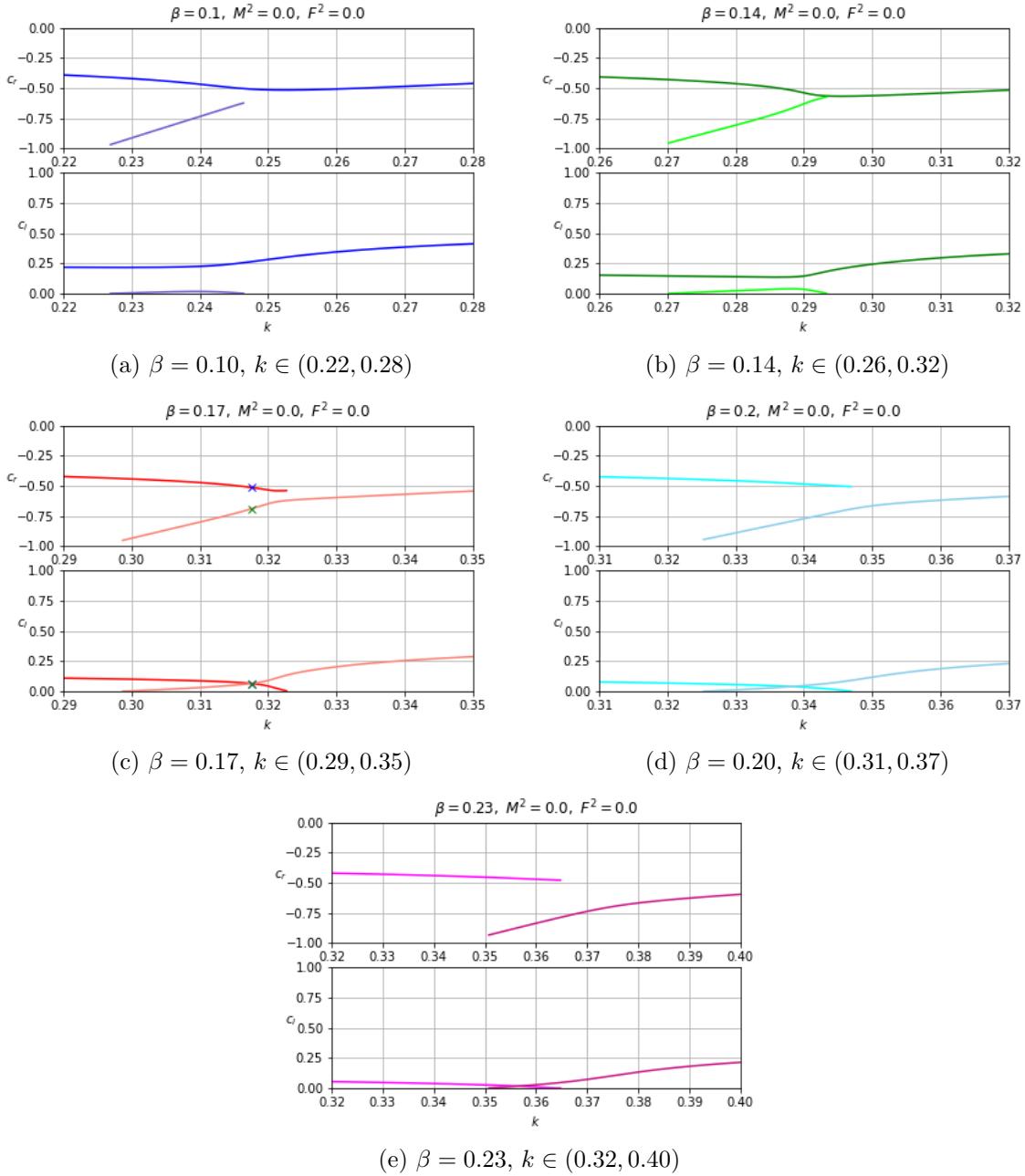


Figure 5.14: Plots of the eigenvalue,  $c$ , showing all unstable modes for particular fixed values of  $\beta$  and varied  $k$  ( $M = F^2 = 0$ ) given in Figure 5.13. The crosses on Figure 5.14c correspond to the eigenfunctions shown in Figure 5.15.

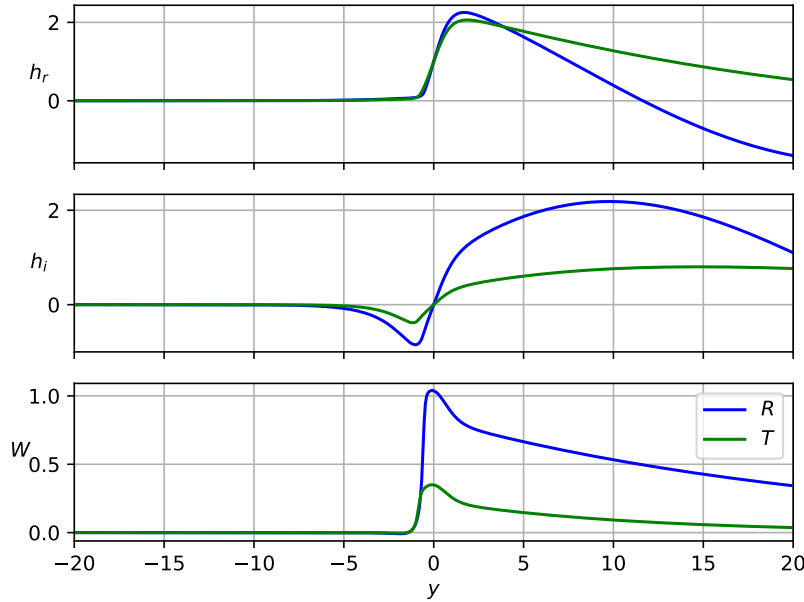


Figure 5.15: Plots of the real and imaginary parts of eigenfunctions for  $\beta = 0.17$ ,  $k = 0.316$ , ( $M = F^2 = 0$ ) close to the exchange of dominance, normalised so that  $h(0) = 1$ . These correspond to the points on Figure 5.14c. The Wronskian,  $W(y)$ , is defined in equation (5.107).

For each value of  $\beta$  we can calculate, using the neutral mode in §5.2, the value of  $k$  and  $c_r$  at which the trapped mode becomes unstable. The neutral mode lies on the curve

$$\beta = 2k^2 (1 - k^2)^{1/2}, \quad (5.105)$$

when  $F^2 = M = 0$ . The eigenvalue is then given by  $c = k^2 - 1$ . These can be calculated analytically and are shown in Table 5.1. The numerical solutions in Figure 5.14 agree well with the analytic values with the analytic neutral mode corresponding to the limit, as  $k$  decreases, with  $c_i \rightarrow 0$ ; i.e. the unstable mode always lies on the larger  $k$  side of the neutral mode (as established by Lipps, 1965).

As discussed by Dickinson and Clare (1973), two configurations are possible when the two

$\beta$	$k$	$c$
0.10	0.2266	-0.9487
0.14	0.2696	-0.9273
0.17	0.2984	-0.9109
0.20	0.3252	-0.8943
0.23	0.3504	-0.8772

Table 5.1: Values of the wavenumber,  $k$ , and eigenvalue,  $c$ , on the neutral mode at specific value of  $\beta$  used in Figure 5.14.

modes overlap in parameter space. For smaller  $\beta$ , e.g. Figures 5.14a and 5.14b, we see that the analytic neutral mode is contiguous with an unstable mode which quickly re-stabilises as  $k$  is increased. At larger values of  $\beta$ , e.g. Figures 5.14c, 5.14d, and 5.14e, the analytic neutral mode instead transforms into the unstable trapped mode.

## 5.7 Mode of Maximum Growth

It is important to establish the most unstable mode (largest  $\sigma = kc_i$ ) in any linear instability problem since its eigenfunction can often predict the structure of an unstable system at the onset of the nonlinear phase when outside forcing is minimal.

For the vortex sheet profile (§4), all modes  $k > 0$  are unstable, and modes with increasingly large wavenumber,  $k$ , are increasingly unstable, which can present a modelling problem. This cascade failure can be arrested by including viscous effects or, as in this chapter, by smoothing the shear, thereby introducing a finite interaction distance between CRWs and introducing a large  $k$  cutoff after which there are no unstable modes. In particular, this means that provided the profile is unstable there exists a wavenumber  $k = k_{max}$  which maximises the growth rate  $\sigma = \sigma_{max}$ .

When  $\beta = 0$  only a single local maximum exists, which must also be the global maximum. When  $M = F^2 = 0$  also, Michalke (1964) find this maximum to be

$$k_{max}(M = 0, \beta = 0, F^2 = 0) = 0.4446, \quad \sigma_{max} = 0.1898 \quad (5.106)$$

(note that Michalke (1964) use a slightly different shear profile,  $U(y) = (1 + \tanh y)/2$ , leading to  $\sigma_{max} = 0.0949$ , however this can easily be transformed to  $U(y) = \tanh y$ ; the transformed growth rate is given above).

### 5.7.1 Variation with $\beta$

As discussed in the previous section (§5.6), introducing  $\beta > 0$  leads to an additional mode, the radiating mode, on top of the trapped mode; this introduces a second local growth rate maximum at smaller  $k$ . The radiating mode generally stabilises at moderate  $k$ ; therefore,  $\sigma = kc_i$  can rarely grow significantly large (Figure 5.16). This means firstly that the most unstable mode (at least when  $F^2 = M = 0$ ) is the trapped mode, and secondly, that the wavenumber of maximum growth (WoMG) depends smoothly on  $\beta$  (Figure 5.17).

Increasing  $\beta$  monotonically stabilises all wavenumbers however small wavenumber modes tend to be affected the most since their mutual interaction is most affected by the distance increase between CRWs (e.g. Heifetz et al., 1999). This leads to a steady rise in the WoMG as  $\beta$  increases (Figure 5.17).

### 5.7.2 Variation with $M$

Increasing the magnetic field strength,  $M$ , also monotonically stabilises all wavenumbers since magnetic tension acts against the destabilising forces. This has a greater effect on modes with larger wavenumbers (shorter wavelength) hence the wavenumber of maximal instability steadily decreases as  $M$  increases.

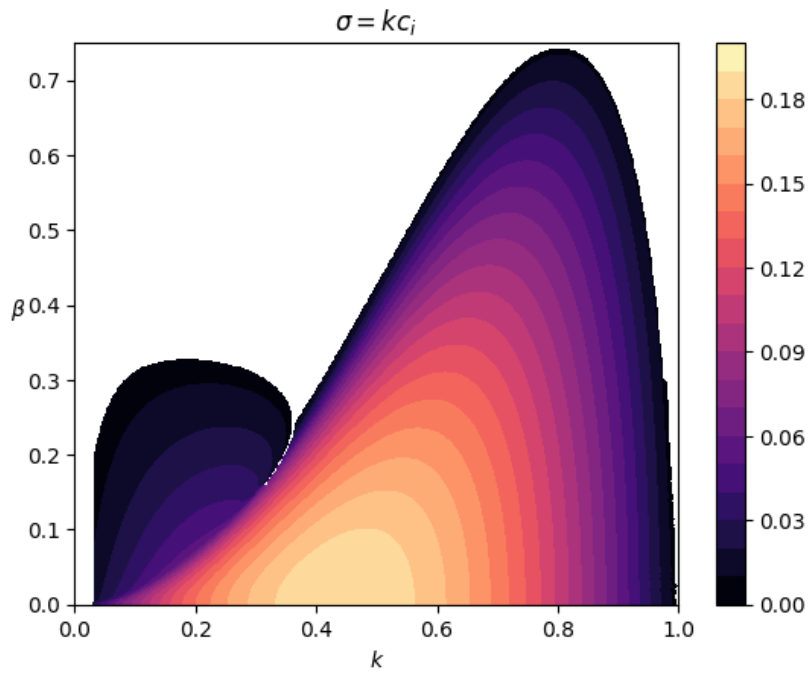


Figure 5.16: Contours of the growth rate,  $\sigma = kc_i$  across varied  $\beta$ ,  $k$ , when  $M = F^2 = 0$ . Stable (white) regions are defined by  $\sigma < 5 \times 10^{-3}$ .

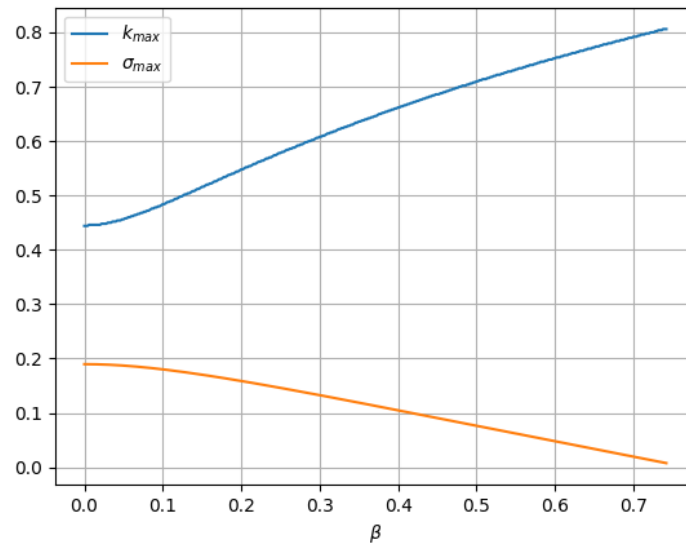


Figure 5.17: The maximum growth rate,  $\sigma_{max}$  (orange), and the wavenumber,  $k_{max}$  (blue), at which this value of  $\sigma$  is attained across varied  $\beta$ , when  $M = F^2 = 0$ .

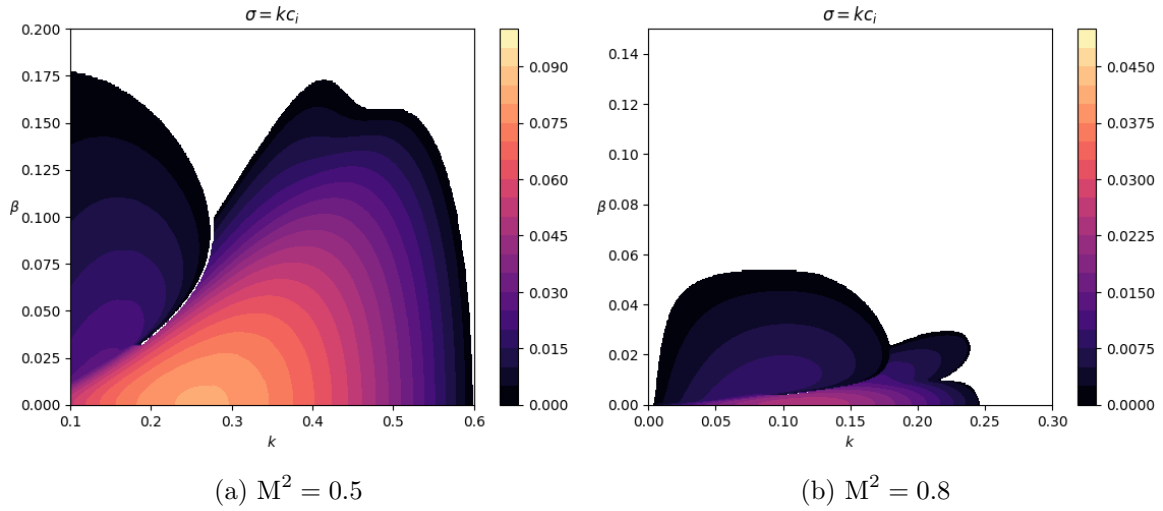


Figure 5.18: Contours of the growth rate,  $\sigma = kc_i$  across varied  $\beta$ ,  $k$ , when  $F^2 = 0$ ,  $M^2 = 0.5$ ,  $0.8$ . Stable (white) regions are defined by  $\sigma < 10^{-3}$ .

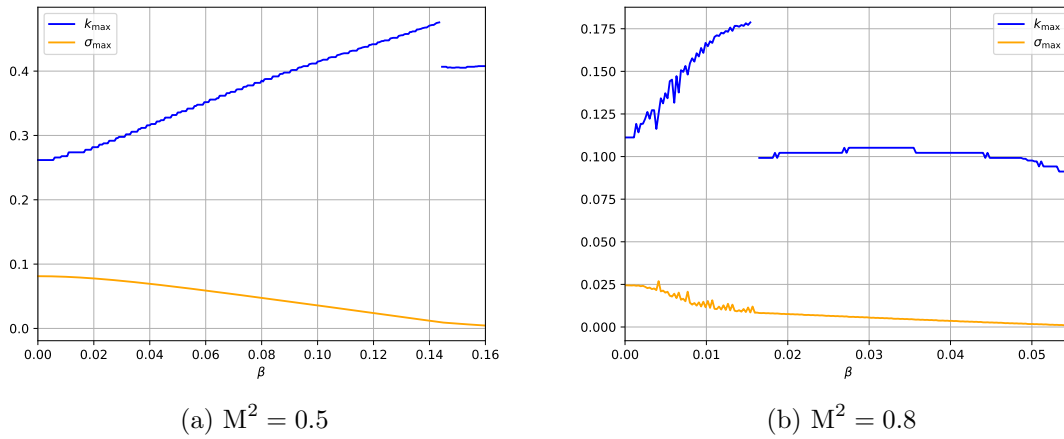


Figure 5.19: The maximum growth rate,  $\sigma_{max}$  (orange), and the wavenumber,  $k_{max}$  (blue), at which this value of  $\sigma$  is attained across varied  $\beta$ , when  $F^2 = 0$ ,  $M^2 = 0.5, 0.8$ . (Note: the numerical imprecision in (b) is due to the smallness of the eigenvalue,  $c$ .)

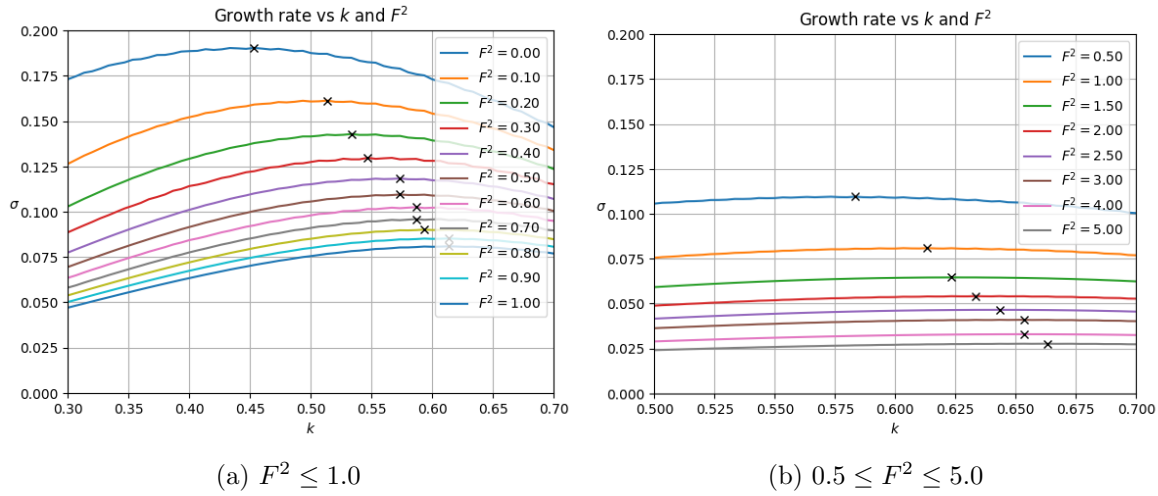


Figure 5.20: Variation of the growth rate,  $\sigma$ , with  $k$  for several values of  $F^2$  ( $\beta = M = 0$ ). The mode of maximum growth is marked with a black cross in each case.

When  $\beta > 0$  the situation is complicated by the presence of the radiating mode. This is generally unimportant when  $M = 0$  since the trapped mode dominates. However, when  $M > 0$ , the radiating mode can dominate, leading to a sudden jump in the WoMG. This occurs at around  $\beta = 0.015$  when  $M^2 = 0.8$  (Figure 5.19). The discontinuity in Figure 5.19b at around  $\beta = 0.145$  is due instead to a jump across the forks of the trapped mode (cf. Figure 5.18b)

Since the radiating mode is not stabilised at small wavenumber (like the trapped mode), the dependence of the WoMG on  $\beta$  behaves differently and no longer increases monotonically (Figure 5.19b). It may be the case that the WoMG tends to zero as  $\beta$  increases however it is difficult to calculate the eigenvalues with sufficient precision when  $k$  and  $c_i$  are small to show this concretely.

### 5.7.3 Variation with $F^2$

Figure 5.20 shows the variation of  $\sigma$  over  $k$  for a range of values of  $F^2$ . For larger  $F^2$  the curve of  $\sigma(k)$  flattens and it becomes more challenging to interpolate and precisely find  $k_{\max}$ . Figure 5.21 shows that the maximum growth rate,  $\sigma_{\max}$ , decreases approximately exponentially towards zero with  $F^2$ , and this could be used to predict  $\sigma_{\max}$  once numerical methods are no longer reliable.

## 5.8 Properties of Unstable Modes

In this section, we investigate two properties of the eigensolution, the Reynolds stress and the eigenfunction breadth.

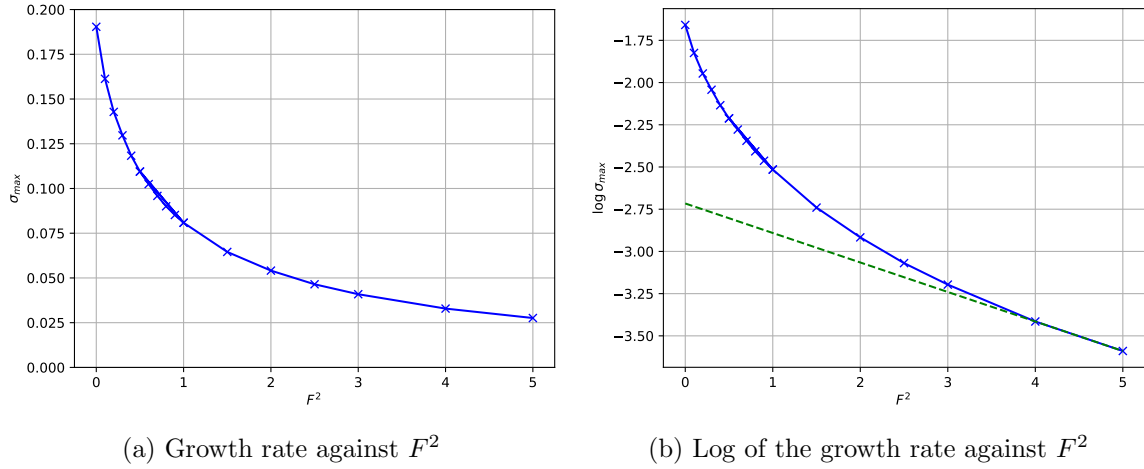


Figure 5.21: Plots showing the maximum growth rate as a function of  $F^2$  when  $\beta = M^2 = 0$ . The asymptote in (b) has gradient  $\lambda = -0.175$ .

### 5.8.1 Reynolds Stress of the Radiating and Trapped Modes

The Wronskian of the real and imaginary parts of the streamfunction,  $h$ , is

$$W = \frac{i}{2} \left( h \frac{dh^*}{dy} - h^* \frac{dh}{dy} \right). \quad (5.107)$$

This can then be related to the Reynolds stress,

$$\tau = -\rho \overline{u'v'} = \rho \frac{k^2}{2} e^{c_i t} W(h_r, h_i) \quad (5.108)$$

(e.g. Foote and Lin, 1950). When  $M = 0$ , the governing equation, (3.23), is

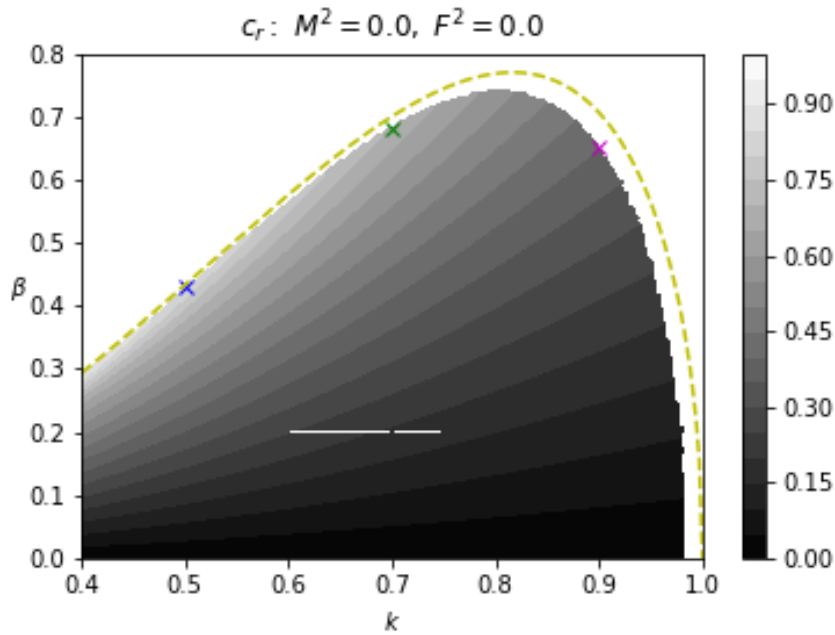
$$h'' - \left( k^2 - F^2 + \frac{\beta + F^2 U - U''}{U - c} \right) h = 0, \quad (5.109)$$

with  $U = \tanh y$  here. Multiplying this by  $h^*$  and subtracting its complex conjugate, one can then obtain an equation for  $W$ ,

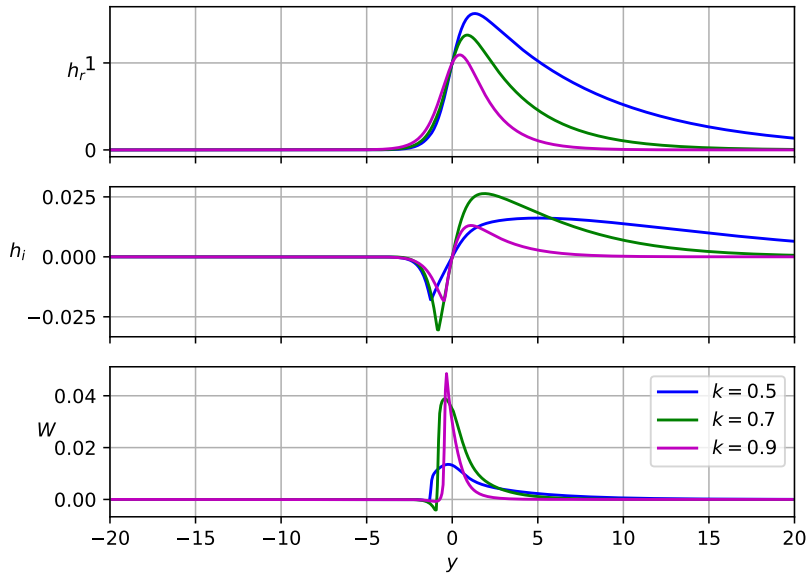
$$\frac{dW}{dy} = -\frac{|h|^2}{|U - c|^2} (\beta + F^2 U - U'') c_i. \quad (5.110)$$

When  $c_i = 0$  the Wronskian, and therefore the Reynolds stress, is constant everywhere except possibly at singularities. With our boundary conditions, that  $h \rightarrow 0$  as  $|y| \rightarrow \infty$ ,  $W$  is also zero at the boundaries. Hence, when  $h$  has a single singularity (which it does, at  $U = \tanh y = c$ , when  $M = 0$ ), a constraint on the neutral mode is that the jump in  $W$  must be zero there. In §5.2 we used this constraint, which is equivalent to

$$\beta + F^2 U - U'' = 0, \quad \text{when } U = c, \quad (5.111)$$

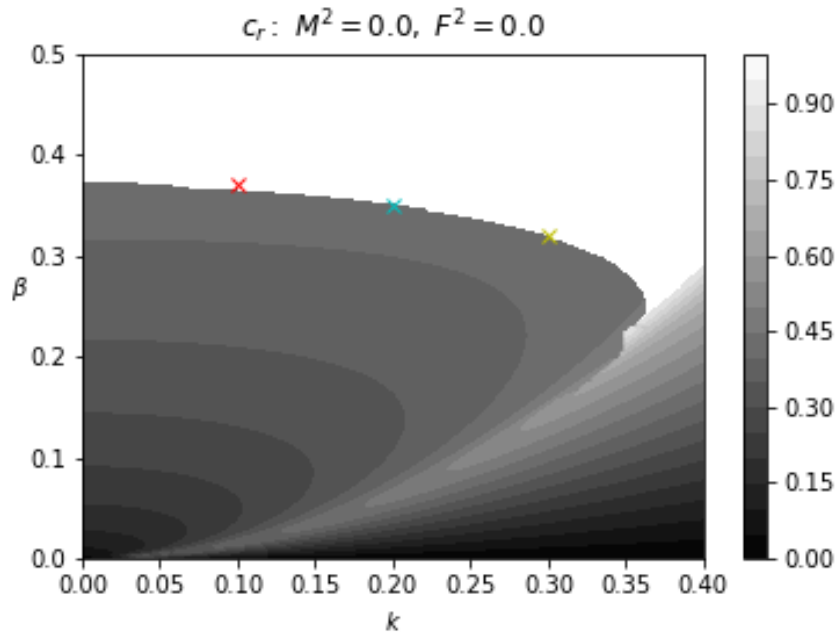


(a) Contour plot of  $c_r$  over  $\beta$ ,  $k$  with three specific points marked,  $(\beta, k) = (0.43, 0.5)$ ,  $(0.68, 0.7)$ ,  $(0.65, 0.9)$ . The yellow dashed curve shows the location of the analytically obtained neutral mode (c.f. §5.2).

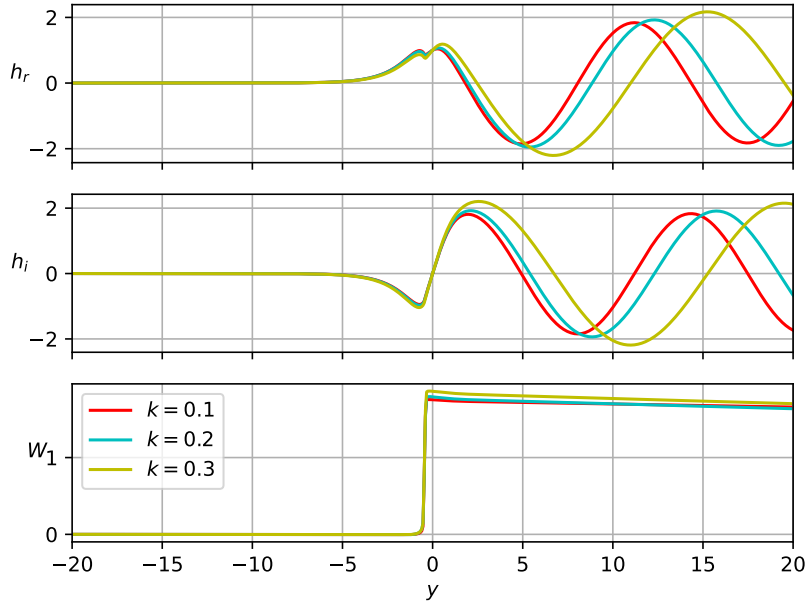


(b) Real and imaginary parts of the (trapped) eigenfunction and their Wronskian, corresponding to the points and eigenvalues shown in Figure 5.22a:  $(k, \beta) = (0.5, 0.43)$ ,  $(0.7, 0.68)$ ,  $(0.9, 0.65)$ .

Figure 5.22: Eigenfunctions of the trapped mode.



(a) A small section of Figure 5.3a showing the phase speed,  $c_r = \Re(c)$ , in  $(\beta, k)$  space, when  $M = F^2 = 0$ . Three points are marked for which  $c_i$  is close to zero.



(b) Real and imaginary parts of the (radiating) eigenfunction and their Wronskian, corresponding to the points and eigenvalues shown in Figure 5.23a:  $(k, \beta) = (0.1, 0.37), (0.2, 0.35), (0.3, 0.32)$ .

Figure 5.23: Eigenfunctions of the radiating mode.

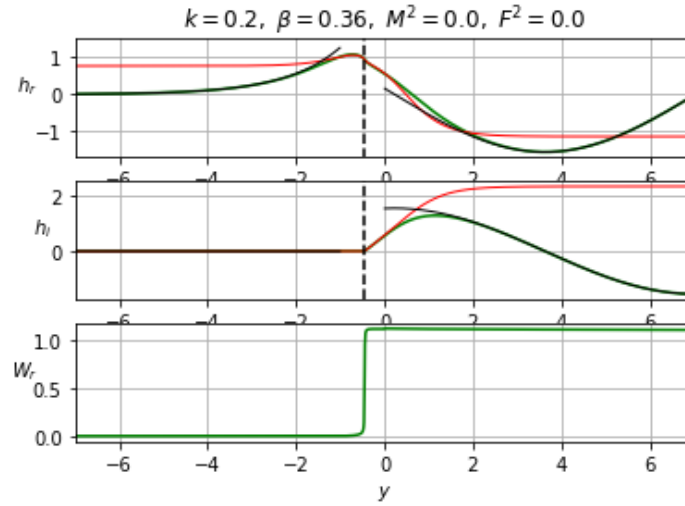


Figure 5.24: The radiating eigenfunction when  $c_i$  is small  $(k, \beta) = (0.2, 0.36)$ , normalised so that  $h(y) = 1$  when  $U(y) = \tanh y = c_r$ . The green line denotes the numerically determined solution and overlaid are the Frobenius solution (red) and the exponential solution (black).

to identify the non-singular neutral mode. The challenge in finding the singular neutral modes is that the jump in  $W$  at  $U = c$  is non-zero, and these modes are not true solutions to the eigenvalue problem, only existing as the limiting case  $c_i \rightarrow 0$ .

Figure 5.22 shows examples of the trapped eigenfunction for small  $c_i$ . The Wronskian,  $W$ , has a small departure from zero close to the critical level where  $U - c_r = 0$ . The radiating mode (Figure 5.23) shows that the Wronskian decays slowly away from the critical level and is still clearly finite at the integration boundary.

In section §5.3 we approximated the singular neutral mode using a Frobenius solution. Figure 5.24 shows that there is good agreement close to the critical level, whilst the exponential solution, derived by approximating  $U$  as a constant when  $y$  is large, can be used to approximate the numerical solution farther away. The jump in the Wronskian,  $W$ , is caused by the presence of the logarithmic singularity of the Frobenius solution.

As  $F^2$  is made larger (for  $\beta > 0$ ,  $M = 0$ ) the eigenfunctions of the radiating and trapped modes remain qualitatively much the same (Figure 5.25), although Rayleigh's criterion can be satisfied for a much larger range of  $\beta$ . The Wronskian,  $W$ , decays more rapidly in the radiating mode case since the coefficient of (5.110) grows with  $F^2$ . Despite this, it still has a fairly significant positive value at the integration boundary. Otherwise, the situation is mostly the same as the  $F^2 = 0$  case.

When  $M > 0$ , the singularity at  $U(y) = c$  bifurcates into two singularities at  $(U - c)^2 = M^2$ . Figures 5.26 and 5.27 show that this leads to a significant increase in the jump of the Wronskian at these points however rather than the two jumps cancelling, say, the Wronskian decays to essentially zero before jumping and decaying again at the second singularity. Of course, the governing equation is no longer (5.110), and the Reynolds stress is not necessarily the relevant quantity to be tracked. The trapped mode, particularly at  $M^2 = 0.8$ , splits into two branches

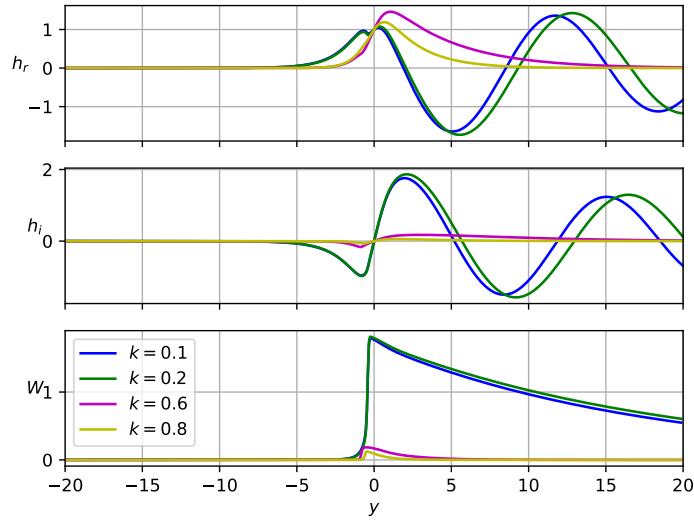


Figure 5.25: Eigenfunctions corresponding to solutions when  $F^2 = 1.0$ . The blue and green curves show radiating modes  $(k, \beta) = (0.1, 0.7)$ ,  $(0.2, 0.7)$ , respectively, and the magenta and yellow curves show trapped modes,  $(k, \beta) = (0.6, 1.2)$ ,  $(0.8, 1.2)$ , respectively. (c.f. Figures 5.6e and 5.6f).

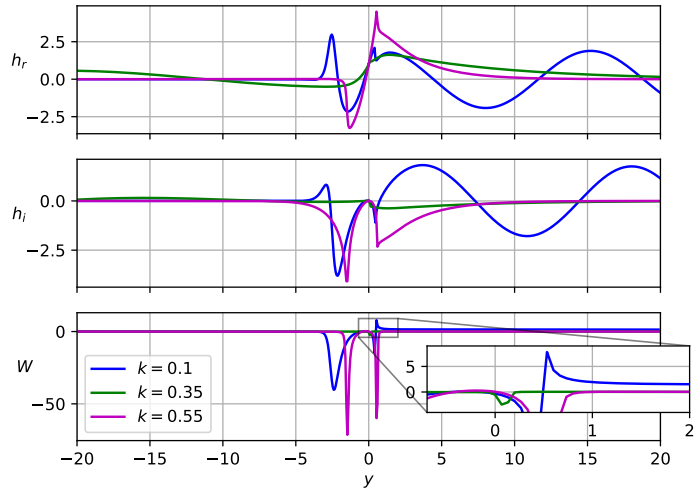


Figure 5.26: Eigenfunctions corresponding to solutions when  $M^2 = 0.5$ . The blue curve shows the radiating mode  $(k, \beta) = (0.1, 0.18)$ , and the green and magenta curves show trapped modes,  $(k, \beta) = (0.35, 0.14)$ ,  $(0.55, 0.12)$ , respectively. (c.f. Figures 5.9c and 5.9d).

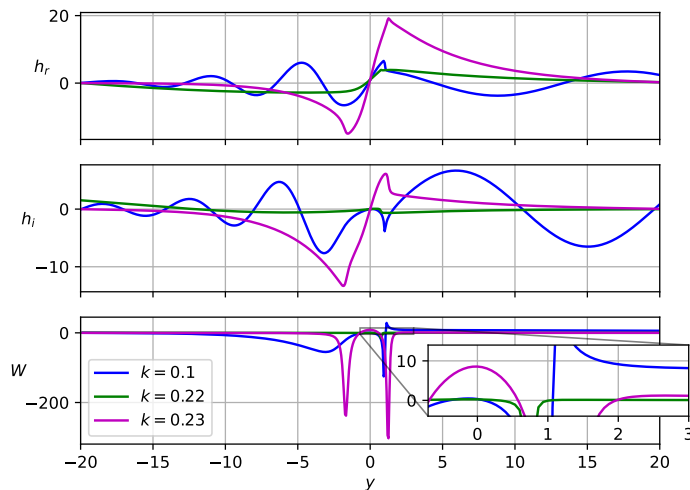


Figure 5.27: Eigenfunctions corresponding to solutions when  $M^2 = 0.8$ . The blue curve shows the radiating mode  $(k, \beta) = (0.1, 0.055)$ , and the green and magenta curves show trapped modes,  $(k, \beta) = (0.22, 0.021)$ ,  $(0.23, 0.005)$ , respectively. (c.f. Figures 5.9e and 5.9f).

(Figures 5.9e and 5.9f). In the first branch, at larger  $\beta$ , slightly smaller  $k$ , the eigenfunction is relatively smooth and its Wronskian is small compared to the other two modes (green, Figures 5.26 and 5.27). In the second branch, at smaller  $\beta$ , the eigenfunction has sharp cusps associated with a large negative  $W$  (pink, Figures 5.26 and 5.27). In both the  $M^2 = 0.5$  and  $M^2 = 0.8$  cases the radiating mode is oscillatory on the north (positive  $y$ ) side of the domain (blue, Figures 5.26 and 5.27). As the wave passes southward through the (almost) singular points it becomes successively more evanescent, although for larger  $M^2$  it may remain oscillatory on the south side of the domain, perhaps since symmetry is broken in the wave dispersion relation with the addition of a magnetic field (e.g. §3.4.1) and hence no regions exist where the propagation of waves is stalled (where  $\beta - U'' = 0$  when  $M^2 = 0$ ). Since this mode is the most unstable, when  $M^2$  is large, this radiating mode may arise in nonlinear simulations, leading to instability with a wavelike, rather than a trapped (vortex-like) form.

## 5.9 Conclusions

In this chapter we have investigated the instability of the smooth fluid profile,  $U = \tanh y$ , the archetypal smooth shear flow. To long wavelength waves, the profile resembles the vortex sheet (§4). Hence, we find the vortex sheet solutions in the limit  $k \rightarrow 0$  ( $\beta = F^2 = \mathcal{O}(k^2)$ ) and a wide range of features not present in the ideal vortex sheet instability. For example, the short-wave cut-off (at  $k = 1$  when  $\beta = M^2 = 0$ ), due to the finite width of the shear layer, which means that modes with sufficiently short wavelength are always stabilised and that a finite wavenumber exists at which the growth rate,  $\sigma = kc_i$ , is maximised. This is not unique to our problem, but we have investigated how this varies with combinations of  $F^2$ ,  $M$ , and  $\beta$ , and offer a mechanistic explanation of why this occurs (§5.7).

In section §5.2 we investigated the presence of non-singular neutral modes when  $M = 0$  and showed a new proof, using the Riemann p-symbol, that there is a unique mode of this type.

This extends similar results ( $F^2 = 0$ ) from Lipps (1962); Howard and Drazin (1964) who also showed that this mode is contiguous with an unstable mode with smaller  $\beta$  ( $\beta > 0$ ). When  $M > 0$ , however, the singularity in (3.23) when  $U(y) = c$  ( $c \in \mathbb{R}$ ) bifurcates into two singularities at  $(U - c)^2 = M^2$ . A single singularity can be removed by setting the numerator,  $\beta + cF^2 - U'' = 0$  at that point, however, two singularities cannot, for general  $U(y)$ , be simultaneously removed. Therefore all neutral solutions (for which  $c \in \text{Ran}(U)$ ) must be singular (§5.4).

A non-zero magnetic field,  $M > 0$ , is not the only case in which singular neutral modes are relevant. Howard and Drazin (1964) predicted, and Dickinson and Clare (1973) showed, the existence of a second mode, predominantly at small  $k$ , separate from the neutral mode. Rayleigh's criterion in the  $\beta$ -plane (Kuo, 1949), that for instability  $\beta - U''$  must change sign somewhere in the domain, means that this mode must eventually stabilise as  $\beta$  is increased (for fixed  $k$  and  $M = F^2 = 0$ ). However, considering the Reynolds stress shows that the boundary of this unstable mode cannot be a true neutral mode (§5.8.1). This makes it difficult to determine the location of the "neutral mode" (and therefore the stability boundary) analytically. One possible technique is constructing a Frobenius solution about the singularity to estimate the form of the eigenfunction close to the boundary (§5.3), however, this solution does not offer a restriction on  $\beta$  and  $k$ .

We investigated some of the properties of the modes, which can be broadly categorised as radiating or trapped based on the asymptotic decay of the eigenfunction on the north (positive  $y$ ) side of the shear layer (Figure 5.11). In general, the non-singular neutral mode acts as a stability boundary for the trapped mode however, where the two modes overlap in parameter space the situation becomes complicated and the neutral mode is sometimes contiguous with a transient mode instead, which quickly stabilises as  $k$  is increased and the trapped mode is instead contiguous with the radiating mode (§5.6.4 and Dickinson and Clare, 1973).

At moderate  $\beta$  (e.g.  $\beta = 0.3$ , Figure 5.16) the trapped mode is stabilised at small wavenumber,  $k$ . The introduction of a magnetic field,  $M > 0$ , monotonically stabilises both modes but impacts shorter wavelengths more significantly due to the enhanced effect of magnetic tension. Readjusting our definition of "moderate"  $\beta$  with  $M$ , this means that when the magnetic field strength is increased to  $M^2 = 0.5$ , and  $\beta = 0.15$ , the growth rates,  $\sigma = kc_i$  of the trapped and radiating modes become roughly equivalent (Figure 5.18a), and when the field strength is further increased to  $M^2 = 0.8$ , and  $\beta = 0.04$ , the trapped mode fully stabilises leaving the radiating mode as dominant (Figure 5.18b).

Given the possible increased significance of the radiating mode when a magnetic is present, further investigation may be required. One possibility would be using the same shear profile as Talley (1983) which is chosen so that the vorticity gradient vanishes everywhere (except at interfaces, where matching conditions must be employed). In the case  $M = 0$ , this choice allows for analytic solutions to be derived and when  $M > 0$  (at least for a uniform magnetic field,  $B' = 0$ ), there seems no reason to expect that the breaking of vorticity conservation will prevent the derivation of analytic solutions. The possibility of analytic solutions is promising since numerical methods can be slow when  $M > 0$ , and the presence of singularities requires a small integration step to navigate the singularity whilst the slow decay of the radiating mode on the north side of the shear layer needs a wide domain size. Additionally, the presence of multiple modes can cause problems with the convergence of the shooting method. We discuss

possible improvements to the numerical methods in the appendix of this chapter, §5.A.

In the final section of this chapter, we investigated some specific properties of the eigensolutions. The first of these properties is the Reynolds stress which can be used as an alternate way of showing the uniqueness of the non-singular neutral mode (e.g. Tollmien, 1935; Foote and Lin, 1950; Howard and Drazin, 1964). Additionally, it shows that the radiating instability has a strong influence extending far on the north side of the shear layer, with the Reynolds stress tending to a finite constant at arbitrarily large  $y > 0$  as  $c_i \rightarrow 0$ . Reynolds stress may not be the correct quantity to investigate when  $M > 0$ , and it might be interesting to include the Maxwell stress and consider the total stress. In this way, it might also be possible to derive the extension to the non-singular neutral mode by requiring the cancellation of the sum of the discontinuities in total stress.

The second property of the eigensolution we showed that the breadth of the eigenfunction decreases as  $F^2$  increases (§6.D); this is particularly relevant since the structure of the eigenfunction will directly affect the nonlinear evolution (§6).

## 5.A Appendix: Shooting Method

We seek eigenvalues,  $c$ , of (3.27), with corresponding eigenfunction,  $G$ , which is related to the surface perturbation,  $h$ , by

$$G = h/(U - c), \quad U = \tanh y, \quad B = 1. \quad (5.112)$$

Since  $h$  is a streamfunction,  $h \in C^1$ , and so  $G \in C^1$  provided that  $c_i \equiv \mathbb{I}(c) \neq 0$ .  $h$  and  $G$  must also satisfy the boundedness condition,  $h, G \rightarrow 0$ , as  $|y| \rightarrow \infty$ .

To outline the method, to find an estimate of the eigenvalue,  $c$ , (for particular  $\beta, k, M, F^2$ ), we choose an initial guess  $c_0$ , and calculate the corresponding function,  $G_0$ , by numerical integration of (3.27). We then test to see whether  $G_0$  satisfies the conditions given above. If it does not, we then “improve” our estimate ( $c_1$ ) and repeat until a sufficiently good estimate ( $c_n$ ) of a true eigenvalue is obtained. We guarantee that all eigenvalues are found by using a range of initial conditions,  $c_0$ , which can be bounded by the conditions on  $c$  derived in §3.6.

**Numerical integration** Equation (3.27) is a second-order ODE with an infinite domain. One way of integrating this equation is to transform it into a first-order Ricatti equation, as in Michalke (1964), and transform the independent variable,  $y$ , so that the domain becomes finite (e.g.  $z = \tanh y$ ). This, however introduces singularities (e.g. at  $z = \pm 1$ ).

Instead, we write (3.27) as a pair of first-order equations by introducing  $H = G'$  so that (3.27) becomes

$$G' = H, \quad (5.113a)$$

$$H' = (k^2 - C(y))G + D(y)H, \quad (5.113b)$$

where

$$C(y) = \frac{(\tanh y - c)(\beta + cF^2)}{(\tanh y - c)^2 - M^2}, \quad (5.114a)$$

$$D(y) = \frac{2 \operatorname{sech}^2(y)(\tanh y - c)}{(\tanh y - c)^2 - M^2}. \quad (5.114b)$$

We then deal with the infinite domain by replacing the Dirichlet boundary conditions at  $y = \pm\infty$  with Robin boundary conditions at finite  $y = \pm D$ . These conditions are obtained from the asymptotic approximation of  $G$  as  $|y| \rightarrow \infty$  (§4.2.2), which is

$$G(y) = \begin{cases} C_+ e^{-\alpha_+ y}, & y > +D, \\ C_- e^{\alpha_- y}, & y < -D, \end{cases} \quad (5.115)$$

where  $\alpha_{\pm}$  is the root of

$$\alpha_{\pm}^2 = k^2 + \frac{(c \mp 1)(\beta + cF^2)}{(c \mp 1)^2 - M^2} \quad (5.116)$$

with positive real part. Written in terms of  $G$  and  $H$ , the derived Robin boundary conditions

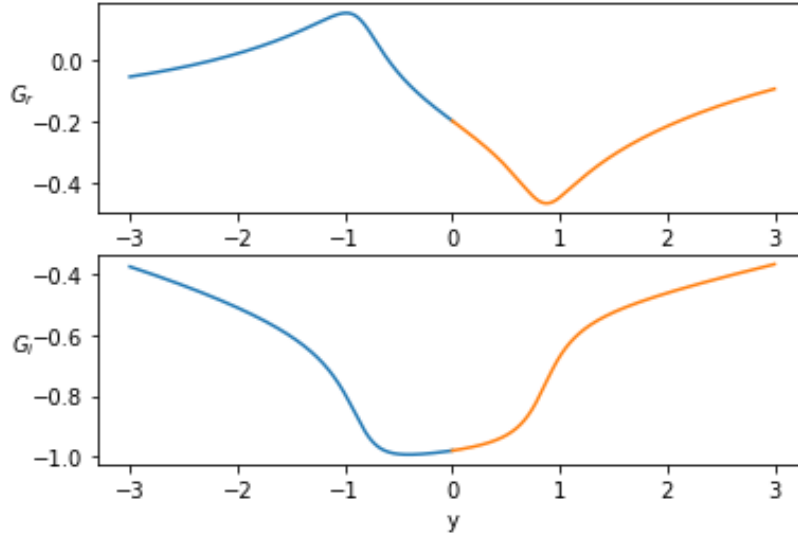


Figure 5.28: Plot of the normalised eigensolution of (3.27) with  $k = 0.5$ ,  $\beta = 0$ ,  $M^2 = 0.5$ , and  $F^2 = 0.5$ . The separate shots from the left and right are given in blue and orange, and the solution is only shown over  $(-3, 3)$  but is calculated fully over the domain  $(-10, 10)$  with Robin boundary conditions.

are therefore

$$\alpha_+ G(+D) + H(+D) = 0, \quad (5.117a)$$

$$\alpha_- G(-D) - H(-D) = 0. \quad (5.117b)$$

This is a very good approximation even for moderate values of  $D$  since  $\tanh$  tends to its limiting values exponentially quickly.

**Improving the estimate,  $c_n$**  To get improved estimates of  $c$ ,  $c_n \rightarrow c_{n+1}$ , we define an objective function,  $f[G_n]$ , such that  $f$  depends smoothly on  $c_n$  and  $f[G](c) = 0$  for exact eigenvalues,  $c$ . Hence, finding improved estimates,  $c_{n+1}$ , corresponds to root-finding of  $f$ , which is achieved using a secant method. Although it is not the most natural choice of  $f$ <sup>1</sup>, we find that good convergence is obtained when

$$f[G_n] = G_n(0^-) H_n(0^+) - G_n(0^+) H_n(0^-), \quad (5.118)$$

where the different subscripts correspond to separate integrations from  $y \pm D$  to  $y = (\pm)0$  using the initial conditions

$$G(\pm D), H(\pm D) = \varepsilon, \mp \alpha_{\pm} \varepsilon, \quad (5.119)$$

for arbitrary  $\varepsilon$ . In this way the boundary conditions at  $y = \pm D$  are always satisfied whilst (since (3.27) is linear) the free choice of  $\varepsilon$  can be used to guarantee that  $G_n$  is continuous everywhere (at  $y = 0$  in particular). The numerical integration also guarantees that  $G$  is

<sup>1</sup>a more obvious choice may be to integrate from one side of the domain, say  $y = -D$ , to the other and use  $f = H(+D)/G(+D) - \alpha_+$ , but we found this gives less reliable convergence

continuously differentiable ( $H$  is continuous) except at  $y = 0$ , with zeroes of the objective function, (5.118) corresponding to this final condition.

Figure 5.28 shows an example of a converged eigenfunction estimate,  $G_n$ , with the separate integrations over positive and negative  $y$  highlighted. Some examples of contours of the objective function are shown in Figure 5.29. The converged estimate of the root is given in the two cases and the root-finding algorithm corresponds to moving on paths of decreasing  $f$ , hence convergence is not guaranteed as  $f$  does not uniformly increase away from zeros. Figure 5.30 shows the regions where the shooting method converges (yellow) and diverges (blue).

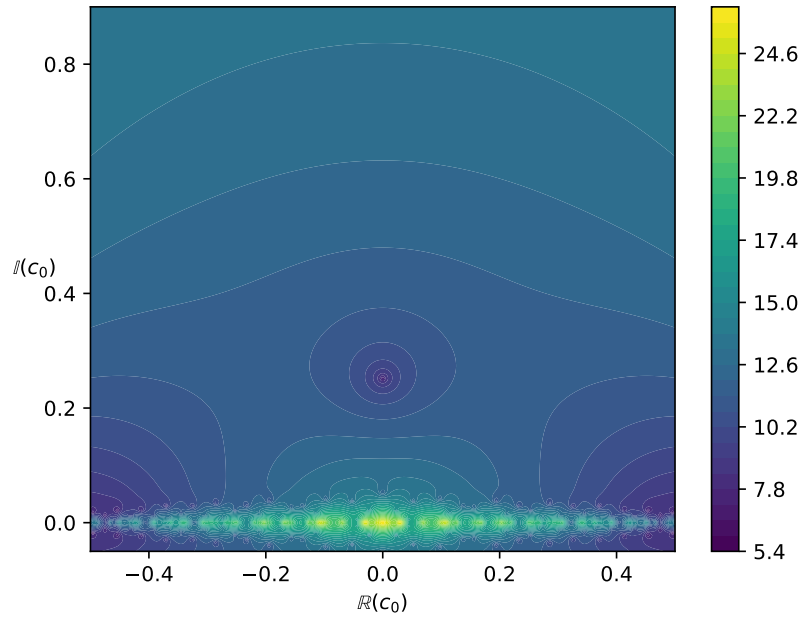
The accuracy of the shooting method is dependent on the step size and method of numerical integration, and also on the presence of nearby singularities in the continuation of  $G$  to complex domain,  $y \in \mathbb{C}$ , which occur at

$$y = \tanh^{-1}(c \pm M), \quad (5.120)$$

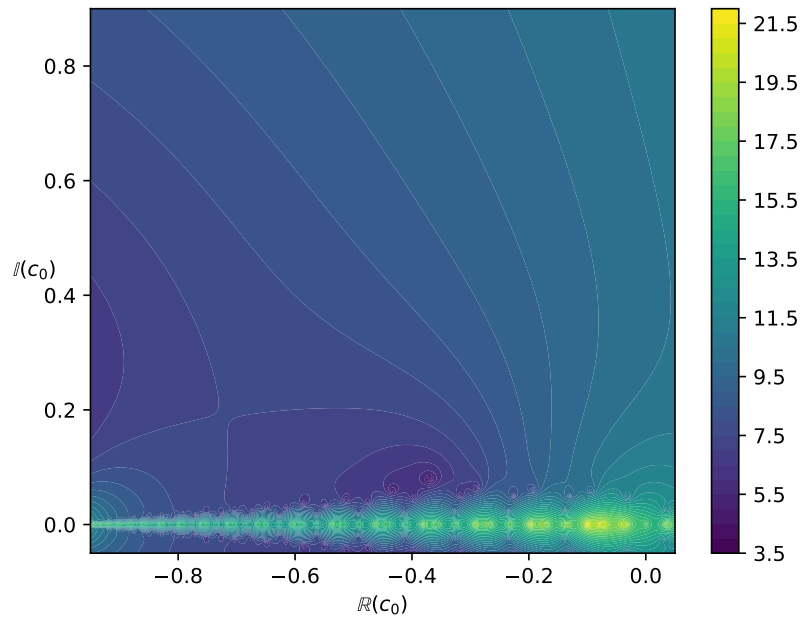
(§5.4) the imaginary part of which is

$$\mathbb{I}(y) = \frac{1}{2} \tan^{-1} \left( \frac{2c_i}{1 + |c \pm M|^2} \right). \quad (5.121)$$

Therefore, the numerical error is often larger for small  $c_i$ . This is demonstrated in the large values of  $f$  for  $c_0$  close to the real axis (Figure 5.29).

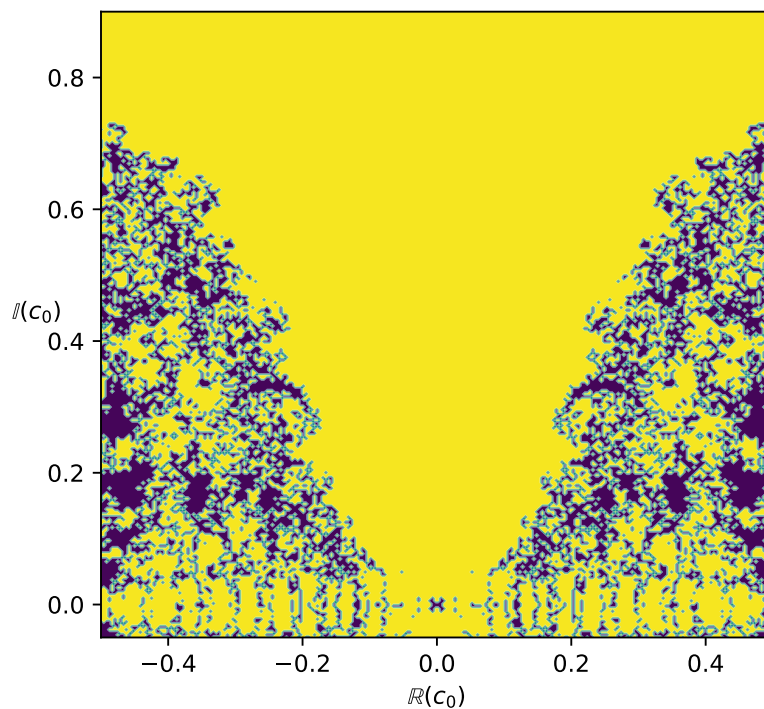


(a)  $(k, M^2, \beta, F^2) = (0.5, 0.005, 0.0, 0.3)$ ,  $c \approx 0.25176i$ .

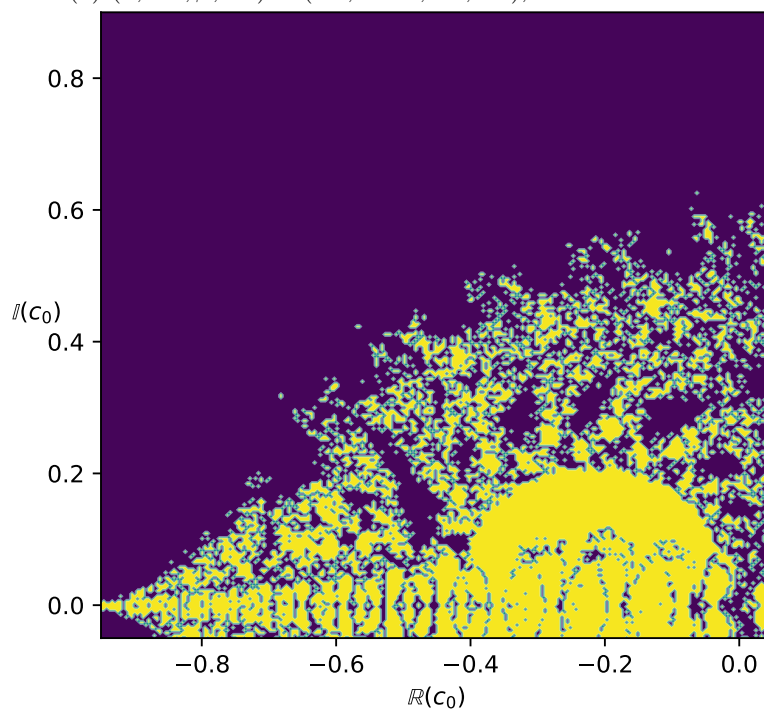


(b)  $(k, M^2, \beta, F^2) = (0.1, 0.0, 0.4, 0.3)$ ,  $c \approx -0.37447 + 0.05967i$ .

Figure 5.29: Contour plots of the logarithm of the objective function,  $\log |f[G]|$ , for a range of input values of  $c_0$ . The topology of  $f$  determines the convergence of the shooting method, Figure 5.30.



(a)  $(k, M^2, \beta, F^2) = (0.5, 0.005, 0.0, 0.3)$ ,  $c \approx 0.25176i$ .



(b)  $(k, M^2, \beta, F^2) = (0.1, 0.0, 0.4, 0.3)$ ,  $c \approx -0.37447 + 0.05967i$ .

Figure 5.30: Contour plots showing regions where the shooting method converges (yellow) and diverges (blue) for a range of values of  $c_0$ . Compare with the corresponding plots of the objective function,  $f$ , in Figure 5.29.



## Chapter 6

# Vortex Disruption in Rotating, Magnetised Fluids

### 6.1 Introduction

Vortex disruption describes the phenomenon whereby a vortex breaks apart as a result of some feature of its evolution. In most systems, vortices will inevitably break apart, although we can think of some, such as the Great Red Spot of Jupiter or the vortex-like structure of galaxies, that do persist for extraordinary lengths of time. In the context of fluid dynamics, however, the only common system that allows for eternal vortices is two-dimensional inviscid hydrodynamics, since there is no mechanism in this case for the vortex to dissipate energy. It is natural then to ask what physics we could add to the model to allow for dissipation or vortex break-up. In the first case, the simplest addition is, of course, viscosity (or hyperviscosity). In this case, it is easy to show that the total energy must decay and so must also the vortex. However, coefficients of viscosity (e.g. Reynolds numbers) are often exceptionally large, particularly in astrophysical contexts, with resultant decay time scales on orders of the lifetime of the Universe (e.g. Gough, 2007). Instead, we might look to a mechanism that can occur in  $\beta$ -plane hydrodynamics and its offshoots whereby vortices steadily lose energy through the emission of Rossby waves (Reznik, 2010; Kravtsov and Reznik, 2020) or to the vertical break-up of vortices due to the elliptical instability (Kerswell, 2002). Each of these mechanisms leads to a steady energy dissipation from the vortex. However, adding a magnetic field to two-dimensional hydrodynamics gives rise to rapid and dramatic instability.

Vortex disruption in magnetised fluids arises due to an important theory of Batchelor (1956), which shows that the vorticity of an evolving vortex will inevitably tend towards uniformity over its radius. Vorticity is conserved by fluid packets and so this property indicates that any passive scalar will evolve in the same way inside a vortex, also spreading out to uniformity over long enough time scales (Rhines and Young, 1983). In two-dimensional MHD, the magnetic flux,  $A$ , is a scalar quantity conserved by the flow that becomes passive in the (kinematic) limit where the initial magnetic energy is significantly lower than kinetic ( $M \approx 0$ ). As such, in the presence of a (finite) vortex, the magnetic flux will be swept to uniformity within the vortex, leading to a large flux gradient, corresponding to a large magnetic field, at the boundary

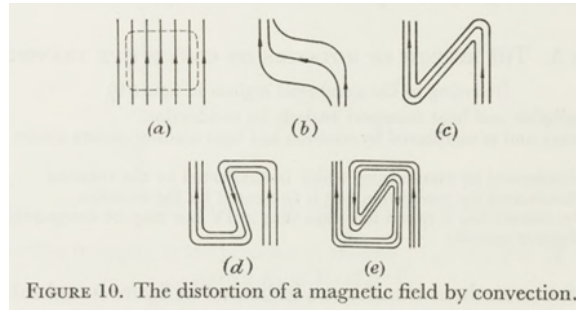


Figure 6.1: A pictographic explanation of the phenomenon of *flux expulsion* given by Weiss (1964).

between the vortex and its quiescent surroundings. This mechanism of flux expulsion can also be described by the action of a conducting fluid on magnetic field lines (Weiss, 1964). In this explanation, the magnetic field lines are “frozen in” to the fluid and so the vortex motion winds the field lines tightly around the vortex centre. This leads to an accumulation of field lines at the boundary of the vortex, which reconnect to form closed magnetic loops (Parker, 1966). Meanwhile, Ohmic dissipation inside the vortex causes the field there to decay (Figure 6.1), resulting in a thin but strong magnetic field forming around the vortex (Figure 6.2).

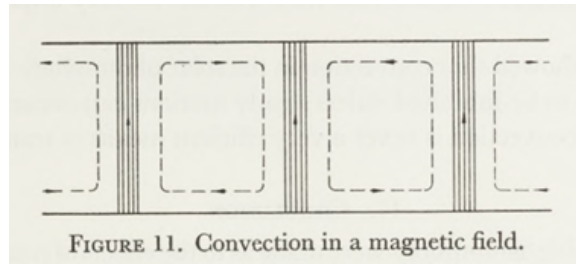


Figure 6.2: The steady state following *flux expulsion* by convective rolls when there is no reaction of the magnetic field back upon the fluid, given by Weiss (1964).

Flux expulsion generally occurs on times that scale with  $\eta^{-1/3}$  (Weiss, 1966; Moffatt and Kamkar, 1983, nondimensionally:  $\sim \text{Rm}^{1/3}$ ), where  $\eta$  is the magnetic resistivity, although it can be accelerated by non-uniformity of the vortex, e.g. Kelvin-Helmholtz braids (Jones et al., 1997). The magnetic field that forms around the vortex is fed by flux expulsion and dissipates by Ohmic decay, thus leading to an estimate  $\sim \eta^{-1/3}$  of its equilibrium strength and an increase  $\sim \eta^{-2/3}$  in the magnetic energy (Weiss, 1966). As mentioned earlier, the magnetic Reynolds number,  $\text{Rm} = UL/\eta$ , can be very large in astrophysical fluids, and this equilibrium field can become orders of magnitude larger than the initial mean field. As such, even if the initial fluid is essentially kinematic, there is no guarantee that the final state will be, and numerous authors have shown that small fields can rapidly become dynamically significant (e.g. Frank et al., 1996; Malagoli et al., 1996; Palotti et al., 2008). Mak et al. (2017) estimate that the magnetic field becomes dynamically relevant when  $M^2 \text{Rm}^\alpha \sim 1$ , where  $M^{-1} = U\sqrt{\rho\mu_0}/B$  is the Alfvén-Mach number and  $\alpha$  is a constant that depends on the

	$Re = UL/\nu$	$Rm = UL/\eta$	Notes
Ting et al. (1986)	10-100	10-100	1
Frank et al. (1996)	†	†	1
Malagoli et al. (1996)	†	†	1
Jones et al. (1997)	†	†	1
Keppens et al. (1999)	†	$10^3 \sim 10^5$	1
Baty et al. (2003)	†	$\sim 3 \times 10^6$	1
Palotti et al. (2008)	*	$10^3 - 5 \times 10^4$	1
Mak (2013)	500	50 – 1000	2,3
Gilbert et al. (2016)	$10^8 - 10^{11}$	$10^6 - 10^8$	2,5
Mak et al. (2017)	500	50 – 1000	2
Dritschel et al. (2018)	†	$8 \times 10^2 - 5 \times 10^4$	2,6
Fraser et al. (2021)	* ( $\sim 1000$ )	250 – 1000	2
Dritschel and Tobias (2023)	†	200 – 3200	4,6

Table 6.1: Table summarising the development in simulations of vortex disruption. (\*Not provided. † No explicit diffusion. <sup>1</sup>Compressible MHD. <sup>2</sup>Incompressible MHD. <sup>3</sup>Hydrostatic SWMHD. <sup>4</sup>Non-hydrostatic SWMHD. <sup>5</sup>Axisymmetric flow restriction. <sup>6</sup>Doubly-periodic domain.)

particular geometry of the equilibrium field. The numerical simulations of Mak et al. (2017) suggest that in two dimensions  $\alpha \approx 1.10$ , whilst the axisymmetric model of Gilbert et al. (2016) leads to a lower estimate  $\alpha = 2/3$ . Subsequent simulations by Kondic et al. (2024) have confirmed to a high precision that  $\alpha = 1$ , at least in two-dimensional MHD.

Vortex disruption has been observed in the Earth’s magnetosphere (Hasegawa et al., 2004; Hwang et al., 2020, 2022) and may be responsible for momentum transport and vorticity mixing within the Solar tachocline (Dritschel et al., 2018; Fraser et al., 2021).

In §6.2 we discuss our numerical model which is validated by comparison with existing results in two-dimensional MHD, particularly those of Mak et al. (2017). We then introduce Coriolis forces in §6.4 on the  $f$ -plane, and we shall discuss how the processes of flux expulsion and vortex disruption change in the quasi-geostrophic model. Numerically obtained disruption estimates are presented in §6.3, after which we investigate the mechanisms behind the differences found between this and the non-rotating (2DMHD) case. Flux expulsion and the homogenisation of potential vorticity depend on the shape of the streamlines (Rhines and Young, 1983). Therefore, the key difference in the evolution of these vortices is the shape of the vortex produced by the shear instability under the modified action of QGMHD, in which potential vorticity, rather than the relative vorticity, is conserved. Thus, in §6.4, we investigate the kinematic evolution of the vortex and shape of the streamlines. Similar studies, looking at the shape and evolution of QG vortices, have been performed by, e.g., Rhines and Young (1982); Held et al. (1995), although not for the purpose of vortex disruption. In the final sections we then present some further observations of the evolution of the flow.

## 6.2 Numerical Model and Verification

The nonlinear simulations shown in the rest of this chapter will be based upon the quasi-geostrophic MHD equations (Zeitlin, 2013) for which we provided a full derivation in §2, along with semi-periodic boundary conditions, detailed in §6.A.3. To these equations, we add a Laplacian diffusion operator, which prevents the cascade to ever smaller scales which would eventually become impossible to model numerically. Unfortunately, adding this term will lead to a more rapid energy loss from the system than is strictly physical since the Reynolds numbers used here are significantly smaller than those observed astrophysically. Over short enough time frames, moderate-Reynolds simulations should nonetheless agree well with those at large Reynolds numbers. We define the hydrodynamic and magnetic Reynolds numbers as

$$\text{Re} = \frac{UL}{\nu}, \quad \text{Rm} = \frac{UL}{\eta}. \quad (6.1)$$

To briefly revisit, we have first the vorticity equation,

$$\frac{\partial q}{\partial t} + \mathcal{J}(h, q) - \text{M}^2 \mathcal{J}(A, \nabla^2 A) = \frac{1}{\text{Re}} \nabla^2 \omega, \quad (6.2)$$

where  $\omega(x, y, t)$  is (the vertical component of) the absolute vorticity,  $q(x, y, t)$  is (the vertical component of) the potential vorticity,  $A(x, y, t)$  is the magnetic flux function, and  $h(x, y, t)$  is the streamfunction denoted  $h$  for consistency since it also corresponds to the surface height perturbation. The quantities  $q$ ,  $\omega$ , and  $h$  are related by

$$q = \omega - F^2 h + \beta y, \quad \omega = \nabla^2 h. \quad (6.3)$$

Both  $A$  and  $h$  are defined up to an arbitrary constant, so particular values depend on our choice of boundary conditions. The magnetic flux equation,

$$\frac{\partial A}{\partial t} + \mathcal{J}(h, A) = \frac{1}{\text{Rm}} \nabla^2 A, \quad (6.4)$$

can be derived from the induction equation.

We evolve these equations using a pseudo-spectral (Fourier-Chebyshev) code in a wide, periodic channel from an initial state of a zonal tanh-profile flow plus some small-amplitude semi-random noise. The details of this numerical method are outlined in §6.A. In short, this method is designed to be efficient, and reliable so that each simulation can be run on a single high-performance processor in time scales of around a day. We have generally used resolutions up to  $\leq 1024 \times 1024$  and moderately-high Reynolds numbers of  $\text{Re} \approx 1000$ ,  $\text{Rm} \approx 500$ . These match many previous studies and are chosen to reveal dynamic features of flux expulsion as clearly as possible.

### 6.2.1 Linear Development

Although, in this chapter, we are primarily interested in the nonlinear development of the instability, it is important to start from firm ground and verify that the shear instability investigated in §5 is well-represented in our numerical simulations.

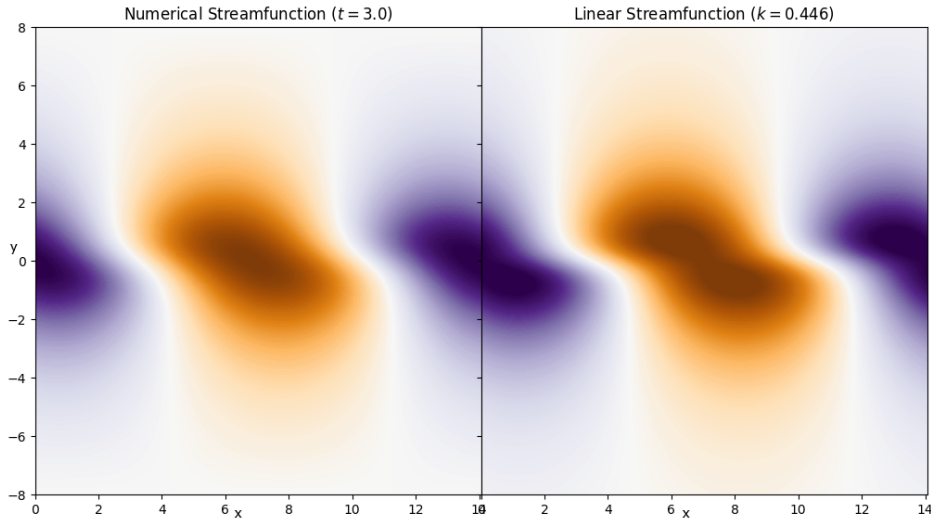


Figure 6.3: Comparison at  $M = \beta = F^2 = 0$  between the numerical streamfunction,  $h$ , at  $t = 3$ , with  $Re, Rm = 1000, 500$  and the linear eigenfunction,  $h$ , with critical  $k = 0.446$ .

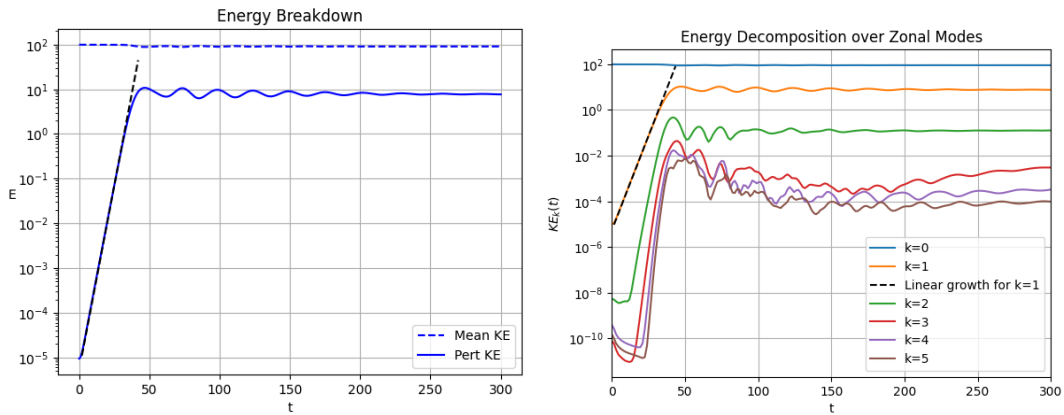


Figure 6.4: Plots of the kinetic energy split into its mean flow and perturbed components (left) and split using a Fourier mode decomposition (right) as compared to the expected energy growth (black dashed line) from linear theory ( $2\sigma = 2 \times 0.190$ ). This simulation was run with parameters  $M = \beta = F^2 = 0$ , and  $Re, Rm = 1000, 500$ .

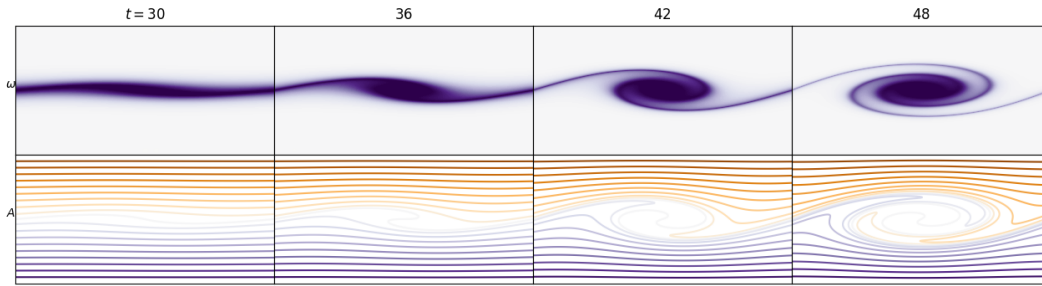


Figure 6.5: Grid showing (relative) vorticity and magnetic field lines (contours of  $A$ ) during the early nonlinear evolution of the kinematic ( $M = 0$ ) instability ( $\text{Re} = 1000$ ,  $\text{Rm} = 500$ ).

The zonal flow is built into the equations of motion (§6.A.2) about which we add a small perturbation (detailed in §6.A.4) to trigger the instability. The exact form of this initial perturbation is relatively unimportant since only the eigenfunctions of the unstable modes grow exponentially and all but the most unstable (largest growth rate,  $\sigma = kc_i$ ) mode will become negligible after a relatively short time. As nonlinearity sets in, the dominant modes will then be integer multiples of the unstable mode. In simulations the domain length,  $L$ , is generally chosen to correspond to the most unstable mode,  $L = 2\pi/k_{\max}$ , so that the only available modes in the system are integer multiples of the critical wavenumber. Generally, only the lowest order mode is significantly unstable and most other modes initially decay until nonlinearity becomes significant (Figure 6.3).

The eigenfunction of the instability is discussed in §5.8. Initially, we will consider the case with  $\beta = F^2 = 0$ , and  $M$  small (and  $k$  fixed by the maximum of  $kc_i$ ), so the eigenfunction remains essentially the same (Figure 6.3). For  $M \gtrsim 0$ , the values of  $k_{\max}$  and  $\sigma_{\max}$  vary little from the  $M = 0$  case as can be seen in Table 6.2 so we opt to maintain the domain size,  $L$ , as we vary  $M$  to give a better comparison between these cases.

### 6.2.2 Nonlinear Kelvin-Helmholtz Evolution

As nonlinear terms become important, the linear instability is saturated and the growth of the eigenfunction is arrested. At this time, the remaining modes grow to unity in amplitude and so it becomes less meaningful to talk about the evolution of the flow in terms of discrete modes. Instead, observing the evolution of the vorticity in Figure 6.5, we see that kinks created by the growth of the eigenfunction are advected by the mean flow and begin to roll up into a vortex.

As the roll-up of the vortex continues we see the formation of Kelvin-Helmholtz “braids” around a central, more uniform patch of vorticity. This occurs as vorticity is drawn by the flow into the central vortex, leaving behind increasingly thin strips which then wrap around the vortex. These braids become increasingly thin until the process is disrupted by diffusion. At this point, shown in Figure 6.6, the vorticity resembles a “cat’s eye” shape which is tilted by the flow. As the flow continues to evolve, the small-scale features are ironed out and the vortex tends towards a state of solid body rotation as the vorticity is homogenised (Prandtl, 1904; Batchelor, 1956). At this point, diffusion now predominantly affects the  $k = 1$  mode and so the time scale of the diffusion of the remaining vortex is of the order of  $\text{Re}(= 1000)$ .

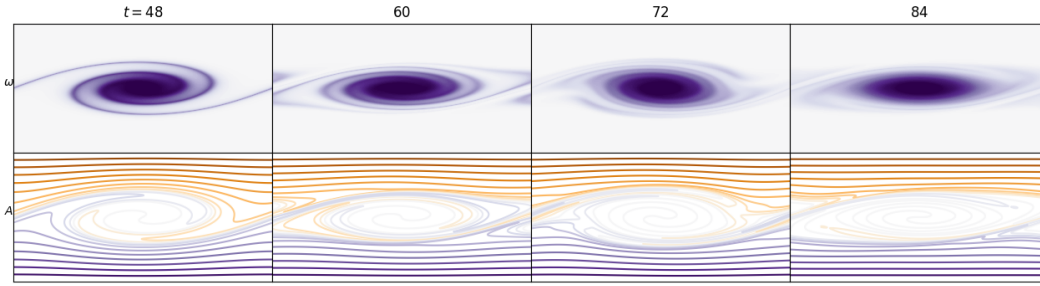


Figure 6.6: Grid showing (relative) vorticity and magnetic field lines (contours of  $A$ ) during the nonlinear evolution of the kinematic ( $M = 0$ ) instability ( $\text{Re} = 1000$ ,  $\text{Rm} = 500$ ).

### Flux Expulsion

As we simulate the evolution of the vorticity we also evolve  $A$  which, in kinematic flows (with  $M = 0$ ), behaves as a passive tracer plus some small additional diffusion. The dynamics of  $A$  can therefore be described by the theory of Rhines and Young (1983) who show that any passive tracer will be homogenised within vortices in the same way as vorticity. Although in our case the vortex is non-uniform, the same theory applies and the rate of expulsion can even be accelerated (e.g. Jones et al., 1997). The evolution of the distribution of  $A$  then determines the strength of the magnetic field through the inversion of  $\mathbf{B} = \nabla \times A \hat{\mathbf{z}}$  although the process can be separately described, in the asymptotic limit  $\text{Rm} \ll 1$ , by the movement of magnetic field lines due to the frozen-in theorem (Alfvén, 1942) and magnetic reconnection (Parker, 1955). Either view of the dynamics leads to the same result; that magnetic field is eliminated from the centre of the vortex and a secondary, amplified field forms at the edges of the vortex (Weiss, 1964). This can be seen in the dense patch of field lines around the vortex in, e.g., Figure 6.6.

### Secondary Instabilities

Secondary instabilities may be possible that could affect vortex disruption, a point which has not been investigated in previous literature. Such instabilities generally require the introduction of additional physics, such as continuous stratification, compressibility, or a third dimension. One exception is the sub-harmonic pairing instability, which can occur after a row of several vortices is generated by the linear instability. We have verified that this can occur in our simulations when a larger domain width,  $L_x$ , is used, but for all the simulations that we present in our results,  $L_x$  is chosen specifically so that the  $k = 1$  mode has the maximal (linear) growth rate. Since the sub-harmonic instability is unstable only to larger wavelengths, none of which are permitted in the spectral method, this instability is prevented.

### 6.2.3 Magnetohydrodynamic Evolution

We now attempt the more difficult challenge of verifying our results with those of Mak et al. (2017) (as well as comparing them to many of the other references given in Table 6.1). Firstly, we verify that the essential picture of evolution remains the same (see Figure 6.7 and description below). For very small magnetic field strength (e.g.  $M = 0.01$ ) the evolution of the flow is essentially kinematic with possibly some enhanced diffusion around the edges of the vortex

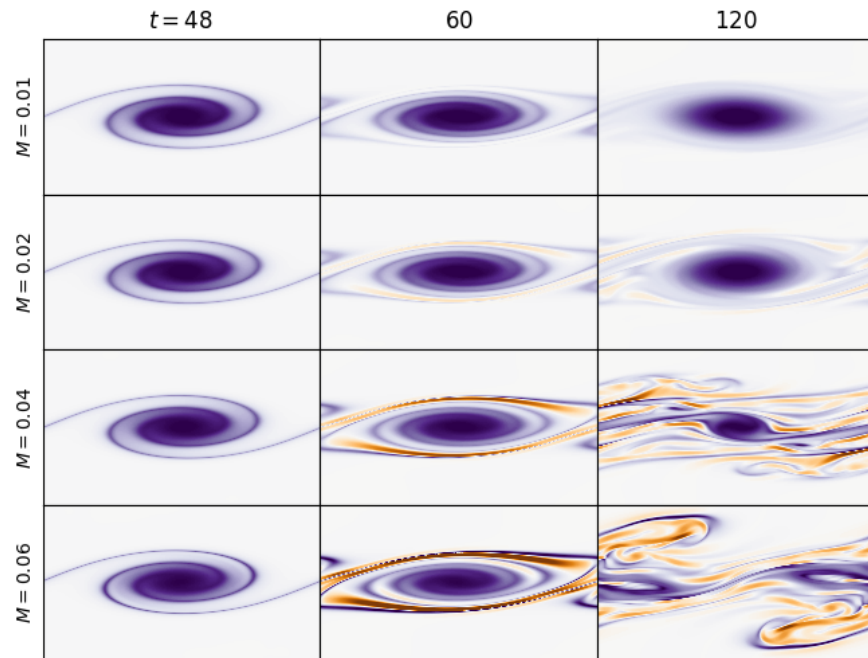
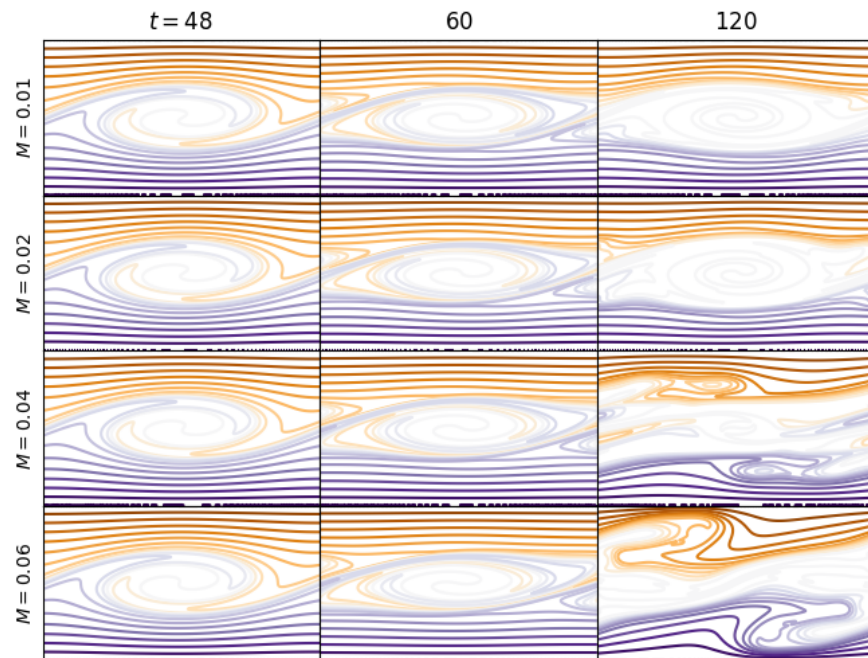
(a) (Relative) vorticity,  $\omega$ .(b) Contours of the magnetic flux,  $A$  (representing magnetic field lines).

Figure 6.7: Snapshots of the flow at increasing values of the non-dimensionalised initial magnetic field strength,  $M$ , (top-to-bottom) at three time steps (left-to-right). ( $Re = 1000$ ,  $Rm = 500$  in simulations).

where the magnetic field is most amplified. As the initial field strength increases slightly ( $0.02 \lesssim M \lesssim 0.06$ ) we see that the initial vortex still develops unchanged but then flux is quickly expelled and a strong magnetic field forms around the vortex. The magnetic hoop stress from this field leads to positive vorticity generation and the disruption (or destruction) of the initial vortex. As  $M$  increases further (not presented), the magnetic field disrupts the linear or weakly nonlinear instability and prevents vortex formation. For a strong field,  $M > 1$ , the tanh profile is linearly stable and the flow remains steady.

### Estimate of the Disruption Scaling

The approximate values of  $M$  given above for weak and very weak fields depend on the value of  $\text{Rm}$  since the magnetic field amplification due to flux expulsion is arrested by magnetic diffusion. Examining the equations of motion can lead to different scalings for when the magnetic field becomes important (e.g. Mak, 2013; Gilbert et al., 2016; Mak et al., 2017) so we provide a derivation here and explain these different results.

Firstly, let us assume that on short time scales negligible magnetic flux is lost from the edge of the vortex and so the total variation in magnetic flux is preserved over the vortex. As this is homogenised in the interior of the vortex, the gradient of the magnetic flux (i.e. the magnetic field strength) is condensed into a small region at the edge of the vortex, say into some length  $\ell$  (compared to the length scale of the vortex,  $L$ ). If we assume this amplified field scales like  $b$ , compared to a scaling of the initial field,  $B$ , then from flux conservation,

$$BL = b\ell. \quad (6.5)$$

A second equation can be derived from the balance in the equation for the advection-diffusion of magnetic flux, (2.45),

$$\frac{\partial A}{\partial t} + \mathcal{J}(h, A) = \frac{1}{\text{Rm}} \nabla^2 A. \quad (6.6)$$

Assuming that the dominant terms on the left side arise from the advection of the mean flow, then this side is  $\sim 1$  due to nondimensionalisation. The dominant term on the right side is the one corresponding to the diffusion of the amplified field, hence  $\nabla^2 A \sim bL^2/B\ell^2$ . This leads to an estimate for the saturation of flux expulsion when  $bL^2/B\ell^2 \sim \text{Rm}$ , or equivalently,

$$\left(\frac{b}{B}\right)^3 \sim \text{Rm}. \quad (6.7)$$

What remains is to estimate when this amplified field becomes important in the evolution of the vortex, described by the vorticity equation, (2.49),

$$\frac{\partial q}{\partial t} + \mathcal{J}(h, q) - M^2 \mathcal{J}(A, \nabla^2 A) = \frac{1}{\text{Re}} \nabla^2 \omega, \quad (6.8)$$

where, in this case,  $q = \omega = \nabla^2 h$  since  $\beta = F^2 = 0$ . In a (statistically) steady vortex, the balance is between the time,  $\frac{\partial q}{\partial t}$ , and advective,  $\mathcal{J}(h, q)$ , derivatives which are both  $\mathcal{O}(1)$  due to the original non-dimensionalisation. The size of the Lorentz force,  $\mathcal{J}(A, \nabla^2 A)$ , is less obvious, and one might expect a scaling like  $(\ell/L)^{-4}$  since it consists of four spatial derivatives and  $A = \mathcal{O}(1)$ . Instead, Mak et al. (2017) show that the  $x$  and  $y$  derivatives cancel out, at

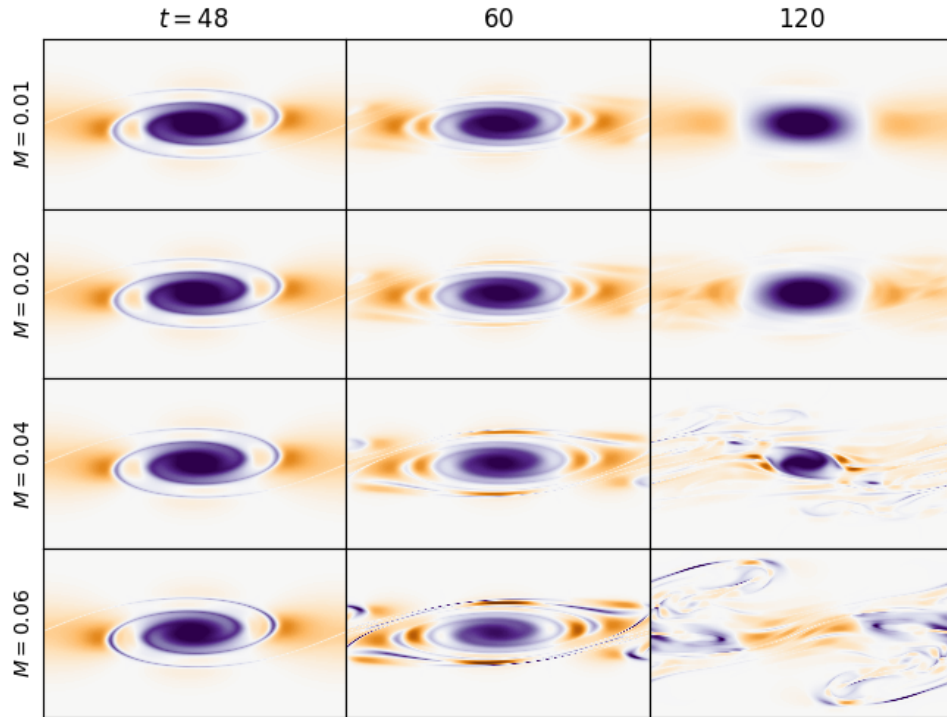


Figure 6.8: Snapshots of the Okubo-Weiss parameter,  $W$ , (defined in §6.C), where vorticity-dominated regions (blue) and those regions where the shear is more important (orange) are distinguished. Large patches of vorticity-dominated flow are identified as vortices with the integral of  $W$  giving some estimate of its strength. This allows us to quantify, as the magnetic field strength,  $M$ , increases, the breakup of the Kelvin-Helmholtz vortex by magnetic effects ( $\text{Re} = 1000$ ,  $\text{Rm} = 500$  in simulations).

leading order, so a scaling  $\sim (\ell/L)^{-3}$  is more appropriate. With axisymmetric restrictions on the field shape Gilbert et al. (2016) derive a reduced scaling  $\sim (\ell/L)^{-2}$ , showing that, in general, the asymmetric geometry of the field is important. Using the cubic scaling, as is relevant here, gives an estimate that the magnetic field will become dynamically important when

$$M^2 \text{Rm} \sim 1. \quad (6.9)$$

Figure 6.7 shows, for  $M = 0.01, 0.02, 0.04, 0.06$ , and  $\text{Rm} = 500$ , how the dynamics significantly change as the Lorentz term enters the leading order balance. For these values of  $M$ ,  $M^2 \text{Rm} = 0.05, 0.20, 0.80, 1.80$ , and it is clear that the evolution is very different in these latter two cases (when  $M^2 \text{Rm} \sim 1$ ), with the vortex becoming significantly disrupted and developing into MHD turbulence.

### Quantifying Disruption

Although, from Figure 6.7, it is clear that the “amount of disruption” increases as we increase  $M$  it would be useful to quantify the degree. To do this, Mak et al. (2017) introduce a

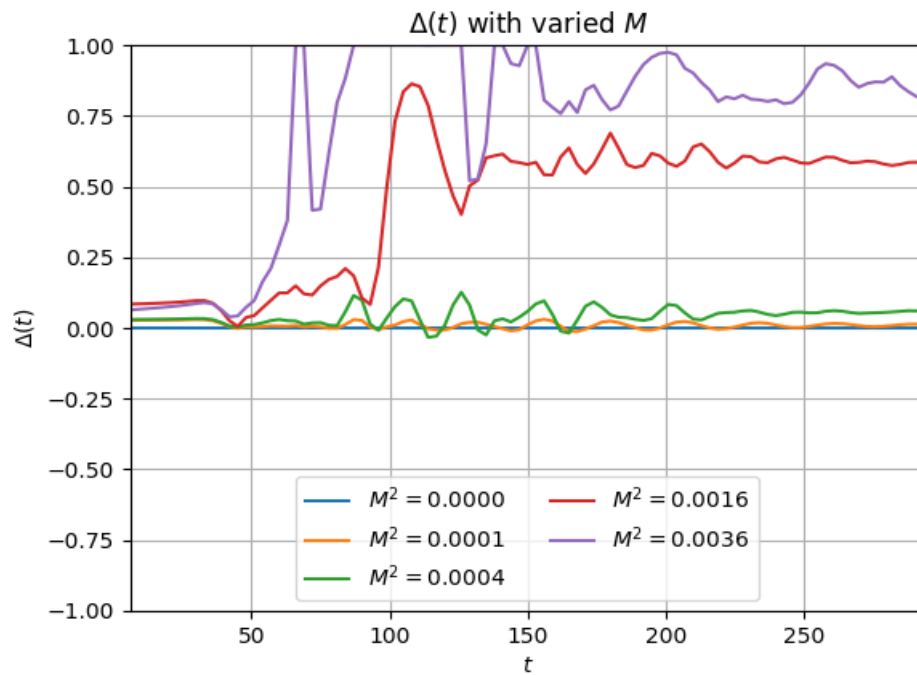


Figure 6.9: Plots of  $\Delta(t)$  using the Okubo-Weiss parameter in Figure 6.8.  $\Delta(t)$  approaches 1 (fully disrupted) as  $M$  is increased and although  $\Delta$  initially varies greatly with time, it eventually approaches a constant value, which can be compared with scaling estimates (§6.2.3) and results of Mak et al. (2017) ( $F^2 = \beta = 0$ ,  $Re = 1000$ ,  $Rm = 500$  in simulations).

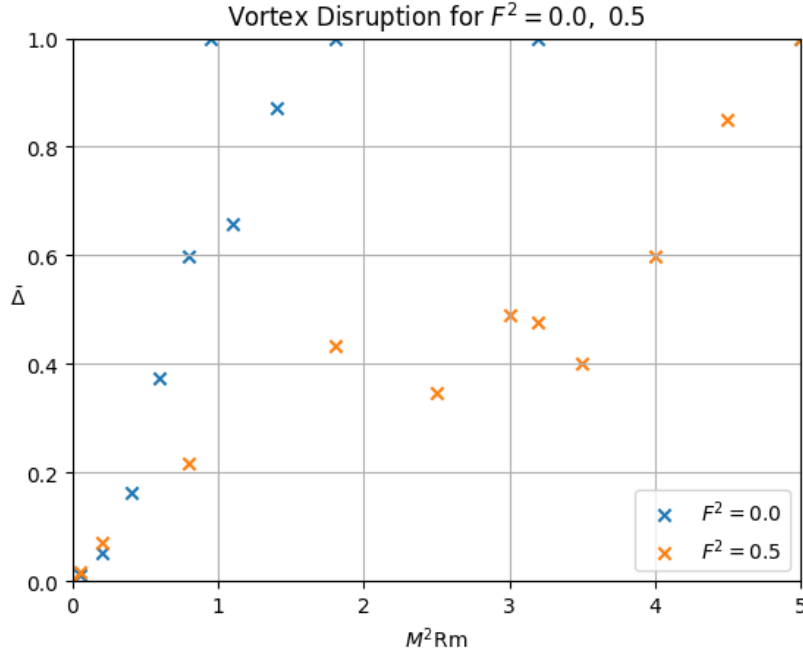


Figure 6.10: A comparison of the theoretical scaling of disruption,  $M^2 Rm$ , against the numerically determined disruption,  $\bar{\Delta}$ , for a number of simulations with fixed  $Rm = 500$  and  $F^2 = 0.0, 0.5$ .

disruption parameter,  $\Delta$ , defined as

$$\Delta(M; t) = 1 - \frac{\int_{A_M(t)} W(x, y, t; M) dA}{\int_{A_0(t)} W(x, y, t; M = 0) dA} \quad (6.10)$$

where the domain of integration,  $A_M(t)$ , for inverse Alfvén-Mach  $M$ , is the time-dependent area deemed to be part of the vortex (see §6.C.4), and  $W$  is the Okubo-Weiss field defined as the Gaussian curvature of  $h$ ,

$$W(h(x, y, t)) = \left( \frac{\partial^2 h}{\partial x \partial y} \right)^2 - \frac{\partial^2 h}{\partial x^2} \frac{\partial^2 h}{\partial y^2} \quad (6.11)$$

(see §6.C.2). The Okubo-Weiss parameter compares the relative dominance of vorticity and shear in the fluid. For example, see Figure 6.8 in which we plot  $W$  for the vorticity field from Figure 6.7. The Mak disruption parameter,  $\Delta$ , meanwhile, quantifies the disruption of a magnetohydrodynamic ( $M > 0$ ) vortex relative to a kinematic one ( $M = 0$ ).  $\Delta$  is scaled so that  $\Delta = 1$  represents the absolute break-up of the vortex while  $\Delta = 0$  indicates a vortex equivalent to the kinematic one.

Since  $\Delta(t)$  is a function of time we then define  $\bar{\Delta}$  as an average over some finite time of the simulation before it becomes too diffused but after disruption has set in. For this case, we will choose the time slice 150 – 180 over which time-frame it can be seen, from Figure 6.9, that the value of  $\Delta(t)$  begins to settle to a constant value. Plotting  $\bar{\Delta}$  for a wide range of values

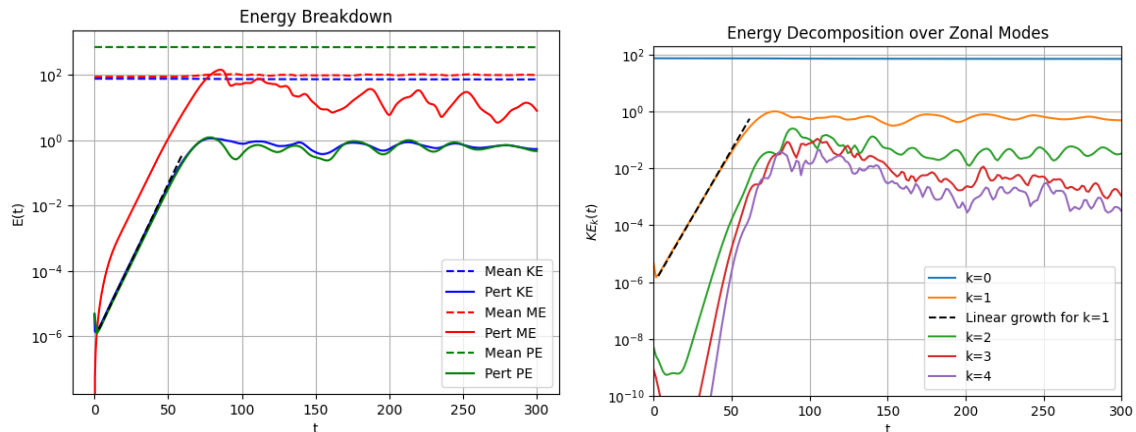


Figure 6.11: The potential, magnetic and kinetic energies split into mean and perturbation components (left) and a breakdown of the kinetic energy into its Fourier modal components (right) for a QGMHD simulation with  $F^2 = 0.5$ ,  $\beta = 0.0$ ,  $M = 0.08$ ,  $\text{Re} = 1000$ ,  $\text{Rm} = 500$ .

of  $M$  (and fixed  $\text{Rm} = 500$ ) we obtain the blue crosses of Figure 6.10 which show agreement between the theoretical scaling that disruption sets in when  $M^2\text{Rm} \sim 1$  and the numerically determined disruption.

### 6.3 $f$ -plane QGMHD - Disruption Scaling

With the simulations of 2DMHD, we have verified the results of Mak et al. (2017) and validated our numerical code. Now seeking to extend existing results to quasi-geostrophic flows we begin by setting  $F^2 = 0.5$  (keeping  $\beta = 0$ ) and repeating the variation of  $M$  that we performed in the previous section. This choice of parameters corresponds to a (shallow) stratified fluid on an  $f$ -plane with increasing magnetic field strength. These simulations are performed on a slightly smaller domain corresponding to reducing  $L_x$  so that the maximal growth rate of instability is tracked (cf. §6.E.3). The energy growth is once again compared (e.g. Figure 6.11) to the expected growth rate from linear theory (§5) and good agreement is found.

The vortex disruption,  $\Delta(t)$ , can be calculated in the usual way although now the denominator is a simulation with  $F^2 = 0.5$ , but still with  $M = 0$ .  $\Delta(t)$  is plotted in Figure 6.12 and we can see that disruption has decreased significantly due to the increase on  $F^2$ .

The disruption scaling,  $M^2\text{Rm} \sim 1$ , is broken by the introduction of  $F^2$  as values of  $M^2$  much larger than 0.002 ( $M \approx 0.045$ ) lead to end-states where a coherent vortex persists. In section §6.2.3 we defined  $\bar{\Delta}$  as the average of  $\Delta(t)$  over the times  $150 < t < 180$  since this was the rough time interval at which the simulations have settled into a post-disruption (uniformly turbulent) state. With  $F^2$  non-zero, the initial instability takes longer to develop (growth rate,  $\sigma(F^2 = 0.0) = 0.190 \rightarrow \sigma(F^2 = 0.5) = 0.109$ ) and so the linear instability does not saturate until roughly  $t = 75$ . As such, we define  $\bar{\Delta}$ , for  $F^2 = 0.5$ , as an average over  $180 < t < 210$ .

These values of  $\bar{\Delta}$  against  $M^2\text{Rm}$  are the orange crosses in Figure 6.10 and we find that the relationship remains roughly linear but the gradient decreases significantly. This is verified

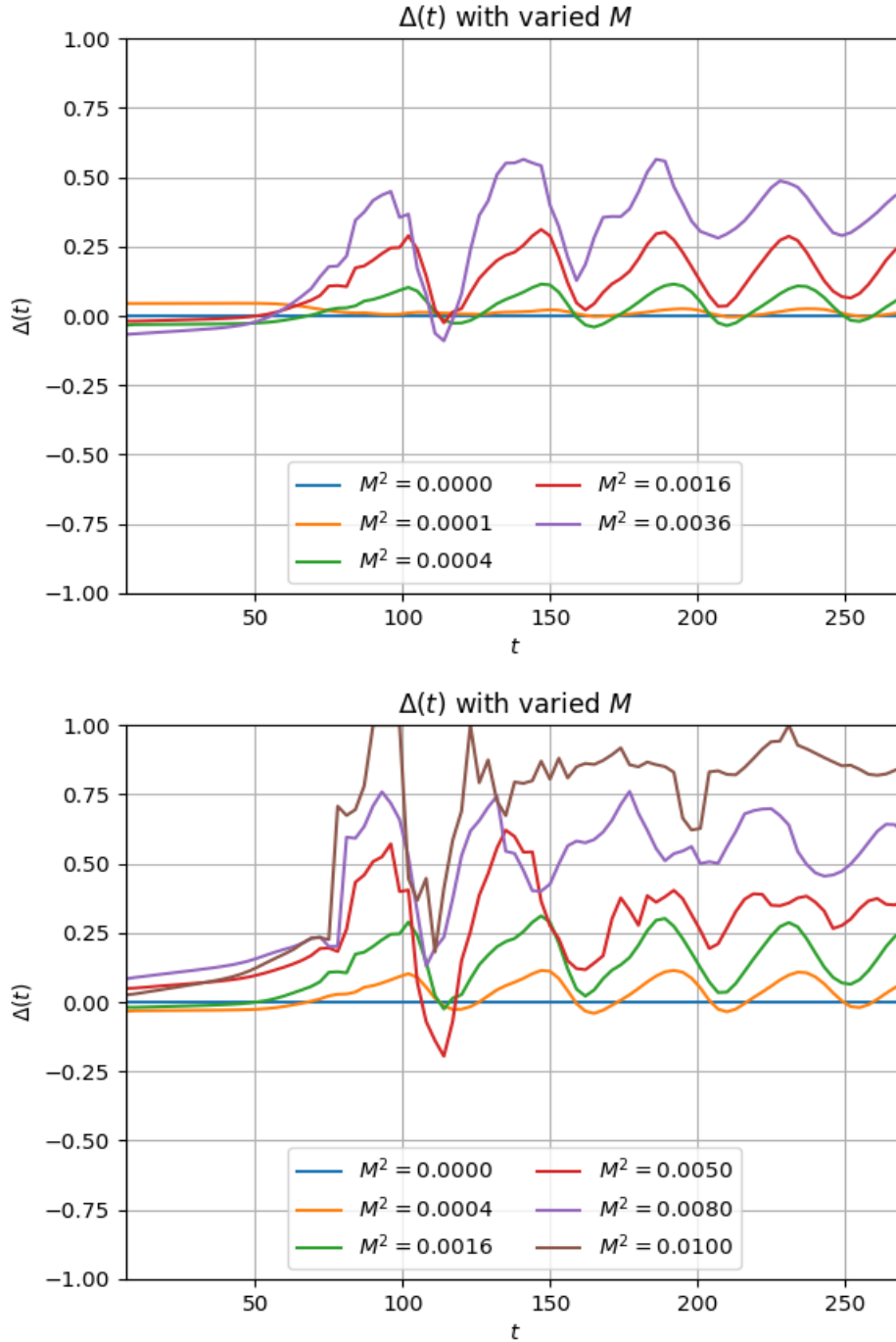


Figure 6.12: Plots of the disruption,  $\Delta(t)$ , for simulations with  $F^2 = 0.5$ .  $\Delta = 1$  indicates that no vortex is present whilst  $\Delta = 0$  indicates that a vortex equivalent to the QG ( $M = 0$ ) one is present. The top plot uses the same values of  $M^2$  as Figure 6.9 ( $F^2 = 0.0$ ) and shows a significant decrease in disruption. The bottom plot shows a wider range of  $M^2$  showing the variation of  $\bar{\Delta} : 0 \rightarrow 1$ . ( $Re = 1000$ ,  $Rm = 500$ )

by a linear regression of  $\log \bar{\Delta}$  against  $\log M^2 \text{Rm}$  which shows that the gradient decreases by a factor of  $\sim 1.57$ .

## 6.4 *f*-plane QGMHD - Kinematic Evolution

To get a clearer picture of the causes of the reduced disruption found in the previous section (§6.3) we will consider the kinematic problem, with  $M = 0$ ,

$$\frac{\partial q}{\partial t} + \mathcal{J}(h, q) = \frac{1}{\text{Re}} \nabla^4 h, \quad (6.12)$$

$$\frac{\partial A}{\partial t} + \mathcal{J}(h, A) = \frac{1}{\text{Rm}} \nabla^2 A, \quad (6.13)$$

$$q = \nabla^2 h - F^2 h \quad (6.14)$$

i.e. our system reduces to a decoupled set of advection-diffusion equations for potential vorticity,  $q$ , and magnetic flux,  $A$ . Since  $A$  behaves here as a passive scalar, we expect its dynamics can be fairly generally predicted:  $A$  will be homogenised in areas where the flow is vortical or relatively turbulent (e.g. Weiss, 1964; Tao et al., 1998). This leaves us with the task of predicting the evolution of the potential vorticity.

### 6.4.1 Potential Vorticity Dynamics

The following short section is not intended to be an extensive review of the dynamics of potential vorticity (e.g. Pedlosky, 1987; Majda and Wang, 2006; Zeitlin, 2007; Vallis, 2017). Rather, we shall highlight some important features of potential vorticity that seem relevant to simulations of a zonal flow with monotonic shear.

Firstly, the evolution of potential vorticity is governed by

$$\frac{Dq}{Dt} = \frac{1}{\text{Re}} \nabla^4 h; \quad (6.15)$$

$q$  is therefore at leading-order materially conserved when the Reynolds number is large (usually  $\text{Re} = 1000$  in our simulations); the diffusion is often negligible except where fine structure develops. Since we also have impenetrable lateral ( $y$ ) boundaries and periodic zonal ( $x$ ) boundaries, preventing any motion from or into the domain, the potential vorticity is also generally conserved.

If we briefly return to simple (non-rotating,  $F^2 = 0$ ) two-dimensional flow we then have  $q \rightarrow \omega = \nabla^2 h$ , where  $\omega$  is the relative vorticity ( $\nabla \times \mathbf{u} = \omega \hat{\mathbf{z}}$ ). It is well-known then that enstrophy (square vorticity,  $Z = \frac{1}{2} \int \omega^2$ ) cascades to small scales whilst kinetic energy (square velocity) cascades to large scales. The net result of this dual cascade is that two-dimensional flows tend to form large vortices, with the only upper bound being the size of the domain.

Introducing  $F^2$  has two significant effects on the flow. Firstly, it brings in a new natural length scale: the Rhines scale (Rhines, 1975), which, among other things, arrests the inverse cascade of energy at a finite scale, in turn limiting the formation of large vortices. One interpretation of this effect is that the flow appears to adapt itself (from the non-rotating case) to weaken large gradients of potential vorticity (e.g. Read et al., 2020), which would otherwise result from the

overturning of potential vorticity in a large vortex. Additionally, the breaking of symmetry between the zonal and meridional directions ( $x$  and  $y$ ) leads to a preference towards motion directed along lines of constant background vorticity, i.e. in the zonal direction, leading, on the planetary scale, towards a preference for jet, rather than vortex formation.

### Background Vorticity

Suppose  $h = \int_y U(y) + \tilde{h}$ , so that  $\tilde{h} = 0$  initially, then, the potential vorticity,

$$q = \nabla^2 h - F^2 h, \quad (6.16)$$

can be divided into three components: the relative vorticity  $\omega = \nabla^2 h$ , the background vorticity,  $b = -F^2 \int U$ , and the perturbation surface vorticity,  $s = -F^2 \tilde{h}$ . Outside the shear layer,  $|y| \gg 0$ ,  $b \approx -F^2 |y|$ , and therefore moving a packet of fluid relative to the background vorticity gradient leads to a respective increase or decrease in  $\omega$ , conserving  $q$ . As the potential vorticity tends to uniformity around the vortex, the relative vorticity becomes weaker at the lateral extents of the vortex (large  $|y|$ ) but remains high around  $y \approx 0$ .

### Vortex formation with $F^2$ varied

The net result of non-zero  $F^2$  is that a more elliptical vortex is produced as  $F^2$  increases (Figure 6.13,  $t = 200$ ), that is until the lateral extent of the vortex is so reduced that it lies within the shear region and the approximation  $|U| \approx 1$ , leading to  $b \approx -F^2 |y|$ , is no longer valid. The precursor to elliptisation can be seen in the change in the growth rate of instability as  $F^2$  is increased, which cannot lead to stability, but monotonically decreases the growth rate (Figure 6.14). The growth of the instability perturbs the surface, requiring a transfer of energy from the mean flow to the perturbation potential and the kinetic energy.

We demonstrate a correlation between the lateral extent of the vortices and the growth rate  $\sigma$  in Figure 6.15. Since the semi-major and semi-minor axes are not necessarily aligned with  $x$  and  $y$ , we first calculate the ellipticity of each vortex (cf. Appendix 6.D), then, using the known value of  $L_x$  (varying with  $F^2$ ), calculate the lateral extent  $\mathcal{L}$ .

Over enough time these elliptical vortices flatten into a wide jet as diffusion is accelerated at the corners, a process which can be seen in the lowest row of Figure 6.13. We will examine, in §6.4.2, how the ellipticity of the vortex changes the structure of the magnetic field produced. Then in §6.6, we will see how these magnetic fields enhance the formation of jets.

#### 6.4.2 Magnetic Field Growth

It is then natural to ask how the change in the shape of vortices affects flux expulsion and the formation of the secondary magnetic field (the primary field refers to the initial, zonal, spatially uniform field). In the case  $F^2 = 0$  (Figure 6.16) we see initially ( $t = 50$ , top row) that the outer magnetic field lines quickly circularise whilst the inner field lines are bent in the centre of the vortex. The top row of Figure 6.16 also shows the magnetic Jacobian, and we see that initially, its amplitude is small since it depends on the third derivative of  $A$ . As flux expulsion continues, we see in the second row ( $t = 60$ ) that the magnetic field maintains its shape but the Lorentz force is significantly amplified. Shortly after this ( $t = 70$ ), the flux

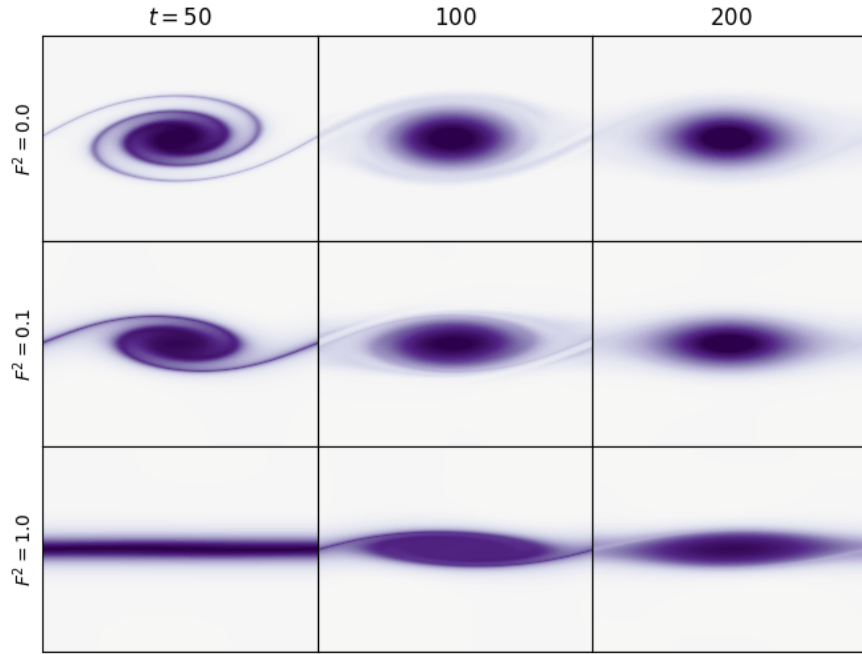


Figure 6.13: Snapshots of the relative vorticity,  $\omega = \nabla^2 h$ , at increasing  $F^2$ , showing a tendency towards jet-like, rather than vortex-like, dynamics. When  $F^2$  is larger, the linear instability also grows more slowly, matching predictions ( $\text{Re} = 1000$ ).

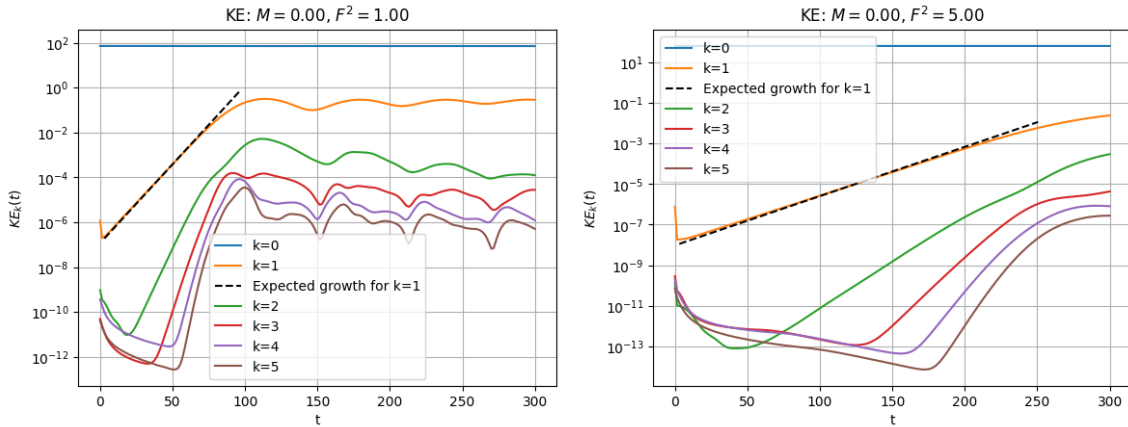


Figure 6.14: Energy of discrete Fourier modes over time for simulations with  $F^2 = 1.0$  (left) and  $F^2 = 5.0$  (right) showing agreement with the expected growth rate of the  $k = 1$  mode from linear instability analysis ( $\text{Re} = 1000$ ,  $\text{Rm} = 500$ ,  $M, \beta = 0$ ).

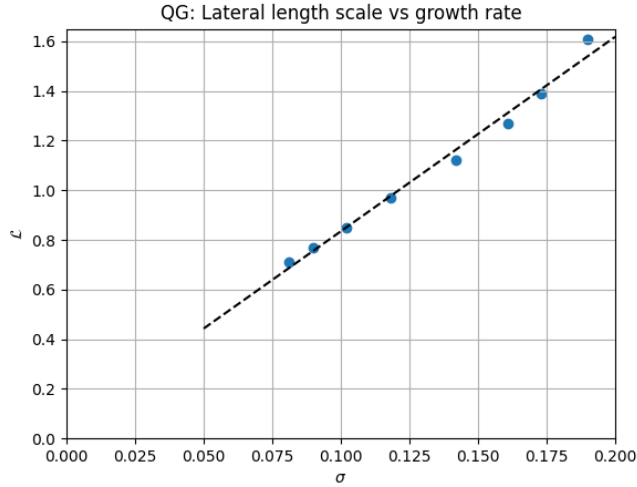


Figure 6.15: Lateral extent of the vortices,  $\mathcal{L}$  against the growth rate,  $\sigma$ .

homogenises within the vortex and the secondary magnetic field is no longer supported from within. Meanwhile, diffusion begins to disperse the swept flux, reducing the field strength and magnitude of the Jacobian.

Taking the maximum of the Jacobian at a range of time steps, we obtain the curve in Figure 6.17, which highlights the initial exponential growth due to the linear shear instability followed by a transition to super-exponential growth due to the flux expulsion. This is arrested, and we enter a decay phase as the magnetic field diffuses and disperses. Even in the kinematic case, this decay is not monotonic, as the vortex is inhomogeneous. Increasing  $F^2$ , we see that the distinction between the linear growth and flux expulsion regimes is obscured as the time scales of these two processes become intertwined. In particular, the eventual maximum of the magnetic Jacobian decreases as  $F^2$  increases since flux expulsion ends up acting over a longer period and there is time for significant magnetic flux to dissipate out of the vortex.

For a range of values of  $F^2$ , we see in Figure 6.18a a steady decline in the maximum of the Jacobian. Similarly, in Figure 6.18b, we see the maximum of the magnetic field strength,  $|\mathbf{B}|$ , decreases. For this value of  $\text{Rm}$ , the (non-dimensional) expected field strength and Jacobian magnitudes are

$$\mathcal{J}(A, \nabla^2 A) \sim \text{Rm}, \quad |\mathbf{b}| \sim \text{Rm}^{1/3}, \quad (6.17)$$

$$\sim 500, \quad \sim 7.94. \quad (6.18)$$

These values are generally exceeded due to inhomogeneities in the vortex, particularly around the Kelvin-Helmholtz braids (cf. Figure 6.16).

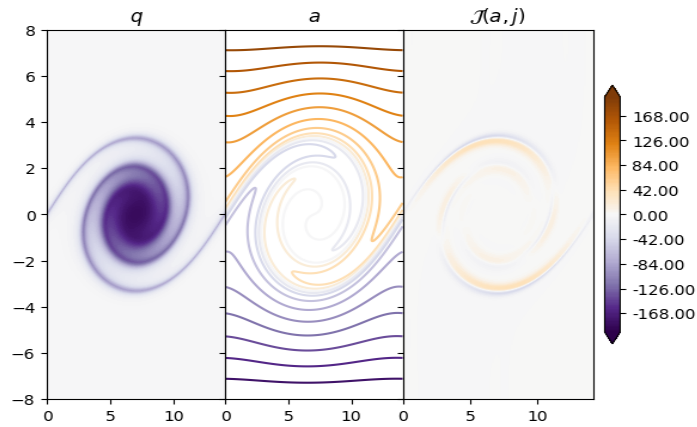
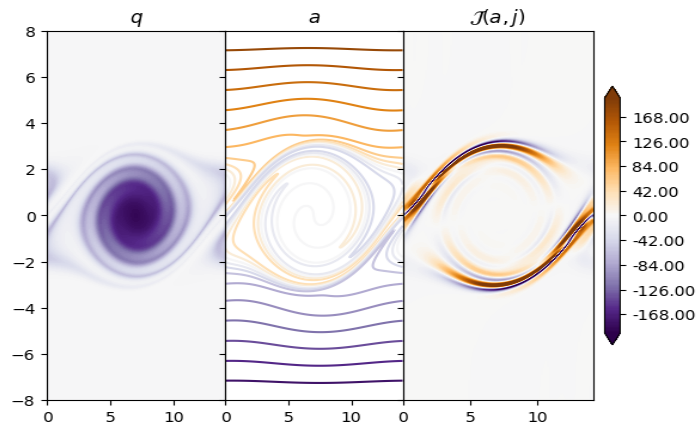
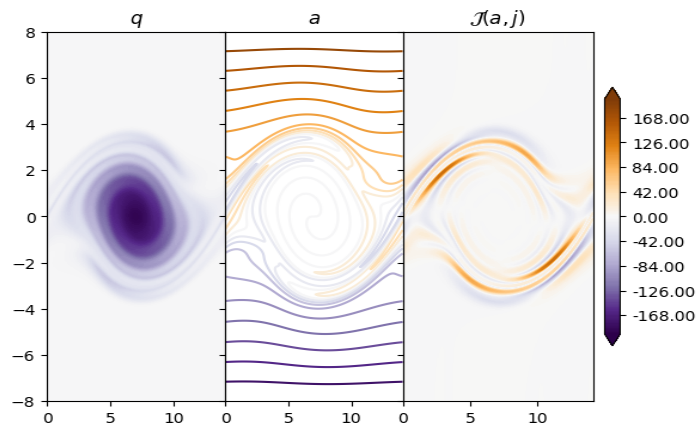
(a)  $t = 50$ (b)  $t = 60$ (c)  $t = 70$ 

Figure 6.16: The relative vorticity,  $\omega = \nabla^2 h$ , magnetic field lines,  $A$ , and magnetic Jacobian  $\mathcal{J}(A, \nabla^2 A)$  at three times just after saturation of the linear instability ( $t \approx 50$ ) ( $\text{Re} = 1000$ ,  $\text{Rm} = 500$ ,  $\beta = F^2 = M = 0$ ).

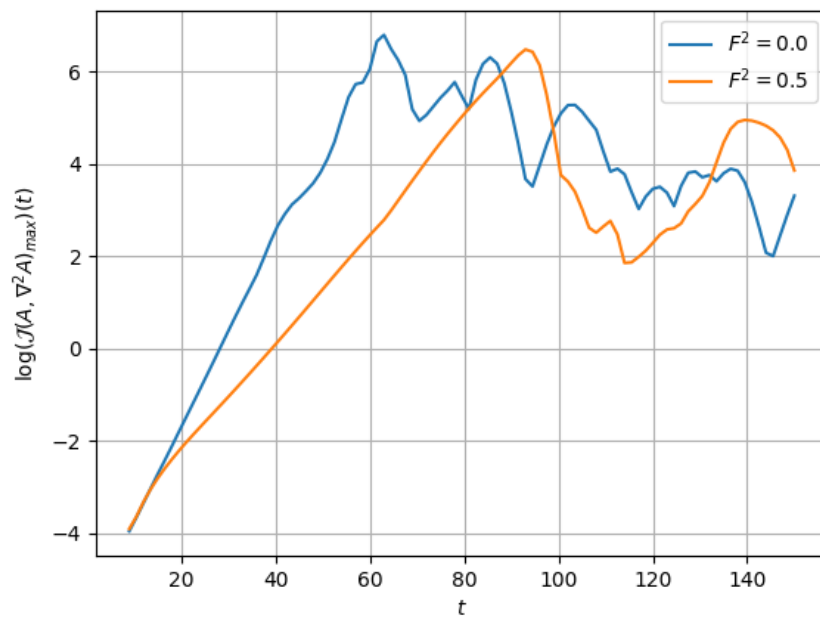


Figure 6.17: Logarithm of the (spatial) maximum of the magnetic Jacobian,  $\mathcal{J}(A, \nabla^2 A)$ , over time for two simulations with  $F^2 = 0.0, 0.5$  showing the initial phase of exponential growth (straight line) transitioning into super-exponential growth during the flux expulsion stage, followed by algebraic dissipative decay ( $\text{Re} = 1000, \text{Rm} = 500, \beta = M = 0$ ).

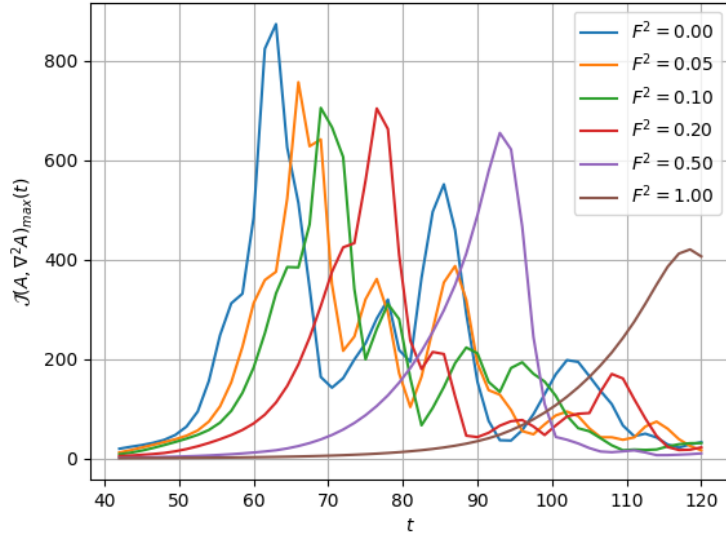
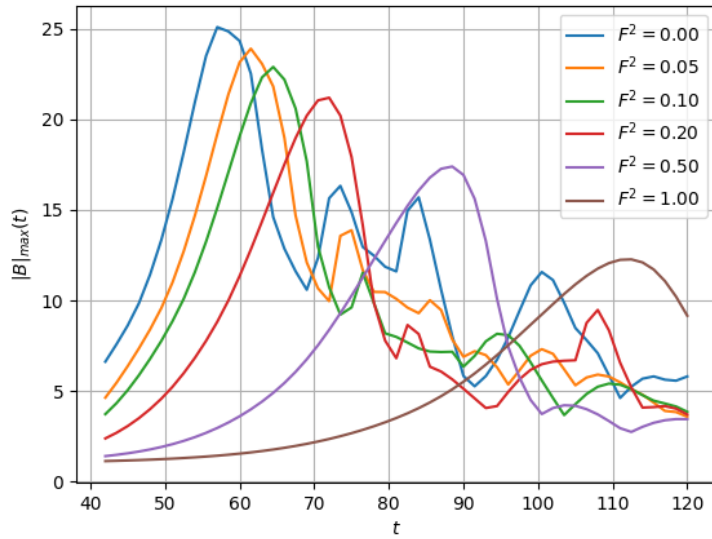
(a) Spatial maximum of the magnetic Jacobian,  $\mathcal{J}(A, \nabla^2 A)$ ,(b) Maximum of the magnetic field strength,  $|\mathbf{B}|$ 

Figure 6.18: Maxima of the magnetic Jacobian and field strength for several kinematic simulations with varied  $F^2$  showing a decrease in the (temporal) maximum of both quantities as  $F^2$  is increased ( $\text{Re} = 1000$ ,  $\text{Rm} = 500$ ,  $\beta = M = 0$ ).

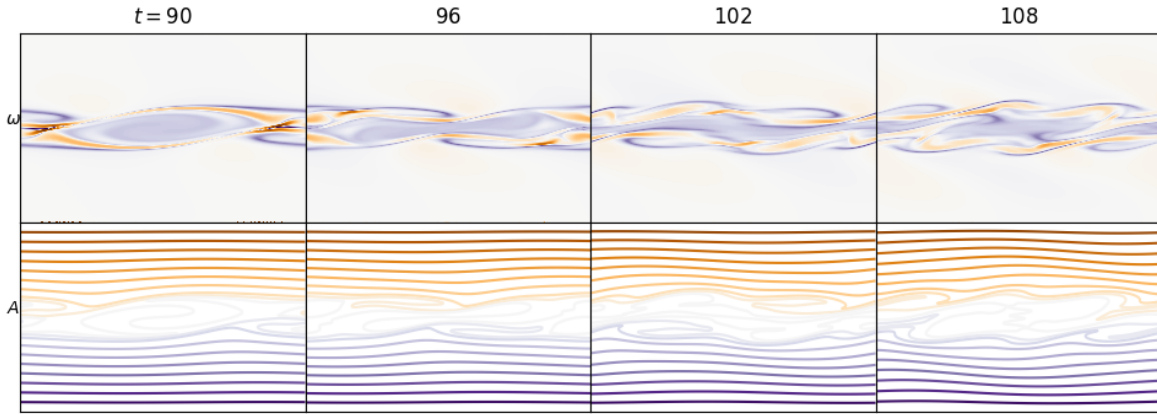


Figure 6.19: The relative vorticity,  $\omega = \nabla^2 h$ , and magnetic field lines (contours of  $A$ ) during the main disruption stage corresponding to the peak and trough of  $\Delta$  ( $90 \lesssim t \lesssim 120$ , cf. Figure 6.12). The parameters for this simulation are  $F^2 = 0.5$ ,  $\beta = 0.0$ ,  $M = 0.08$ ,  $\text{Re} = 1000$ ,  $\text{Rm} = 500$  but the qualitative description (in text) remains unchanged for a surprisingly wide range of  $M$  and a reasonably wide range of  $F^2$ .

## 6.5 $f$ -plane QGMHD - General Observations

### 6.5.1 Oscillations of $\Delta$

An interesting feature of the disruption plots is the change in the qualitative description of the time dependence of  $\Delta$  as  $F^2$  increases (compare Figure 6.9 and Figure 6.12). In the  $F^2 = 0.0$  case (Figure 6.9), disruption increases until around  $t = 100$  before settling to a constant value as dissipation sets in. With  $F^2 = 0.5$ , however, the disruption takes longer to develop initially (note here that the linear instability does not saturate until around  $t = 75$  unlike the  $F^2 = 0$  case where the instability saturates by  $t = 45$ ) but then rapidly increases at around  $t = 90$ , then rapidly decreases at around  $t = 110$ , before oscillating around a roughly constant value for  $t \gtrsim 150$ . Particularly surprising is that this qualitative description depends very little on the value of  $M$ . Additionally, this sudden spike in the disruption seems to be accompanied by no significant change in the kinetic energy (Figure 6.11) although the increase in disruption does align with the peak in the perturbation component of the magnetic energy.

The reasons for the disruption spike and the long-term oscillations of  $\Delta$  can be observed in Figure 6.19. As flux is expelled from the vortex, a magnetic field builds up roughly uniformly at its edges. Since the vortices are more elliptical now though, the Lorentz force ( $\mathcal{J}(A, \nabla^2 A)$ ) is not uniform and is greater where the curvature of the vortex is larger. This leads to large vorticity gradients developing predominantly at the large- $y$  edges of the vortex. As this region is disrupted magnetic flux is rapidly homogenised here (leading to the development of a zonal magnetic field, see §6.6) and the flow becomes essentially kinematic. This patch of vorticity now propagates due to the presence of the mean flow and the vortex rotation leading to vorticity waves which propagate zonally, in opposite directions, on either side of the vortex. The regular deformation of the central vortex by these vorticity waves results in the oscillations of  $\Delta(t)$ . Provided these waves are not too large, the central vortex will survive and  $\Delta(t)$  settles down to a constant value  $< 1$ .

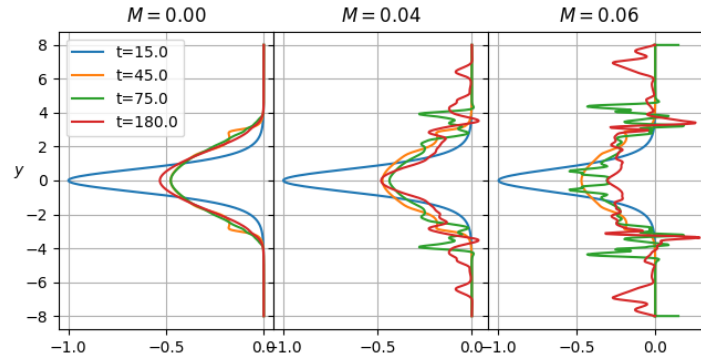


Figure 6.20: Relative vorticity,  $\bar{\omega}(y)$ , averaged over  $x$ , for  $M = 0.00, 0.04, 0.06$  at several times ( $F^2 = 0, \beta = 0, \text{Re} = 1000, \text{Rm} = 500$ ).

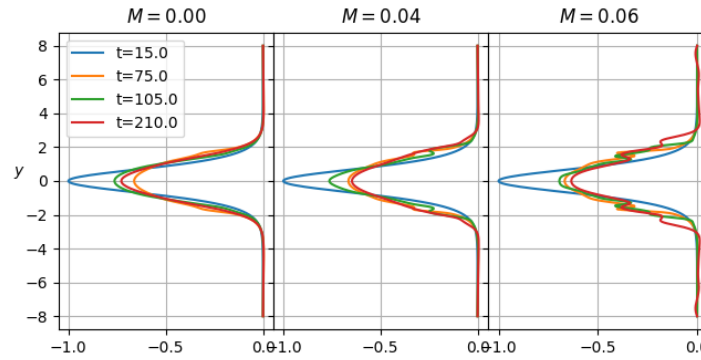


Figure 6.21: Relative vorticity,  $\bar{\omega}(y)$ , averaged over  $x$ , for  $M = 0.00, 0.04, 0.06$  at several times ( $F^2 = 0.5, \beta = 0, \text{Re} = 1000, \text{Rm} = 500$ ).

## 6.6 $f$ -plane QGMHD - Mean Flow Changes

We discussed in the preceding sections how increasing  $M$  can disrupt the vortex usually formed following a shear instability. In a more general sense, this is akin to breaking the enstrophy cascade to large scales and the onset of truly magnetohydrodynamic evolution, with vorticity spreading across the domain on small scales. Figure 6.20 shows the  $x$ -averaged vorticity, with the vorticity gradient rapidly tending towards homogeneity.

We have also seen that introducing  $F^2 \neq 0$  can weaken shear instability and flux expulsion, reducing vortex disruption. This reduces the spreading of vorticity - compare Figures 6.20 and 6.21. Vortex disruption,  $\bar{\Delta}$ , is reduced from around  $\bar{\Delta} = 0.6, 0.9$  ( $M = 0.04, 0.06, M^2\text{Rm} = 0.8, 1.8$ ) in the case  $F^2 = 0.0$ , to around  $\bar{\Delta} = 0.2, 0.4$  when  $F^2 = 0.5$  (see Figure 6.10).

A better comparison of the long-term dynamics of these systems comes from choosing a larger  $M$  so that  $\bar{\Delta}$  for  $F^2 = 0.5$  is roughly equivalent to the values with  $F^2 = 0.0$ .  $M = 0.08, 0.10$  ( $M^2\text{Rm} = 3.2, 5.0$ ) are good choices which lead to approximately equivalent values of  $\bar{\Delta}$ .

We have calculated the disruption parameter,  $\Delta$ , for many values of  $F^2$ , and we can use these values to match the value of  $\Delta$  between simulations rather than the value of  $M$ . Doing so

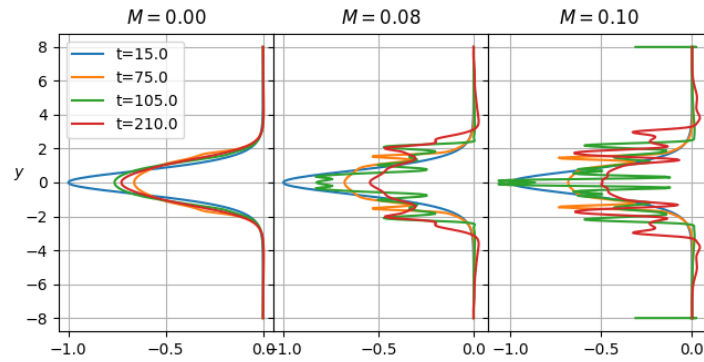


Figure 6.22: Relative vorticity,  $\bar{\omega}(y)$ , averaged over  $x$ , for  $M = 0.00, 0.08, 0.10$  at several times ( $F^2 = 0.5$ ,  $\beta = 0$ ,  $\text{Re} = 1000$ ,  $\text{Rm} = 500$ ).

we can see the clear evidence of disruption (Figure 6.22). An interesting long-term effect now appears where the relative vorticity,  $\omega$ , remains within the shear region and does not disperse further. This is due to the anisotropy introduced by  $F^2 > 0$ . However, it is unclear exactly why this dispersion pattern is produced.

## 6.A Numerical Method

### 6.A.1 Equations of Motion

$$\frac{\partial q}{\partial t} + \mathcal{J}(h, q) - M^2 \mathcal{J}(A, \nabla^2 A) = \frac{1}{\text{Re}} \nabla^4 h, \quad (6.19)$$

$$\frac{\partial A}{\partial t} + \mathcal{J}(h, A) = \frac{1}{\text{Rm}} \nabla^2 A, \quad (6.20)$$

$$q = \nabla^2 h - F^2 h + \beta y. \quad (6.21)$$

We wish to simulate the flow through a channel of a fluid subject to equations (6.19), (6.20), and (6.21). We assume that the flow is periodic in the  $x$ -direction, with period  $2\pi L_x$ , and set the channel width to be  $2L_y$  (i.e. walls at  $y = \pm L_y$ ), with  $L_y$  sufficiently large so that the boundaries themselves have a minimal effect of the evolution of the flow in the centre of the channel, whilst not so large that the details of the interesting dynamics in the centre of the channel are lost in the resolution. With this setup, we simulate the flow spectrally with Fourier-Chebyshev modes.

### 6.A.2 Basic State

We will examine the evolution of flows with initial state  $\mathbf{u}(x, y, t = 0) = U(y)\hat{\mathbf{x}}$ ,  $\mathbf{b}(x, y, t = 0) = B(y)\hat{\mathbf{x}}$ . Since we also wish for this flow to be represented at the boundaries, it is often useful to build this basic state directly into our governing equations and use as our variables the perturbation about this basic state, i.e.

$$A = - \int_{-L_y}^{L_y} B \, dy + \tilde{a}(x, y, t), \quad (6.22)$$

$$h = - \int_{-L_y}^{L_y} U \, dy + \tilde{h}(x, y, t), \quad (6.23)$$

$$q = -U' + F^2 \int_{-L_y}^{L_y} U \, dy + \beta y + \tilde{q}. \quad (6.24)$$

Substituting these expressions into the governing equations, (6.19)-(6.21), we obtain

$$\begin{aligned} \frac{\partial \tilde{q}}{\partial t} + \mathcal{J}(\tilde{h}, \tilde{q}) + (\beta + F^2 U - U'') \frac{\partial \tilde{h}}{\partial x} + U \frac{\partial \tilde{q}}{\partial x} \\ - M^2 \mathcal{J}(\tilde{a}, \nabla^2 \tilde{a}) + M^2 B'' \frac{\partial \tilde{a}}{\partial x} - M^2 B \nabla^2 \frac{\partial \tilde{a}}{\partial x} = \frac{1}{\text{Re}} \nabla^4 \tilde{h} - \frac{1}{\text{Re}} U''', \end{aligned} \quad (6.25)$$

$$\frac{\partial \tilde{a}}{\partial t} + \mathcal{J}(\tilde{h}, \tilde{a}) - B \frac{\partial \tilde{h}}{\partial x} + U \frac{\partial \tilde{a}}{\partial x} = \frac{1}{\text{Rm}} \nabla^2 \tilde{a} - \frac{1}{\text{Rm}} B', \quad (6.26)$$

$$\tilde{q} = \nabla^2 \tilde{h} - F^2 \tilde{h}. \quad (6.27)$$

For the particular flow

$$U(y) = \tanh y, \quad B(y) = 1, \quad (6.28)$$

we have (dropping tildes),

$$\frac{\partial q}{\partial t} + \mathcal{J}(h, q) + (\beta + \tanh y (F^2 + 2 \operatorname{sech}^2 y)) \frac{\partial h}{\partial x} + \tanh y \frac{\partial q}{\partial x} - M^2 \left( \mathcal{J}(a, \nabla^2 a) + \frac{\partial \nabla^2 a}{\partial x} \right) = \frac{1}{\operatorname{Re}} \nabla^4 h - \frac{6}{\operatorname{Re}} \operatorname{sech}^2 y \left( \tanh^2 y - \frac{1}{3} \right), \quad (6.29)$$

$$\frac{\partial a}{\partial t} + \mathcal{J}(h, a) - \frac{\partial h}{\partial x} + \tanh y \frac{\partial a}{\partial x} = \frac{1}{\operatorname{Rm}} \nabla^2 a, \quad (6.30)$$

$$q = \nabla^2 h - F^2 h. \quad (6.31)$$

### 6.A.3 Boundary Conditions

Equation (6.29) is fourth-order whilst equation (6.30) is of order two. Therefore six boundary conditions must be specified at  $y = \pm L_y$ .

Firstly, we choose

$$h = 0 \quad \text{at} \quad y = \pm L_y. \quad (6.32)$$

Since  $h$  is analogous to the streamfunction, this condition enforces zero net flow through the channel and impermeability of the walls. The absolute value of  $h$  is irrelevant since our evolution equations depend only on derivatives of  $h$ . This covers two of our boundary conditions.

The third and fourth boundary conditions are

$$q = 0 \quad \text{at} \quad y = \pm L_y. \quad (6.33)$$

Since

$$q = \nabla^2 h - F^2 h, \quad (6.34)$$

and  $h = 0$  at  $y = \pm L_y$ , condition (6.33) is equivalent to the stress-free condition

$$\frac{\partial u}{\partial y} = -\frac{\partial^2 h}{\partial y^2} = 0 \quad (6.35)$$

at the walls.

Finally, the boundary conditions on  $a$  can be chosen to be

$$a = 0 \quad \text{at} \quad y = \pm L_y. \quad (6.36)$$

This corresponds to fixed net flux through the channel.

### 6.A.4 Initial Conditions

We must also consider initial conditions for  $q$ ,  $a$ , and  $h$ . Since we have built in the basic flow and field to our governing equations, we need only initialise with a perturbation that breaks the symmetry and allows for interesting dynamics to develop.

The simplest way of achieving this is to define

$$h = \text{pert}(x, y), \quad a = 0, \quad \text{at } t = 0, \quad (6.37)$$

and from this calculate  $q$  through (6.31). Since  $a$  is updated at every time step by equation (6.30), the initial perturbation in  $h$  will immediately propagate to  $a$ . We then set

$$\text{pert}(x, y) = F(x)G(y), \quad (6.38)$$

where

$$F(x) = m_\alpha \cos(\alpha x) + \sum_{j \in \mathbb{N}} m_j \cos\left(j \frac{x - \bar{x}_j}{L_x}\right), \quad (6.39)$$

with  $m_j$  amplitude coefficients for the initial perturbation and noise,  $\alpha$  the wavenumber of the initial perturbation (generally  $k_{\max}$ ), and  $\bar{x}_j$  random coefficients in the range  $(-1, 1)$ , and

$$G(y) = \begin{cases} -e^{-y^2}, & \text{or} \\ \mathcal{L}^{-1}\left(e^{-y^2}\right), \end{cases} \quad (6.40)$$

where  $\mathcal{L}^{-1}$  is the inverse Laplacian operator.  $\text{pert}(x, y)$  is then a smooth function in  $x$  and  $y$  that approximately satisfies the boundary conditions on  $h$ . The former option is preferred since this allows for analytic computation of the initial energy, but we include the latter for comparison, in the 2DMHD case, with Mak et al. (2017).

### 6.A.5 Normalisation Transformation

The flow is simulated in the bounded domain  $x \in [0, 2\pi L_x)$ , so that the wavenumber of maximal instability corresponds to a single wave across the domain, and  $y \in [-L_y, L_y]$ , which is chosen to be small enough to allow for high-resolution simulation inside the domain, and large enough that the boundaries have a minimal effect on the evolution. This domain can be normalised to  $X \in [0, 2\pi)$ ,  $Y \in [-1, 1]$ , by the transformation

$$x = L_x X, \quad y = L_y Y. \quad (6.41)$$

Applying this transformation to the governing equations is straightforward,

$$\begin{aligned} \frac{\partial q}{\partial t} + \mathcal{J}(h, q) + \frac{1}{L_x} \tanh L_y Y \frac{\partial q}{\partial X} + \frac{1}{L_x} (\beta + \tanh L_y Y (F^2 + 2 \operatorname{sech}^2 L_y Y)) \frac{\partial h}{\partial X} \\ - M^2 \left( \mathcal{J}(a, \nabla^2 a) + \frac{1}{L_x} \frac{\partial \nabla^2 a}{\partial X} \right) = \frac{1}{\operatorname{Re}} \nabla^4 h - \frac{6}{\operatorname{Re}} \operatorname{sech}^2 L_y Y \left( \tanh^2 L_y Y - \frac{1}{3} \right), \end{aligned} \quad (6.42a)$$

$$\frac{\partial a}{\partial t} + \mathcal{J}(h, a) + \frac{1}{L_x} \left( \tanh L_y Y \frac{\partial a}{\partial X} - \frac{\partial h}{\partial X} \right) = \frac{1}{\operatorname{Rm}} \nabla^2 a, \quad (6.42b)$$

$$q = \nabla^2 h - F^2 h, \quad (6.42c)$$

where  $\mathcal{J}(\cdot, \cdot)$  and  $\nabla^2$  now include the normalisation coefficients  $L_x$  and  $L_y$ .

### 6.A.6 Temporal Discretisation

We will treat most terms with a third-order scheme (Adams-Bashforth-3) that balances accuracy with simplicity and runtime. However, the diffusion terms must be treated semi-implicitly (Crank-Nicolson) (Peyret, 2002) to reduce the possibility of numerical instability. Spatial derivatives are dealt with in the next section. Denoting the  $n$ th time step by a superscript, (6.42a)-(6.42c) become

$$\frac{q^{(n+1)} - q^{(n)}}{\Delta t} + \frac{23}{12}\mathcal{N}^{(n)} - \frac{16}{12}\mathcal{N}^{(n-1)} + \frac{5}{12}\mathcal{N}^{(n-2)} = \frac{1}{2} \left( \mathcal{D}^{(n+1)} + \mathcal{D}^{(n)} \right), \quad (6.43a)$$

$$\frac{a^{(n+1)} - a^{(n)}}{\Delta t} + \frac{23}{12}\mathcal{M}^{(n)} - \frac{16}{12}\mathcal{M}^{(n-1)} + \frac{5}{12}\mathcal{M}^{(n-2)} = \frac{1}{2} \left( \mathcal{C}^{(n+1)} + \mathcal{C}^{(n)} \right), \quad (6.43b)$$

$$q^{(n+1)} = (\nabla^2 - F^2) h^{(n+1)}, \quad (6.43c)$$

where

$$\begin{aligned} \mathcal{N}^{(i)} = \mathcal{N}[q^{(i)}, h^{(i)}, a^{(i)}] &= \mathcal{J}(h, q) + \frac{1}{L_x} \tanh L_y Y \frac{\partial q}{\partial X} \\ &+ \frac{1}{L_x} (\beta + \tanh L_y Y (F^2 + 2 \operatorname{sech}^2 L_y Y)) \frac{\partial h}{\partial X} \\ &- M^2 \left( \mathcal{J}(a, \nabla^2 a) + \frac{1}{L_x} \frac{\partial \nabla^2 a}{\partial X} \right) \\ &+ \frac{6}{\operatorname{Re}} \operatorname{sech}^2 L_y Y \left( \tanh^2 L_y Y - \frac{1}{3} \right) - \frac{F^2}{\operatorname{Re}} \nabla^2 h, \end{aligned} \quad (6.44a)$$

$$\mathcal{M}^{(i)} = \mathcal{M}[q^{(i)}, h^{(i)}, a^{(i)}] = \mathcal{J}(h, a) + \frac{1}{L_x} \left( \tanh L_y Y \frac{\partial a}{\partial X} - \frac{\partial h}{\partial X} \right), \quad (6.44b)$$

and

$$\mathcal{D}^{(i)} = \mathcal{D}[q^{(i)}, h^{(i)}, a^{(i)}] = \frac{1}{\operatorname{Re}} \nabla^2 q, \quad (6.45a)$$

$$\mathcal{C}^{(i)} = \mathcal{C}[q^{(i)}, h^{(i)}, a^{(i)}] = \frac{1}{\operatorname{Rm}} \nabla^2 a. \quad (6.45b)$$

### 6.A.7 Spatial Discretisation

Based on the geometry of our problem, we will use a pseudo-spectral Fourier-Chebyshev basis and at each time step calculate the values  $u_{kj}$  where

$$u(x, y_j) = \sum_k \hat{u}_k(y_j) e^{ikx}. \quad (6.46)$$

The  $y_j$  here are the specially selected collocation points. It is trivial to differentiate or integrate the Fourier modes since  $\frac{\partial u_k}{\partial x} = ik u_k$  and the nonlinear terms can be calculated by using an FFT to perform the multiplication in physical space. The Chebyshev modes are more complicated to differentiate, but we can calculate the nonlinear terms directly since the  $y_j$  correspond to points in physical space. The derivatives,  $\frac{\partial}{\partial y}$ , can be calculated using matrix multiplication. This does however raise the question of the inverse derivatives which comes up when using (6.43c) to calculate  $h^{(n+1)}$  and also in (6.43a) since the diffusion is treated semi-implicitly. As we will see, in both of these problems we can derive an operator of the form  $(D^2 - aI)$ , and therefore solve the inverse problem rapidly and accurately using the solver described later.

Denoting the Chebyshev  $n$ th differential matrix by  $D^n$ , and writing so that the operator (acting on  $(n+1)$  terms) in all three equations takes the form  $(D^2 - aI)$ , we obtain

$$\left( D^2 - L_y^2 \left( \frac{k^2}{L_x^2} + \frac{2\text{Re}}{\Delta t} \right) I \right) q^{(n+1)} = 2\text{Re}L_y^2 \left[ \frac{23}{12}\mathcal{N}^{(n)} - \frac{16}{12}\mathcal{N}^{(n-1)} + \frac{5}{12}\mathcal{N}^{(n-2)} - \frac{q^{(n)}}{\Delta t} - \frac{\nabla^2 q^{(n)}}{2\text{Re}} \right], \quad (6.47a)$$

$$\left( D^2 - L_y^2 \left( \frac{k^2}{L_x^2} + \frac{2\text{Rm}}{\Delta t} \right) I \right) a^{(n+1)} = 2\text{Rm}L_y^2 \left[ \frac{23}{12}\mathcal{M}^{(n)} - \frac{16}{12}\mathcal{M}^{(n-1)} + \frac{5}{12}\mathcal{M}^{(n-2)} - \frac{a^{(n)}}{\Delta t} - \frac{\nabla^2 a^{(n)}}{2\text{Rm}} \right], \quad (6.47b)$$

$$\left( D^2 - L_y^2 \left( \frac{k^2}{L_x^2} + F^2 \right) I \right) h^{(n+1)} = L_y^2 q^{(n+1)}, \quad (6.47c)$$

where

$$\mathcal{N} = \mathcal{J}(h, q) + \frac{ik}{L_x} [\tanh L_y Y q + (\beta + \tanh L_y Y (F^2 + 2 \text{sech}^2 L_y Y)) h] \quad (6.48a)$$

$$- M^2 \left( \mathcal{J}(a, \nabla^2 a) + \frac{ik}{L_x} \nabla^2 a \right) + \frac{6}{\text{Re}} \text{sech}^2 L_y Y \left( \tanh^2 L_y Y - \frac{1}{3} \right) - \frac{F^2}{\text{Re}} \nabla^2 h, \quad (6.48b)$$

$$\mathcal{M} = \mathcal{J}(h, a) + \frac{ik}{L_x} (\tanh L_y Y a - h), \quad (6.48c)$$

and

$$\nabla^2 f = \left( \frac{D^2}{L_y^2} - \frac{k^2}{L_x^2} \right) f, \quad (6.49a)$$

$$\mathcal{J}(f, g) = \frac{1}{L_x L_y} [\mathcal{F}(\mathcal{F}^{-1}(ikf)\mathcal{F}^{-1}(Dg) - \mathcal{F}^{-1}(Df)\mathcal{F}^{-1}(ikg))], \quad (6.49b)$$

with  $\mathcal{F}$  and  $\mathcal{F}^{-1}$  corresponding to the Fourier and inverse Fourier transforms respectively.

## 6.B Fast (Quasi-Tridiagonal Matrix) Solver

### 6.B.1 Transformation to normal form

We consider here the general problem of solving, in Chebyshev spectral space, the differential equation

$$\phi''(y) - a\phi(y) = b(y), \quad (6.50)$$

along with boundary conditions  $\phi(y = \pm 1) = \phi_{\pm}$ .

Let

$$\phi(y) = \sum_{j=0}^{N_y} \phi_j T_j(y), \quad (6.51)$$

where  $T_j$  are the Chebyshev polynomials of the first kind and  $\phi_j$  are the Chebyshev coefficients. The second derivative of  $\phi$ ,  $\phi^{(2)}$ , can then also be expressed in terms of  $T_j$  as

$$\phi^{(2)}(y) = \sum_{j=0}^{N_y-1} \phi_j^{(2)} T_j(y). \quad (6.52)$$

A useful recurrence relationship exists between the coefficients  $\phi_j^{(2)}$  and  $\phi_j$  (e.g. Boyd, 2001; Peyret, 2002), namely

$$P_j \phi_{j-2}^{(2)} + Q_j \phi_j^{(2)} + R_j \phi_{j+2}^{(2)} = \phi_j, \quad 2 \leq j \leq N_y - 1, \quad (6.53)$$

where

$$P_j = \frac{c_{j-2}}{4j(j-1)}, \quad Q_j = \frac{-e_{j+2}}{2(j^2-1)}, \quad R_j = \frac{e_{j+4}}{4j(j+1)}, \quad (6.54)$$

and

$$c_j = \begin{cases} 2, & \text{if } j = 0, \\ 1, & \text{if } j > 0, \end{cases}, \quad e_j = \begin{cases} 1, & \text{if } j \leq N_y - 1, \\ 0, & \text{if } j > N_y - 1. \end{cases} \quad (6.55)$$

Following Mak (2013), we then consider the coefficients of (6.50) at each mode. This gives

$$\phi_j^{(2)} - a\phi_j = b_j. \quad (6.56)$$

Substituting (6.56) into (6.53), we obtain

$$p_j \phi_{j-2} + q_j \phi_j + r_j \phi_{j+2} = f_j, \quad 2 \leq j \leq N_y - 1, \quad (6.57)$$

where

$$p_j = aP_j, \quad q_j = aQ_j - 1, \quad r_j = aR_j, \quad (6.58)$$

and

$$f_j = -(P_j b_{j-2} + Q_j b_j + R_j b_{j+2}). \quad (6.59)$$

Note that  $P$ ,  $Q$ , and  $R$  are capitalised in the definition of  $f$ . Further, although  $b_j$  is undefined for  $j > N_y - 1$ , it never enters the problem since it is always preceded by a zero.

These  $N_y - 2$  equations are then supplemented by the boundary conditions  $\phi(y = \pm 1) = \phi_{\pm}$  which can be expressed in terms of the coefficients  $\phi_j$  as

$$\sum_{j=0}^{N_y-1} \phi_j = \phi_+, \quad \sum_{j=0}^{N_y-1} (-1)^j \phi_j = \phi_-, \quad (6.60)$$

or equivalently

$$\sum_{j=1}^{N_y/2} \phi_{2j-2} = \frac{\phi_+ + \phi_-}{2}, \quad \sum_{j=1}^{N_y/2} \phi_{2j-1} = \frac{\phi_+ - \phi_-}{2}. \quad (6.61)$$

The system now decouples, with the odd and even modes each forming a quasi-tridiagonal linear problem (tridiagonal plus a single full row). We can therefore adapt the QTD solver of Thual (1986) (Peyret, 2002, summarised in) to solve this system in  $\mathcal{O}(N_y)$  operations.

### 6.B.2 Solving a Split-Quasi-Tridiagonal System

We wish to solve the system given by (6.57) and (6.61). Let us assume that  $\phi$  obeys the recurrence relationship

$$\phi_j = X_{j-2} \phi_{j-2} + Y_{j-2}. \quad (6.62)$$

Then, for  $j = N_y - 1, N_y - 2$ ,

$$p_{N_y-1}\phi_{N_y-3} + q_{N_y-1}\phi_{N_y-1} = f_{N_y-1}, \quad (6.63)$$

$$p_{N_y-2}\phi_{N_y-4} + q_{N_y-2}\phi_{N_y-2} = f_{N_y-2}, \quad (6.64)$$

by (6.57), and hence

$$X_{N_y-3} = \frac{-p_{N_y-1}}{q_{N_y-1}}, \quad Y_{N_y-3} = \frac{f_{N_y-1}}{q_{N_y-1}}, \quad (6.65)$$

$$X_{N_y-4} = \frac{-p_{N_y-2}}{q_{N_y-2}}, \quad Y_{N_y-4} = \frac{f_{N_y-2}}{q_{N_y-2}}. \quad (6.66)$$

For  $j \leq N_y - 3$ ,

$$p_j\phi_{j-2} + q_j\phi_j + r_j\phi_{j+2} = f_j. \quad (6.67)$$

Substituting (6.67) into (6.62) with  $j = j + 2$ , we obtain

$$p_j\phi_{j-2} + q_j\phi_j + r_j(X_j\phi_j + Y_j) = f_j, \quad (6.68)$$

which can be rearranged to give

$$\phi_j = \frac{-p_j}{q_j + r_jX_j}\phi_{j-2} + \frac{f_j - r_jY_j}{q_j + r_jX_j}, \quad (6.69)$$

and hence  $X_j$  and  $Y_j$  obey the recurrence relation

$$X_{j-2} = \frac{-p_j}{q_j + r_jX_j}, \quad Y_{j-2} = \frac{f_j - r_jY_j}{q_j + r_jX_j}, \quad 0 \leq j \leq N_y - 1. \quad (6.70)$$

Using this formula, the coefficients  $\phi_j$  can be calculated provided initial values  $\phi_0, \phi_1$ . To calculate these, we assume that  $\phi_j$  can be expressed as a function of  $\phi_0, \phi_1$  by the relation

$$\phi_j = \theta_j\phi_{j \bmod 2} + \lambda_j \quad 0 \leq j \leq N_y - 1. \quad (6.71)$$

Trivially,  $\theta_0, \theta_1 = 1, \lambda_0, \lambda_1 = 0$  and, using (6.62),

$$\begin{aligned} \phi_{j+2} &= X_j\phi_j + Y_j, \\ \implies \phi_{j+2} &= X_j(\theta_j\phi_j + \lambda_j) + Y_j, \\ \implies \theta_{j+2} &= X_j\theta_j, \quad \lambda_{j+2} = X_j\lambda_j + Y_j. \end{aligned} \quad (6.72)$$

We can then substitute this expression for  $\phi_j$  into (6.61), which gives that

$$\begin{aligned} \left( \sum_{j \text{ even}} \theta_j \right) \phi_0 + \left( \sum_{j \text{ even}} \lambda_j \right) &= \frac{\phi_+ + \phi_-}{2}, & \left( \sum_{j \text{ odd}} \theta_j \right) \phi_1 + \left( \sum_{j \text{ odd}} \lambda_j \right) &= \frac{\phi_+ - \phi_-}{2}, \\ \phi_0 &= \frac{\phi_+ + \phi_- - 2 \sum_{j \text{ even}} \lambda_j}{2 \sum_{j \text{ even}} \theta_j}, & \phi_1 &= \frac{\phi_+ - \phi_- - 2 \sum_{j \text{ odd}} \lambda_j}{2 \sum_{j \text{ odd}} \theta_j}. \end{aligned} \quad (6.73)$$

**Summary** The algorithm can therefore be summarised as:

1. Calculate  $X_{N_y-1}$ ,  $X_{N_y-2}$ ,  $Y_{N_y-1}$ , and  $Y_{N_y-2}$  using (6.65) and (6.66) and hence all  $X_j$ ,  $Y_j$  from (6.70).
2. Calculate  $\theta_j$ ,  $\lambda_j$  using the initial values and the recurrence relation (6.72).
3. Finally, calculate  $\phi_0$ ,  $\phi_1$  using (6.73) and thus all  $\phi_j$  using (6.62).

### 6.B.3 Solving in Fourier-Chebyshev space

The method above shows how the differential equation

$$\phi''(y) - a\phi(y) = b(y) \quad (6.74)$$

can be solved efficiently in  $\mathcal{O}(N_y)$  steps. This has a clear application to the inversion of the Laplacian operator (as well as many others) in Fourier-Chebyshev space since for each Fourier wavenumber,  $k$ , the problem can be expressed in exactly the above form with  $a = k^2$  (or  $a = a(k)$ ). We will show now that a final significant performance enhancement can be achieved by treating, e.g., the Laplacian inversion problem not as a series of  $N_x$  matrix inversions, but rather as the inversion of a rank-4 ( $N_x \times N_x \times N_y \times N_y$ ) tensor with  $b$  a rank-2 ( $N_x \times N_y$ ) tensor.

To efficiently solve, in Fourier-Chebyshev space, a problem of the form

$$(D^2 - a(k)I)\phi = \mathbf{b}, \quad (6.75)$$

where  $\phi$ ,  $\beta_k$  are variables defined at the collocation points  $y_j$ , we apply the following method.

#### Pre-Processing

- Calculate the rank-1 tensors  $P_j$ ,  $Q_j$ ,  $R_j$  for every  $j \in \{0, \dots, N_y - 1\}$  and the rank-2 tensors  $p_{kj}$ ,  $q_{kj}$ ,  $r_{kj}$ ,  $X_{kj}$ ,  $\theta_{kj}$  for each  $k \in \{0, \dots, N_x - 1\}$ ,  $j \in \{0, \dots, N_y - 1\}$ .

#### At each time step

1. Calculate the coefficients  $f_{kj}$  from  $\hat{b}_{kj}$  using (6.59).
2. Calculate  $Y_{k,N_y-2}$ ,  $Y_{k,N_y-3}$ ,  $Y_{kj}$  and  $\lambda_{kj}$  using (6.65), (6.66), (6.70), and (6.72) respectively.
3. Use these to calculate  $\hat{\phi}_{kj}$  from (6.73) and (6.62)

### 6.B.4 Example: The Vorticity Equation

As an example of the execution of the above method, we provide the Python code for solving the vorticity equation (6.47a) and our vectorised code for solving the QTD system.

```

1 class QTDSolve2D():
2     # Class to generate and solve the system of equations
3     # (D2-a(k) I)u=w
4     # where a(k) is an array of length Nx

```

```

5 # Input: w is an (Nk,Ny) array of Chebyshev spectral coefficients.
6 # Output: An (Nk,Ny) array u of spectral coefficients.
7 # (D2 denotes the Chebyshev second derivative, and I the identity, matrix)
8 # bcs can be defined but is usually an Nk array of zeros, i.e. u(y=+-1)=0.
9
10 def __init__(self, Nk, Ny, a):
11     if a.shape != (Nk,):
12         raise ValueError("a is required to be a 1D array of length Nk={}".
13 format(Nk))
14
15     self.Nk = Nk
16     self.Ny = Ny
17
18     self.P = np.zeros((1,Ny-2))
19     self.Q = np.zeros((1,Ny-2))
20     self.R = np.zeros((1,Ny-2))
21
22     self.Pprime = np.zeros((Nk,Ny-2))
23     self.Qprime = np.zeros((Nk,Ny-2))
24     self.Rprime = np.zeros((Nk,Ny-2))
25
26     self.X = np.zeros((Nk,Ny-2))
27     self.theta = np.zeros((Nk,Ny))
28
29     self.setup(a)
30
31 def setup(self, a):
32     # Setup helper vars
33     c = np.ones(self.Ny)
34     c[0] += 1
35     e = np.ones(self.Ny)
36     for i in range(1,5):
37         e[-i] = 0
38
39     # Generate the arrays P, Q, R
40     for i in range(2,self.Ny):
41         self.P[0,i-2] = c[i-2]/(4*i*(i-1))
42         self.Q[0,i-2] = -e[i-2]/(2*(i**2-1))
43         self.R[0,i-2] = e[i]/(4*i*(i+1))
44
45     # Now use these to generate P', Q', R'
46     # Note that, wrt notes, P'=p, Q'=q, R'=r
47     for k in range(self.Nk):
48         for i in range(0,self.Ny-2):
49             self.Pprime[k,i] = a[k]*self.P[0,i]
50             self.Qprime[k,i] = a[k]*self.Q[0,i] - 1
51             self.Rprime[k,i] = a[k]*self.R[0,i]
52
53     # Finally, we calculate X and theta
54     for k in range(self.Nk):
55         self.X[k,-1] = -self.Pprime[k,-1]/self.Qprime[k,-1]
56         self.X[k,-2] = -self.Pprime[k,-2]/self.Qprime[k,-2]
57         for i in range(self.Ny-5,-1,-1):
58             self.X[k,i] = -self.Pprime[k,i]/(self.Qprime[k,i]+self.Rprime[

```

```

59     self.theta[k,0],self.theta[k,1] = 1,1
60     for i in range(2,self.Ny):
61         self.theta[k,i] = self.X[k,i-2] * self.theta[k,i-2]
62
63     def solve(self, w, k, bcs):
64         # Solve the lap. int. problem using the QTD method of Thual (1986)
65
66         # First, transform w -> f (following the transformation of the entire
67         system to a QTD matrix)
68         f = -(self.P[:,self.Ny-4]*w[:,self.Ny-4]+self.Q[:,self.Ny-4]*w[:,2:
69         self.Ny-2]+self.R[:,self.Ny-4]*w[:,4:self.Ny])
70
71         f = np.append(f,-(self.P[:,self.Ny-4]*w[:,self.Ny-4:self.Ny-2] + self
72         .Q[:,self.Ny-4]*w[:,self.Ny-2:]),axis=1)
73
74         # Next generate Y
75         Y = np.zeros((self.Nk,self.Ny-2),dtype=np.complex_)
76         Y[:,self.Ny-3],Y[:,self.Ny-4] = f[:,self.Ny-3]/self.Qprime[:,self.Ny
77         -3], f[:,self.Ny-4]/self.Qprime[:,self.Ny-4]
78
79         for i in range(self.Ny-5,-1,-1):
80             Y[:,i] = (f[:,i]-self.Rprime[:,i]*Y[:,i+2])/(self.Qprime[:,i]+self
81             .Rprime[:,i]*self.X[:,i+2])
82
83         # Calculate lambda
84         lamb = np.zeros((self.Nk,self.Ny),dtype=np.complex_)
85         for i in range(2,self.Ny):
86             lamb[:,i] = self.X[:,i-2]*lamb[:,i-2]+Y[:,i-2]
87
88         # Finally calculate u
89         u = np.zeros((self.Nk,self.Ny),dtype=np.complex_)
90         u[:,0] = (bcs[:,0]+bcs[:,1]-2*np.sum(lamb[:,::2],axis=1))/np.sum(2*
91         self.theta[:,::2],axis=1)
92         u[:,1] = (bcs[:,0]-bcs[:,1]-2*np.sum(lamb[:,1::2],axis=1))/np.sum(2*
93         self.theta[:,1::2],axis=1)
94         for i in range(2,self.Ny):
95             u[:,i] = self.X[:,i-2]*u[:,i-2]+Y[:,i-2]
96
97     return u

```

Listing 6.1: Definition of the QTD class

```

1 self.q_solver = QTDSolverClass.QTDSolve2D(Nx, Ny, Ly**2*(self.ks[:,0]**2/Lx
2 **2+2*Re/dt))

```

Listing 6.2: Initialisation of the QTD class

```

1 def q_Update(self):
2     # Generate the new value of q from the vorticity equation
3
4     order = 3 # Adams-Bashforth order (currently fixed)
5
6     # Zero result
7     rhs = np.zeros((self.Nx,self.Ny),dtype=np.complex_)
8
9     # Calculate the RHS
10

```

```
11     # Add on the AB_terms
12     for m in range(order):
13         rhs += (2*self.Re*self.Ly**2)*self.ABcoeffs[order-1,m]*self.hyd_terms[
14             m,[:, :]]
15
16     # Add on the time derivative term
17     rhs -= (2*self.Re*self.Ly**2/self.dt)*self.q
18
19     # Add on the diffusion term
20     rhs -= self.Ly**2*nmc.Laplacian(self.q, self.ks, self.C2_spec, self.Lx,
21         self.Ly)
22
23     # Solve for new q
24     return self.q_solver.solve(rhs, self.ks, np.zeros((self.Nx, 2)))
```

Listing 6.3: Inverting the vorticity equation for  $q$

## 6.C The Okubo-Weiss Parameter

### 6.C.1 Definition

Consider a null point  $(x_0, y_0)$  in a two-dimensional flow, where  $\mathbf{u} = \left(\frac{dx}{dt}, \frac{dy}{dt}\right) = (0, 0)$ . Assuming that this point is “not too singular”, we can write down the first-order perturbation of this flow,

$$\frac{d}{dt} \begin{pmatrix} x \\ y \end{pmatrix} = \begin{pmatrix} \left(\frac{\partial u}{\partial x}\right)_{\mathbf{x}_0} & \left(\frac{\partial u}{\partial y}\right)_{\mathbf{x}_0} \\ \left(\frac{\partial v}{\partial x}\right)_{\mathbf{x}_0} & \left(\frac{\partial v}{\partial y}\right)_{\mathbf{x}_0} \end{pmatrix} \begin{pmatrix} x \\ y \end{pmatrix} \quad (6.76)$$

The matrix above depends on our choice of axes,  $\hat{\mathbf{x}}, \hat{\mathbf{y}}$ . However, we can define some physical parameters, which in Cartesian geometry take the form

- Divergence:  $\gamma := \left(\frac{\partial u}{\partial x} + \frac{\partial v}{\partial y}\right)_{\mathbf{x}_0}$
- Vorticity:  $\omega := \left(\frac{\partial v}{\partial x} - \frac{\partial u}{\partial y}\right)_{\mathbf{x}_0}$
- Normal Strain:  $\alpha := \left(\frac{\partial u}{\partial x} - \frac{\partial v}{\partial y}\right)_{\mathbf{x}_0}$
- Shearing Strain:  $\beta := \left(\frac{\partial v}{\partial x} + \frac{\partial u}{\partial y}\right)_{\mathbf{x}_0}$

With these parameters, the flow about the null point can be written as

$$\frac{d}{dt} \begin{pmatrix} x \\ y \end{pmatrix} = \frac{1}{2} \begin{pmatrix} \gamma + \alpha & -\omega + \beta \\ \omega + \beta & \gamma - \alpha \end{pmatrix} \begin{pmatrix} x \\ y \end{pmatrix}. \quad (6.77)$$

The eigenvalues of this flow are given by the solutions,  $\lambda$ , of

$$\begin{vmatrix} \gamma + \alpha - 2\lambda & -\omega + \beta \\ \omega + \beta & \gamma - \alpha - 2\lambda \end{vmatrix} = 0 \quad (6.78)$$

which gives

$$\lambda_1 = \frac{1}{2} \left( \gamma + (\alpha^2 + \beta^2 - \omega^2)^{1/2} \right), \quad \lambda_2 = \frac{1}{2} \left( \gamma - (\alpha^2 + \beta^2 - \omega^2)^{1/2} \right). \quad (6.79)$$

For divergence free flows ( $\gamma = \nabla \cdot \mathbf{u} = 0$ ), the characteristics of the flow about a null point  $(x_0, y_0)$  are therefore determined entirely by the parameter,

$$W =: \frac{1}{4} (\alpha^2 + \beta^2 - \omega^2) = \frac{1}{4} \left[ \left( \frac{\partial u}{\partial x} - \frac{\partial v}{\partial y} \right)^2 + \left( \frac{\partial v}{\partial x} + \frac{\partial u}{\partial y} \right)^2 - \left( \frac{\partial v}{\partial x} - \frac{\partial u}{\partial y} \right)^2 \right], \quad (6.80)$$

known as the Okubo-Weiss Vortex parameter (Okubo, 1970; Weiss, 1991) (this is the Hunt et al. (1988) Q-criterion in 3D). If  $W > 0$ ,  $\lambda_1, \lambda_2$  are real,  $(x_0, y_0)$  is a saddle point, and the flow is hyperbolic at this point, with inflow along the characteristic defined by the eigenvector of  $\lambda_2$ , and outflow along the eigenvector of  $\lambda_1$ . If instead,  $W < 0$ , then the eigenvalues  $\lambda_1, \lambda_2$  are a complex conjugate pair and purely imaginary. Hence the flow around the null point is a vortex with no net in/outflow. In the (physically unlikely) case that  $W = 0$ , we instead

must look towards the quadratic terms of our expansion to determine the characteristics of the flow.

### 6.C.2 The O-W Parameter for QG Flows

In the QG system, the leading order flow,  $(u_0, v_0)$ , is divergence-free and thus can be expressed by a streamfunction,  $h$ , defined by  $\mathbf{u}_0 = -\nabla \times h\hat{\mathbf{z}}$ . Substituting this into our definition for  $W$ , we find that

$$W(h(x, y, t)) = \left( \frac{\partial^2 h}{\partial x \partial y} \right)^2 - \frac{\partial^2 h}{\partial x^2} \frac{\partial^2 h}{\partial y^2}, \quad (6.81)$$

i.e.  $W$  is the Gaussian curvature of  $h$ .

### 6.C.3 Example: Two-dimensional MHD

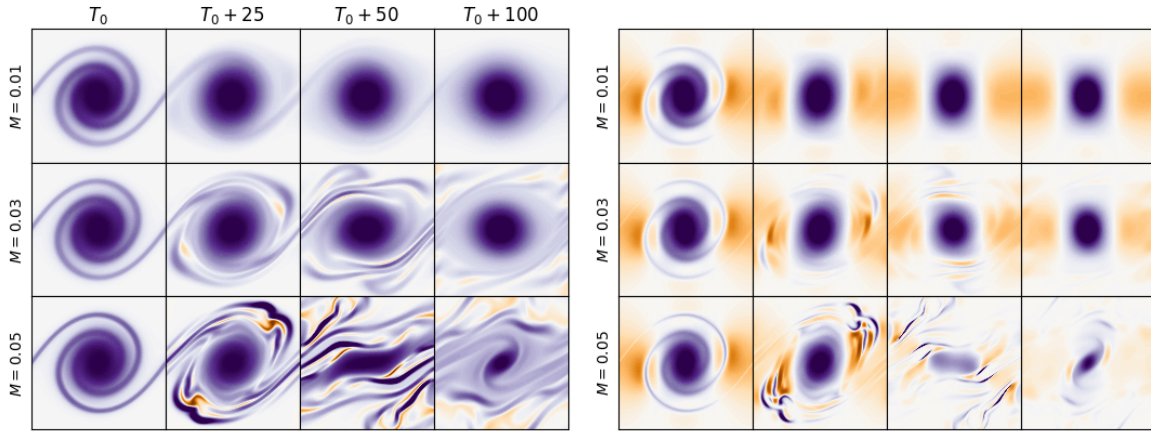


Figure 6.23: Plots of the vorticity,  $\omega$  (left), and the vortex parameter,  $W$  (right), for three flows with increasing disruption ( $\text{Re} = \text{Rm} = 500$ ,  $N_x = N_y = 512$ ,  $M = 0.01, 0.03, 0.05$ ,  $F^2 = \beta = 0$ ,  $L_x = 2\pi/0.446$ ,  $L_y = 8.0$ ; plot for  $|y| \leq L_y/2$ ).

The presence of a vortex corresponds to a large, uniform, region of negative  $W$  (blue, right side of Figure 6.23). As this vortex is disrupted the region of negative  $W$  decreases in size, corresponding to the vortex remnant. The region surrounding this which, on the left of Figure 6.23, is dominated by negative vorticity, does not correspond to a vortex, but rather vortical turbulence, and does not correspond to negative  $W$ .

### 6.C.4 The Mak Disruption Parameter

Mak et al. (2017) introduce a parameter,  $\Delta(t)$ , which uses the Okubo-Weiss parameter defined above to define the disruption of a vortex in magnetohydrodynamic, relative to kinematic, flows. With

$$W(P; x, y, t) = W_M(x, y, t) \quad (6.82)$$

known ( $P$  our run parameters,  $M$ ,  $\text{Re}$ ,  $\beta$ , etc.) we first define a vortex as any region  $A_M(t)$  where

$$W(x, y, t) < -0.2\sigma(t), \quad (6.83)$$

with  $\sigma(t)$  the standard deviation of  $W$ . This metric is often used in oceanography (e.g. Isern-Fontanet et al., 2006; Waugh et al., 2006) and the arbitrary constant, 0.2, is used primarily since it reliably gives the “correct” vortex boundaries and it matches the value used in Mak et al. (2017).

For most flows the parent vortex is simple to identify (e.g. Figure 6.23). However, in severely disrupted cases (see  $M = 0.05$  in Figure 6.23) the parent vortex can be divided and new vortical regions can form, not necessarily originating from the initial instability. Since the instability has zero phase speed in 2DMHD, Mak et al. (2017) adopt the convention of defining the parent vortex as the region (with  $W < -0.2\sigma$ ) which is contiguous to the centre of the domain. The disruption parameter  $\Delta$  is now defined by a relative integral of  $W$  over this region in kinematic and magnetic cases, i.e.,

$$\Delta(M; t) = 1 - \frac{\int_{A_M(t)} W_M(x, y, t; M) dA}{\int_{A_0(t)} W_M(x, y, t) dA}, \quad (6.84)$$

so that  $\Delta = 0$  represents a vortex identical to the one produced in kinematic simulations, whilst  $\Delta = 1$  represents a completely disrupted one. Note that whilst  $\Delta \leq 1$  is certainly true,  $\Delta$  is not necessarily positive.

We must deviate slightly from Mak et al. (2017) since the zonal phase speed of instability is non-zero when  $\beta \neq 0$ , although we would expect no lateral motion of the vortex due to the symmetry of our equations. As such, we opt for the definition that the parent vortex is the region  $A$  (with  $W < -0.2\sigma$ ) which is contiguous to the point where  $y = 0$  and  $x$  is the maximum of the  $k = 1$  component of the streamfunction  $h$ . This gives essentially identical results to Mak et al. (2017) when  $\beta, F^2 = 0$  and extends well when  $\beta > 0$ .

An additional improvement that is sometimes implemented is to define  $\bar{\Delta}(t)$  (sometimes with the bar dropped) from the method above with the exception that  $h \rightarrow \bar{h}$ , with  $\bar{h}$  defined for  $i \geq N$  as

$$\bar{h}(x, y, t_i) = \frac{1}{\sum_j w_j} \sum_{j=i-N}^{i+N} w_j h(x - \theta(t), y, t_j), \quad w_j = e^{-\frac{1}{2} \left( \frac{t_j - t_i}{\sigma} \right)^2}, \quad (6.85)$$

where  $\theta(t)$  is the phase of the  $k = 1$  mode and is constant when  $\beta = 0$ . The limit  $\sigma \rightarrow 0$  recovers the value of  $h$  at a single time step, whilst  $\sigma \rightarrow \infty$  would give a uniform weighting over the time steps  $\{t_{i-N}, \dots, t_{i+N}\}$ .

### 6.C.5 Example: Calculating $W$ with a Gaussian-averaging of $h$

Figure 6.24 shows an example of the averaging defined in (6.85) for one simulation. By averaging with large  $\sigma$  the sporadic structures that appear around the vortex disappear and the main vortex region becomes clear. Otherwise, see, e.g., the top row, these sporadic structures may be connected with the vortex by regions of negative  $W$  leading to irregular derived vortex regions. The breaking and recombination of these sporadic structures with the central vortex can lead to chaotically variation of  $W$ .

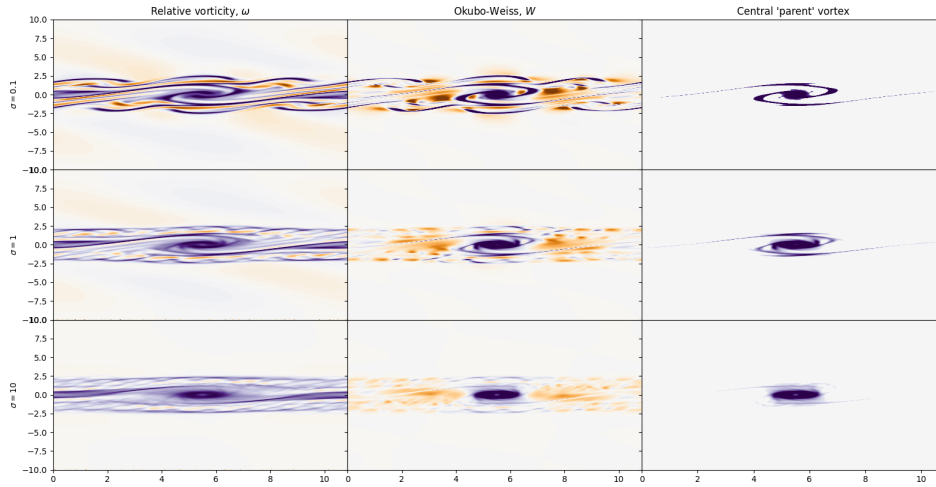


Figure 6.24: An example of calculating  $W$  after averaging  $h$  over several time with a Gaussian weighting. The rows show different values of  $\sigma$  with time steps weighted by (6.85).

## 6.D Ellipticity and Eccentricity

The simplest method for calculating the ellipticity of a vortex is to calculate the lengths of its semi-major and semi-minor axes. Using a snapshot of a given simulation these lengths can be estimated with a step-by-step method as follows:

1. Estimate the centre of the vortex.

The simulations above are set up in such a way that the centre of the vortex is expected to appear in the centre of the domain and this is usually realised here. However, there is no guarantee that this is the case, particularly when  $\beta \neq 0$  and unstable modes have a non-zero phase speed.

To estimate the centre then, we first assume that the symmetry in  $y$  guarantees the vortex appearing on the axis  $y = 0$ . We then calculate  $\omega$  over this line and take a Fourier transform of the data. The phase of the  $k = 1$  mode then gives a reliable estimate of the vortex centre.

2. Find the offsets of the two axes.

One might expect that vortices are always aligned with the flow and hence the two axes are in the  $\hat{y}$  and  $\hat{x}$  directions. This, however, seems often not to be the case and vortices end up tilting (and sometimes wobbling) due to the shearing strain acting on either side. To estimate the offset at a particular time, then, we draw a circle around the centre of the vortex and take the minimum and maximum of the streamfunction on this circle as the directions of the semi-major and semi-minor axes. From several tests, it seems that this estimate is essentially fixed with respect to the radius of the circle and so it is only required that the circle be entirely contained within the (undisrupted) region of the vortex.

3. Calculate the lengths of the two axes.

The length of the semi-major axis is now taken to be the radius of the circle from the above step. The length of the semi-minor axis is now calculated by interpolating to

find the distance from the centre at which the values of the streamfunction match. The streamfunction,  $h$ , is used here rather than e.g.  $q$  or  $\omega$ , since it is generally monotonic as we extend outwards from the centre of the vortex.

We can see how this method operates graphically in Figure 6.25.

Using the semi-major and minor axes,  $a$ , and  $b$ , we can calculate two interesting parameters for the ellipse: the ellipticity,

$$\eta = 1 - \frac{b}{a}, \quad (6.86)$$

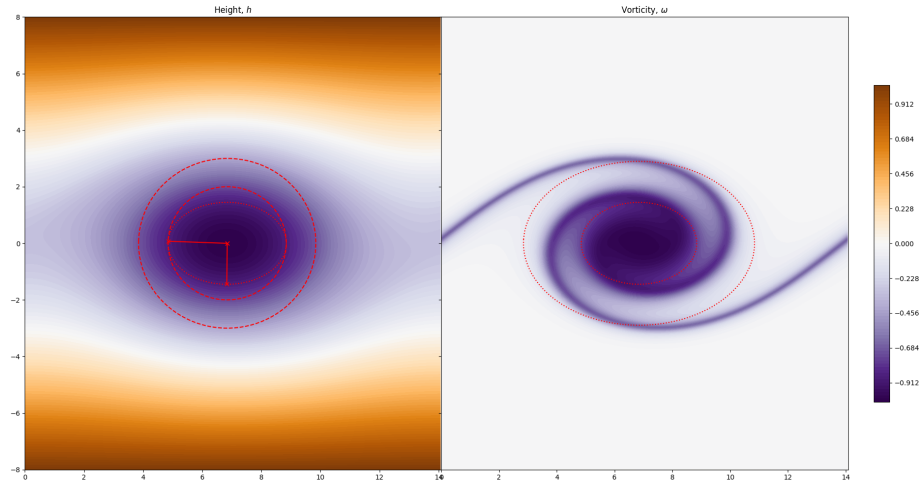
and the eccentricity

$$e = \sqrt{1 - \frac{b^2}{a^2}}, \quad (6.87)$$

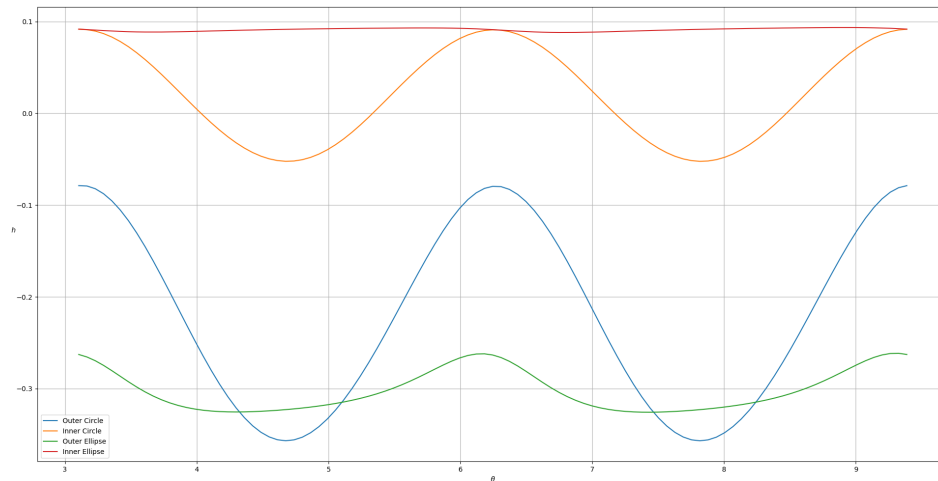
which are related by

$$\eta = 1 - \sqrt{1 - e^2}, \quad (6.88)$$

and take values in the range  $[0, 1)$ , with  $\eta = e = 0$  defining a circle, and  $\eta = e = 1$  defining a line.



(a) Plots of the streamfunction,  $h$ , and the relative vorticity,  $\omega$ , at a moment in simulation  $U040$ . The construction lines are added by which the semi-major and semi-minor axis lengths can be calculated. At this moment, we find the semi-major axis length,  $a = 2.0$ , and the semi-minor axis length,  $b = 1.448$ . This gives an ellipticity  $\eta = 0.276$ .



(b) We plot the value of the streamfunction,  $h$ , over the construction circles (dashed in the contour plots above) and calculated ellipses (dotted). We use  $h$  over the circles to estimate the angles of the semi-major/minor axes and expect the values of  $h$  over the ellipse to be approximately constant. This last point is not realised exactly since the vortex is not a perfect ellipse and changes its tilt slightly as we move outwards.

Figure 6.25: Constructions used to calculate the ellipticity.

## 6.E Growth Rate Tables

### 6.E.1 2DMHD Simulations

Name	$F^2$	$M$	Field-Varying Simulations				
			Sim $k_1$	Hydro $\sigma$	Actual $\sigma$	Ideal $k_1$	Max $\sigma$
U110	0.0	0.00	0.446	0.190	0.190	0.446	0.190
U111	0.0	0.005	0.446	0.190	0.190	0.445	0.190
U112	0.0	0.01	0.446	0.190	0.190	0.445	0.190
U113	0.0	0.02	0.446	0.190	0.189	0.445	0.190
U114	0.0	0.04	0.446	0.190	0.189	0.445	0.190
U115	0.0	0.06	0.446	0.190	0.188	0.445	0.189
U116	0.0	0.08	0.446	0.190	0.188	0.444	0.189
U117	0.0	0.10	0.446	0.190	0.187	0.442	0.188
U118	0.0	0.20	0.446	0.190	0.181	0.432	0.181
U119	0.0	0.30	0.446	0.190	0.169	0.416	0.170

Table 6.2: Table of the wavenumber,  $k$ , and growth rate,  $\sigma$ , expected in simulations with  $M \geq 0$  (central column) compared to the wavenumber from linear theory that maximises growth rate (right column).

### 6.E.2 QG $F^2$ -varied Simulations

Table 6.3 shows a selection of the simulations used section §6.4. One of the important points here is that  $k_1$  (or equivalently  $L_x = 2\pi/k_1$ ) is determined, for each value of  $F^2$ , so that the linear growth rate,  $\sigma$ , is maximised. From  $\sigma$  we then also provide an estimate of the saturation time of the linear instability,  $T_0 \sim 1/\sigma$ , which is dependent on the amplitude of initial perturbations. The values in Table 6.3 are taken from our linear analysis (§5) but agree well with numerically calculated values (e.g. Figure 6.14).

QG Simulations, $F^2$ varied				
Name	$F^2$	Wavenumber, $k_1$	Linear Growth Rate, $\sigma$	Saturation Time, $T_0$
U040	0.0	0.446	0.190	42.1
U210	0.001	0.447	0.190	-
U211	0.005	0.451	0.189	-
U212	0.01	0.457	0.188	-
U213	0.02	0.466	0.184	-
U214	0.03	0.473	0.180	-
U215	0.04	0.479	0.178	-
U041	0.05	0.483	0.173	46.2
U216	0.06	0.491	0.172	-
U217	0.08	0.499	0.167	-
U042	0.1	0.505	0.161	49.7
U218	0.15	0.522	0.153	-
U043	0.2	0.535	0.142	56.3
U219	0.25	0.547	0.136	-
U044	0.4	0.567	0.118	67.8
U045	0.6	0.587	0.102	78.4
U046	0.8	0.600	0.090	88.9
U047	1.0	0.610	0.081	98.8
U048	3.0	0.647	0.041	195
U049	5.0	0.658	0.028	286

Table 6.3: Parameters for a selection of simulations. ( $Re = 1000$ ,  $Rm = 500$ ,  $M = \beta = 0$ )

### 6.E.3 QG $M$ -varied Simulations

Name	$F^2$	$M$	Field-Varying Simulations				
			Sim $k_1$	Hydro $\sigma$	Actual $\sigma$	Ideal $k_1$	Max $\sigma$
U120	0.5	0.00	0.578	0.109	0.109	0.578	0.109
U121	0.5	0.005	0.578	0.109	0.109	0.578	0.109
U122	0.5	0.01	0.578	0.109	0.109	0.578	0.109
U123	0.5	0.02	0.578	0.109	0.109	0.578	0.109
U124	0.5	0.04	0.578	0.109	0.109	0.578	0.109
U125	0.5	0.06	0.578	0.109	0.109	0.578	0.109
U126	0.5	0.08	0.578	0.109	0.108	0.577	0.108
U127	0.5	0.10	0.578	0.109	0.107	0.575	0.107
U128	0.5	0.20	0.578	0.109	0.102	0.564	0.102
U129	0.5	0.30	0.578	0.109	0.092	0.546	0.093

Table 6.4: Table of the wavenumber,  $k$ , and growth rate,  $\sigma$ , expected in simulations with  $M \geq 0$  (central column) compared to the wavenumber from linear theory that maximises growth rate (right column).

# Chapter 7

## Conclusions

Shear instabilities are common dynamical features in many systems and, in the Sun, may be integral to the maintenance and development of the global differential rotation and magnetic field. Additionally, rotation (the Coriolis force) has an important role in the dynamics of astrophysical bodies on a wide range of scales yet previous studies into magnetohydrodynamic shear instabilities have neglected its effect (Chandrasekhar, 1961; Kent, 1966b; Hughes and Tobias, 2001; Mak et al., 2016, and many others). Here, we have introduced rotation using a rapidly rotating approximation, obtaining the quasigeostrophic shallow-water MHD equations (Zeitlin, 2013). These equations are based on the well-known quasigeostrophic (QG) equations, originally derived to model flows in the terrestrial atmosphere (Charney, 1948). Reduced models, such as the QG model, are excellent tools for investigating the interplay of physical effects (here: shear; rotation,  $\beta$ ; stratification,  $F^2$ ; and magnetic field,  $M$ ) when numerical efficiency is desired.

### 7.1 Summary

This thesis has investigated shear flow instabilities in the QG SWMHD model (Zeitlin, 2013), which can be derived, in the limit of rapid rotation, from the rSWMHD equations of Gilman (2000). In Chapter 2, we discussed some of the basic properties of this model, including deriving the dispersion relation of waves under the influence of a constant magnetic field and zonal flow. These waves possess some characteristics of Rossby and Alfvén waves but also feel the effect of stratification, since these waves move the free surface in their propagation thereby slowing them.

In Chapter 3, we attempted to derive general shear instability theorems from the linearised equations. Unsurprisingly, similar to 2DMHD (Kent, 1966b) and SWMHD (Mak, 2013), the criteria of Rayleigh (1913) and Fjørtoft (1950) proved impossible to extend usefully. Principally, this is because these theorems represent statements about the absolute vorticity profile and vorticity is not conserved in magnetohydrodynamic flows. A more fruitful investigation was the generalisation of the semicircle theorem of Howard (1961) (see also Chandra, 1973; Pedlosky, 1987; Hughes and Tobias, 2001; Mak et al., 2016). In this, we defined a semicircle (for  $F^2 > 0$ ) within which the complex phase speed of unstable modes must lie (also ex-

tending, in the absence of magnetic field, the result of Pedlosky 1987). Interestingly, unlike the semicircle of Hughes and Tobias (2001), this boundary does not tend to zero when the magnetic energy  $B^2$ , is greater than the kinetic energy  $U^2$ , suggesting the possible existence of instability in a regime previously assumed to be stable. So far though, we have been unable to find unstable modes of this kind.

Wave properties may be one way to explain some of the interesting features of the semicircle bound. Firstly, stratification introduces an upper bound on the speed of Rossby waves, perhaps leading to the finite extent of the semicircle (the radius is unbounded in the large wavenumber limit when  $F^2 = 0$ ). Secondly, the counter-propagating Rossby wave picture of instability suggests that the  $B^2 > U^2$  stability criterion arises since counter-propagating Rossby waves, which are sped up by an Alfvén factor in opposite directions, cannot phase-lock and induce instability. Given that we cannot prove the  $B^2 > U^2$  criterion, perhaps instability via a different mechanism, e.g. wave over-reflection, may be possible. This mechanism would act on Rossby waves propagating laterally on the planetary vorticity gradient.

These interesting results motivated the study of particular profiles, with a twofold aim: to investigate the instability mechanism and the combined effect of the physical parameters of rotation, stratification, and magnetic field ( $\beta$ ,  $F^2$ ,  $M^2$ ). To simplify the instability mechanism, we have only looked at uniform field profiles so that the instability mechanism is shear-driven and the magnetic field largely acts (initially) through magnetic tension. It would, of course, be interesting to study profiles with non-uniform magnetic field on otherwise stable shear profile (e.g. Kent, 1968; Chen and Morrison, 1991; Wang et al., 2022), and there is the famous magnetorotational instability of Balbus and Hawley (1998) which shows the possible destabilising effect of (a vertical) magnetic field on differentially rotating flows that are hydrodynamically stable.

Following the historical path, in Chapter 4 studied the piecewise constant vortex sheet velocity profile. This problem is simplified since the lateral structure of modes is limited to exponential decay away from an infinitesimally thin interface. However, this means the propagation of waves away from the interface, along the planetary vorticity gradient, is visible. This can be compared with the propagation of Rossby waves in the next profile, which has a combined planetary and shear vorticity gradient.

As the vortex sheet profile has piecewise constant velocity, the eigenvalue problem is straightforward and reduces to a cubic equation, similar to the dispersion relation of Kuo (1949) ( $\beta > 0$ ,  $F^2 = M = 0$ ). Kuo's dispersion relation has one real root and a complex conjugate pair of solutions. The root with a positive imaginary part of the eigenvalue ( $\text{I}(c) > 0$ ) corresponds to the unstable root. The QG SWMHD dispersion relation we derived possesses complex conjugate solutions if and only if  $M^2 < 1$ , with three real roots if  $M^2 > 1$ . This corresponds to the 2DMHD dispersion relation (Michael, 1955).

The vortex sheet problem can also be derived as the long-wavelength asymptotic limit of unbounded shear profiles that tend exponentially to a constant. In the limiting process, however, not only the wavenumber but also  $\beta$  and  $F^2$  are required to be asymptotically small. It is perhaps unsurprising, then, that the effect of these on the vortex sheet instability is limited. As  $F^2$  increases, the instability weakens slightly and the lateral extent of the eigenfunction decreases, corresponding to the inclusion of free surface effects. As  $\beta$  increases,

the phase speed of the instability becomes more westward, the growth rate decreases, and the eigenfunction becomes more wavelike. These features appear as the instability gains a Rossby wave-like character due to the planetary vorticity gradient.

An interesting limit is when  $\beta$  is non-zero and  $M^2 \rightarrow 1$ : the eigenvalue,  $c$ , tends to zero in this limit, and the eigenfunction becomes increasingly localised to the interface as the decay coefficient,  $\alpha_{\pm}$ , tends to infinity. This contrasts the independence of the eigenfunction from  $M^2$  when  $\beta = 0$  (and  $F^2 = 0$ ).

The tanh profile is a natural follow-up to the vortex sheet profile, since it smooths out the unphysical velocity profile discontinuity whilst analytical limits still exist. It has been well-studied, in various contexts, in the past (Garcia, 1956; Lin, 1955; Michalke, 1964; Dickinson and Clare, 1973; Drazin and Howard, 1966). Lin (1955) and Michalke (1964) found that an important effect of smoothing the discontinuity is the introduction of a short-wavelength stability boundary that does not exist for the vortex sheet profile. In the CRW description (Bretherton, 1966), the short-wavelength cutoff exists because there is a finite communication distance between Rossby waves on either side of inflexion points, where  $U'' = 0$ . The destabilising influence of CRWs is dampened over this gap, proportional to  $e^{kL}$  (Heifetz et al., 1999), where  $L$  is the wave separation.

Increasing  $M$  and  $\beta$  is stabilising and it becomes more difficult for CRWs to phase-lock, decreasing the short-wave cutoff. The stabilising influence of  $\beta$  overcomes the destabilising effect of reducing the gap between inflexion points, where  $\beta - U'' = 0$ . In the absence of magnetic field, increasing  $\beta$  also introduces a long-wavelength cutoff; as  $\beta$  is further increased, the gap between inflexion points closes and they are eventually eliminated, stabilising the flow as the long-wavelength and short-wavelength cutoffs are brought together (Kuo, 1949; Dickinson and Clare, 1973).

Stratification, measured by  $F^2$ , also has a stabilising influence but primarily affects the growth rate of the modes, since increasing  $F^2$  requires a conversion of more of the free (shear) kinetic energy into potential energy of the perturbation, rather than the perturbation kinetic energy; hence the growth rate of unstable modes is generally reduced. The wavenumber of the short wavelength cutoff increases slightly (bounded above by  $k = 1$ ) as  $F^2$  increases, and this effect may be due to a decrease in the potential vorticity gradient on the northern side of the domain, where the structure of the unstable mode decays more slowly, due to  $F^2$ .

The tanh profile also admits a second unstable mode when  $\beta > 0$  and  $M \lesssim 1$ . This was predicted by Drazin and Howard (1962) and found by Dickinson and Clare (1973) and is generally called the radiating mode due to its lateral structure (Talley, 1983), which is significantly more wavelike than the trapped mode (the unique mode when  $\beta = 0$ ). This mode may be better explained by over-reflection (e.g. Lindzen and Tung, 1978) than by CRWs. In kinematic ( $M = 0$ ) flows the radiating mode is subdominant and the eigenstructure of the trapped mode is the one that would develop in simulations. In MHD flows, we have found that the radiating mode can however be dominant, since magnetic tension stabilises short wavelength modes more.

In Chapter 6 we then investigated the nonlinear evolution of the tanh profile instability and the phenomena of flux expulsion and vortex disruption. Mak et al. (2017) and Kondic et al. (2024) have established that, in 2D MHD, vortex disruption occurs when  $M^2 \text{Rm} \sim 1$ , meaning

that even very weak large-scale magnetic fields can be condensed into strong small-scale fields that can disrupt the formation of large-scale structures such as vortices.

The first important result of Chapter 6 is that increasing  $F^2$  (the stratification) increases the magnetic field strength required to disrupt the vortex. This is a surprising result since we showed in Chapter 4 and Chapter 5 that increasing  $F^2$  reduces the shear instability growth rate and thus produces a weaker vortex which we might expect would be more easily disrupted. There seem to be two reasons for the decreased disruption. Firstly, the magnetic field that forms around the weakened vortex is itself weaker, and secondly, the geometry of the vortex reduces the curvature of the magnetic field and therefore reduces the Lorentz force and magnetic hoop stresses that act on the vortex.

## 7.2 Future Work

The equations of QG SWMHD are excellent for modelling large-scale phenomena in rapidly rotating astrophysical systems, e.g., the solar tachocline. One of the key advantages they possess, relative to the rSWMHD equations, is that the fastest (gravity) waves are filtered out so that simulations can be numerically stable with larger time steps. The gravity waves that are filtered out are not generally associated with vorticity propagation so, particularly in the context of shear instabilities, it is generally expected that the important dynamics of rotating shallow water are preserved in quasigeostrophic flows. This has been verified in hydrodynamic flows but not yet in magnetohydrodynamic ones, and therefore a clear route for further work is a comparison between these two models. In particular, Mak et al. (2016) found “tongues of instability” for arbitrary large Froude number,  $Fr$ , and  $M$  approaching unity. In Chapter 2 we require the Froude number to be  $\mathcal{O}(\text{Ro})$  (since  $F^2 = Fr/\text{Ro}$ ) and so features such as this can not be well-represented.

We also showed in Chapter 2 that an unbounded shear basic state is incompatible with the rotating shallow water equations due to an unbounded increase/decrease in the free-surface height. One way to compare the differences between rotating SWMHD and QG SWMHD would be to study the instability of a jet profile since this basic state is compatible with the rSWMHD and QG SWMHD equations. This would extend the linear instability work of Mak et al. (2016) and could also be extended to the nonlinear regime (Mak, 2013). Jet profiles may well be extremely relevant to the solar tachocline and other astrophysical systems. Some authors have also shown the existence of transient jets in the near-surface solar shear layer (e.g. Kuridze et al., 2016).

In Chapter 3 we established a finite semicircular bound on the complex phase speed of unstable modes, which does not tend to zero as  $M^2 \rightarrow 1$ ; it is independent of  $M^2$  when  $\beta > 0$ ,  $F^2 > 0$  and  $M^2$  is sufficiently small. This indicates that instability may be possible when  $M^2 > 1$ , although we have been unable to find it in this work. Another possibility is that the semicircle bound includes neutrally stable modes. In Chapter 4 we showed that there exist neutrally stable eigenmodes of the vortex sheet profile and these may be contiguous to the unstable radiating mode found in Chapter 5, which we also showed has an increased relevance when  $M^2 \lesssim 1$  since this mode can become dominant. One possible avenue for further investigating the radiating mode and the neutral boundary is to consider the profile of Talley (1983), which extends work done by Rayleigh (1913) and Chandrasekhar (1961) by using a profile that has

piecewise constant vorticity. This is important as it guarantees that the eigenvalue problem can be solved analytically like the vortex sheet profile; however, it also allows for unstable radiating modes to exist. Since the problem can be solved analytically, it is significantly easier to establish stability boundaries compared to the tanh profile where, as shown in Chapter 5, singularities of the governing equation make this a challenging endeavour.

In Chapter 6 we largely investigated cases where a single vortex emerges from the linear shear instability, expels flux, and can then develop a secondary instability. Naturally, this is not the only state that can emerge from linear instability; for example, several distinct vortices can be formed if the domain is enlarged along the  $x$ -axis. These vortices can then undergo a secondary vortex-pairing instability that will compete with the vortex disruption instability. The time scales of both instabilities are affected by the presence of rotation and stratification ( $\beta$  and  $F^2$ ), so different regimes may emerge.

We have also conducted preliminary investigations into the effect of  $\beta$  on vortex disruption. Analysis with  $\beta$ -variation is complicated by the non-zero phase speed of instability, which results in vortices moving relative to the mean flow frame. Initially, at least, vortex disruption is affected similarly by  $\beta$  as by  $F^2$ , with the lateral extent of vortices reduced, and disruption decreasing as  $\beta$  increases. This is due to the introduction of a constant potential vorticity gradient, far from the shear layer, as  $\beta$ ,  $F^2$ , become non-zero. A new regime will likely emerge when  $\beta \gtrsim 4/3\sqrt{3}$ , the (kinematic) stability boundary. The effect of  $\beta$  on vortex disruption is important to regions such as the solar tachocline where  $\beta$  is larger than  $F^2$ .



# Bibliography

- Acheson, D. J. and R. Hide (1973). Hydromagnetics of rotating fluids. *Reports on Progress in Physics* 36(2), 159.
- Alfvén, H. (1942). Existence of electromagnetic-hydrodynamic waves. *Nature* 150(3805), 405–406.
- Arnol'd, V. I. (1965). *Vladimir I. Arnol'd - Collected Works*. Springer, Berlin, Heidelberg.
- Balbus, S. A. and J. F. Hawley (1998). Instability, turbulence, and enhanced transport in accretion disks. *Reviews of modern physics* 70(1), 1.
- Balmforth, N. J. and P. J. Morrison (1999). A necessary and sufficient instability condition for inviscid shear flow. *Studies in Applied Mathematics* 102(3), 309–344.
- Batchelor, G. K. (1956). On steady laminar flow with closed streamlines at large Reynolds number. *Journal of Fluid Mechanics* 1(2), 177–190.
- Batchelor, G. K. (1967). *An Introduction to Fluid Dynamics*. Cambridge Mathematical Library. Cambridge University Press.
- Baty, H., R. Keppens, and P. Comte (2003). The two-dimensional magnetohydrodynamic Kelvin–Helmholtz instability: Compressibility and large-scale coalescence effects. *Physics of Plasmas* 10(12), 4661–4674.
- Blumen, W. (1972). Geostrophic adjustment. *Reviews of Geophysics* 10(2), 485–528.
- Boyd, J. P. (2001). *Chebyshev and Fourier Spectral Methods* (Second (Revised) ed.). Lecture Notes in Engineering. Mineola, NY: Dover Publications.
- Bretherton, F. P. (1966). Baroclinic instability and the short wavelength cut-off in terms of potential vorticity. *Quarterly Journal of the Royal Meteorological Society* 92(393), 335–345.
- Busse, F. H. (1994). Convection driven zonal flows and vortices in the major planets. *Chaos: An Interdisciplinary Journal of Nonlinear Science* 4, 123.
- Cally, P. S. (2000). A sufficient condition for instability in a sheared incompressible magnetofluid. *Solar Physics* 194, 189–196.
- Chandra, K. (1973). Hydromagnetic stability of plane heterogeneous shear flow. *Journal of the Physical Society of Japan* 34(2), 539–542.
- Chandrasekhar, S. (1961). *Hydrodynamic and Hydromagnetic Stability* (Dover ed.). International series of monographs on physics. Oxford University Press.
- Charbonneau, P. (2014). Solar Dynamo Theory. *Annual Review of Astronomy and Astrophysics* 52, 251–290.
- Charney, J. G. (1948). On the scale of atmospheric motions. *The Atmosphere - A Challenge* 17(2), 251–265.
- Chen, C.-C. and P. H. Diamond (2020). Potential vorticity mixing in a tangled magnetic field. *The Astrophysical Journal* 892(1), 24.

- Chen, X. L. and P. J. Morrison (1991). A sufficient condition for the ideal instability of shear flow with parallel magnetic field. *Physics of Fluids B: Plasma Physics* 3(4), 863–865.
- Christensen-Dalsgaard, J. (2002, Nov). Helioseismology. *Rev. Mod. Phys.* 74, 1073–1129.
- Christensen-Dalsgaard, J. and M. J. Thompson (2007). 3. observational results and issues concerning the tachocline. In D. Hughes, R. Rosner, and N. Weiss (Eds.), *The Solar Tachocline*, pp. 53–85. Cambridge University Press.
- Davies, C. R. and D. W. Hughes (2011). The mean electromotive force resulting from magnetic buoyancy instability. *The Astrophysical Journal* 727(2), 112.
- De Sterck, H. (2001). Hyperbolic theory of the “shallow water” magnetohydrodynamics equations. *Physics of Plasmas* 8(7), 3293–3304.
- de Szoëke, R. A. (1999). An improved bound for the complex phase speed of baroclinic instability. *Journal of Physical Oceanography* 29(1), 83–91.
- Dellar, P. J. (2002). Hamiltonian and symmetric hyperbolic structures of shallow water magnetohydrodynamics. *Physics of Plasmas* 9(4), 1130–1136.
- Dickinson, R. E. and F. J. Clare (1973). Numerical study of the unstable modes of a hyperbolic-tangent barotropic shear flow. *Journal of Atmospheric Sciences* 30(6), 1035–1049.
- Dikpati, M., P. S. Cally, and P. A. Gilman (2004). Linear analysis and nonlinear evolution of two-dimensional global magnetohydrodynamic instabilities in a diffusive tachocline. *The Astrophysical Journal* 610(1), 597.
- Dikpati, M. and P. A. Gilman (2001a). Analysis of hydrodynamic stability of solar tachocline latitudinal differential rotation using a shallow-water model. *The American Astronomical Society* 551(1), 536–564.
- Dikpati, M. and P. A. Gilman (2001b). Flux-transport dynamos with  $\alpha$ -effect from global instability of tachocline differential rotation: A solution for magnetic parity selection in the Sun. *The Astrophysical Journal* 559(1), 428.
- Dikpati, M., P. A. Gilman, and M. Rempel (2003). Stability analysis of tachocline latitudinal differential rotation and coexisting toroidal band using a shallow-water model. *The Astrophysical Journal* 596(1), 680.
- Dikpati, M., S. W. McIntosh, G. Bothun, P. S. Cally, S. S. Ghosh, P. A. Gilman, and O. M. Umurhan (2018). Role of interaction between magnetic Rossby waves and tachocline differential rotation in producing solar seasons. *The Astrophysical Journal* 853(2), 144.
- Drazin, P. G., D. N. Beaumont, and S. A. Coaker (1982). On Rossby waves modified by basic shear, and barotropic instability. *Journal of Fluid Mechanics* 124, 439–456.
- Drazin, P. G. and L. N. Howard (1962). The instability to long waves of unbounded parallel inviscid flow. *Journal of Fluid Mechanics* 14(2), 257–283.
- Drazin, P. G. and L. N. Howard (1966). Hydrodynamic stability of parallel flow of inviscid fluid. *Advances in Applied Mathematics* 9, 1–89.
- Dritschel, D. G., P. H. Diamond, and S. M. Tobias (2018). Circulation conservation and vortex breakup in magnetohydrodynamics at low magnetic Prandtl number. *Journal of Fluid Mechanics* 857, 38–60.
- Dritschel, D. G. and S. M. Tobias (2023). The magnetic non-hydrostatic shallow-water model. *Journal of Fluid Mechanics* 973, A17.
- Duguid, C. D., P. J. Bushby, and T. S. Wood (2023). Shear-driven magnetic buoyancy in the solar tachocline: The mean electromotive force due to rotation. *Monthly Notices of the Royal Astronomical Society* 520(1), 527–541.
- Eckart, C. (1963). Extension of Howard’s circle theorem to adiabatic jets. *The Physics of Fluids* 6(8), 1042–1047.

- Fedotova, M. A., D. A. Klimachkov, and A. S. Petrosyan (2020). The shallow-water magnetohydrodynamic theory of stratified rotating astrophysical plasma flows: Beta-plane approximation and magnetic Rossby waves. *Plasma Physics Reports* 46, 50–64.
- Fjørtoft, R. (1950). *Application of integral theorems in deriving criteria of stability for laminar flows and for the baroclinic circular vortex*. Grøndahl & søns boktr., I kommisjon hos Cammermeyers boghandel.
- Foote, J. R. and C. C. Lin (1950). Some recent investigations in the theory of hydrodynamic stability. *Quarterly of Applied Mathematics* 8(3), 265–280.
- Frank, A., T. W. Jones, D. Ryu, and J. B. Gaalaas (1996). The magnetohydrodynamic Kelvin–Helmholtz instability: A two-dimensional numerical study. *Astrophysical Journal* 460, 777–793.
- Fraser, A. E., P. W. Terry, E. G. Zweibel, M. J. Pueschel, and J. M. Schroeder (2021). The impact of magnetic fields on momentum transport and saturation of shear-flow instability by stable modes. *Physics of Plasmas* 28(2), 022309.
- Garcia, R. V. (1956). Barotropic waves in straight parallel flow with curved velocity profile. *Tellus* 8(1), 82–93.
- Gilbert, A. D., S. D. Griffiths, and D. W. Hughes (2025). Magnetic diffusion and dynamo action in shallow water magnetohydrodynamics. In review.
- Gilbert, A. D., J. Mason, and S. M. Tobias (2016). Flux expulsion with dynamics. *Journal of Fluid Mechanics* 791, 568–588.
- Gilbert, A. D., X. Riedinger, and J. Thuburn (2014). On the form of the viscous term for two dimensional Navier–Stokes flows. *Quarterly Journal of Mechanics and Applied Mathematics* 67(2), 205–228.
- Gill, A. E. (1982). *Atmosphere-ocean dynamics*, Volume 30. Academic press.
- Gilman, P. A. (1969). Baroclinic, Alfvén and Rossby waves in geostrophic flow. *Journal of Atmospheric Sciences* 26(5), 1003–1009.
- Gilman, P. A. (2000). Magnetohydrodynamic “shallow water” equations for the solar tachocline. *The Astrophysical Journal Letters* 544(1), L79.
- Gilman, P. A. and M. Dikpati (2002). Analysis of instability of latitudinal differential rotation and toroidal field in the solar tachocline using a magnetohydrodynamic shallow-water model. i. instability for broad toroidal field profiles. *The Astrophysical Journal* 576(2), 1031.
- Gilman, P. A. and P. A. Fox (1997, jul). Joint instability of latitudinal differential rotation and toroidal magnetic fields below the solar convection zone. *The Astrophysical Journal* 484(1), 439.
- Gnevyshev, V. G. and V. I. Shvira (1990). On the evaluation of barotropic-baroclinic instability parameters of zonal flows on a beta-plane. *Journal of Fluid Mechanics* 221, 161–181.
- Gough, D. (2007). 1. an introduction to the solar tachocline. In D. Hughes, R. Rosner, and N. Weiss (Eds.), *The Solar Tachocline*, pp. 3–30. Cambridge University Press.
- Green, S. I. (1995). *Fluid Vortices*, Volume 30 of *Fluid Mechanics And Its Applications*. Dordrecht: Kluwer Academic Publishers.
- Griffiths, S. D. (2008). The limiting form of inertial instability in geophysical flows. *Journal of Fluid Mechanics* 605, 115–143.
- Griffiths, S. D. (2021). Private communication.
- Gupta, A. S. (1992). Hydromagnetic stability of a stratified parallel flow varying in two directions. *Astrophys Space Sci* 198, 95–100.
- Hale, G. E. (1908). On the probable existence of a magnetic field in sun-spots. *Terrestrial Magnetism and Atmospheric Electricity* 13(4), 159–160.
- Hall, R. E. (1980). A note on a semicircle theorem. *Dynamics of Atmospheres and Oceans* 5(2), 113–121.

- Hasegawa, H., M. Fujimoto, T.-D. Phan, H. Reme, A. Balogh, M. W. Dunlop, C. Hashimoto, and R. TanDokoro (2004). Transport of solar wind into Earth's magnetosphere through rolled-up Kelvin–Helmholtz vortices. *Nature* 430(7001), 755–758.
- Hasimoto, H. (1969). Note on hydromagnetic stability of three-dimensional parallel flow. *Journal of the Physical Society of Japan* 27(3), 798–798.
- Heifetz, E., C. H. Bishop, and P. Alpert (1999). Counter-propagating rossby waves in the barotropic rayleigh model of shear instability. *Quarterly Journal of the Royal Meteorological Society* 125(560), 2835–2853.
- Heifetz, E. and J. Mak (2014). Magnetohydrodynamic shear instabilities arising from interacting vorticity waves. *WIT Transactions on Engineering Sciences* 82, 371–380.
- Heifetz, E., J. Mak, J. Nycander, and O. M. Umurhan (2015). Interacting vorticity waves as an instability mechanism for MHD shear instabilities. *arXiv.org* 767, 199–225.
- Heifetz, E. and J. Methven (2005). Relating optimal growth to counterpropagating Rossby waves in shear instability. *Physics of Fluids* 17(6), 064107.
- Heinonen, R. A., P. H. Diamond, M. F. D. Katz, and G. E. Ronimo (2023). Generation of momentum transport in weakly turbulent  $\beta$ -plane magnetohydrodynamics. *Phys. Rev. E* 107, 025202.
- Held, I. M., R. T. Pierrehumbert, S. T. Garner, and K. L. Swanson (1995). Surface quasi-geostrophic dynamics. *Journal of Fluid Mechanics* 282, 1–20.
- Helmholtz, H. (1868). On discontinuous fluid motions. *Phil. Mag* 36(4), 337–346.
- Heng, K. and A. Spitkovsky (2009, sep). Magnetohydrodynamic shallow water waves: Linear analysis. *The Astrophysical Journal* 703(2), 1819–1831.
- Hide, R. (1969). On hydromagnetic waves in a stratified rotating incompressible fluid. *Journal of Fluid Mechanics* 39(2), 283–287.
- Hillier, A. (2020). Ideal MHD instabilities, with a focus on the Rayleigh–Taylor and Kelvin–Helmholtz instabilities. In D. MacTaggart and A. Hillier (Eds.), *Topics in magnetohydrodynamic topology, reconnection and stability theory*, Volume 591 of *CISM International Centre for Mechanical Sciences: Courses and Lectures*, Chapter 1, pp. 1–36. Springer.
- Høiland, E. (1953). On two-dimensional perturbation of linear flow. *Geofys. Publ.* 18(9), 1–12.
- Holton, J. R. (1979). Equatorial wave-mean flow interaction: A numerical study of the role of latitudinal shear. *Journal of Atmospheric Sciences* 36(6), 1030–1040.
- Horstmann, G. M., G. Mamatsashvili, A. Giesecke, T. V. Zaqarashvili, and F. Stefani (2023). Tidally forced planetary waves in the tachocline of solar-like stars. *The Astrophysical Journal* 944(1), 48.
- Howard, L. N. (1961). Note on a paper of John W. Miles. *Journal of Fluid Mechanics* 10(4), 509–512.
- Howard, L. N. (1964). The number of unstable modes in hydrodynamic stability problems. *Journal de mécanique* 8, 433–443.
- Howard, L. N. and P. G. Drazin (1964). On instability of parallel flow of inviscid fluid in a rotating system with variable coriolis parameter journal of mathematics and physics. *Journal of Mathematics and Physics* 43(1-4), 83–99.
- Huerre, P. and M. Rossi (1998). Hydrodynamic instabilities in open flows. In C. Godrèche (Ed.), *Hydrodynamics and nonlinear instabilities*, Chapter 02, pp. 81–294. Cambridge University Press.
- Hughes, D. W. and S. M. Tobias (2001). On the instability of magnetohydrodynamic shear flows. *The Royal Society* 457(2010), 1365–1384.
- Hunt, J., A. Wray, and P. Moin (1988). Eddies, streams, and convergence zones in turbulent flows. In *Studying Turbulence Using Numerical Simulation Databases, 2. Proceedings of the 1988 Summer Program*, pp. 193–208.

- Hunter, S. (2015). *Waves in Shallow Water Magnetohydrodynamics*. Ph. D. thesis, University of Leeds.
- Hwang, K.-J., K. Dokgo, E. Choi, J. L. Burch, D. G. Sibeck, B. L. Giles, H. Hasegawa, H. S. Fu, Y. Liu, Z. Wang, et al. (2020). Magnetic reconnection inside a flux rope induced by Kelvin–Helmholtz vortices. *Journal of Geophysical Research: Space Physics* 125(4), e2019JA027665.
- Hwang, K.-J., J. M. Weygand, D. G. Sibeck, J. L. Burch, M. L. Goldstein, C. P. Escoubet, E. Choi, K. Dokgo, B. L. Giles, C. J. Pollock, et al. (2022). Kelvin–Helmholtz vortices as an interplay of magnetosphere-ionosphere coupling. *Frontiers in Astronomy and Space Sciences* 9, 895514.
- Isern-Fontanet, J., E. García-Ladona, and J. Font (2006). Vortices of the Mediterranean Sea: An altimetric perspective. *Journal of physical oceanography* 36(1), 87–103.
- Jeffreys, H. (1926). On the dynamics of geostrophic winds. *Quart. J. Roy. Meteor. Soc* 52(217), 85–104.
- Jones, C. A., J. Rotvig, and A. Abdulrahman (2003). Multiple jets and zonal flow on Jupiter. *Geophysical Research Letters* 30(14), 906.
- Jones, C. A., M. J. Thompson, and S. M. Tobias (2010). The solar dynamo. *Space Science Reviews* 152, 591–616.
- Jones, T. W., J. B. Gaalaas, D. Ryu, and A. Frank (1997). The MHD Kelvin–Helmholtz instability. II. the roles of weak and oblique fields in planar flows. *The Astrophysical Journal* 482(1), 230.
- Kent, A. (1966a). Instability of laminar flow of a perfect magnetofluid. *The Physics of Fluids* 9(7), 1286–1289.
- Kent, A. (1966b). *Stability of laminar flows of a perfect magnetofluid*. Ph. D. thesis, University of Glasgow.
- Kent, A. (1968). Stability of laminar fluid flow along a parallel field. *Journal of Plasma Physics* 2(4), 543–556.
- Keppens, R., G. Tóth, R. H. J. Westermann, and J. P. Goedbloed (1999). Growth and saturation of the Kelvin–Helmholtz instability with parallel and antiparallel magnetic fields. *Journal of Plasma Physics* 61(1), 1–19.
- Kerswell, R. R. (2002). Elliptical instability. *Annual Review of Fluid Mechanics* 34 (Volume 34, 2002), 83–113.
- Kondic, T., S. Griffiths, and D. Hughes (2024). The scaling of the magnetic field due to flux expulsion. In prep.
- Krause, F. and K.-H. Rädler (2016). *Mean-field magnetohydrodynamics and dynamo theory*. Elsevier.
- Kravtsov, S. and G. Reznik (2020). Monopoles in a uniform zonal flow on a quasi-geostrophic-plane: Effects of the Galilean non-invariance of the rotating shallow-water equations. *Journal of Fluid Mechanics* 909, A23.
- Kundu, P. K. and I. M. Cohen (2002). *Fluid Mechanics* (Second ed.). San Diego: Academic Press.
- Kuo, H.-I. (1949). Dynamic instability of two-dimensional nondivergent flow in a barotropic atmosphere. *Journal of Atmospheric Sciences* 6, 105–122.
- Kuridze, D., T. V. Zaqarashvili, V. Henriques, M. Mathioudakis, F. P. Keenan, and A. Hanslmeier (2016). Kelvin–Helmholtz instability in solar chromospheric jets: theory and observation. *The Astrophysical Journal* 830(2), 133.
- Lahaye, N. and V. Zeitlin (2022). Coherent magnetic modon solutions in quasi-geostrophic shallow water magnetohydrodynamics. *Journal of Fluid Mechanics* 941, A15.
- Lamb, H. (1993). *Hydrodynamics* (Sixth ed.). Cambridge Mathematical Library. Cambridge University Press.
- Lighthill, M. J. (1957). The fundamental solution for small steady three-dimensional disturbances to a two-dimensional parallel shear flow. *Journal of Fluid Mechanics* 3(2), 113–144.
- Lin, C. C. (1945). On the stability of two-dimensional parallel flows: Part I. general theory. *Quarterly of Applied Mathematics* 3(2), 117–142.
- Lin, C. C. (1955). *The theory of hydrodynamic stability* (Reprinted with corrections. ed.). Cambridge monographs on mechanics and applied mathematics. Cambridge: Oxford University Press.

- Lindzen, R. S. (1988). Instability of plane parallel shear flow (toward a mechanistic picture of how it works). *pure and applied geophysics* 126, 103–121.
- Lindzen, R. S. and J. W. Barker (1985). Instability and wave over-reflection in stably stratified shear flow. *Journal of Fluid Mechanics* 151, 189–217.
- Lindzen, R. S. and K. K. Tung (1978). Wave overreflection and shear instability. *Journal of Atmospheric Sciences* 35(9), 1626 – 1632.
- Lipps, F. B. (1962). The barotropic stability of the mean winds in the atmosphere. *Journal of Fluid Mechanics* 12, 397–407.
- Lipps, F. B. (1965). The stability of an asymmetric zonal current in the atmosphere. *Journal of Fluid Mechanics* 21(2), 225–239.
- Lipps, F. B. (1970). Barotropic stability and tropical disturbances. *Monthly Weather Review* 98(2), 122–131.
- Majda, A. and X. Wang (2006). *Nonlinear dynamics and statistical theories for basic geophysical flows*. Cambridge University Press.
- Mak, J. (2013). *Shear instabilities in shallow-water magnetohydrodynamics*. Ph. D. thesis, University of Leeds.
- Mak, J., S. D. Griffiths, and D. W. Hughes (2016). Shear flow instabilities in shallow-water magnetohydrodynamics. *Journal of Fluid Mechanics* 788, 767–796.
- Mak, J., S. D. Griffiths, and D. W. Hughes (2017). Vortex disruption by magnetohydrodynamic feedback. *Physical Review Fluids* 2, 113701.
- Malagoli, A., G. Bodo, and R. Rosner (1996). On the nonlinear evolution of magnetohydrodynamic Kelvin–Helmholtz instabilities. *Astrophysical Journal* v. 456, p. 708–718.
- Marche, F. (2007). Derivation of a new two-dimensional viscous shallow water model with varying topography, bottom friction and capillary effects. *European Journal of Mechanics - B/Fluids* 26(1), 49–63.
- McIntyre, M. E. and M. A. Weissman (1978). On radiating instabilities and resonant overreflection. *Journal of Atmospheric Sciences* 35(7), 1190 – 1196.
- Michael, D. H. (1953). Stability of plane parallel flows of electrically conducting fluids. *Mathematical Proceedings of the Cambridge Philosophical Society* 49(1), 166–168.
- Michael, D. H. (1955). The stability of a combined current and vortex sheet in a perfectly conducting fluid. *Mathematical Proceedings of the Cambridge Philosophical Society* 51(3), 528–532.
- Michalke, A. (1964). On the inviscid instability of the hyperbolic tangent velocity profile. *Journal of Fluid Mechanics* 19(4), 543–556.
- Miesch, M. S. (2005). Large-scale dynamics of the convection zone and tachocline. *Living Reviews in Solar Physics* 2(1), 1–139.
- Miesch, M. S., A. S. Brun, and J. Toomre (2006). Solar differential rotation influenced by latitudinal entropy variations in the tachocline. *The Astrophysical Journal* 641, 618–625.
- Miles, J. W. (1958). On the disturbed motion of a plane vortex sheet. *Journal of Fluid Mechanics* 4, 538–552.
- Miles, J. W. (1961). On the stability of heterogeneous shear flows. *Journal of Fluid Mechanics* 10(4), 496–508.
- Moffatt, H. K. (1978). *Field generation in electrically conducting fluids*. Cambridge University Press, Cambridge, London, New York, Melbourne.
- Moffatt, H. K. and H. Kamkar (1983). The time-scale associated with flux expulsion. In A. M. Soward (Ed.), *Stellar and Planetary Magnetism, Proceedings of the Workshop held 25-29 August, 1980 in Budapest, Hungary*, pp. 91. New York: Gordon and Breach Science.
- Morse, P. M. and H. Feshbach (1953). *Methods of Theoretical Physics*. International Series in Pure and Applied Physics. New York: McGraw-Hill.

- Márquez-Artavia, X., C. A. Jones, and S. M. Tobias (2017). Rotating magnetic shallow water waves and instabilities in a sphere. *Geophysical & Astrophysical Fluid Dynamics* 111(4), 282–322.
- Northrop, T. G. (1956). Helmholtz instability of a plasma. *Physical Review Journals* 103(5), 1150–1154.
- Obukhov, A. M. (1949). On the problem of geostrophic wind. *Izvestija – Geography and Geophysics* 13, 281–306. In Russian.
- Okubo, A. (1970). Horizontal dispersion of floatable particles in the vicinity of velocity singularities such as convergences. *Deep Sea Research and Oceanographic Abstracts* 17(3), 445–454.
- Palotti, M. L., F. Heitsch, E. G. Zweibel, and Y.-M. Huang (2008). Evolution of unmagnetized and magnetized shear layers. *The Astrophysical Journal* 678(1), 234.
- Parker, E. N. (1955). Hydromagnetic dynamo models. *Astrophysical Journal* 122, 293.
- Parker, R. L. (1966). Reconnexion of lines of force in rotating spheres and cylinders. *Proceedings of the Royal Society of London. Series A. Mathematical and Physical Sciences* 291(1424), 60–72.
- Pedlosky, J. (1963). Baroclinic instability in two-layer systems. *Tellus* 15(1), 20–25.
- Pedlosky, J. (1964). The stability of currents in the atmosphere and the ocean: Part I. *Journal of Atmospheric Sciences* 21(2), 201–219.
- Pedlosky, J. (1987). *Geophysical Fluid Dynamics* (Second ed.). Springer New York.
- Petrosyan, A., D. Klimachkov, M. Fedotova, and T. Zinyakov (2020). Shallow water magnetohydrodynamics in plasma astrophysics. waves, turbulence, and zonal flows. *Atmosphere* 11(4), 314.
- Peyret, R. (2002). *Spectral methods for incompressible viscous flow*, Volume 148 of *Applied Mathematical Sciences*. Springer.
- Prandtl, L. (1904). Über Flüssigkeitsbewegung bei sehr kleiner Reibung (‘On fluid motion with very small friction.’). *Verhandl. d. III Intl. Math. Kongr., Heidelberg, Germany (also NACA Tech. Memo)* 452, 484–491.
- Priest, E. (2014). *Magnetohydrodynamics of the Sun*. Cambridge University Press.
- Raphaldini, B., M. Dikpati, S. McIntosh, and A. S. W. Teruya (2024). Spectra of solar shallow-water waves from bright point observations. *Astronomy & Astrophysics* 692, A102.
- Raphaldini, B., M. Dikpati, and C. F. M. Raupp (2023). Quasi-geostrophic MHD equations: Hamiltonian formulation and nonlinear stability. *Comp. Appl. Math.* 42, 57.
- Raphaldini, B. and C. Raupp (2020). Nonlinear MHD Rossby wave interactions and persistent geomagnetic field structures. *Proceedings of the Royal Society A* 476(2241), 20200174.
- Ray, T. P. and A. I. Ershkovich (1983, 10). Kelvin–Helmholtz instabilities in a sheared compressible plasma. *Monthly Notices of the Royal Astronomical Society* 204(3), 821–831.
- Rayleigh, L. (1880). On the stability, or instability, of certain fluid motions. *Proc. London Math. Soc.* 9, 57–70.
- Rayleigh, L. (1913). On the stability of the laminar motion of an inviscid fluid. *Cambridge University Press* 6, 1001–1010.
- Read, P., D. Kennedy, N. Lewis, H. Scolan, F. Tabataba-Vakili, Y. Wang, S. Wright, and R. Young (2020). Baroclinic and barotropic instabilities in planetary atmospheres: energetics, equilibration and adjustment. *Nonlinear Processes in Geophysics* 27(2), 147–173.
- Reznik, G. M. (2010). Dynamics of localized vortices on the beta plane. *Izvestiya, Atmospheric and Oceanic Physics* 46, 784–797.
- Rhines, P. B. (1975). Waves and turbulence on a beta-plane. *Journal of Fluid Mechanics* 69(3), 417–443.

- Rhines, P. B. and W. R. Young (1982). Homogenization of potential vorticity in planetary gyres. *Journal of Fluid Mechanics* 122, 347–367.
- Rhines, P. B. and W. R. Young (1983). How rapidly is a passive scalar mixed within closed streamlines? *Journal of Fluid Mechanics* 133, 133–145.
- Rossby, C.-G. (1939). Relation between variations in the intensity of the zonal circulation of the atmosphere and the displacements of the semi-permanent centers of action. *Journal of Marine Research* 2, 38–55.
- Satomura, T. (1981). An investigation of shear instability in a shallow water. *Journal of the Meteorological Society of Japan* 59(1), 148–167.
- Schecter, D. A., J. F. Boyd, and P. A. Gilman (2001). “Shallow-water” magnetohydrodynamic waves in the solar tachocline. *The Astrophysical Journal* 551(2), L185.
- Schmitt, D. (1993). The solar dynamo. In *Symposium-International Astronomical Union*, Volume 157, pp. 1–12. Cambridge University Press.
- Schou, J., H. M. Antia, S. Basu, R. S. Bogart, R. I. Bush, S. M. Chitre, J. Christensen-Dalsgaard, M. P. D. Mauro, W. A. Dziembowski, A. Eff-Darwich, et al. (1998). Helioseismic studies of differential rotation in the solar envelope by the solar oscillations investigation using the Michelson Doppler Imager. *The Astrophysical Journal* 505(1), 390.
- Shivamoggi, B. K. and D. K. Rollins (2001). Linear stability theory of zonal shear flows with a free surface. *Geophysical and Astrophysical Fluid Dynamics* 95, 31–53.
- Spiegel, E. A. (2007). 2. reflections on the solar tachocline. In D. Hughes, R. Rosner, and N. Weiss (Eds.), *The Solar Tachocline*, pp. 31–50. Cambridge University Press.
- Spiegel, E. A. and J.-P. Zahn (1992, November). The solar tachocline. *Astron. Astrophys.* 265, 106–114.
- Squire, H. B. (1933). On the stability of three-dimensional disturbances of viscous fluid flow between parallel walls. *Proceedings of the Royal Society of London* 142, 621–628.
- Synge, J. L. (1933). The stability of heterogeneous liquids. *Transactions of the Royal Society of Canada* 27, 1.
- Talley, L. D. (1983). Radiating barotropic instability. *Journal of Physical Oceanography* 13(6), 972 – 987.
- Tao, L., M. R. E. Proctor, and N. O. Weiss (1998). Flux expulsion by inhomogeneous turbulence. *Monthly Notices of the Royal Astronomical Society* 300(3), 907–914.
- Taylor, G. I. (1915). I. eddy motion on the atmosphere. *Philosophical Transactions of the Royal Society A* 215, 1–26.
- Teruya, A. S. W., B. Raphaldini, and C. F. M. Raupp (2022). Ray tracing of MHD Rossby waves in the solar tachocline: Meridional propagation and implications for the solar magnetic activity. *Frontiers in Astronomy and Space Sciences* 9, 856912.
- Thelen, J.-C. (2000). Non-linear  $\alpha\omega$ -dynamoes driven by magnetic buoyancy. *Monthly Notices of the Royal Astronomical Society* 315(1), 165–183.
- Thompson, M. J., J. Christensen-Dalsgaard, M. S. Miesch, and J. Toomre (2003). The internal rotation of the Sun. *Annual Review of Astronomy and Astrophysics* 41(1), 599–643.
- Thomson, W. (1871). Hydrokinetic solutions and observations. *The London, Edinburgh, and Dublin Philosophical Magazine and Journal of Science* 42(281), 362–377.
- Thual, O. (1986). *Transition vers la turbulence dans des systèmes dynamiques apparentés à la convection*. Ph. D. thesis, Nice.
- Thuburn, J. and P. Haynes (1996). Bounds on the growth rate and phase velocity of instabilities in a non-divergent barotropic flow on a sphere: A semicircle theorem. *Quarterly Journal of the Royal Meteorological Society* 122(531), 779–787.

- Ting, A. C., W. H. Matthaeus, and D. Montgomery (1986). Turbulent relaxation processes in magnetohydrodynamics. *The Physics of fluids* 29(10), 3261–3274.
- Tobias, S. M., P. H. Diamond, and D. W. Hughes (2007).  $\beta$ -plane magnetohydrodynamic turbulence in the solar tachocline. *The Astrophysical Journal* 667(1), L113.
- Tobias, S. M. and N. O. Weiss (2007). 13. the solar dynamo and the tachocline. In D. W. Hughes, R. Rosner, and N. O. Weiss (Eds.), *The Solar Tachocline*, pp. 319–346. Cambridge University Press.
- Tollmien, W. (1935). Ein allgemeines Kriterium der Instabilität laminarer Geschwindigkeits-verteilungen. *Nachr. Wiss Fachgruppe, Göttingen, Math. Phys.* 1, 79.
- Umurhan, O. M. (2013). The equations of magnetoquasigeostrophy. arXiv preprint arXiv:1301.0285.
- Vallis, G. K. (2017). *Atmospheric and oceanic fluid dynamics : Fundamentals and large-scale circulation* (Second ed.). Cambridge University Press.
- Vasil, G. M., K. Julien, and N. A. Featherstone (2021). The rotational influence on solar convection. *PNAS* 118(31), e2022518118.
- Wang, C., A. Gilbert, and J. Mason (2022). Critical-layer instability of shallow-water magnetohydrodynamic shear flows. *Journal of Fluid Mechanics* 943, A24.
- Wasow, W. (1948). The complex asymptotic theory of a fourth order differential equation of hydrodynamics. *Annals of Mathematics* 49(4), 852–871.
- Watson, M. (1980). Shear instability of differential rotation in stars. *Geophysical & Astrophysical Fluid Dynamics* 16(1), 285–298.
- Waugh, D. W., E. R. Abraham, and M. M. Bowen (2006). Spatial variations of stirring in the surface ocean: A case study of the Tasman Sea. *Journal of Physical Oceanography* 36(3), 526–542.
- Weiss, J. (1991). The dynamics of enstrophy transfer in two-dimensional hydrodynamics. *Physica D: Nonlinear Phenomena* 48(2-3), 273–294.
- Weiss, N. O. (1964). Convection in the presence of restraints. *Philosophical Transactions of the Royal Society of London. Series A, Mathematical and Physical Sciences* 256(1067), 99–147.
- Weiss, N. O. (1966). The expulsion of magnetic flux by eddies. *Proceedings of the Royal Society of London. Series A. Mathematical and Physical Sciences* 293(1434), 310–328.
- Yavneh, I., J. C. McWilliams, and M. J. Molemaker (2001). Non-axisymmetric instability of centrifugally stable stratified Taylor–Couette flow. *Journal of Fluid Mechanics* 448, 1–21.
- Zaqarashvili, T. V., M. Albekioni, J. L. Ballester, Y. Bekki, L. Biancofiore, A. C. Birch, M. Dikpati, L. Gizon, E. Gurgenashvili, E. Heifetz, et al. (2021). Rossby waves in astrophysics. *Space Science Reviews* 217, 1–93.
- Zaqarashvili, T. V., R. Oliver, and J. L. Ballester (2009). Global shallow water magnetohydrodynamic waves in the solar tachocline. *The Astrophysical Journal* 691(1), L41–L44.
- Zaqarashvili, T. V., R. Oliver, J. L. Ballester, and B. M. Shergelashvili (2007). Rossby waves in “shallow water” magnetohydrodynamics. *Astronomy & Astrophysics* 470(3), 815–820.
- Zeitlin, V. (2007). *Nonlinear dynamics of rotating shallow water*, Volume 2 of *Edited series on advances in nonlinear science and complexity*. Amsterdam ; London : Elsevier Science.
- Zeitlin, V. (2013). Remarks on rotating shallow-water magnetohydrodynamics. *Nonlinear Processes in Geophysics* 20, 893–898.
- Zeitlin, V., C. Lusso, and F. Bouchut (2015). Geostrophic vs magneto-geostrophic adjustment and nonlinear magneto-inertia-gravity waves in rotating shallow water magnetohydrodynamics. *Geophysical & Astrophysical Fluid Dynamics* 109(5), 497–523.